



## Synthesis, Characterisation and Analysis of Ruthenium Pincer Complexes with Strongly -acidic Ligands

**Jørgensen, Mike S.B.**

*Publication date:*  
2022

*Document Version*  
Publisher's PDF, also known as Version of record

[Link back to DTU Orbit](#)

*Citation (APA):*  
Jørgensen, M. S. B. (2022). Synthesis, Characterisation and Analysis of Ruthenium Pincer Complexes with Strongly -acidic Ligands. DTU Chemistry.

---

### General rights

Copyright and moral rights for the publications made accessible in the public portal are retained by the authors and/or other copyright owners and it is a condition of accessing publications that users recognise and abide by the legal requirements associated with these rights.

- Users may download and print one copy of any publication from the public portal for the purpose of private study or research.
- You may not further distribute the material or use it for any profit-making activity or commercial gain
- You may freely distribute the URL identifying the publication in the public portal

If you believe that this document breaches copyright please contact us providing details, and we will remove access to the work immediately and investigate your claim.



---

# Synthesis, Characterisation and Analysis of Ruthenium Pincer Complexes with Strongly $\pi$ -acidic Ligands

PhD thesis

---

Author:

Mike S.B. Jørgensen

Supervisors:

Martin Nielsen

Susanne Lis Mossin

Kgs. Lyngby, January 2022



*Non fasces nec opes, sola artis sceptrā perennant*  
Tycho Brahe



THIS PAGE IS INTENTIONALLY LEFT BLANK.

To:  
Nikolaj, Villads and Saphina

# Preface

In the interface between inorganic and organic chemistry the best of two worlds is found, namely, organometallic chemistry. Even though this field dates back to Cadet's "*liqueur fumante de l'arsenic*" in the mid 18<sup>th</sup> century it is only within the last six or seven decades organometallic chemistry have gained its rightful attention. In the still increasing list of interesting, novel organometallic compounds scientists have over the years put efforts into understanding the novel chemical bonding motifs that have both directly and indirectly furnished the development of general bonding theories. Not only has organometallic chemistry been of great interest to academia but also the chemical industry has greatly benefitted from the development of *Grignard* and *Friedel-Crafts* reagents. More recently, organometallic compounds are of vast importance to processes such as those named after *Ziegler* and *Natta*, *Fischer* and *Tropsch*, but industrial synthetic procedures originally developed by *Knowels* and *Grubbs* are also getting evermore so important.

The increasing demand for energy and the climate changes have forced the research in *green chemistry* to develop with an unprecedented pace. In this regard, organometallic compounds are of great potential as these species often show remarkable catalytic activity in a variety of different transformations with high selectivity while operating under mild conditions. Thus, the development of protocols to rationally designed complexes that shows the desired reactivity and selectivity are of crucial importance.

The work presented in this thesis will hopefully contribute to the development of new highly active catalysts, mainly focused on hydrogenation reactions. Equally important, it is the author's hope that this thesis can contribute to the fundamental understanding of the chemical properties and reactivity patterns of zero-valent ruthenium complexes exhibiting rare bonding motifs.

This PhD thesis represents the work that was conducted between May 2018 - September 2021 as a part of the PhD studies of the present writer. The work was performed under the supervision of Assoc Prof Martin Nielsen and Assoc Prof Susanne Lis Mossin at the Department of Chemistry, Technical University of Denmark.

# Acknowledgments

During my PhD studies I have met many persons who have encouraged, inspired and helped me during the project.

First and foremost, I would like to thank my supervisor Martin Nielsen for allowing me to work on this project. I have not only been introduced to the exciting and versatile chemistry of ruthenium, but I have also been introduced to the overwhelmingly many possibilities within the frameworks of organometallic chemistry and its applications. Especially, I am thankful that my supervisor has been easily approachable and has always taken the time, even when he had little time himself, to answer my questions related to the chemistry that comprise this project. Additionally, I am thankful that my secondary supervisor Susanne Lis Mossin has shown interest in my project and has always been willing to answer my questions related to both chemistry and spectroscopy.

During my PhD studies I spent 2 months (the stay was shortened due to the Covid-19 pandemic) at the Department of Inorganic Chemistry at the Georg-August University in Göttingen, Germany, in the group of Prof. Sven Schneider. I am thankful that Prof. Schneider would host my external stay, which greatly refined my technical skills and knowledge regarding low-valent pincer complexes and complexes with peculiar spin states. I am deeply grateful for the many fruitful discussions regarding my project in which Prof. Schneider took great interest. In addition, I would like to thank his group for the great and friendly accommodation which was given. Especially, I would like to thank Dr Daniel Delony who mentored me during my stay in the Schneider group. He, more than anyone, taught me the necessary techniques required to handle the chemistry that made up my project.

During my studies, I had the pleasure to share the laboratory with Mathias Thor Nielsen, Alexander Tobias Nikol and Dr Danielle Lobo Nielsen. Their joyful spirit and humor, although of fluctuating quality, as well as their discussions about chemistry have been both educating and made a pleasant setting for my studies. Additionally, I would like to thank Luca Piccirilli and Mathias Thor Nielsen for their invaluable discussions about my project and their friendship. I am especially thankful for the outstanding proofreading

provided by Alexander Tobias Nikol.

I would like to thank the entire Martin Nielsen group which has always been ready to help me, and for their valuable discussions about my project. Furthermore, I would like to express my gratitude to Assoc. Prof. René Wugt Larsen for his assistance with measuring and processing IR data and to Prof. Kasper Planeta Kepp for introducing me to Density Functional Theory. Not least, I would like to express my sincere gratitude to the technical staff at the DTU NMR Center, especially to PhD Kasper Enemark-Rasmussen who has been overwhelmingly helpful with his expertise in NMR spectroscopy.

Lastly, I owe great gratitude to my closest family. Thank you for your support and for always believing in me, and encouraging me.

January 2022

Mike S.B. Jørgensen

# Abstract

In this thesis, the results of five sub-projects from the PhD project are presented and discussed. Of these results, the synthesis and characterisation of a series of related carbonyl hydrido complexes of  $\text{Ru}^{\text{II}}$  will be presented first. Each of these complexes has been spectroscopically and structurally characterised. The crystallographic models were refined by means of both the Independent Atom Model (IAM) and the Hirschfeld Atom Refinement (HAR) method. The models represented by each of the refinement methods were compared together as well as compared to the spectroscopic characteristics of each compound in order to gain potential correlations of the spectroscopic observables and the Ru-H bond distance.

Synthesis, characterisation and reactivity studies of a series of ruthenium nitrosyl complexes make up for a substantial volume of this thesis. During these investigations, a series of unprecedented zero-valent five-coordinate Ru-halido complexes were unearthed. The new Ru-halide species were accessed by computational methods as well as single-crystal X-ray diffraction and spectroscopic characterisation. Additionally, some of the new nitrosyl species have been screened for catalytic activity in transfer hydrogenation of organic carbonyl derivatives and a selection of results will be presented in this thesis.

The complex commercially distributed as "Ru-MACHO" is known as a highly active catalyst in a variety of hydrogenation reactions, and is utilised in both industry and academia. Despite the high scientific values of this compound, no irrefutable proof of the proposed structure has, so far, been communicated. However, during the PhD studies that are represented by this thesis, a high quality crystal structure of the Ru-MACHO compound was obtained. Additionally, the reaction product for the reaction between Ru-MACHO and chloroform was elucidated by means of single-crystal X-ray diffraction. These results point to a general protocol for the synthesis of chlorido species via chloride-hydride exchange.

The thesis is divided into seven chapters. The first chapter gives the reader a general introduction to the fields of pincer, carbonyl and nitrosyl chemistry. Then follows five chapters dedicated to a presentation and discussion of the main results obtained in the five projects (one per chapter). The sixth chapter is written as a draft for a journal paper. The seventh chapter serves as a general conclusion and future perspectives of the works presented throughout this thesis.

# Resumé

De under dette ph.d.-projekt opnåede resultater diskuteres i den foreliggende afhandling, som er inddelt i fem delprojekter. Først præsenteres syntese og karakterisering af en serie af relaterede carbonylhydrido-forbindelser af  $\text{Ru}^{\text{II}}$ . For hver af disse forbindelser foreligger spektroskopisk karakterisering samt en krystalstruktur-bestemmelse opnået ved enkelt-krystal Röntgen diffraktion. Modelleringen af disse enkrystalstrukturer er foretaget både med den traditionelle Independent Atom Model (IAM) samt den mindre udbredte Hirschfeld Atom Refinement (HAR). Endvidere sammenlignes de resulterende modeller med hinanden og hver især med spektroskopiske data for derved at belyse en eventuel sammenhæng for Ru-H bindingslængden.

Syntese, karakterisering samt reaktivitetsstudier af en række nye nitrosyl forbindelser af Ru danner grundlag for en stor del af denne afhandling. Under disse arbejder blev der fremstillet en række halido forbindelser af  $\text{Ru}^0$ , hvilke er de første af sin slags. Disse nye forbindelser er blevet undersøgt spektroskopisk og krystallografisk samt beregningskemisk v.h.a. tæthedsfunktionale teori (DFT). Ydermere er en række nitrosylkomplekser undersøgt for deres katalytiske aktivitet i overførelseshydrogeneringsreaktioner af carbonyl derivater, og et udvalg af disse resultater præsenteres, og diskuteres i nærværende afhandling.

Komplekset med det kommercielle navn "Ru-MACHO" er kendt for at udvise høj katalytisk aktivitet i en lang række af hydrogeneringsreaktioner, som anvendes i både industri og grundforskning. Til trods for forbindelsens høje kommercielle og videnskabelige værdi har dens molekylære struktur ikke været endegyldigt fastslået, indtil nu. I dette arbejde er det nemlig lykkedes at opnå en enkrystalstruktur af høj kvalitet, der endeligt afdækker strukturen af den formodede forbindelse. Ydermere, er reaktionsproduktet fra reaktionen mellem Ru-MACHO og chloroform bestemt krystallografisk. Dette arbejde antyder en generel protokol for syntesen af dichlorido forbindelser ud fra kommercielle chloridohydrido-komplekser.

Denne afhandling er delt op i syv kapitler. Kapitel 1 giver læseren en generel introduktion til pincer-, carbonyl- og nitrosylkemi. Derpå følger fem kapitler dedikeret til præsentation samt diskussion af resultaterne opnået i de fem delprojekter (ét projekt pr. kapitel). Det femte kapitel (kapitel 6) er skrevet som et udkast til en artikel. Kapitel 7 er tiltænkt som en generel konklusion samt perspektivering over de arbejder, der er udført i forbindelse med denne afhandling.

# Abbreviations

- ADP = Atomic Displacement Parameter
- BArF = tetrakis(2,4,6-tris(trifluoromethyl)phenyl)borate
- CCSD = Cambridge Crystallographic Structure Database
- DCM = dichloromethane
- DMSO = dimethylsulfoxide
- EADP = Equal Atomic Displacement Parameter
- *fac* = facial
- Et<sub>2</sub>O = diethyl ether
- FC = Fermi-Contact
- HAR = Hirschfeld Atom Refinement
- HMBC = Heteronuclear Multiple Bond Correlation
- IAM = Independent Atom Model
- IR = Infrared
- LS = Least-Squares
- *mer* = Meridional
- MLC = Metal-Ligand-Cooperation
- MO = Molecular Orbital
- MPV = Meerwein-Ponndorf-Verley
- NaOEt = sodium ethoxide
- NMR = Nuclear Magnetic Resonance
- Pr<sub>2</sub>PNP = bis(2-diisopropylphosphinoethyl)amine



- Ref = Reference
- RIGU = Rigid Group
- SADI = Same Distance
- SALCAO = Symmetry Adapted Linear Combination of Atomic Orbitals
- SDF = Self-Diffusion Coefficient
- SOC = Spin Orbit Coupling
- SPS = Solvent purification system
- TBA = Tetrabutylammonium
- TBME = *tert*-butylmethylether
- TH = Transfer Hydrogenation
- THF/thf = tetrahydrofuran
- TMS = Tetramethylsilane

# Contents

<b>1</b>	<b>General introduction</b>	<b>1</b>
1.1	$\pi$ -acidic ligands . . . . .	3
<b>2</b>	<b><i>Trans</i>-influence as a measure in catalyst design</b>	<b>11</b>
2.1	Interpretation of the <i>trans</i> -influence . . . . .	12
2.1.1	Chemical shifts in hydrido complexes of transition metals . . . . .	13
2.1.2	The transition metal-hydrogen bond . . . . .	15
2.1.3	X-ray crystallography . . . . .	16
2.2	Characterisation of Novel Hydridocarbonyl Complexes . . . . .	16
2.2.1	Structure of the (iPr <sub>2</sub> PNP)RuH(NCMe)(CO) cation . . . . .	17
2.2.2	(iPr <sub>2</sub> PNP)RuHBr(CO) - (2) . . . . .	21
2.2.3	(iPr <sub>2</sub> PNP)RuHI(CO) - (3) . . . . .	25
2.2.4	(iPr <sub>2</sub> PNP)RuH(CN)(CO) - (4) . . . . .	28
2.2.5	(iPr <sub>2</sub> PNP)RuH(N <sub>3</sub> )(CO) - (5) . . . . .	31
2.2.6	(iPr <sub>2</sub> PNP)RuH(NCS/SCN)(CO) - (6) . . . . .	35
2.3	Discussion and conclusions . . . . .	37
<b>3</b>	<b>Characterisation and reactivity of PNP ruthenium nitrosyl complexes</b>	<b>42</b>
3.1	Nitrogen NMR spectroscopy . . . . .	43
3.2	Vibrational spectroscopy of NO complexes . . . . .	44
3.3	Results and discussion . . . . .	45
3.4	The parent complex <b>1</b> and <b>1a</b> . . . . .	46
3.5	Reactions of <b>1</b> and <b>1a</b> . . . . .	46
3.5.1	Reaction with base in ethanol . . . . .	46
3.5.2	Characterisation of [( <sup>i</sup> Pr <sub>2</sub> PNP)RuClH(NO)]Cl · HCl . . . . .	50
3.5.3	Reaction of <b>2</b> with iodomethane → <b>4</b> . . . . .	52
3.5.4	Reaction of <b>1/1a</b> with base in aprotic solvent → complex <b>5</b> . . . . .	54
3.5.5	Reaction of <b>5</b> with electrophiles → complex <b>6</b> and a diphenylte- trazenido complex . . . . .	61

3.6	Diphenylene PNP-Ru(NO) - complex 8 . . . . .	65
3.7	Conclusions . . . . .	67
<b>4</b>	<b>Catalytic transfer hydrogenation</b>	<b>72</b>
4.0.1	Aesthetic but arid: A <i>trans</i> -diacetato complex . . . . .	78
4.1	Conclusions . . . . .	80
<b>5</b>	<b>The structure of the ruthenium-MACHO catalyst</b>	<b>82</b>
5.1	Results and discussion . . . . .	83
5.2	Conclusions and outlook . . . . .	88
<b>6</b>	<b>Intrinsic Geometric Distortion of 5-Coordinate Halido Complexes of Ruthenium(0)</b>	<b>90</b>
<b>7</b>	<b>General conclusions and perspectives</b>	<b>102</b>
	<b>Appendices</b>	<b>124</b>
<b>A</b>	<b>General Instrumentation</b>	<b>125</b>
<b>B</b>		<b>127</b>
B.1	General synthesis protocol for (2)-(6) . . . . .	127
B.1.1	NMR spectroscopy of (1) . . . . .	133
B.2	Computational details . . . . .	136
B.3	Crystallographic details . . . . .	136
<b>C</b>		<b>139</b>
C.1	Experimentals . . . . .	139
C.1.1	Synthesis and spectroscopy of [ $(^i\text{Pr}_2\text{PNP})\text{RuClH}(\text{NO})$ ] $\text{Cl} \cdot \text{HCl}$ . .	139
C.1.2	Synthesis of complex 8 . . . . .	141
C.1.3	Synthesis of $(^i\text{Pr}_2\text{PNP})\text{Ru}(\text{NO})$ , 5 . . . . .	143
C.1.4	Synthesis of 6 . . . . .	147
C.1.5	Synthesis of 4 . . . . .	150
C.2	Miscellaneous spectral information . . . . .	152
C.3	Crystal structure of a 6-coordinate enamido-ruthenium(II) complex . . .	155
C.4	Crystallographic details . . . . .	157
<b>D</b>		<b>159</b>
<b>E</b>		<b>163</b>

# List of Figures

1.1	Generic structure of a pincer complex. . . . .	3
1.2	Representation of $\pi$ -backbonding from a metal-centered d orbital into a ligand centered $\pi^*$ -orbital. Arrows represent direction of donation. . . . .	3
1.3	The effect of $\pi$ -bonding on $\Delta_O$ for a generic metal ion when (a) associated with $\pi$ -donor ligands and (b) associated with $\pi$ -acceptor ligands in $O_h$ symmetry. $\sigma$ -interactions have been omitted for clarity. The vertical energy scale is schematic. . . . .	4
1.4	Stabilisation of $\pi X \rightarrow \pi M$ interaction by a $\pi$ -acceptor ligand (here: CO) in the <i>trans</i> -position to the $\pi$ -donor ligand, X. . . . .	5
1.5	MO diagram for the free nitric oxide radical. Contributions from the s(N,O) orbitals have been omitted for clarity. Adapted from ref. <sup>1</sup> . . . . .	6
1.6	MO diagram for a generic six-coordinated $L_5M(NO)$ species in $C_{4v}$ symmetry. Adapted from ref. <sup>2-6</sup> The orange box indicates which orbitals are associated with $n$ in the Enemark-Feltham notation: $\{MNO\}^n$ . . . . .	8
1.7	Structural change and orbital correlation diagram for the $\{CoNO\}^8$ upon symmetry change in the coordination sphere reported by Enemark <i>et al.</i> <sup>7</sup> The coordinate system specified in (a) is applicable to (b). The vertical energy axis is schematic. . . . .	9
1.8	Statistics showing the distribution of M-N-O angles for terminal nitrosyl complexes. . . . .	10
2.1	The supposed transition state of an electrophile here: a generic carbonyl compound approaching the catalytic species. The hydride bond is elongated in conjunction with a shortening of the <i>trans</i> -Ru-X bond illustrating the similarity with the assymetric stretch of the H-Ru-X entity indicates by the arrows. . . . .	11
2.2	Schematic representation of the two main electronic effects of <i>trans</i> -influence. . . . .	12
2.4	Schematic representation of the cat ionic Ru(II)-hydrido complex published by Gibson <i>et al.</i> in 2004 (see main text for reference). . . . .	17
2.3	IAM model of the crystal structure of the cation of the intermediate complex (1). Hydrogens on all carbon atoms has been omitted for clarity. Plotted at 50% propability level. . . . .	18
2.5	Box plot showing the distribution of bond lengths between a transition metal and a hydrido ligand (blue) and the distribution of bond lengths between a transition metal and an acetonitrile ligand (red). In all complexes, the acetonitrile ligand is coordinated in a <i>trans</i> -fashion relative to the terminal hydrido ligand. . . . .	19

2.6	Solid state infrared spectrum of the parent complex salt, (1). . . . .	19
2.7	$^1\text{H}$ -NMR spectra (left column) and $^1\text{H}$ -decoupled $^{31}\text{P}$ -NMR spectra (right column) of (1) in $\text{C}_6\text{D}_6$ (blue) and $\text{CD}_2\text{Cl}_2$ (black). . . . .	20
2.8	Crystal structure of complex (2) complex after IAM refinement. Hydrogen atoms on all carbon atoms has been omitted for clarity. Plotted at 50% probability level. . . . .	21
2.9	Experimental and simulated IR spectra for (2). . . . .	23
2.10	$^1\text{H}$ -decoupled $^{31}\text{P}$ -NMR spectrum (left). $^1\text{H}$ -NMR spectrum (right) in the hydride region of complex (2). . . . .	24
2.11	Crystal structure of the titled complex after IAM refinement. Hydrogens on all carbon atoms has been omitted for clarity. Plotted at 50% probability level. . . . .	25
2.12	Experimental and simulated IR spectra for (3). . . . .	27
2.13	$^1\text{H}$ -decoupled $^{31}\text{P}$ -NMR spectrum (left). $^1\text{H}$ -NMR spectrum (right) in the hydride region of complex (3). . . . .	28
2.14	Crystal structure of the titled complex after IAM refinement. Hydrogens on all carbon atoms has been omitted for clarity. Plotted at 50% probability level. . . . .	28
2.15	Experimental and simulated IR spectra for (4). . . . .	30
2.16	$^1\text{H}$ -decoupled $^{31}\text{P}$ -NMR spectrum (left). $^1\text{H}$ -NMR spectrum (right) in the hydride region of complex (4). . . . .	31
2.17	Crystal structure of the titled complex after IAM refinement. Hydrogens on all carbon atoms has been omitted for clarity. Plotted at 50% probability level. . . . .	31
2.18	Infrared spectrum of compound (5). . . . .	34
2.19	$^1\text{H}$ -decoupled $^{31}\text{P}$ -NMR spectrum (left). $^1\text{H}$ -NMR spectrum (right) in the hydride region of complex (5). . . . .	34
2.20	Crystal structure of the titled complex after IAM refinement. Hydrogens on all carbon atoms has been omitted and isopropyl substituents on P has been ghosted out for clarity. Plotted at 50% probability level. . . . .	35
2.21	Infrared spectrum of compound mixture (6). . . . .	36
2.22	$^1\text{H}$ -decoupled $^{31}\text{P}$ -NMR spectrum (left). $^1\text{H}$ -NMR spectrum (right) in the hydride region of complex mixture (6). . . . .	37
2.23	Dihydridocarbonylruthenium(II). . . . .	38
2.24	$\pi$ -donation from an axial donor ligand, such as, halide, and $\pi$ -acceptance from a equatorial ligand such as phosphine or carbonyl. . . . .	39
2.25	Vibrational frequencies and NMR chemical shifts presented in Table 2.10 plotted against the IAM-refined Ru-H distances. . . . .	41
3.1	Schematic representation of the metal nitrosyl complexes bearing negatively charged NO ligand with linear coordination geometry. . . . .	42
3.2	Vibrational stretching frequency ranges for the $\nu(\text{NO})$ mode in transition metal nitrosyls. Adapted from Ref. <sup>8</sup> . . . . .	44

3.3	$^1\text{H}$ -decoupled $^{31}\text{P}$ -NMR spectrum of the mixture of <b>1</b> in ethanol/triethylamine mixture immediately prior to heating (left) show the distribution of species converts into one upon heating at $80^\circ\text{C}$ for 1 h (right). . . . .	47
3.4	$^1\text{H}$ -NMR spectrum shows the hydride signal from a generated hydrido species upon re-dissolving of the initially generated product mixture from the reaction in ethanolic triethylamine. . . . .	48
3.5	Dark green complexes formed in the reaction of <b>1</b> and <b>1a</b> respectively with ethanolic $\text{Et}_3\text{N}$ at $80^\circ\text{C}$ for 1 h. Hydrogens on all carbon atoms has been removed for clarity. Thermal ellipsoids are plotted at 50% probability level. . . . .	49
3.6	Hydride region of the reaction product from the reaction described in Scheme 3.2.	50
3.7	Crystal structure of the chloridohydridoruthenium(II) complex containing co-crystallised HCl. All hydrogens on carbon atoms have been omitted for clarity. For the same reason, two isopropyl groups are ghosted out. Thermal ellipsoids are plotted at 50% probability level. . . . .	50
3.8	IR spectrum in the range of the $\tilde{\nu}(\text{NO}) = 1821\text{ cm}^{-1}$ and $\tilde{\nu}(\text{Ru-H}) = 1847\text{ cm}^{-1}$ modes of powdered crystals of chloridohydridoruthenium(II). . . . .	51
3.9	Crystal structure of the cation in <b>4</b> . All hydrogen atoms on carbon atoms associated with the PNP ligand is omitted for clarity. Thermal ellipsoids are plotted at 50% probability level. . . . .	53
3.10	Infrared vibrational absorbance at $1815\text{ cm}^{-1}$ related to the $\nu(\text{NO})$ stretching mode.	54
3.11	<b>Left:</b> $^1\text{H}$ -NMR in the aromatic region showing a doublet of doublets as well as a merged doublet of triplets (insert). <b>Right:</b> $^{31}\text{P}$ -NMR spectrum shows two doublets from chemically nonequivalent phosphine groups. . . . .	55
3.12	Square planar complex <b>5</b> . All hydrogen atoms have been omitted for clarity. Thermal ellipsoids are plotted at 50% probability level. . . . .	55
3.13	IR spectrum of <b>5</b> in the characteristic region of the diagnostic frequencies of the $\nu(\text{NO})$ and $\nu(\text{C}=\text{C})$ modes. . . . .	56
3.14	Left: $^1\text{H}$ -NMR in the characteristic region (aromatic). Right: The full $^{31}\text{P}$ -NMR spectrum. . . . .	57
3.15	Schematic representation of the peroxo nitrosyl complex presented by Milstein and co-workers. All distances and angles are expressed in Ångström and degrees respectively. . . . .	57
3.16	Crystal structure of complex <b>7</b> obtained from the solid-state-gas-phase-reaction between a single-crystal of <b>5</b> and atmospheric oxygen. Hydrogen on carbon atoms have been omitted for clarity and the isopropyl groups on phosphorus have been ghosted out. Thermal ellipsoids are plotted at 50% probability level. . . . .	58
3.17	Show the basal plane for the distorted trigonal bipyramidal complex <b>7</b> and highlight the <i>trans</i> coordination of $\text{O}_2\text{--NO}$ . . . . .	59

3.18	Statistical comparison of the O-O bond distances in peroxo ligands in (a) transition metal complexes across the periodic table and (b) Ru-peroxo complexes. Data is obtained from CCSD. . . . .	60
3.19	IR spectra <b>8</b> when in high-vacuum (black line) and after $\sim 3$ min of venting the sample compartment with atmospheric oxygen. The bands at 900 to 800 $\text{cm}^{-1}$ have been scaled with a factor of 5 for clarity, showing the growth of the characteristic peak of a metal-peroxide. . . . .	60
3.20	Crystal structure of complex <b>6</b> . Hydrogen on carbon atoms associated with the PNP ligand have been omitted for clarity. Thermal ellipsoids are plotted at 50% probability level. . . . .	61
3.21	$^1\text{H}$ - $^{31}\text{P}$ coupled $^1\text{H}$ -NMR spectrum (a) reveals the double doublet signal from one proton merges into one broad signal in (b) upon $^1\text{H}$ - $^{31}\text{P}$ -decoupling. . . . .	62
3.22	IR spectrum in the characteristic region of <b>6</b> showing the $\nu(\text{NO})$ and $\nu(\text{C}=\text{C})$ stretching modes. . . . .	62
3.23	Crystal structure of the tetrazenido complex obtained from the reaction of <b>5</b> with azidobenzene. (a) (and b): Hydrogen atoms have been omitted for clarity. a): All atoms associated with the tetrazenido ligand is ghosted out for clarity. b): All carbon atoms on the P-ligators as well as the P-atom on the ethylene side of the PNP ligand are ghosted out for clarity. . . . .	64
3.24	Geometry around the ruthenium atom and within the tetrazenido ligand showing the assymetry across the $\text{N}_4$ -core. . . . .	65
3.25	Crystal structure of the complex <b>8</b> . All hydrogens on carbon atoms have been omitted for clarity. Thermal ellipsoids are plotted 75% probability level. . . . .	65
3.26	IR spectrum in the fingerprint region of complex <b>8</b> shows the strong absorption at 1725 $\text{cm}^{-1}$ as well as a another strong absorption at 1458 $\text{cm}^{-1}$ followed by a series of relatively strong bands associated with the aromatic rings. . . . .	67
3.27	Schematic representation of the scale for increasing $\nu(\text{NO})$ absorption energy among related square planar $\text{Ru}^0$ complexes in this work. . . . .	68
4.1	Berke's rhenium(I) complexes used in (de)hydrogenation reactions with amino borane as hydrogen source. . . . .	74
4.2	<i>Trans</i> -dihydrido nitrosyl complex of rhenium(I) used in catalytic TH of ketones with isopropanol as $\text{H}_2$ -source. . . . .	75
4.3	Representative reaction scheme for the TH reactions presented in this thesis. . .	76
4.4	Crystallographic indication of a hydroxido species. The $\text{BPh}_4^-$ counterion and all hydrogens on carbon atoms have been omitted for clarity. Thermal ellipsoids on Ru, (NO), Cl, O and P atoms are plotted at 30% probability level. All other atoms were refined isotropically. . . . .	78

4.5	Crystal structure of the diacetato complex. Disorder in the anion and isopropyl substituents on phosphorus have been ghosted out and all hydrogens on carbon atoms have been omitted for clarity. Thermal ellipsoids are plotted at 50% probability level.	79
4.6	IR spectrum of the diacetato complex shown in Figure 4.5.	80
5.1	Structure of the Ru-MACHO and Ru-MACHO-BH catalysts.	82
5.2	Overlay of the $^1\text{H}$ -NMR spectra of Ru-MACHO measured in $\text{CDCl}_3$ (black) and toluene- $d_8$ (red).	83
5.3	IR spectrum of the commercially available (Sigma-Aldrich) Ru-MACHO complex. The inset clearly show two different $\nu(\text{CO})$ modes and at least two $\nu(\text{Ru}-\text{H})$ modes.	84
5.4	Crystal structure of the $\text{RuCl}_2$ -MACHO obtained from the reaction between commercial Ru-MACHO and chloroform under ambient conditions. All hydrogen atoms on carbon atoms have been omitted for clarity. Thermal ellipsoids are plotted at 50% probability level.	85
5.5	Crystal structure of the Ru-MACHO pre-catalyst showing significant disorder in the co-crystallised DMSO solvent. All hydrogens on carbon atoms have been omitted for clarity. Thermal ellipsoids are plotted at 50% probability level.	86
5.6	Crystal structure of the Ru-MACHO after solvent masking have been applied to the structure in Figure 5.5. All hydrogens on carbon atoms have been omitted for clarity. Thermal ellipsoids are plotted at 50% probability level.	87
B.1	$^1\text{H}$ -NMR spectrum of (2). Referenced against TMS.	128
B.2	$^1\text{H}$ -NMR spectrum of (3). Referenced against TMS.	129
B.3	$^1\text{H}$ -NMR spectrum of (4). Referenced against TMS.	130
B.4	$^1\text{H}$ -NMR spectrum of (5). Referenced against TMS.	131
B.5	$^{31}\text{P}$ -NMR spectrum of (5). As evident by the septet at $-157.66$ to $-131.33$ ppm the sample still contains $[\text{TBA}]\text{PF}_6$ .	132
B.6	$^1\text{H}$ -NMR spectrum of (6). Referenced against TMS.	132
B.7	$^{31}\text{P}$ -NMR spectrum of (6).	133
B.8	$^{19}\text{F}$ -NMR spectrum of (1) in $\text{CD}_2\text{Cl}_2$ . Showing the characteristic doublet of the $\text{PF}_6^-$ anion.	133
B.9	$^{19}\text{F}$ -NMR spectrum of (1) in $\text{C}_6\text{D}_6$ . Showing the characteristic doublet of the $\text{PF}_6^-$ anion.	134
B.10	$^1\text{H}$ -NMR spectrum of (1) in $\text{CD}_2\text{Cl}_2$ .	134
B.11	$^1\text{H}$ -NMR spectrum of (1) in $\text{C}_6\text{D}_6$ .	135
C.1	$^1\text{H}$ -NMR spectrum of the crystals obtained for $\text{RuClH}$ . A rather much lowfield shifted amine proton, indicates extensive hydrogen bonding as revealed in the crystal structure which contains co-crystallised $\text{HCl}$ . As such, it is expected that the spectrum is influenced by the pH being different from neutral.	140



C.2	$^{31}\text{P}$ -NMR spectrum of the crystals obtained for $\text{RuClH}$ . . . . .	140
C.3	IR spectrum of powderised crystals of $[(^i\text{Pr}_2\text{PNP})\text{RuClH}(\text{NO})]\text{Cl} \cdot \text{HCl}$ . .	141
C.4	IR spectrum of complex <b>8</b> . . . . .	142
C.5	$^1\text{H}$ -NMR spectrum of the complex <b>5</b> . . . . .	143
C.6	$^{31}\text{P}$ -NMR spectrum of the complex <b>5</b> . . . . .	144
C.7	IR spectrum of the complex <b>5</b> . . . . .	144
C.8	$^1\text{H}$ -NMR spectrum of a $\text{C}_6\text{D}_6$ solution of <b>5</b> under an atmosphere of $\text{O}_2$ . . .	146
C.9	$^{31}\text{P}$ -NMR spectrum of a $\text{C}_6\text{D}_6$ solution of <b>5</b> under an atmosphere of $\text{O}_2$ . .	146
C.10	$^1\text{H}$ -NMR spectrum (400 MHz) of a $\text{C}_6\text{D}_6$ solution of <b>6</b> . . . . .	147
C.11	$^1\text{H}$ -NMR spectrum (400 MHz) of a $\text{C}_6\text{D}_6$ solution of <b>6</b> . $^1\text{H}$ - $^{31}\text{P}$ decoupled. .	148
C.12	$^{13}\text{C}$ -NMR spectrum (800 MHz) of a $\text{C}_6\text{D}_6$ solution of <b>6</b> . . . . .	148
C.13	$^{31}\text{P}$ -NMR spectrum (400 MHz) of a $\text{C}_6\text{D}_6$ solution of <b>6</b> . . . . .	149
C.14	$^1\text{H}$ -NMR spectrum (600 MHz, methanol- $d_4$ ) of the iodidomethyl complex <b>4</b> revealing different isomers are present in solution. . . . .	150
C.15	$^{13}\text{C}$ -NMR spectrum (150 MHz, methanol- $d_4$ ) of the iodidomethyl complex <b>4</b> revealing different isomers are present in solution with two characteristic triplets at 1.39 and -1.01 ppm respectively. . . . .	151
C.16	$^1\text{H}$ -NMR spectrum of the mixture of <b>1</b> in ethanol/triethylamine mixture after heating for 1 h at $80^\circ\text{C}$ showing signals of generated acetaldehyde at 10.23 ppm (q, $J = 2.8$ Hz) and 2.65 ppm (d, $J = 2.9$ Hz). Referenced against benzene- $d_6$ . . . . .	152
C.17	$^1\text{H}$ -NMR spectrum of the reaction mixture after <b>1</b> was heated to $80^\circ\text{C}$ for 30 min in ethanolic triethylamine, followed by evaporation of volatiles followed by addition of toluene- $d_8$ reveals the characteristic triplet signal at -3.8 ppm of one hydride coordinates <i>cis</i> to two P atoms ( $J = 15.8$ Hz). . . . .	153
C.18	$^{31}\text{P}$ -NMR spectrum (162 MHz) of the product mixture after <b>1</b> was heating to $80^\circ\text{C}$ for 30 min in ethanolic triethylamine, followed by evaporation of volatiles followed by addition of toluene- $d_8$ shows two main products at 78.94 ppm and 71.36 ppm. . . . .	153
C.19	$^1\text{H}$ -NMR spectrum of the product mixture from the reaction between <b>2</b> and triethylamine hydrochloride. The spectrum contains small amounts of residual triethylamine hydrochloride as well as other unidentified products. .	154
C.20	$^{31}\text{P}$ -NMR spectrum (162 MHz) of the product mixture from the reaction of <b>2</b> with triethylamine hydrochloride. The spectrum reveals additional products that remain unidentified. . . . .	154
C.21	6-coordinate enamido complex of ruthenium(II) formed in the reaction of <i>tert</i> - butoxide and <b>1/1a</b> (1:1) in aprotic solvent. All hydrogens on carbon atoms have been omitted and the isopropyls on phosphorus have been ghosted out for clarity. Thermal ellipsoids are plotted at 35% probability level. . . . .	155

E.1	$^{31}\text{P}$ -NMR spectrum of ruthenium-MACHO in $\text{CDCl}_3$ . Singlet peaks are observed at 48.33, 46.80 and 27.98 ppm. . . . .	163
E.2	$^{31}\text{P}$ -NMR spectrum of ruthenium-MACHO in toluene- $d_8$ . Singlet at 52.46 ppm. . . . .	164

# List of Tables

2.1	Selected structural parameters for ruthenium pincer complexes that exhibits <i>trans</i> -hydrido-acetonitrile coordination. . . . .	18
2.2	Difference in geometric- and refinement parameters between the IAM, HAR and DFT models for complex (2). Ruthenium to phosphorous distances have been omitted as these are invariant . . . . .	22
2.3	Selected structural parameters (IAM) for all crystallographically characterised transition metal pincer complexes that exhibits <i>trans</i> -hydridobromido coordination. . . . .	23
2.4	Difference in geometric- and refinement parameters between the IAM, HAR and DFT models for complex (3). Ruthenium to phosphorous distances have been omitted as these are invariant. . . . .	25
2.5	Selected bond lengths (IAM) for structurally characterised pincer ligand supported <i>trans</i> -iodidohydrido transition metal complexes. . . . .	26
2.6	Difference in geometric- and refinement parameters between the IAM, HAR and DFT models for complex (4). Ruthenium to phosphorous distances have been omitted as these appear, for all practical purposes, invariant. . . . .	29
2.7	Selected bond lengths (IAM) for structurally characterised cyanidohydrido transition metal complexes found in the CCSD. . . . .	29
2.8	Difference in geometric- and refinement parameters between the IAM, HAR and DFT models for complex (5). Ruthenium to phosphorous distances have been omitted as these appear, for all practical purposes, invariant. . . . .	32
2.9	Geometry around the central metal ion in transition metal hydrido azido complexes found in literature. Colour code for models containing two independent molecules: <b>component 1</b> , <b>component 2</b> . . . . .	33
2.10	Summary of spectral and geometric data for the complexes (2)-(5). Data obtained from literature is indicated by reference. . . . .	40
3.1	Summary of selected geometric parameters reflected in the asymmetric unit of the $C_s$ symmetric molecule, [ $(i\text{Pr}_2\text{PNP})\text{RuClH}(\text{NO})$ ] $\text{Cl} \cdot \text{HCl}$ . . . . .	51
3.2	Summary of geometric and spectroscopic characteristics for the complexes <b>1a</b> - <b>8</b> . . . . .	71
4.1	Selected list of conditions used in the optimisation process using 1.3 mmol acetophenone and 3 mL isopropanol as solvent to 0.5 mole [Ru] relative to substrate. . . . .	76

4.2	Induction times. Conditions: 1.3 mmol acetophenone, 10 mol% NaOH, 15 min reaction time after added substrate. Temp: 90 °C. . . . .	77
4.3	Self-diffusion coefficients (SDF) determined by DOSY NMR in THF at 25 °C. . . . .	79
5.1	Selected bond lengths and angles for the Ru-MACHO complex. . . . .	88
B.1	Crystallographic experimental and refinement (IAM) details. . . . .	137
B.2	Crystallographic experimental and Hirschfeld atom refinement details for the complexes (2)-(5). . . . .	138
C.1	NMR chemical shift assignment of complex <b>8</b> . NMR experiments (600 MHz, C <sub>2</sub> D <sub>2</sub> ) and assignments have been conducted by the NMR Center at the Technical University of Denmark; experimentalist: PhD Kasper Enemark-Rasmussen. . . . .	142
C.2	NMR chemical shift assignment of complex <b>5</b> . "=" indicates the "side" of the PNP ligand with <i>sp</i> <sup>2</sup> carbons. NMR experiments (600 MHz, C <sub>6</sub> D <sub>6</sub> ) and assignments have been conducted by the NMR Center at the Technical Univeristy of Denmark; experimentalist: PhD Kasper Enemark-Rasmussen. . . . .	145
C.3	NMR chemical shift assignment of complex <b>6</b> . NMR experiments (C <sub>6</sub> D <sub>6</sub> ) and assignments have been conducted by the NMR Center at the Technical Univeristy of Denmark; experimentalist: PhD Kasper Enemark-Rasmussen. . . . .	149
C.5	Assignment of isomer B observed for complex <b>4</b> . NMR experiments (600 MHz, methanol- <i>d</i> <sub>4</sub> ) and assignments have been conducted by the NMR Center at the Technical Univeristy of Denmark; experimentalist: PhD Kasper Enemark-Rasmussen. . . . .	151
C.4	Assignment of isomer A observed for complex <b>4</b> . NMR experiments (600 MHz, methanol- <i>d</i> <sub>4</sub> ) and assignments has been conducted by the NMR Center at the Technical Univeristy of Denmark; experimentalist: PhD Kasper Enemark-Rasmussen. . . . .	152
C.6	Selected geometrical data. . . . .	155
C.7	Crystallographic details. . . . .	156
C.8	Crystallographic details of the complexes described in main text. . . . .	158
D.1	Experimental crystallographic details on [( <sup>1</sup> Pr <sub>2</sub> PNP)Ru(OAc) <sub>2</sub> (NO)]BF <sub>4</sub> . . . . .	160
D.2	NMR chemical shift assignment of the diacetato complex presented in Section 4.0.1. NMR experiments (600 MHz, C <sub>2</sub> D <sub>2</sub> ) and assignments have been conducted by the NMR Center at the Technical University of Denmark; experimentalist: PhD Kasper Enemark-Rasmussen. . . . .	161
E.1	Crystallographic details for the RuCl <sub>2</sub> -MACHO and the Ru-MACHO complex for both models with and without solvent of crystallisation. . . . .	165
E.2	Selected bond lengths and angles for RuCl <sub>2</sub> -MACHO . . . . .	166

# Chapter 1

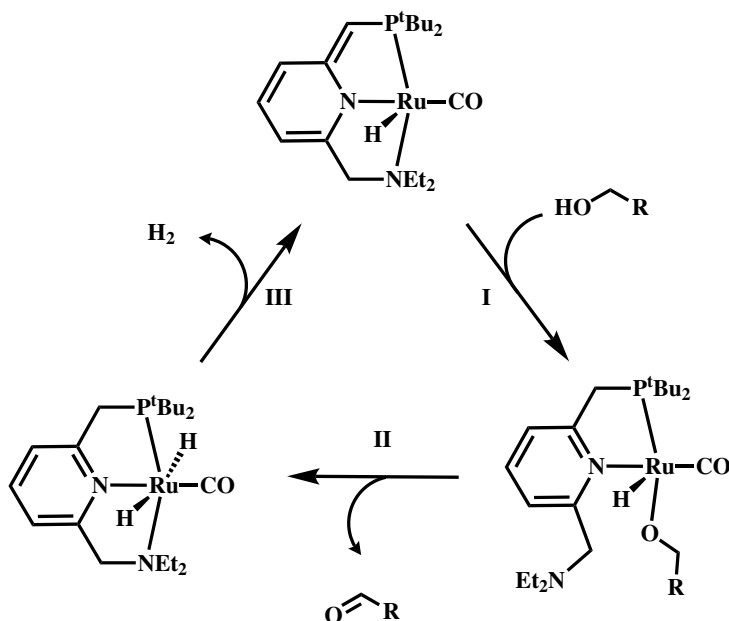
## General introduction

This chapter provides a general introduction to the chemistry that will be discussed in this thesis. As will become apparent, the main topics of this work revolve about the chemistry of low-valent coordination compounds of ruthenium and their physico-chemical characteristics. All compounds presented in this work have the following two ligand scaffolds in common: 1) All complexes exhibit a tridentate PNP pincer ligand meridionally coordinated. 2) all complexes will in addition to the PNP pincer ligand be comprised with either of the two strongly  $\pi$ -acidic ligands carbonyl ( $\text{C}\equiv\text{O}$ ) or its isoelectronic lighter counterpart nitrosonium ( $\text{N}\equiv\text{O}^+$ ). The aim of this thesis is to build a fundamental understanding which upon a rational design of new ruthenium based future homogeneous catalysts can succeed. First, an account on the general chemistry of PNP pincer ligands and, second, the general aspects of carbonyl- and nitrosyl ligands and their influence on the electronic structure of the central metal ion will be introduced briefly. In this thesis, the carbonyl complexes that will be presented are assumed as being spectator ligands only, hence, this ligand is more briefly introduced. As the nitrosyl ligand appears somewhat more elusive with respect to the stereochemistry of its metal complexes, a more thorough introduction on this exciting topic will be provided.

### Pincer ligands

The term "pincer ligand" was first coined more than 30 years ago by van Koten<sup>9</sup> in the discussion of the NCN ligand structure that was used to isolate the unprecedented true organometallic nickel(III) complex, published in 1983.<sup>10</sup> As such, a "pincer ligand" was originally defined as being monoanionic with the general formula  $[\text{2,6}-(\text{ECH}_2)_2\text{C}_6\text{H}_3]^-$  where E is a neutral 2-electron donor (amine, phosphine, sulfide etc.) connected as substituents *via* a methylene group to the 2- and 6 positions on the central aryl ring (ECE).<sup>11</sup> Even though the coinage of the pincer ligand was undertaken by the end of the 1980s, the first examples of such can be dated back to Moulton and Shaw who in 1976 reported a series of  $(^t\text{Bu}_2\text{PCP})\text{ML}_n$  complexes.<sup>12</sup> In recent years, the definition of pincer ligands has been markedly extended to a point where an exact definition is washed out and now

includes both mono-, di-, trianionic and neutral tridentate ligands.<sup>13–16</sup> However, the vast amount of different combinations of flanking ligands and backbones in the pincer ligand architecture allows for a rich volume of possibilities for fine-tuning of steric- and electronic properties of the pincer complex without inducing significant geometrical modifications around the central metal ion. The tridentate ligand framework makes pincer complexes robust towards thermal and chemical degradation as is evident in that Shaw’s (PCP)Ni(II) complex could be sublimed in air at 240 °C<sup>12</sup> and many other PNP complexes retain their molecular integrity under strongly oxidising and reducing conditions.<sup>17–22</sup> Scheme



Scheme 1.1: Catalytic cycle for the acceptorless dehydrogenation of alcohols which also represents half of the reaction mechanism for the direct formation of amides from alcohols and amines, as presented by Gunanathan and Milstein.

1.1 shows the mechanism for the acceptorless dehydrogenation of alcohols proposed by Gunanathan and Milstein.<sup>23</sup> This particular complex shows a number of features to the pincer ligand scaffold as schematically represented. In step I, proton abstraction from the incoming alcohol to the pincer ligand side arm restores the aromatic structure of the ligand. The transformation from a mono anionic amido species to a neutral amino (pyridine) species and de-coordination of the hemilabile diethylamino-arm of the pincer ligand allow for alkoxide coordination. In II, the alkoxide undergoes  $\beta$ -hydride elimination to generate an aldehyde and re-coordination of the pincer sidearm extrudes the aldehyde and generates a *trans*-dihydrido pincer complex which, in III undergoes an intramolecular  $\gamma$ -proton abstraction under the elimination of dihydrogen, closing the catalytic cycle by reformation of the starting enamide complex. Other aspects of the intriguing versatility of pincer ligands can be seen in the ability of stabilising square-planar compounds with interesting spin-states such as oxo-diyl-iridium(III)<sup>24</sup>, imido-iridium(III/IV/V)<sup>25</sup> and nitrene-diyl-platinum(II).<sup>26</sup>

The easy chemical tunability of pincer complexes has, not surprisingly, been extensively utilised in homogeneous catalysis, especially (de)hydrogenation reactions.<sup>27,28</sup> Traditionally, hydrogenation reactions work through oxidative addition of dihydrogen to the metal center. Thus, relying on the propensity of the metal center to undergo 2-electron redox changes. However, certain PNP pincer ligands afford so-called *metal-ligand-corporation* (MLC) as is described in Scheme 1.1, in which the ligand takes an active part in

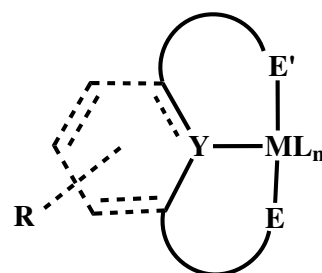


Figure 1.1: Generic structure of a pincer complex.

the mechanistic cycle, such that, no redox chemistry is located at the metal center. This feature has been particularly beneficial in the development of first row transition metal homogeneous catalytic (de)hydrogenation reactions, as the first row transition metals are known to undergo one-electron redox chemistry, which is avoided when MLC mechanisms are dominant.<sup>29</sup> Figure 1.1 shows the generic structure of a pincer complex. The ligand may be aliphatic or aromatic with various electron donating/withdrawing substituents. E and E' may or may not differ to allow for both steric and electronic tuning. The ligand backbone can vary in length and elemental composition and, thus, can be varied in selective electronic and steric tuning.  $L_n$  compose the auxiliary ligand sphere.

## 1.1 $\pi$ -acidic ligands

$\pi$ -Acidic ligands, or  $\pi$ -acceptors are a class of ligands with energetically low-lying unoccupied molecular orbitals of  $\pi$ -symmetry. A metal ion with filled orbitals of  $\pi$ -symmetry ( $d_{xy}$ ,  $d_{xz}$ ,  $d_{yz}$ , that is,  $t_{2g}$  in  $O_h$  symmetry) can donate electron density into the empty ligand molecular orbitals. This interaction is represented in Figure 1.2 where filled metal centered

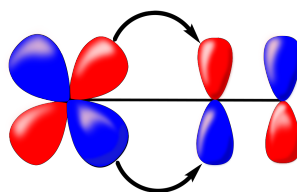


Figure 1.2: Representation of  $\pi$ -backbonding from a metal-centered d orbital into a ligand centered  $\pi^*$ -orbital. Arrows represent direction of donation.

orbital donates electron density into a ligand molecular orbital. This ligand-centered molecular orbital is having  $\pi^*$ -symmetry. Therefore, back-donation to the ligand weakens the intra-ligand  $\pi$ -bond while the metal-ligand bond is strengthened as the M-L interaction is bonding in nature. The effect on the ligand field splitting energy ( $\Delta_O$ ) is opposite in sign to when the metal is associated with  $\pi$ -donor ligands. This effect is shown in the qualitative molecular orbital diagram in Figure 1.3.

When the ligand's p orbitals are filled, the ligand serves as  $\pi$ -donors making the bonding  $t_{2g}$  set mostly ligand-centered and the corresponding antibonding interaction mostly metal-

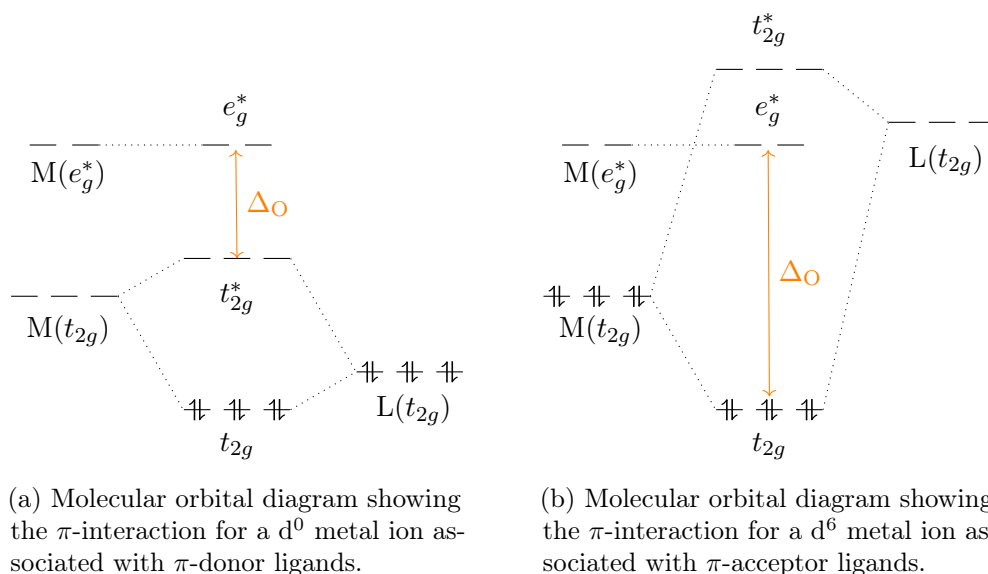


Figure 1.3: The effect of  $\pi$ -bonding on  $\Delta_O$  for a generic metal ion when (a) associated with  $\pi$ -donor ligands and (b) associated with  $\pi$ -acceptor ligands in  $O_h$  symmetry.  $\sigma$ -interactions have been omitted for clarity. The vertical energy scale is schematic.

centered and effectively  $\Delta_O$  decreases. Conversely, the empty  $t_{2g}$  set in  $\pi$ -acceptor ligands, that are typically associated with the ligand's  $\pi^*$ -orbitals as depicted in Figure 1.2, and the bonding  $\pi$ -interactions are largely metal centered. Consequently,  $\Delta_O$  increases. As such,  $\pi$ -acidic ligands are often depicted as *strong-field ligands* (relative to  $\pi$ -donors, that are in general classified as *weak-field ligands*, or  $\sigma$ -only ligands) and are mostly associated with metal ions in low oxidation states with exceptions such as  $W^{IV}Cl_2(CO)O(PMePh_2)_2$ ,<sup>30</sup>  $W^{IV}(NR)(S_2CNEt_2)_2$ <sup>31</sup> and  $[(PNN)Re^{IV/V}(CO)(O)_2]^{0/+}$ .<sup>32</sup>

## Carbon monoxide as ligand

IUPAC classifies an organometallic compound, as a metal-containing compound bonded through carbon to an organyl group.<sup>33,34</sup> As such, the presence of a CO ligand alone does not formally, merit the classification of a compound as "organometallic". However, the CO ligand is probably the most important ligand in the chemistry normally considered as organometallic<sup>35</sup> such by exclusion of carbonyl complexes, the field of organometallic chemistry would suffer from a dramatic amputation in perspective of volume as transition metal carbonyl complexes comprise almost 60,000 entries in the Cambridge Crystallographic Structure Database (CCSD).

The CO ligand is the prototypical  $\pi$ -acceptor ligand and forms stable complexes with metals in low oxidation states as illustrated by the classic examples:  $Ni(CO)_4$ ,<sup>36</sup>  $M(CO)_5$  ( $M=Fe, Ru, Os$ ),<sup>37-40</sup>  $Co(CO)_4$ <sup>41</sup> and Collman's reagent,  $Na_2[Fe(CO)_4]$ , which is a useful reagent in organic synthesis.<sup>42</sup> Carbon monoxide is an interesting molecule on its own account. As for example the polarity is known to be  $^-CO^+$ <sup>43</sup> which is a clear violation of the ground rule introduced at the low-level chemistry studies that *the negative charge is*



polarised towards the most electronegative element. Additionally, the valence of carbon is highly unusual as carbon normally forms 4 bonds. As such, CO has been called *an isolated embarrassment to introductory chemistry teachers*.<sup>44</sup> Most notably, despite that the first reported carbonyl complex ( $\text{PtCl}_2(\text{CO})_2^*$ ) dates back to Schützenberger in 1868,<sup>46</sup> the nature of the M-CO bond still appears to be of great debate, yet, vibrational spectroscopy have been established as the main and most powerful tool for the quantification of  $\pi$ -back-donation in the M-CO bonding whereas the  $\sigma$ -parameter in the M-C and C-O bonds still appears to be under dispute.<sup>47-53</sup> The energy of the  $\nu(\text{CO})$  stretching mode for metal complexes has been suggested as a diagnostic probe for the quantification of the  $\pi$ -donor strength of a *trans* ligand in metal complexes of low oxidation states. This approach is useful in complexes where repulsive filled-filled destabilising interactions between the metal  $\pi$ -symmetric orbitals and the donating p orbitals of the ligand gets stabilised by a *trans*- $\pi$ -acceptor ligand,<sup>54,55</sup> as schematised below in Figure 1.4.

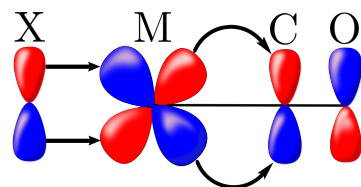
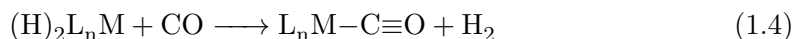
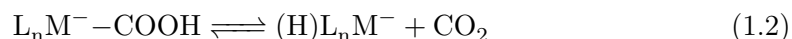
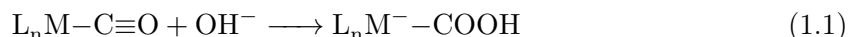


Figure 1.4: Stabilisation of  $\pi\text{X} \rightarrow \pi\text{M}$  interaction by a  $\pi$ -acceptor ligand (here: CO) in the *trans*-position to the  $\pi$ -donor ligand, X.

When carbon monoxide coordinates to a metal center the carbon atom can obtain a positive partial charge. Therefore, it is subject to nucleophilic attack from incoming electrophiles such as hydroxide in the important syngas systems, as depicted below:<sup>56,57</sup>



Starting from a metal carbonyl in step 1.1, the mechanism proceeds analogously to the Hieber base reaction<sup>58</sup> with nucleophilic attack on the carbonyl carbon atom. The generated metallacarboxylic acid undergoes spontaneous decarboxylation and generates a hydrido metallate under the extrusion of  $\text{CO}_2$  in step 1.2. In the case of  $[\text{HFe}(\text{CO})_4]^-$ , this species is known to form dihydride complexes in the presence of protons<sup>58-60</sup> as described in step 1.3. In the last step (1.4), introduction of carbon monoxide to the complex affords reductive elimination of  $\text{H}_2$  and coordination of CO convolutes the catalytic cycle. The electrophilicity of the carbon atom is generally more pronounced in the cases where close to no  $\pi$ -backbonding is occurring, as in the cationic carbonyls  $[\text{M}(\text{CO})_4][\text{Sb}_2\text{F}_{11}]_2$ ,<sup>61</sup> where  $\text{M} = \text{Pd}, \text{Pt}$ , and  $[\text{M}(\text{CO})_6][\text{Sb}_2\text{F}_{11}]_2$ ,<sup>49</sup> where  $\text{M} = \text{Fe}, \text{Ru}, \text{Os}$  where strong intermolecular

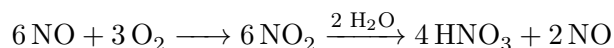
\*Interestingly, the solid state structure was determined as late as in 1996 by Bagnoli *et al.*<sup>45</sup>

C...F interactions are observed.

Intramolecular nucleophilic "attack" on carbonyl ligands can also happen via *migratory insertion* in which an organic group migrates from the metal to an unsaturated ligand (like  $\text{C}\equiv\text{O}$ )<sup>62</sup> as has been intensely studied for the complex  $\text{MeMn}(\text{CO})_5$ . By treating this molecule with  $^{13}\text{CO}$  the complex  $(\text{CH}_3\text{C}\{\text{O}\})\text{Mn}(\text{CO})_4(^{13}\text{CO})$  could be obtained, thus, proving that the migration of the methyl group into the M-CO bond does only occur for already coordinated carbonyl ligands. In addition, the labeled carbonyl moiety was coordinated *cis* to the acyl group which proves that *cis*-coordination is a prerequisite.

## Nitric oxide as ligand

Nitrogen monoxide (or nitric oxide) plays an important role, not only in coordination chemistry, but also as neurotransmitter<sup>63</sup> in higher mammals, and it is a vital part of the human immune response. As such, NO was announced as *Molecule of the year 1992*.<sup>64-66</sup> NO is naturally produced by nitroso bacteria in soil<sup>67</sup> and by lightning-induced oxidation of atmospheric dinitrogen<sup>68</sup> where it reacts with oxygen and water forming nitric acid, thus, contributing to the formation of acid rain:



Almost all modern day chemists may have worked with nitrosyl complexes in one way or another. Most likely in introductory freshman laboratory courses in chemical analysis where the black coloration of a mixture of nitrate ions and sulfuric acid in the presence of ferrous sulfate ( $\text{FeSO}_4$ ) makes the basis of the infamous "brown ring test"<sup>69</sup> as the strongly coloured  $[\text{Fe}(\text{NO})(\text{OH}_2)_5]^{2+}$  is formed,<sup>70</sup> which was unambiguously proven by Monsch and Klüfers whom communicated the crystal structure in 2019.<sup>71</sup>

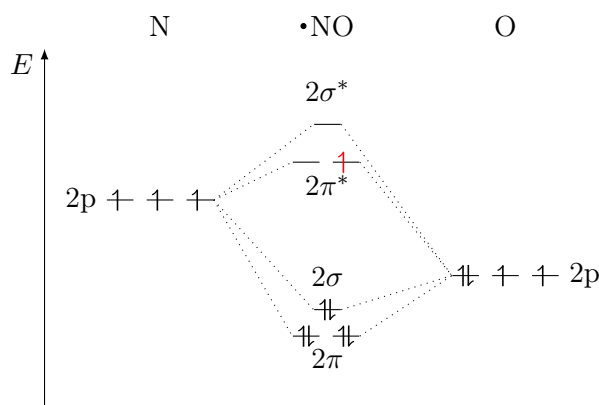
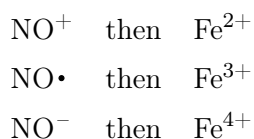


Figure 1.5: MO diagram for the free nitric oxide radical. Contributions from the s(N,O) orbitals have been omitted for clarity. Adapted from ref.<sup>1</sup>.

As can be realised from the simple MO diagram depicted in Figure 1.5, the electronic structure of the free NO molecule has radical character. The unpaired electron occupies the  $\pi^*$ -orbitals and, as such, the bond-order is easily deduced to 2.5, which agrees well

with a bond length of 1.154 Å<sup>1</sup> and as such, falls well in between the N≡N distance of 1.098 Å and 1.208 Å for O=O.<sup>72</sup> A triad of interrelated molecules can therefore be conveniently rationalised such that the free molecule has a doublet electronic ground state configuration, [Li<sub>2</sub><sup>2-</sup>]2π<sup>4</sup>2σ<sup>2</sup>2π<sup>\*1†</sup> which upon oxidation yields the electronic singlet species N≡O<sup>+</sup> ([Li<sub>2</sub><sup>2-</sup>]2π<sup>4</sup>2σ<sup>2</sup>2π<sup>\*0</sup>) which is isoelectronic with N<sub>2</sub>, CN<sup>-</sup> and CO. The electronic and chemical similarities between N≡O<sup>+</sup> and N<sub>2</sub> transition metal complexes were the basis for the argumentation by Enemark and Feltham<sup>73</sup> that M-NO complexes could serve as important model molecules in research of artificial nitrogen fixation. On reduction of the free NO molecule the N=O<sup>-</sup> species is formed with an electronic ground state isoelectronic to O<sub>2</sub>, thus, adopts a triplet electronic ground state configuration ([Li<sub>2</sub><sup>2-</sup>]2π<sup>4</sup>2σ<sup>2</sup>2π<sup>\*2</sup>). It is clear, that the fewer electrons occupying the π<sup>\*</sup>-orbitals the better the π-acceptor, as such, the NO<sup>+</sup> species is a better π-acceptor than the other isoelectronic species, *vide infra*, with the nitroxylide ion as the expected poorest π-acid. It should now have become apparent to the reader, that the different possible charges on the NO ligand, and as such, several different ways to distribute charges within a nitrosyl coordination compound make the bookkeeping of electrons an unwieldy task as the oxidation state cannot directly be derived by simple means as illustrated below for the historically and clinically important<sup>74</sup> nitroprusside anion, [Fe(NO)(CN)<sub>5</sub>]<sup>2-</sup>: if



Jørgensen coined this type of redox-active ligands as *non-innocent*.<sup>75</sup> To account for these different possible electronic states of metal nitrosyl compounds, the Enemark-Feltham notation was suggested.<sup>76</sup> In this notation, the M-NO fragment is treated as the entity {MNO}<sup>*n*</sup> where *n* is the sum of electrons associated with the metal d orbitals and the electrons associated with the NO π<sup>\*</sup> molecular orbital. It is highly important to note that the Enemark-Feltham notation makes no assumption about the actual distribution of electrons between the metal and the NO ligand. In the example above, the nitroprusside ion has been denoted in the Enemark-Feltham notation as {FeNO}<sup>6</sup>.

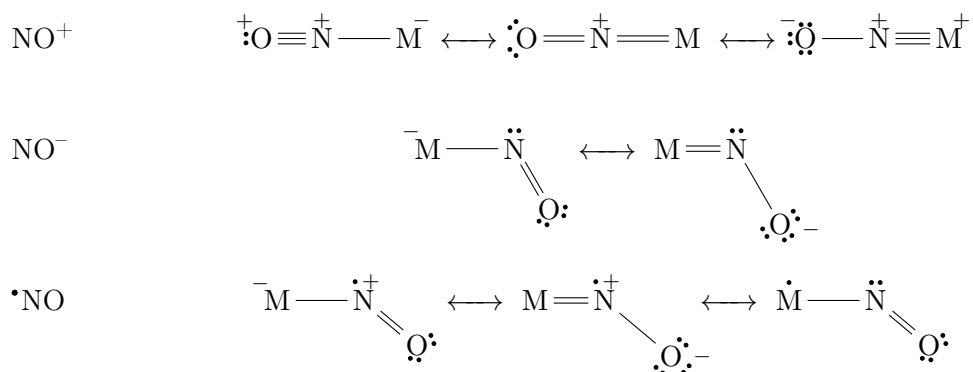
### Bonding modes of the NO ligand

The Lewis structures of :N≡O<sup>+</sup> and :N=O: clearly indicate from the difference in the hybridisation of the atoms, that there should be a direct correlation between the energy of the ν(NO) vibrational mode and the M-N-O angle. Unfortunately, this is not the case, as will be explained in further detail in Chapter 3. The extra electron that follows the NO molecule (relative to CO) leads to valence peculiarities as described previously. NO complexes may be regarded as nitrosonium (NO<sup>+</sup>) or nitroxyl (NO<sup>-</sup>) complexes with linear

---

<sup>†</sup>[Li<sub>2</sub><sup>2-</sup>] = 1σ<sup>2</sup>1σ<sup>\*2</sup>2σ<sup>2</sup>2σ<sup>\*2</sup>

or bond M-N-O angles, respectively, with neutral  $\bullet\text{NO}$  representing an intermediate. For the purpose of electron bookkeeping, the nitrosonium formalism is thought as a reductive association of NO with the metal, such that a 1-electron transfer from the incoming  $\bullet\text{NO}$  to the metal followed by an electron pair donation to the metal via the  $2\sigma$ -orbital (Figure 1.5) of the generated nitrosonium ion. As such,  $\text{NO}^+$  is depicted as a 3-electron donor in analogy with the nitrido and carbyne ligands.<sup>77</sup> On the contrary, the  $\text{NO}^-$  formalism requires the NO ligand to be a 1-electron donor as the metal functions as a reducing agent on the incoming  $\bullet\text{NO}$  molecule.<sup>78</sup> These aspects of donation are summarised in Scheme 1.2 below:



Scheme 1.2: Different resonance structures of the M-NO bonding motifs represented by Lewis structures.

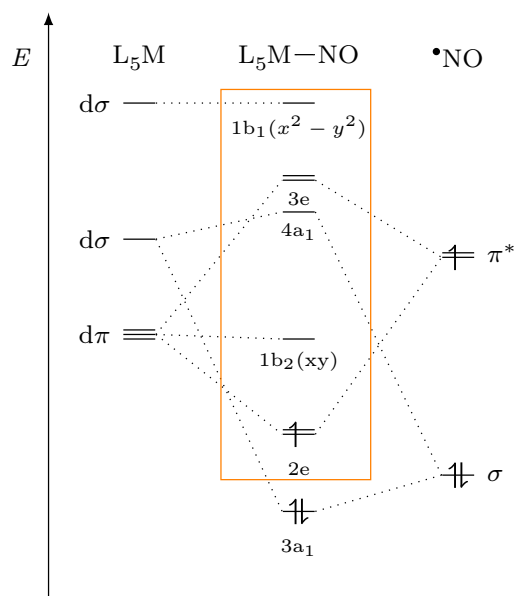


Figure 1.6: MO diagram for a generic six-coordinated  $\text{L}_5\text{M}(\text{NO})$  species in  $C_{4v}$  symmetry. Adapted from ref.<sup>2-6</sup> The orange box indicates which orbitals are associated with  $n$  in the Enemark-Feltham notation:  $\{\text{MNO}\}^n$ .

The bonding modes depicted in Scheme 1.2 can be rationalised by the generic molecular orbital (MO) diagram provided in Figure 1.6 which qualitatively shows the energy change

of the metal d-orbitals upon coordination of  $\bullet\text{NO}$  (which here have been reduced to its essentials: A  $\sigma$ -donor orbital localised on N, and a pair of acceptor orbitals, ( $\pi^*$ ) coordinates to an  $\text{L}_5\text{M}$  fragment and thereby form a six-coordinate complex of which the highest symmetry is  $C_{4v}$ . The  $3a_1$  orbital has primarily N character and is bonding with respect to the M-NO. The  $2e$  orbital has mostly metal character ( $d_{xz}$  and  $d_{yz}$ ), thus, it is  $\pi$ -symmetric and therefore is bonding with respect to M and N and antibonding with respect to N and O; forming a metal nitrogen bond with multiple bond character. The  $1b_2$  ( $d_{xy}$ ) orbital is non-bonding and localised on the metal as is the  $1b_1$  ( $d_{x^2-y^2}$ ) orbital which is higher in energy when the lobes are located on the cartesian coordinate axes in the  $xy$ -plane. The  $4a_1$  is the antibonding combination of the  $d_{z^2}$  and  $\sigma(\text{NO})$  orbitals. The relative energies of the  $2e$  and  $4a_1$ , and, thereby also the relative energies of  $d_{z^2}$  and  $\pi^*(\text{NO})$  orbitals are of crucial importance. When the  $2e$  set is lower in energy than the  $4a_1$  orbital, the  $2e$  set will be filled first causing a decrease in the N-O bond order which ultimately leads to M-N-O bending. If the  $4a_1$  orbital is lower in energy than the  $2e$  degenerate set, the M-L  $\sigma$ -interaction will be weakened and this will ultimately result in ligand (L) dissociation and concomitant generation of a pentacoordinate MNO species. Complexes with the electronic configuration:  $(3a_1)^2(2e)^4$  correspond to the normal "backbonding" situation and thus have three bonding interactions. As far as the MNO fragment is concerned, presence of electrons in the non-bonding orbitals play, if any, only a minor role. In Figure 1.6, the basis of the Enemark-Feltham notation is indicatively provided by the orange box. The

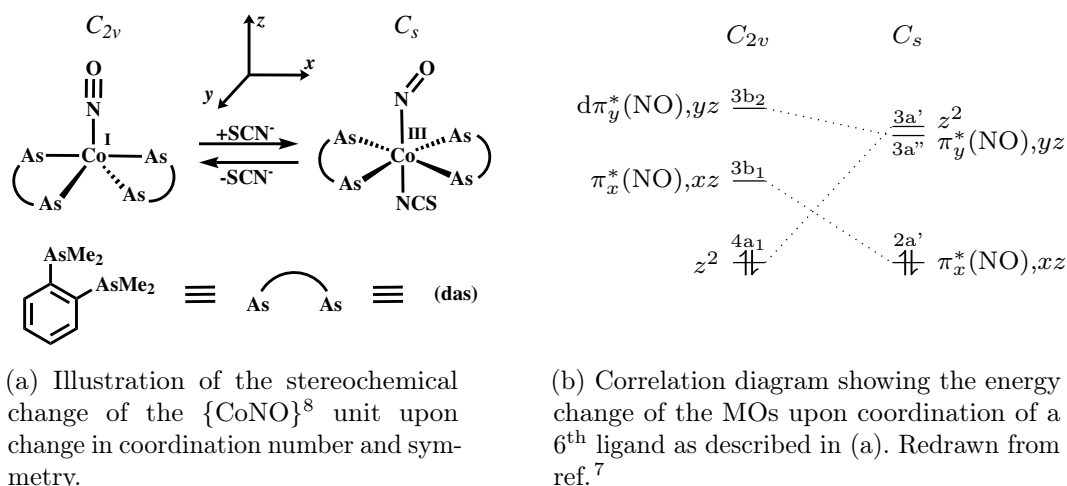


Figure 1.7: Structural change and orbital correlation diagram for the  $\{\text{CoNO}\}^8$  upon symmetry change in the coordination sphere reported by Enemark *et al.*<sup>7</sup> The coordinate system specified in (a) is applicable to (b). The vertical energy axis is schematic.

aforementioned electron configuration,  $(3a_1)^2(2e)^4$  would be  $\{\text{MNO}\}^4$  and the configuration  $(3a_1)^2(2e)^4(1b_2)^2$  would be  $\{\text{MNO}\}^6$  etc. In lower symmetries than  $C_{4v}$ , the degeneracy of the  $2e$  and  $3e$  set will be lifted; however, the discussion remains unchanged.<sup>79,80</sup> Bending of the M-N-O angle depends mainly on the relative energy of the  $4a_1$  and  $3e$  orbitals. This is conveniently illustrated by the  $\{\text{CoNO}\}^8$  complexes shown in Figure 1.7a. From

the correlation diagram in Figure 1.7b it is clear, that upon coordination of a 6<sup>th</sup> ligand, the  $d_{z^2}$  orbital increases in energy such that it exceeds the the antibonding  $\pi^*$  orbital which is mainly localised on the NO ligand, and as such, electrons are transferred to the  $\pi^*(NO)$  orbital effectively causing a rehybridisation of the N atom from  $sp$  to  $sp^2$ . The molecular orbital evaluations presented here are in agreement with the observation that many bent M-NO complexes undergo electrophilic attack on the N atom of the nitrosyl ligand, including protonation<sup>7,81–85</sup> and linear, formally, nitrosonium complexes undergo nucleophilic attack.<sup>86–92</sup> For the sake of completeness, it shall be mentioned here that O-centered nucleophilic reactivity for terminally bound NO have also been reported,<sup>93</sup> however, this type of reactivity appear to be exceedingly rare and, as such, should be regarded as "exotica".

In literature, mostly electrophilic reactivity of coordinated nitric oxide is reported. This may be explained by the statistical abundance of formally regarded nitrosonium species. The histogram depicted in Figure 1.8 shows the statistics over the M-N-O bond angles for all terminal M-NO (M being a transition metal) compounds deposited in the Cambridge Crystallographic Structure Database (CCSD). It is clear, that compounds exhibiting linear ( $\sim 160^\circ - 180^\circ$ ) by far comprise the most statistically significant geometry. The "double hump" shows,

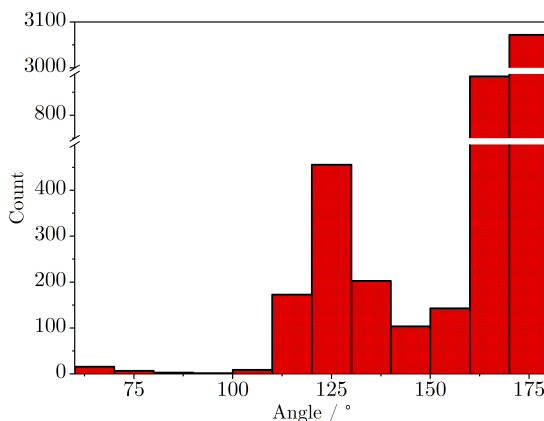


Figure 1.8: Statistics showing the distribution of M-N-O angles for terminal nitrosyl complexes.

that intermediate M-N-O bending is somewhat less prominent than is the strongly bent geometries. Interestingly, structures with M-N-O angles below  $90^\circ$ , although only few, are reported. However, some of these alarmingly acute angles are likely due to severe disorder and poor crystal quality.<sup>94,95</sup> Other complexes showing acute, or close-to-acute M-N-O angles have been subject in photochromic studies in which the acute-angled species is a light-induced linkage isomer. In these studies, a single-crystal of a nitrosyl complex is subjected to light during the diffraction experiment to produce a metastable state in which the NO ligand is bound through oxygen (or both O and N).<sup>96–99</sup> These photochromic materials have been suggested as potential candidates for the development of holographic memory devices.<sup>100,101</sup>

## Chapter 2

# *Trans*-influence as a measure in catalyst design

When being concerned about catalytic reactions that involve atom- or group transfer from a catalytic species to a substrate, one can imagine that the auxiliary ligand set must have an influence on the catalyst's acceptor/donor capacities. If, for example, one is to optimise a transfer hydrogenation reaction the formal addition and donation to- and from a transition metal complex, the strength of the M-H bond is of crucial importance and must be sensitive especially to the ligand *trans* to the hydride ligand that is, the *trans*-influence of ligands causes a weakening of the chemical bond across the metal ion and thus, can not be disregarded in the evaluation of expected reactivity.<sup>102</sup> As was pointed out by Morris *et al.*, the attack from the hydride on electrophiles, such as aldehydes, ketones and esters represents the same geometrical distortion in the first coordination sphere as the asymmetrical vibrational stretching mode (see Figure 2.1). Thus, the energy of this particular mode, would, in principal, allow for estimations about the catalytic activity with respect to hydride- donation/acceptance.<sup>103,104</sup>

A part of this thesis has been concerned with the synthesis of a series of new *trans*-X mono hydrido compounds of PNP-pincer-supported Ru(II) complexes. The solid state structure of these new complexes, and potential catalysts, will be discussed together with their spectroscopic characteristics.

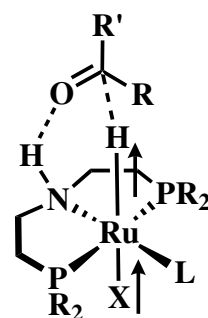


Figure 2.1: The supposed transition state of an electrophile here: a generic carbonyl compound approaching the catalytic species. The hydride bond is elongated in conjunction with a shortening of the *trans*-Ru-X bond illustrating the similarity with the assymetric stretch of the H-Ru-X entity indicates by the arrows.

## 2.1 Interpretation of the *trans*-influence

The observation that a certain type of ligands tend to effect the rate of substitution in coordination complexes of another ligand in the *trans*-position was first extensively utilised in preparative inorganic chemistry by the Soviet chemist Chernyaev who used the phenomenon to synthesise a series of platinum(II) compounds. His works later became of paramount importance in the development of the highly effective anti-cancer drug cisplatin.<sup>105</sup> Later, Basolo and Pearson coined the term "*trans*-effect" as "*the labilization of ligands trans to other ligands*" in 1962<sup>106</sup>. It was then later realised that this *trans*-effect could be divided into two different terms, namely the kinetic *trans*-effect that affected the *rate* of which ligands were substituted and the *trans*-influence that affected the bond-length and, thus, the bonding energy between a ligand and a transition metal, that is, a thermodynamic property per se. Pidcock *et al.* introduced the term "*trans*-influence" in 1966 as the thermodynamic contribution to the labilisation of a *trans*-ligand and disclosed from Nuclear Magnetic Resonance (NMR) spectroscopic data that the origin of the *trans*-influence was mostly dependent on the  $\sigma$ -donating character of the ligand in question.<sup>107</sup> From this observation, many studies of the *trans*-influence by strong  $\sigma$ -donors, such as hydride ( $\text{H}^-$ ) and methyl ( $\text{Me}^-$ ) has been undertaken and, indeed, these ligands show exceptional *trans*-influence<sup>108</sup>.

A very convincing account, based on the Angular Overlap Model, of the *trans*-influence being a consequence of electron destabilising interaction (avoidance of ligands to share the same metal orbitals) was provided by Burdett and Albright in 1979<sup>109</sup> and a schematic representation of their arithmetic approach is provided in Figure 2.2 below.

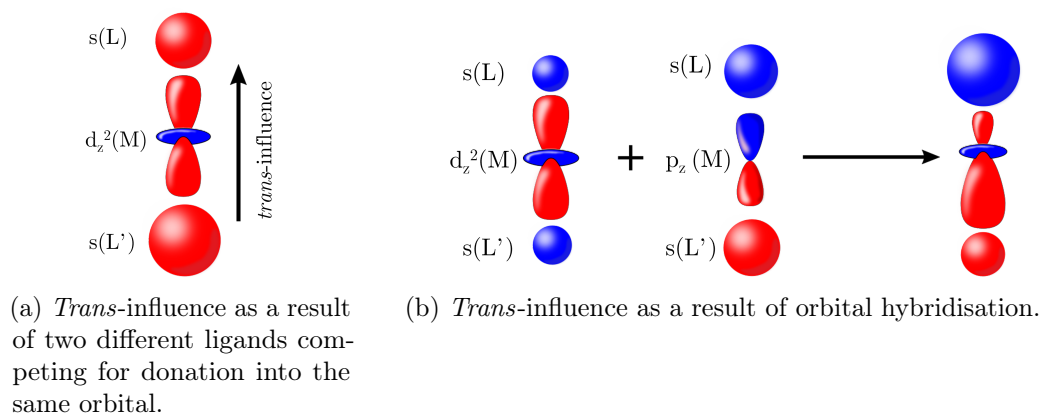


Figure 2.2: Schematic representation of the two main electronic effects of *trans*-influence.

The origin of the *trans*-influence is such, that if a ligand, L, is sharing an orbital with another ligand, L', then the ligand with the smallest overlap integral (L in Figure 2.2a) experience a destabilising effect on the M-L bond. In other words, the weakest  $\sigma$ -electron donor (L) will experience a weakening in the ligand-metal bond and, as such, an elongation in the bonding distance is observed. In Figure 2.2a above, the direction of change in bond distances is indicated by the arrow. Burdett and Albright<sup>109</sup> highlighted



that in low symmetry complexes *trans*-influence can, additionally, occur as a result of metal-centered orbital hybridisation. Detailed calculations on this additional mechanism of the *trans*-influence has later been provided with the clarification that, the strongest  $\sigma$ -donor pushes the nodal plane between the two anti-bonding ligand orbitals (transferred by the appropriate metal p-orbital, here:  $p_z$ ) towards the weakest donor.<sup>110</sup> In Figure 2.2b this is illustrated by mixing the M-L anti-bonding  $e_g^*$  (empty in low-spin octahedral  $d^6$  complexes) with the M-L bonding orbital, which in turn, show anti-bonding interaction between the ligands ( $t_{1u}$  SALCAO in  $O_h$  symmetry). This hybridisation shows an increase in the overlap integral of the M-L' interaction involving the stronger donor (L') and increased destabilisation of the weaker M-L interaction.

### 2.1.1 Chemical shifts in hydrido complexes of transition metals

Because of the difficult task of locating precise positions of hydrogen atoms with standard in-house instrumentation (such as X-ray diffraction experiments), and therefore also hydrido ligands, Nuclear Magnetic Resonance (NMR) spectroscopy is a vastly used technique in the characterisation of metal hydrides. Transition metal hydrido complexes do often exhibit extremely high-field chemical shifts so far observed as low as -59.1 ppm.<sup>111</sup> The surprisingly high-field shifts observed for transition metal hydrides were already addressed by Buckingham and Stephens in 1964.<sup>112</sup> Based on crystal field theory they argued that low lying excited states within the d-orbital manifold were the main phenomenon responsible for the observed chemical shifts. The Buckingham-Stephens model describes the isotropic shielding constant as a sum of diamagnetic- and paramagnetic contributions:  $\sigma = \sigma^d + \sigma^p$  where  $\sigma^d$  depends only on the ground state electronic configuration whereas the  $\sigma^p$  contribution depends on  $t_{2g} \rightarrow e_g$  (singlet electronic states,  $O_h$  symmetry) excitations. This interpretation was later investigated with DFT methods by Ziegler<sup>113</sup> whom, in support of the Buckingham-Stephens model, elaborated that the paramagnetic contribution,  $\sigma^p$ , to the isotropic chemical shift could be divided into a weighted sum of the parallel ( $\sigma_{\parallel}^p$ ) and perpendicular ( $\sigma_{\perp}^p$ ) terms:

$$\sigma^p = \frac{1}{3}\sigma_{\parallel}^p + \frac{2}{3}\sigma_{\perp}^p$$

Due to the ring current density,<sup>114</sup> and thereby the induced magnetic field, the shielding components of  $\sigma^p$  have opposite signs: the induced magnetic field in the parallel case (that is, the external magnetic field is parallel to the M-H bond axis) is parallel to the external magnetic field and the resulting shielding is negative. However, in the  $\sigma_{\perp}^p$  case, the induced magnetic field experienced by the hydrido ligand is antiparallel to the external magnetic field which makes the corresponding shielding parameter positive in sign. In consequence,

the chemical shift,  $\delta$ , (relative to TMS) was described as follows:

$$\begin{aligned}\delta &= \delta^d + \delta^p \\ \delta^d &= \sigma_{\text{TMS}}^d - \sigma_{\text{complex}}^d \\ \delta^p &= \sigma_{\text{TMS}}^p - \sigma_{\text{complex}}^p \\ &\cong -\sigma_{\text{complex}}^p \\ &\cong -\frac{1}{3}\sigma_{\parallel}^p - \frac{2}{3}\sigma_{\perp}^p\end{aligned}$$

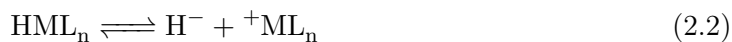
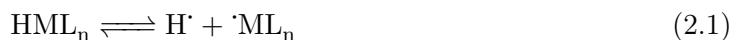
It is clear from Ziegler’s elaboration (above) of the Buckingham-Stephens model that of the magnetic contributions to the chemical shift, the main contributor to the high-field chemical shift is the perpendicular paramagnetic shielding (recall that  $\sigma_{\parallel}^p$  is by nature negative in sign whereas the opposite is true for  $\sigma_{\perp}^p$ ). It has been noted that as the above description of the hydride chemical shift is mainly described via HOMO-LUMO mixing (in an external magnetic field) utilising the filled  $t_{2g}$  set of  $\pi$ -symmetry, it seems apparent that relativistic effects, such as spin-orbit coupling (SOC) which, in turn, is passed by a Fermi-contact (FC) term must have a contribution to the isotropic chemical shielding.<sup>115,116</sup> It was deduced that SOC indeed had a significant contribution to the perpendicular shielding tensor with the effect of enhancing the Buckingham-Stephens terms.<sup>117</sup> As can be found in detailed algebraic examinations of the relativistic contributions to the  $^1\text{H}$ -NMR the following 3 remarks are of fundamental importance:<sup>118</sup>

- Contributions are restricted to the frontier MOs.
- Only MOs that contain contributions from the heavy atom are considered significant.
- Only MOs that contains contributions from  $s$ -type AOs of the light atom can contribute to the relativistic correction.

As hydrido ligands solely bind through the  $1s$  orbital, the hydrogen nucleus is expected to be particularly sensitive to the relativistic effects when directly bonded to transition metal centers.<sup>119</sup> Relations of the relativistic contributions to the paramagnetic shielding of hydrido ligands on a range of Pt(II) complexes and the *trans*-influence have been computationally investigated by Kaupp and co-workers. They found, that by inclusion of relativistic effects the calculated chemical shifts were in satisfactory agreement with values reported in literature within a standard deviation of 0.9 ppm.<sup>120</sup> In the same work it was found that the hydride chemical shift were indeed correlated with the Pt-H bonding distance which again was closely related to the nature of the  $\sigma$ -donation of the *trans* ligand and that less negative chemical shifts are related to longer Pt-H distances. These observations have also been experimentally observed by Olgemöller and Beck<sup>121</sup> for octahedrally coordinated Ir(III) where a linear correlation of  $\tilde{\nu}(\text{IrH})$  vs  $\delta(\text{IrH})$  serve as a convincing argument.

### 2.1.2 The transition metal-hydrogen bond

Unlike many other ligands the hydride ion ( $\text{H}^-$ ) shows remarkable versatile compatibility with different metals in a vast range of formal oxidation states ranging from +7 in  $\text{ReH}_9^{2-}$ <sup>122</sup> to -3 in  $\text{IrH}_3^{6-}$ .<sup>123</sup> The hydrido ligand is regarded as a  $\sigma$ -donor only with the  $1s^2$  electronic structure being the obvious reason. As such, the hydrido ligand is formally considered a  $2e^-$  donor (assuming ionic bonding). The hydrido ligand can serve as both terminal and bridging ligand.<sup>124</sup> As only the former binding mode is of interest to this thesis, the bridging hydrido ligand will be left out of any further discussions. The reactivity of hydrido ligand is dominated by three reaction paths that on their own highlights the different aspects of the metal-hydrogen bond:<sup>125</sup>



Equation 2.1 shows the homolytic bond cleavage which is particularly important with respect to the thermodynamic stability towards hydrogen gas evolution. Equation 2.3 is analogous to any proton dissociation reaction of a Brønsted acid and, thus, is expressed as a pKa value which spans a large range from 44 for  $\text{IrH}_5(\text{PCy}_3)_2$  (in THF)<sup>126,127</sup> to -4 for  $\text{WH}(\text{CO})_3(\text{MeC}(\text{CH}_2\text{PPh}_2)_3)$  (in DCE).<sup>128,129</sup> On a different note, reaction 2.3 is interesting also in the reverse direction as it indicates that simple protonation of metal complexes as a synthetic viable route to new hydrido complexes, as will also be demonstrated in Chapter 3 in this work. Equation 2.2 is the most relevant to this thesis as it expresses the dissociation of a hydride ion. The propensity of a metal hydride complex to undergo this reaction path way, as in reduction reactions of carbonyl derivatives, is expressed as the "hydricity"<sup>125,130,131</sup> and is defined as the Gibbs free energy ( $\Delta G_{\text{H}^-}^\circ$ ) required to remove the hydride ion from the metal complex.<sup>132</sup> The heterolytic cleavage is very solvent sensitive as the polarity of the medium effects the stability of the solvated ions and the tendency of coordination of the solvent to the metal ion influence the equilibrium constant for the hydride transfer reaction.<sup>133,134</sup> The nature of the auxilliary ligands do also influence the hydricity of a metal hydride. It has been observed, that strong  $\sigma$ -donating ligands enhance the hydride transfer step in transition metal catalysed hydrogenation reactions<sup>135,136</sup> by increasing the electron density on the metal and, by consequence, on the hydrido ligand resulting in a higher hydride character.<sup>137</sup>

### 2.1.3 X-ray crystallography

In general, the method of choice for the quantification of *trans*-influence is single-crystal X-ray diffraction because the electron density in a crystal can be directly translated into structural parameters of molecules in the solid state. However, one problem arises when dealing with metal-hydrogen bonding: As photons are diffracted by electrons, and not by nuclei, as is the case for neutrons, the positional precision of the hydrogen atom is often at least one order of magnitude less precise because the single electron on the hydrogen atom accounts for both the electron density around the nucleus and within the bond<sup>138,139</sup> when refining the structure models under the premises of the Independent Atom Model (IAM) originally formulated by Compton in 1915<sup>140</sup>. As such, the hydrido-complexes presented in this thesis are refined with the Hirschfeld Atom Refinement (HAR) method using the recent implementation of the NoSpherA2<sup>141</sup> program in Olex2-1.5<sup>142</sup> that utilises the Orca program (v. 4.2.1). See experimental section for details.

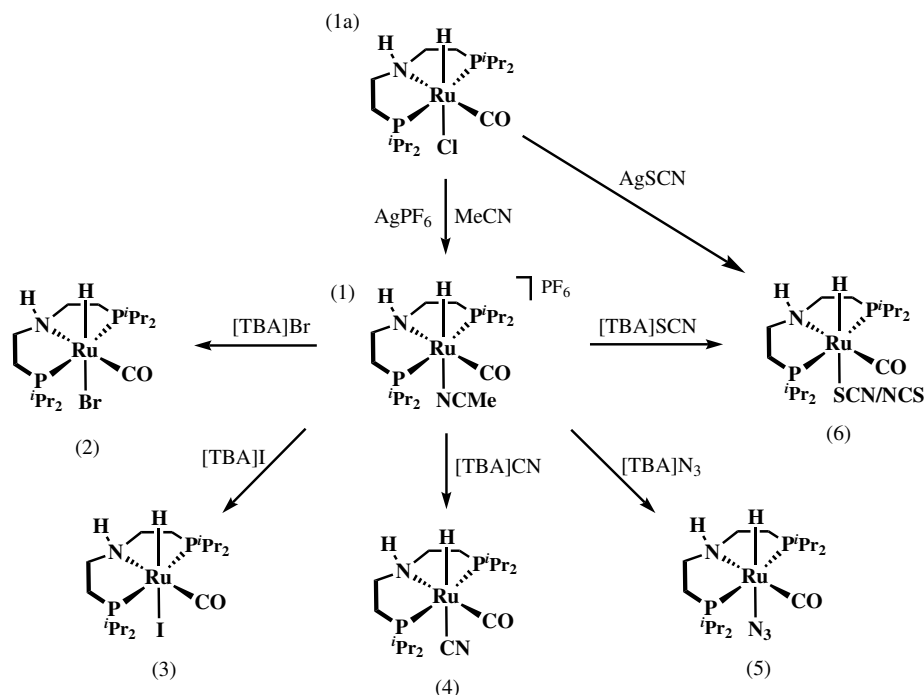
The computational machinery<sup>141,143</sup> behind the Hirschfeld method consists of an initial quantum mechanical wave function calculation using the preliminary IAM refined structure model (obtained from experiment). This makes it possible to partition of the obtained electron density into atomic contributions, the so-called "Hirschfeld atoms". The Hirschfeld atoms are then used in the calculation of the atomic form factors that are subsequently used in the least-square refinement. The HAR method is iterative and, as such, repeated until the structure model has converged. In the following, all comparisons with structures known to literature will be on the basis of the IAM, *vide infra*, models derived in this thesis because the HAR modeling is still not used per default when analysing X-ray diffraction data for metal hydride species.

## 2.2 Characterisation of Novel Hydridocarbonyl Complexes

As indicated in Scheme 2.1 complex (1) serves as an excellent starting material for complexes (2) - (6). Exchange of the chlorido ligand for acetonitrile is easily obtained by chloride abstraction with AgPF<sub>6</sub> in acetonitrile to generate complex (1). After filtering off the AgCl synthesis of (2)-(6) is obtained by addition of the appropriate halide source directly to the aforementioned filtrate. The species (6) can be obtained by addition of thiocyanate to the intermediate complex (1) or by direct reaction of AgSCN with (1a). Unfortunately, a protocol for isolation of the clean linkage isomers\* has not been developed. The synthesis of the compounds presented in this section was conducted straightforward by addition of tetrabutylammonium (TBA) halide/pseudohalide to complex (1) which, in turn, was generated *in situ* as described above. The general synthesis is summarised in Scheme 2.1 (see Appendix B for experimental details).

---

\*Thiocyanate is, as ligand, ambidentate and can coordinate through either sulfur or nitrogen.



Scheme 2.1: Summary of the synthetic procedure of the new *trans*-hydrido complexes of ruthenium(II) studied in this work.

### 2.2.1 Structure of the (iPr<sub>2</sub>PNP)RuH(NCMe)(CO) cation

Colourless high quality crystals of the parent complex, (1), which was formed *in situ* in the synthesis of complexes (2)-(6), was obtained by leaving the filtrate obtained after the reaction between (1a) and AgPF<sub>6</sub>, at  $-30\text{ }^{\circ}\text{C}$  for approximately 3 days. The compound (1) crystallises in the *Pnma* space group and the cation belongs to the *C<sub>s</sub>* point group. The amine proton on the PNP ligand is oriented antiparallel (*anti*) relative to the hydrido ligand.

The PNP-ligand coordinates in a meridional (*mer*) fashion. It makes up the equatorial plane together with the CO ligand, rendering the PNP amine and CO mutually *trans* with the acetonitrile- and hydrido ligands occupying the axial positions. The hexafluorophosphate anion shows short contact with the PNP-amine proton. The Ru-H bond distance of 1.580 Å (IAM) is expected by comparison with other PNP-ligated ruthenium *trans*-hydrido acetonitrile species as reviewed in Table 2.1. The Ru-acetonitrile bonding distance is observed as 2.161 Å which falls within the expected range as compared to other complexes with a similar coordination motif. The closest resemblance to the parent complex known to literature was published by Gibson *et al.* in 2004<sup>144</sup> and reveals a Ru-H bond distance of 1.225 Å as well as a Ru-NCMe bonding distance of 2.160 Å. As such, the Ru-H bond length in the complex by Gibson (see Figure 2.4) is significantly shorter

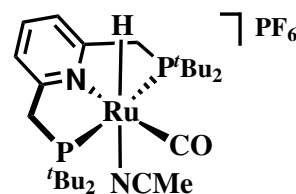


Figure 2.4: Schematic representation of the cationic Ru(II)-hydrido complex published by Gibson *et al.* in 2004 (see main text for reference).

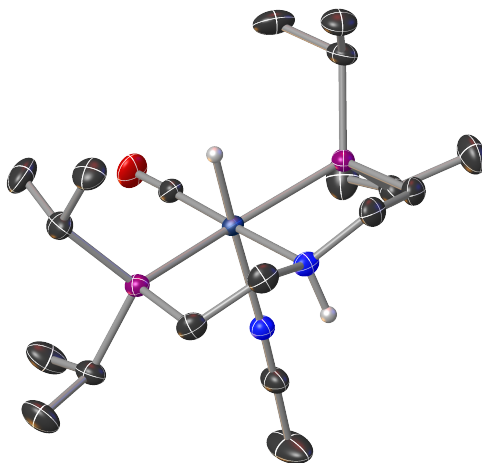


Figure 2.3: IAM model of the crystal structure of the cation of the intermediate complex (1). Hydrogens on all carbon atoms has been omitted for clarity. Plotted at 50% propability level.

than in complex (1), however, the difference in the Ru-NCMe bond distances in the two complexes are surprisingly similar ( $\Delta d = 0.001$  Å). So far, only 16 structures have been published in the Cambridge Crystallographic Structure Database (CCSD) on mononuclear ruthenium coordinated by both hydride and acetonitrile and of these, only 6 are supported by tridentate pincer ligands.<sup>144–158</sup> Table 2.1 below show the Ru-H, Ru-NCMe bond distances as well as type of pincer ligand in terms of coordinating atoms and the Ru-*trans*-L ligand relative to the central pincer ligand atom.

Table 2.1: Selected structural parameters for ruthenium pincer complexes that exhibits *trans*-hydrido-acetonitrile coordination.

Ru-H / Å	Ru-NCMe / Å	Equatorial L	Pincer Type	Ref
1.580	2.161	CO	PNP	this work
1.225	2.160	CO	PNP	144
1.471	2.158	CO	CNC	154
1.541	2.131	PPh <sub>3</sub>	P(O)N(O)P	155
1.717	2.185	CO	NNP(O)	156
1.461	2.211	CO	NNP	157
1.618	2.169	CO	CNC	158

Figure 2.5 shows the comparison with all structurally characterised transition metal complexes with the *trans*-acetonitrile-hydrido (terminal hydrido ligand) coordination motif. The bonding distance from the metal to the coordinated acetonitrile is almost not affected by the auxiliary ligand sphere whereas the metal-hydrido bond lengths show a much larger variation; the extremes being 1.39 Å and 1.925 Å for the smallest and largest bond distance respectively. This reflects the sensitive nature of the geometry of M-H bond to the type of metal, oxidation state and auxiliary ligand sphere.

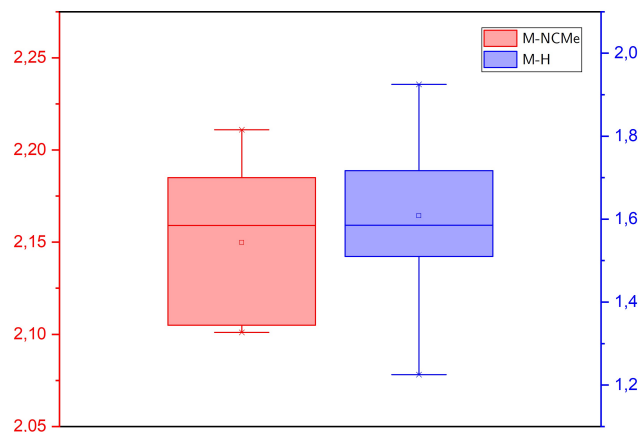


Figure 2.5: Box plot showing the distribution of bond lengths between a transition metal and a hydrido ligand (blue) and the distribution of bond lengths between a transition metal and an acetonitrile ligand (red). In all complexes, the acetonitrile ligand is coordinated in a *trans*-fashion relative to the terminal hydrido ligand.

### Spectroscopic characterisation of (1)

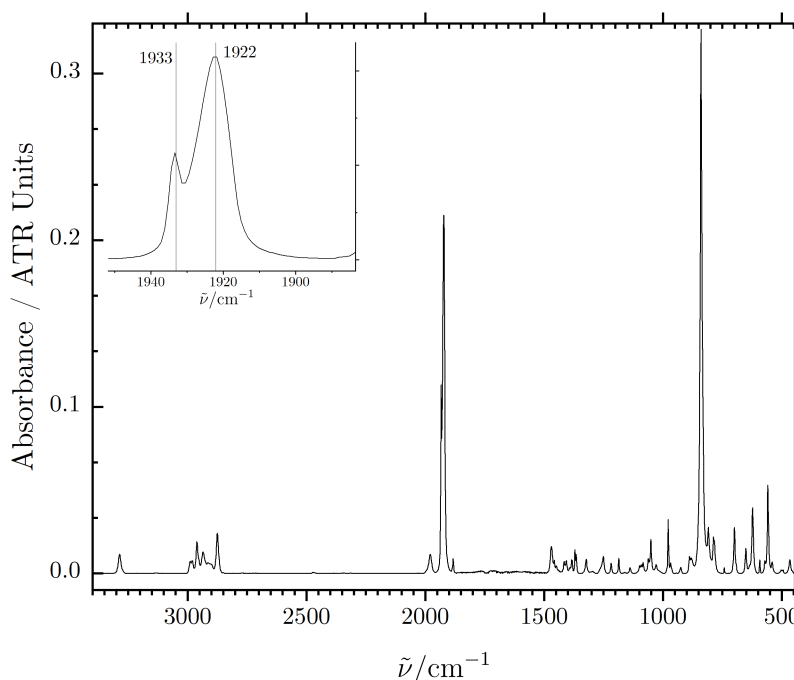


Figure 2.6: Solid state infrared spectrum of the parent complex salt, (1).

The well defined IR spectrum of (1) in Figure 2.6 show the very strong, sharp, characteristic  $\text{C}\equiv\text{O}$  stretch at  $1922\text{ cm}^{-1}$  which, as indicated in the insert, has a small shoulder around  $1933\text{ cm}^{-1}$ . This might be due to the presence of another conformer/isomer. However, in that case, the signal at  $3285\text{ cm}^{-1}$  which is attributed to the N-H stretch would also split up and so would the medium-strong Ru-H stretch at  $1977\text{ cm}^{-1}$ . The sharp band attributed to the amine proton in the PNP ligand indicates that no significant hydrogen bond interaction is present in the solid state. The most intense absorption is the sharp

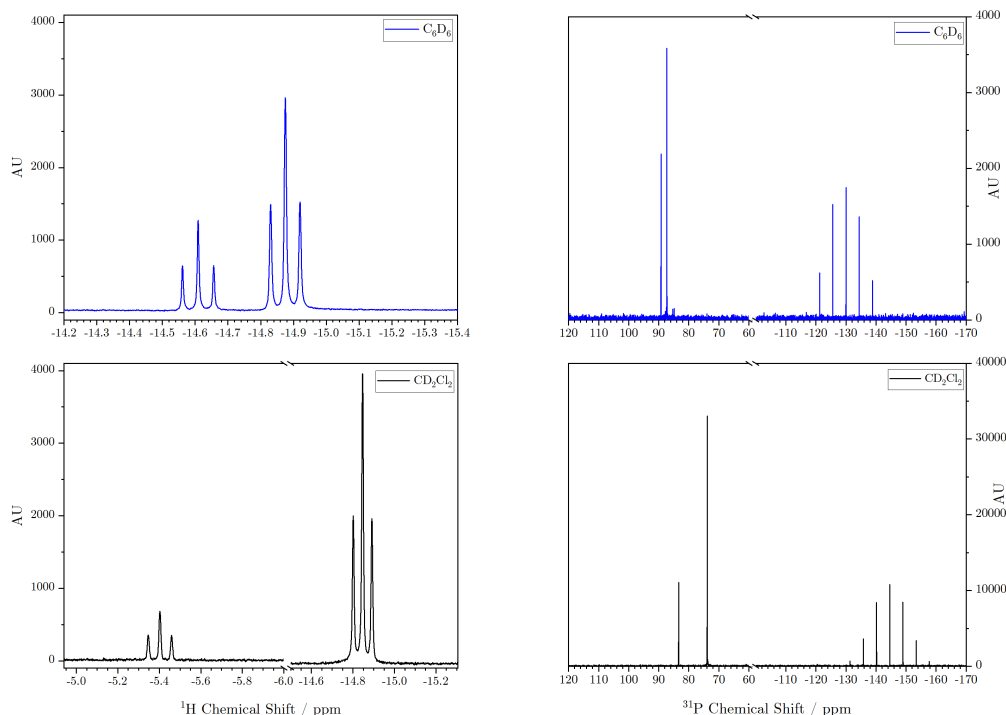


Figure 2.7:  $^1\text{H}$ -NMR spectra (left column) and  $^1\text{H}$ -decoupled  $^{31}\text{P}$ -NMR spectra (right column) of (1) in  $\text{C}_6\text{D}_6$  (blue) and  $\text{CD}_2\text{Cl}_2$  (black).

$\text{PF}_6^-$  signal at  $840\text{ cm}^{-1}$ . Unfortunately, it is not possible to resolve any characteristic bands that originates from coordinated acetonitrile.

The  $^{31}\text{P}$ -NMR spectrum in Figure 2.7 reveals two singlets at 89.23 ppm and 87.33 ppm ( $\text{C}_6\text{D}_6$ ) respectively as well as the characteristic septet at -144.57 ppm ( $\text{PF}_6^-$ ). The  $^{31}\text{P}$ -NMR spectrum in  $\text{CD}_2\text{Cl}_2$  also shows two singlets but at slightly higher field 83.38 ppm and 73.87 ppm respectively. The proton spectrum ( $\text{CD}_2\text{Cl}_2$ ) shows two characteristic triplets ( $\delta = -14.5$  and  $-5.4$  ppm) separated by 9.1 ppm. This large separation between the two hydride-triplets is only observed for this species in this work. The  $^1\text{H}$ -NMR spectrum (see Appendix B.1.1) points at different isomers as many of the same signals appear twice but are slightly shifted. However, as this large separation of the triplets is not observed for any other complex in this thesis, it cannot be ruled out, that the low-field signal arises from a decomposition product. An NMR spectrum of the same batch (crystals) was measured in  $\text{C}_6\text{D}_6$  (blue) to check whether a reaction with dichloromethane could give rise to the low-field signal observed. Indeed the spectrum recorded in  $\text{C}_6\text{D}_6$  differed by having two characteristic hydride triplets close in chemical shift ( $-14.88$  ppm for the major component and  $-14.61$  ppm for the minor component) which is more likely due to *syn/anti*-isomerism. In  $\text{CD}_2\text{Cl}_2$  the characteristic  $^{19}\text{F}$  doublet of the anion is observed at  $-74.00$  to  $-72.11$  ppm (Appendix B, Figure B.8). In  $\text{C}_6\text{D}_6$  the corresponding absorption resonances at  $-72.5$  to  $-70.61$  ppm (Appendix B, Figure B.9).



### 2.2.2 (iPr<sub>2</sub>PNP)RuHBr(CO) - (2)

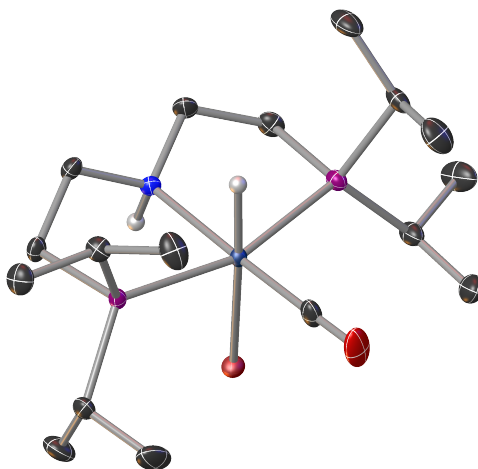


Figure 2.8: Crystal structure of complex (2) complex after IAM refinement. Hydrogen atoms on all carbon atoms has been omitted for clarity. Plotted at 50% probability level.

High quality colourless crystals were obtained at room temperature by slow evaporation of a dilute ( $\sim 5$  mg : 2 mL) solution of the complex in toluene. Complex (2) crystallises in the monoclinic space group  $P2_1/n$ . The molecular symmetry does formally belong to the  $C_1$  point group, however, by ignoring the orientation of the isopropyl substituents on phosphorous, the symmetry can be idealised to the  $C_s$  point group (see Figure 2.8). This complex is isostructural and close to isomorphous to the commercially available chlorido analogue (1a) used in the synthesis of intermediate (1)<sup>159</sup> with the amine proton oriented *syn* to the bromido ligand with an intramolecular (N-H)–I distance of 2.791 Å which is significantly shorter than the sum of the Van der Waals radii (2.93 Å)<sup>160</sup> and thus reveals a weak H $\cdots$ Br interaction.

The PNP ligand is coordinated in a *mer* fashion with the amine moiety in the *trans*-position to the carbonyl ligand. As such, H–Ru–Br bond vector is perpendicular to the basal plane spanned by the PNP- and the carbonyl ligands. The complex is very robust towards reaction with moist air and can therefore be stored on the shelf under ambient conditions for prolonged time. The Ru–H bond distance (IAM) is measured to 1.558 Å which is slightly longer than the corresponding distance in the chlorido complex reported by Gauvin *et al.*<sup>159</sup> whom reported a bond distance of 1.525 Å. Thus, an elongation of the bond of  $\Delta 0.033$  Å is observed when substituting chloride for bromide, indicating a slightly more pronounced *trans*-influence of the bromido ligand compared to the chlorido ligand. By comparison with the N-methylated hydridochlorido congener published by Beller *et al.*<sup>161</sup> (please note that the authors provided two different data sets, thus, two different models for the same compound. The model used for comparison here is the better one [CCSD ID: DAJCUP]), with an intermediate bond distance of 1.542 Å indicative of that

Table 2.2: Difference in geometric- and refinement parameters between the IAM, HAR and DFT models for complex (2). Ruthenium to phosphorous distances have been omitted as these are invariant

Ligand (L)	Ru-L / Å IAM	Ru-L / Å HAR	$\Delta$ (Ru-L) / Å HAR-IAM	Ru-L / Å DFT
H	1.558	1.614	0.056	1.606
Br	2.682	2.682	0.00	2.698
CO	1.834	1.836	0.002	1.827
HN(PNP)	2.183	2.187	0.004	2.225
Refinement Parameters	IAM	HAR		
$R_1$ / %	1.97	1.61		
$wR_2$ / %	4.12	2.53		
Weight	0.013   0.013	0.006   0.006		
	1.21   1.21	0.000   0.000		

substituents on the PNP amine group do have a small influence on the Ru-H bond length. This small influence may not be important in reactions where bifunctional mechanisms are dominant as illustrated in Figure 2.1.

In the refinement protocol of the titled complex an increase in the Ru-H bond on going from 1.558 for the IAM method to 1.614 Å for the HAR method was observed. In contrast, the Ru-P distances remained untouched by switching from IAM- to HAR refinement. When considering the Ru-CO and Ru-N bonds, the Ru-L distances increase with just 0.002 Å and 0.004 Å respectively. The Ru-H bond distance of 1.606 Å as predicted by DFT is similar to the distance observed in the HAR model.

As can be realised from a simple search in the CCSD most of the known ruthenium(II) bromido distances lie in between 2.52 Å to 2.57 Å which makes the Ru-Br bond distance presented here rather long in comparison. It does, however, fall within the expected values as can be concluded by inspection of Table 2.3 that summarises the Br-M-H bond distances from structurally known examples of pincer complexes. One should notice that the long bond length presented by Milstein *et al.* (Table 2.3, Entry 4) is most likely overestimated as the model suffers from severe statistical disorder and co-crystallisation of the analogous chlorido complex. In addition, entry 5 and 6 represents the same 4-coordinate motif in two different conformers (*anti* / *syn*) and solvent of crystallisation (DCM) appear in the model in entry 5. The authors do not provide evidence for whether the coordinative differences are due to solvent of crystallisation or conformation of the molecule. As it was noted for the parent complex (1), *vide supra*, the ligand *trans* to the hydride is not influenced as much by the auxiliary ligand sphere as is the metal hydride distance. Nor does it appear to be much influenced by the type of metal.

Table 2.3: Selected structural parameters (IAM) for all crystallographically characterised transition metal pincer complexes that exhibits *trans*-hydridobromido coordination.

Entry	M	M-H / Å	M-Br / Å	Equatorial L	Pincer Type	Ref
0	Ru	1.558	2.682	CO	PNP	this work
1	Ru	1.585	2.689	CO	CNC	154
2	Ru	1.536	2.624	CO	POP	162
3	Ru	1.643	2.688	CO	NNC	163
4	Ru	1.939	2.669	CO	NNC	163
5	Ir	1.560	2.532	-	PSiP	164
6	Ir	1.565	2.541	-	PSiP	164
7	Ir	1.371	2.616	CO	PSiP	164
8	Fe	1.460	2.516	CO	P(N)N(N)P	165
9	Fe	1.308	2.552	CO	PNP	166
10	Fe	1.455	2.537	CO	PNP	167
11	Fe	1.415	2.547	CO	PNP	168
12	Fe	1.460	2.527	CO	P(NH)N(NH)P	169
13	Fe	1.361	2.516	CO	P(O)N(O)P	170
14	Re	1.476	2.714	NO	PNP	171

## Spectroscopic characterisation of (2)

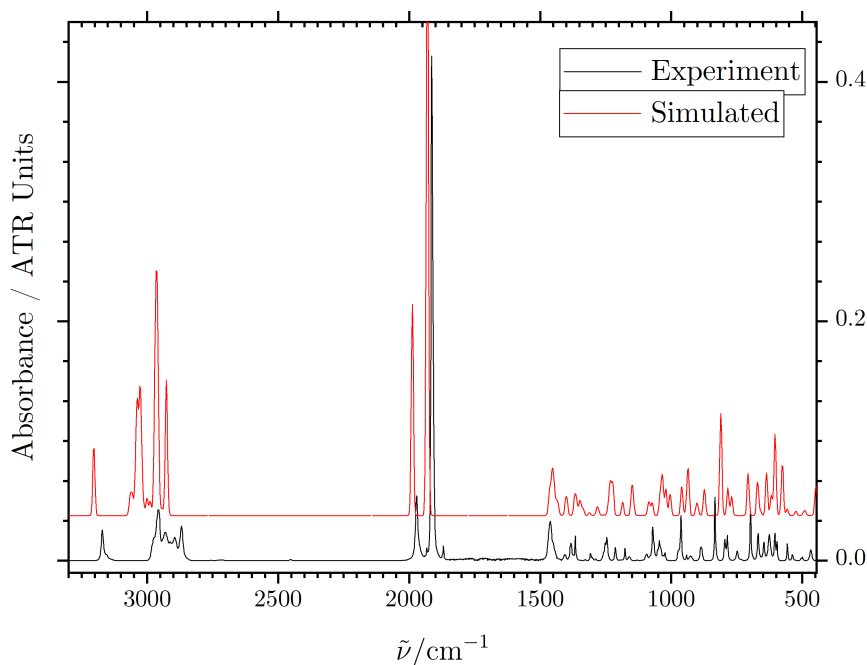


Figure 2.9: Experimental and simulated IR spectra for (2).

The IR spectrum of (2), shown in Figure 2.9 reveals the characteristic strong absorption for the C $\equiv$ O stretch at 1914 cm $^{-1}$  and the Ru-H band with medium intensity at 1971 cm $^{-1}$ . Well-defined resonances for the N-H stretch at 3169 cm $^{-1}$  and the rocking motion

perpendicular to the N-Ru bond vector at  $1463\text{ cm}^{-1}$  are easily resolved. These frequencies are in good agreement the frequencies predicted computationally.

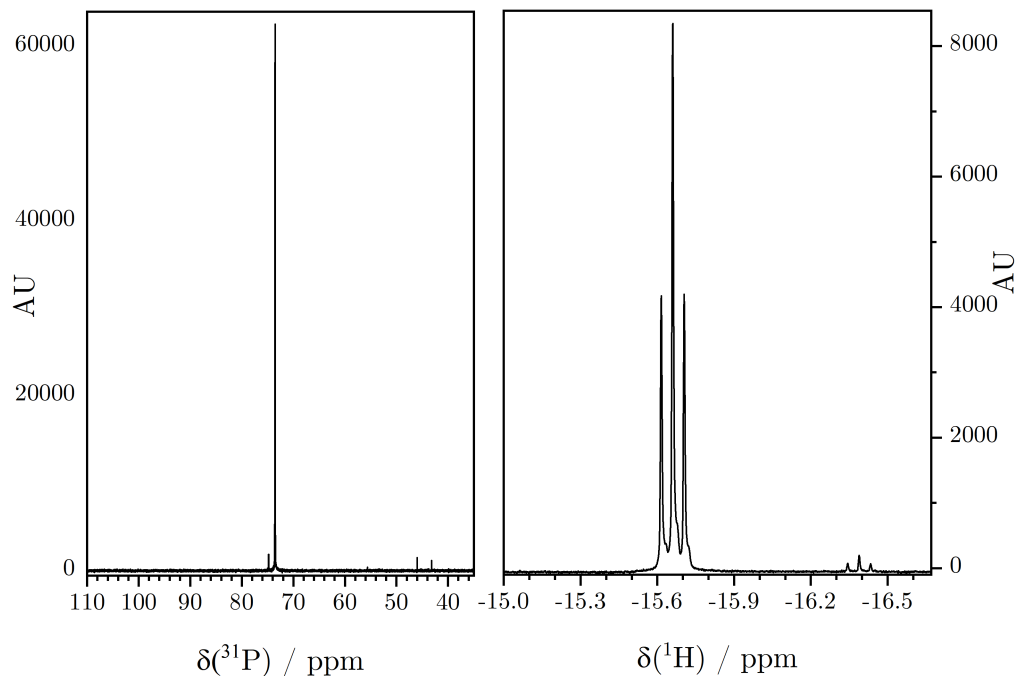


Figure 2.10:  $^1\text{H}$ -decoupled  $^{31}\text{P}$ -NMR spectrum (left).  $^1\text{H}$ -NMR spectrum (right) in the hydride region of complex (2).

As shown in Figure 2.10, the  $^1\text{H}$ -NMR spectrum shows two triplet (coupling to the two P-atoms in the equatorial plane) signals in the hydride region at  $-15.66$  and  $-16.39$  ppm, the former being almost 50 times more intense. The coupling constants for the two signals are identical ( $J = 17.9\text{ Hz}$ ) thus indicating that the second triplet does not arise from a species of different connectivity but is more likely to be an isomer. The  $^{31}\text{P}$ -NMR spectrum shows a sharp, intense signal at  $73.54$  ppm along with a very small shoulder at  $74.79$  ppm.

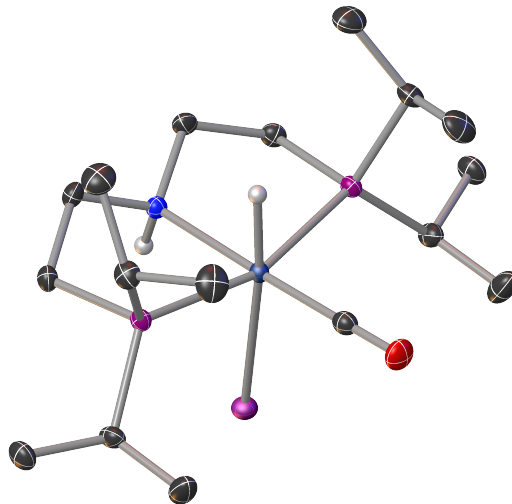
2.2.3 (iPr<sub>2</sub>PNP)RuHI(CO) - (3)

Figure 2.11: Crystal structure of the titled complex after IAM refinement. Hydrogens on all carbon atoms has been omitted for clarity. Plotted at 50% probability level.

Colourless high quality crystals were obtained by leaving a dilute solution of the complex in diethylether at  $-30^{\circ}\text{C}$  for about 2 weeks. Complex (3) crystallised in the monoclinic space group  $P2_1/m$  together with 0.5 molecules of diethylether per asymmetric unit. This complex is isostructural with complex (1a), (2) and (4) (see respective sections) and is also close to isomorphism with the (1a) complex as is the (2) complex, presented in the previous section.

Table 2.4: Difference in geometric- and refinement parameters between the IAM, HAR and DFT models for complex (3). Ruthenium to phosphorous distances have been omitted as these are invariant.

Ligand (L)	Ru-L / Å IAM	Ru-L / Å HAR	$\Delta(\text{Ru-L})$ / Å HAR-IAM	Ru-L / Å DFT
H	1.495	1.561	0.063	1.608
I	2.835	2.853	0.018	2.873
CO	1.835	1.838	0.003	1.828
HN(PNP)	2.199	2.202	0.003	2.231
Refinement Parameter	IAM	HAR		
$R_1$ / %	2.29	1.98		
$wR_2$ / %	4.48			
Weight	0.000   0.000	0.003   0.003		
	2.24   2.24	1.32   1.32		

Inspection of Table 2.4 above reveal a Ru-H bonding distance of 1.495 Å is observed

along with a Ru-I distance of 2.835 Å when using IAM refinement whereas in the HAR refinement, the Ru-H bond is elongated to 1.561 Å. All bond lengths falls well within expected range for a transition metal *trans*-hydridoiodido complex, as can be realised by inspection of published structures deposited in the CCSD (Table 2.5). The PNP ligand is *mer* coordinated and do, together with the carbonyl ligand, constitute the equatorial plane with the hydrido- and iodido ligands in the axial positions and altogether resembles a slightly distorted octahedral geometry. The amine proton is oriented *syn* to the iodido ligand. This arrangement results from the formation of a weak intramolecular H···I hydrogen bond with the H···I distance of 2.836 Å (HAR) which is significantly shorter than the sum of the Van der Waals radii of 3.08 Å.<sup>160</sup> The Ru-P distances remained untouched by going from IAM- to HAR refinement whereas the Ru-N and Ru-CO distances both deviated with only 0.003 Å.

Hydridoiodidoruthenium complexes are exceedingly rare. In fact, only one example of a truly *trans*-hydridoiodidoruthenium compound was structurally characterised by Milstein in 2009.<sup>172</sup> This phosphinite PNP complex was made by hydride abstraction with iodomethane from the corresponding dihydrido complex and thereby underpins its high hydricity.

Table 2.5: Selected bond lengths (IAM) for structurally characterised pincer ligand supported *trans*-iodidohydrido transition metal complexes.

Metal	M-H / Å	M-I / Å	Pincer Type	Ref
Ir	1.316	2.729	PSiP	<sup>164</sup>
Ru	1.526	2.873	P(O)N(O)P	<sup>172</sup>
Ru	1.495	2.835	PNP	this work
Mo	1.680	2.803	PPP	<sup>173</sup>
Rh	1.563	2.818	PNP	<sup>174</sup>
Ir	1.653	2.818	PNP	<sup>174</sup>
Ir	1.439	2.786	PNP	<sup>174</sup>
Ir	1.621	2.799	CCC	<sup>175</sup>

## Spectroscopic characterisation of (3)

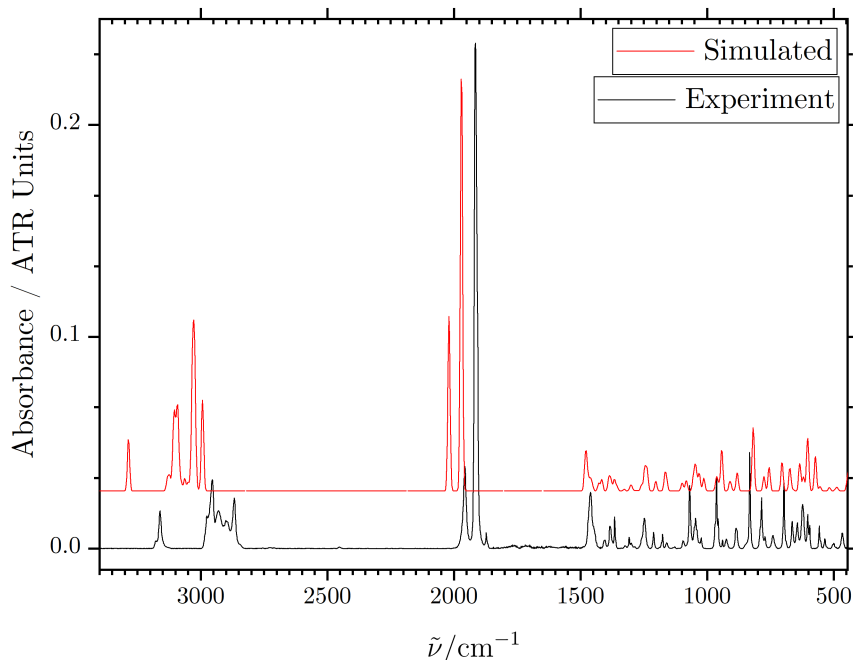


Figure 2.12: Experimental and simulated IR spectra for (3).

Figure 2.12 reveals the strong characteristic CO stretching frequency at  $1915\text{ cm}^{-1}$  and the Ru-H stretch at  $1956\text{ cm}^{-1}$  as a sharp absorbance of medium to strong intensity. The N-H stretch and rocking (perpendicular to the N-Ru bond vector) are well defined as sharp resonances at medium intensity at  $3160\text{ cm}^{-1}$  and  $1461\text{ cm}^{-1}$  respectively. The computational results are generally in good agreement with the experimental values in the fingerprint region. The resonances corresponding to Ru-H,  $\text{C}\equiv\text{O}$ , C-H and N-H stretching frequencies are experimentally observed at lower frequencies than predicted by DFT. However, the numerical differences between theory and experiment are in general acceptably small.

The  $^{31}\text{P}$ -NMR spectrum in Figure 2.13 (left) shows the chemical shift for the clean product at  $72.02\text{ ppm}$ . The left spectrum in Figure 2.13 above shows the expected triplet from coupling of one hydride ligand to two phosphorus nuclei at  $-14.03\text{ ppm}$  with a coupling constant  $J = 18.0$ . The absence of an additional triplet in the spectrum indicates that the present compound is rigid with respect to *syn-anti*-isomerism in the solution state at room temperature.

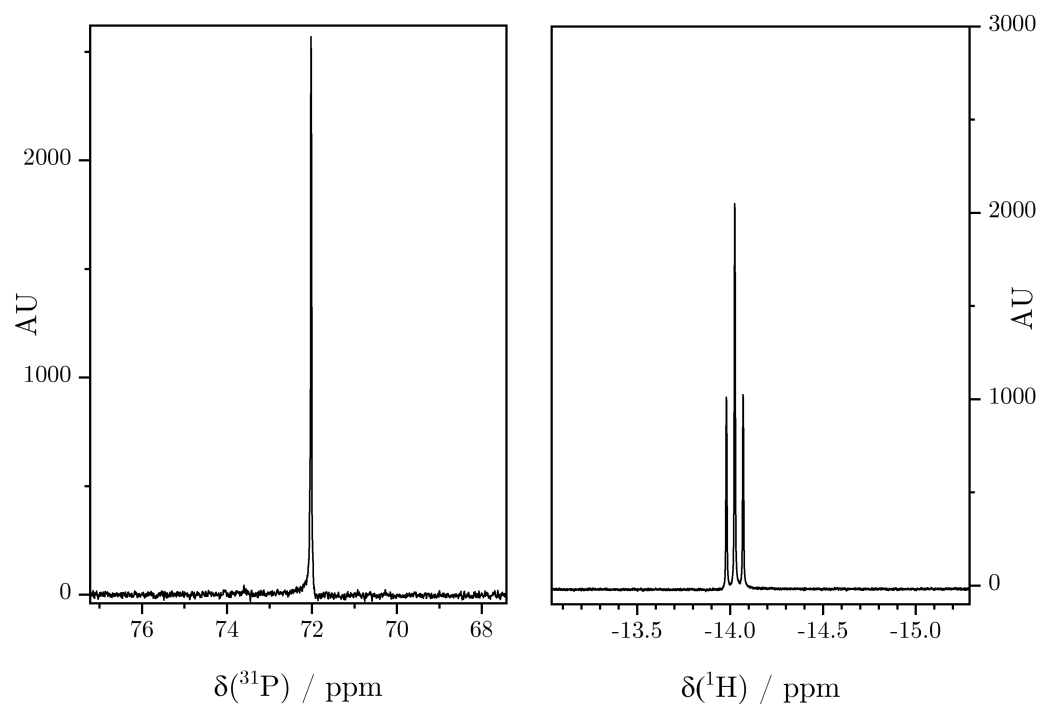


Figure 2.13:  $^1\text{H}$ -decoupled  $^{31}\text{P}$ -NMR spectrum (left).  $^1\text{H}$ -NMR spectrum (right) in the hydride region of complex (3).

#### 2.2.4 (iPr<sub>2</sub>PNP)RuH(CN)(CO) - (4)

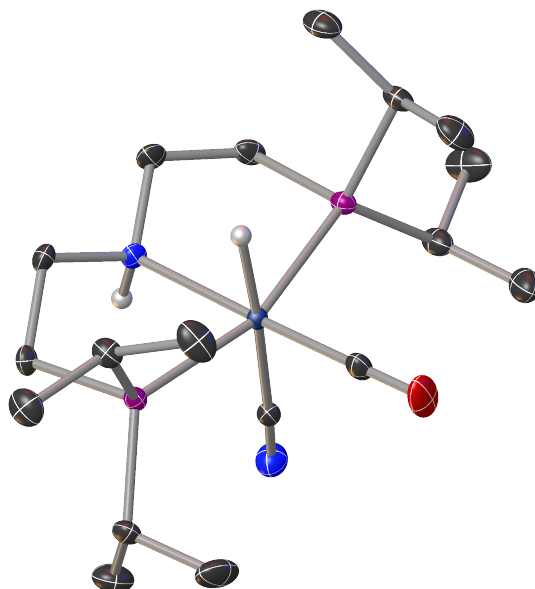


Figure 2.14: Crystal structure of the titled complex after IAM refinement. Hydrogens on all carbon atoms has been omitted for clarity. Plotted at 50% probability level.

High quality crystals were obtained by re-crystallisation from hot acetonitrile by slow cooling to 4°C. This complex is robust towards ambient atmosphere and, as such, no particular precautions need to be taken into account and the compound can safely be handled in air.



Table 2.6: Difference in geometric- and refinement parameters between the IAM, HAR and DFT models for complex (4). Ruthenium to phosphorous distances have been omitted as these appear, for all practical purposes, invariant.

Ligand (L)	Ru-L / Å IAM	Ru-L / Å HAR	$\Delta$ (Ru-L) / Å HAR-IAM	Ru-L / Å DFT
H	1.557	1.629	0.072	1.667
CN	2.092	2.087	-0.005	2.069
CO	1.834	1.836	0.002	1.831
HN(PNP)	2.186	2.190	0.004	2.234
Refinement Parameter	IAM	HAR		
$R_1$ / %	2.97	2.58		
$wR_2$ / %	6.18	4.05		
Weight	0.016   0.016	0.000   0.000		
	1.56   1.56	0.482   0.482		

Compound (4) crystallises in the space group  $P2_1/n$ . By disregarding the orientation of the isopropyl substituents the molecular symmetry can be idealised to  $C_s$ . The ruthenium hydrogen bond distance in the IAM- and the HAR model is 1.557 Å and 1.629 Å respectively. As such, the HAR model is in better agreement with the structure depicted by DFT where the Ru-H distance is calculated to 1.668 Å. Thus a difference 0.072 Å in bond length between the IAM and HAR model is observed. This rather big difference in bond distance should not be neglected when evaluating catalytic reactions where the lability and bond strength of the metal-hydride bond plays a key role. Inspection of Table 2.6 reveals that the most affected metal-ligand bond is the hydrido bond that in the IAM refinement seem significantly underestimated.

Table 2.7: Selected bond lengths (IAM) for structurally characterised cyanidohydrido transition metal complexes found in the CCSD.

Metal	M-H / Å	M-CN / Å	Configuration	Ref
Ru	1.557	2.092	<i>trans</i>	this work
Ru	1.555	2.088	<i>cis</i>	176
Fe	1.646	1.903	<i>trans</i>	177
Pt	1.592	1.999	<i>cis</i>	178
		2.053	<i>trans</i>	
Pd	1.608	2.000	<i>cis</i>	179
		1.996	<i>cis</i>	
Ir	1.508	2.081	<i>trans</i>	180

The number of structurally known terminal cyanidohydrido transition metal complexes known to literature is limited to only 5 examples in the CCSD, hence compound (4) adds to a very rare class of compounds which structural relations are summarised in Table 2.7

below. The scarcity of this class of compounds makes it difficult to do any meaningful structural comparison. However, it is interesting to note that the Ru-H bond distance (IAM) in complex (4) is very similar to the corresponding bond in the Ru-complex presented by Sabo-Etienne<sup>176</sup> in which the *trans*-ligand is a diisopropylamino-isocyanoborane ligand.

### Spectroscopic characterisation of (4)

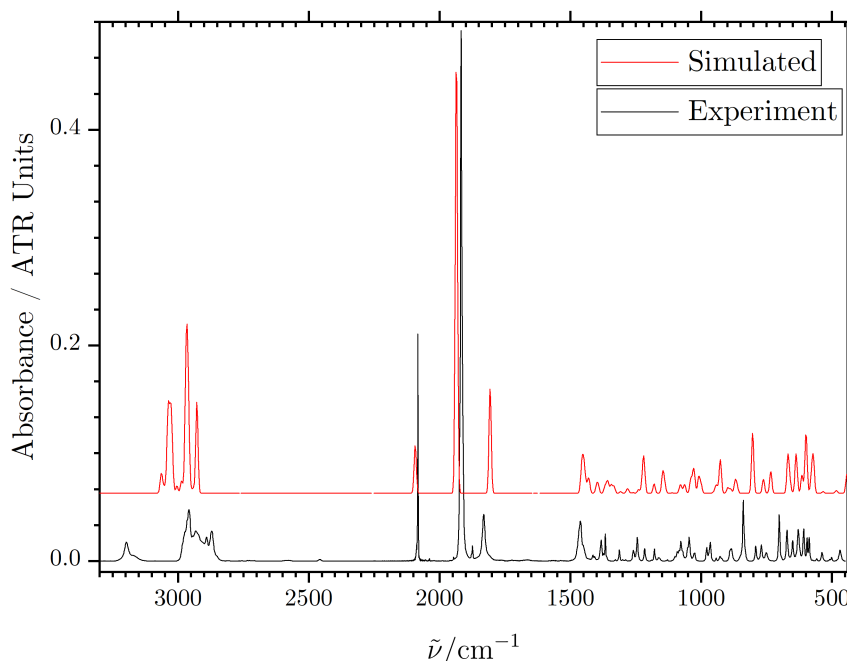


Figure 2.15: Experimental and simulated IR spectra for (4).

The IR spectrum of (4) shown in Figure 2.15 shows a number of interesting bands. The strong, sharp absorbance at  $1918\text{ cm}^{-1}$  is attributed to the  $\nu(\text{C}\equiv\text{O})$  stretching mode. The amine  $\nu(\text{N-H})$  stretch and rocking modes are well defined resonances located at  $3197$  and  $1461\text{ cm}^{-1}$  respectively. Interestingly, the sharp medium-strong absorption band from the  $\nu(\text{Ru-H})$  stretching mode is located at  $1832\text{ cm}^{-1}$  which is significantly lower than for the remaining complexes in this work and is in agreement with a long Ru-H bond, as is indicated in the HAR model. The  $\text{C}\equiv\text{N}$  stretching frequency appears as a strong, sharp band at  $2083\text{ cm}^{-1}$  which is, as expected, lower than the  $\nu(\text{CN})$  mode in KCN ( $2158\text{ cm}^{-1}$ )<sup>181</sup> and within the expected range for ruthenium(II)-cyanido complexes<sup>182–185</sup>.

The  $^{31}\text{P}$ -NMR spectrum depicted in Figure 2.16 (left) shows a sharp singlet at  $78.41$  ppm. The  $^1\text{H}$ -NMR spectrum shows the expected triplet signal (H-P coupling) at  $-9.60$  ppm with a coupling constant  $J = 18.4\text{ Hz}$ . The absence of any other triplet signals in the hydride region of the spectrum indicates, that the complex is very rigid in solution, thus, no *syn-anti*-isomerism is observed.

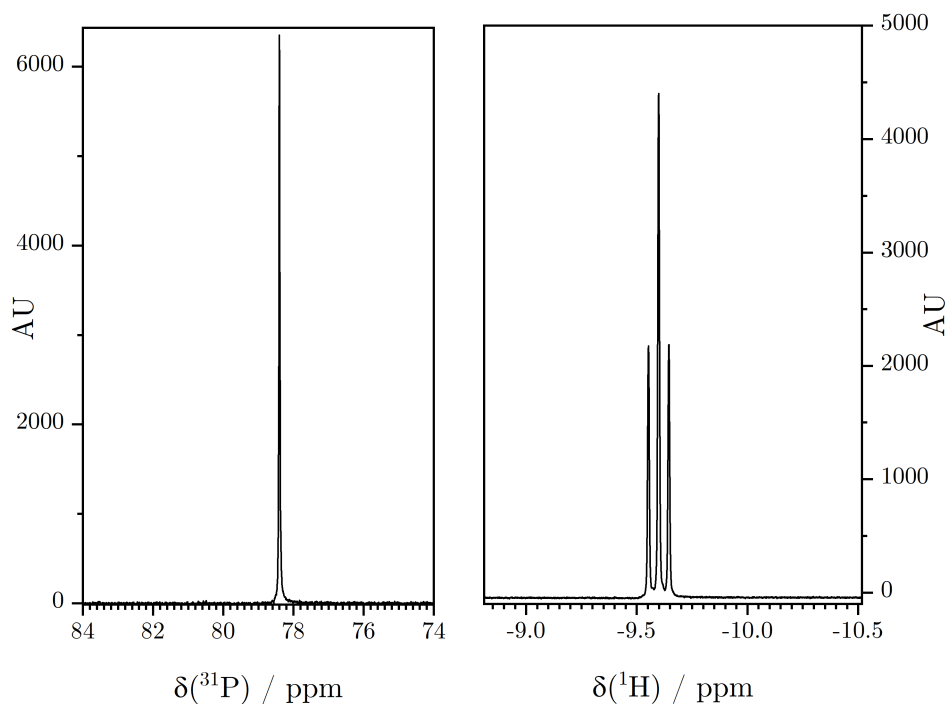


Figure 2.16:  $^1\text{H}$ -decoupled  $^{31}\text{P}$ -NMR spectrum (left).  $^1\text{H}$ -NMR spectrum (right) in the hydride region of complex (4).

### 2.2.5 (iPr<sub>2</sub>PNP)RuH(N<sub>3</sub>)(CO) - (5)

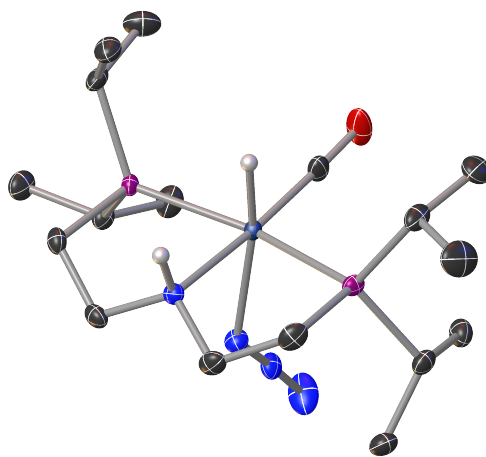


Figure 2.17: Crystal structure of the titled complex after IAM refinement. Hydrogens on all carbon atoms has been omitted for clarity. Plotted at 50% probability level.

Yellow crystals suitable for single-crystal X-ray diffraction were obtained by leaving a concentrated solution of the titled compound in acetonitrile at  $-30\text{ }^{\circ}\text{C}$  for 5 days inside an argon filled glove box. The moderately air sensitive complex must be stored and handled under inert atmosphere. The compound (5) crystallises in the triclinic space group  $P\bar{1}$  and belongs to the symmetry point group  $C_1$  but can be idealised to the  $C_s$  point group by

disregard of the orientation of the isopropyl substituents on the phosphorous atoms.

Table 2.8: Difference in geometric- and refinement parameters between the IAM, HAR and DFT models for complex (5). Ruthenium to phosphorous distances have been omitted as these appear, for all practical purposes, invariant.

Ligand (L)	Ru-L / Å IAM	Ru-L / Å HAR	$\Delta$ (Ru-L) / Å HAR-IAM	Ru-L / Å DFT
H	1.491	1.548	0.057	1.620
N <sub>3</sub>	2.223	2.224	0.001	2.226
CO	1.834	1.834	0.000	1.823
HN(PNP)	2.189	2.191	0.002	2.238
Refinement Parameter	IAM	HAR		
$R_1$ / %	4.18	3.98		
$wR_2$ / %	7.87	5.98		
Weight	0.016   0.016	0.000   0.000		
	0.000   0.000	0.058   0.058		

The PNP ligand is coordinated in a *mer* manner which together with the carbonyl ligand spans the equatorial plane with the azido- and hydrido ligands in the axial positions. In contrast to the structures (1)-(4) and (6), *vide infra*, the amine proton is oriented *syn* to the hydrido ligand. As such, no N-H...N<sub>3</sub> intramolecular hydrogen bond is observed in the titled structure model. In addition, a strong inter molecular hydrogen bond (2.064 Å, HAR / 2.121 Å, IAM) between the amine proton and the azido ligand from a nearby molecule is observed.

When using the IAM refinement Ru-H and Ru-N<sub>3</sub> distances of 1.491 Å and 2.223 Å are observed respectively. By using HAR refinement the Ru-N<sub>3</sub> distance is almost invariant in comparison. However, the Ru-H is significantly increased to 1.548 Å in using the HAR method. As such, the HAR model is in better agreement with the Ru-H distance of 1.620 Å predicted by DFT.

On the same note as for (4), transition metal ions hydride and azide coordination are scarce. Table 2.9 below shows the geometrical parameter for the titled compound as well as for the compounds known to literature.

Interestingly, the structure provided by Małecki and Maroń shows two independent molecules in the asymmetric unit where the components show very different Ru-H bond distances.<sup>187</sup> In both components the azido- and hydrido ligands are coordinated in a *cis* fashion. The authors note the limitations of the Fourier synthesis regarding problems with artifacts close to heavy atoms.

### Spectroscopic characterisation of (5)

The IR spectrum shown in Figure 2.18 exhibits a number of features. Most strikingly, the simulated spectrum show that the  $\nu(\text{CO})$  and  $\nu(\text{RuH})$  stretching modes are very close in

Table 2.9: Geometry around the central metal ion in transition metal hydrido azido complexes found in literature. Colour code for models containing two independent molecules: **component 1**, **component 2**.

Metal	M-H / Å	M-N <sub>3</sub> / Å	<i>trans</i> -L	Ref
Ru	1.491	2.223	N <sub>3</sub>	this work
Ru	1.587	2.108	MeCN	186
Ru	$\left\{ \begin{array}{l} \textcolor{red}{1.577} \\ \textcolor{blue}{1.504} \end{array} \right\}$	$\left\{ \begin{array}{l} \textcolor{red}{2.219} \\ \textcolor{blue}{2.222} \end{array} \right\}$	N <sub>3</sub>	187
Ru	$\left\{ \begin{array}{l} \textcolor{red}{1.627} \\ \textcolor{blue}{1.477} \end{array} \right\}$	$\left\{ \begin{array}{l} \textcolor{red}{2.079} \\ \textcolor{blue}{2.124} \end{array} \right\}$	PPh <sub>3</sub>	188
Ir	1.605	2.085	PPh <sub>3</sub>	189

energy. The shoulder resonance at 1933 cm<sup>-1</sup> is assigned to the  $\nu(\text{RuH})$  stretching and, as such, the strong absorbance at 1906 cm<sup>-1</sup> is assigned to the  $\nu(\text{CO})$  stretching mode based on the fact that clearly these modes are normally the most intense absorbances in this class of compounds. The two strong bands at 2057 cm<sup>-1</sup> and 2027 cm<sup>-1</sup> are both below the stretching frequency for the azide ion in sodium azide ( $\nu(\text{N}_3^-) = 2140 \text{ cm}^{-1}$ )<sup>190</sup> but is significantly closer to the corresponding stretch of 2042 cm<sup>-1</sup> in TBA azide.<sup>191</sup> Both the respective bands fall within the expected range for terminal azido complexes of ruthenium(II).<sup>192–195</sup> It is thus tempting to assign the smaller (however strong) band at 2057 cm<sup>-1</sup> to another unspecified azido species. Based on the coherently visual expression of the IR spectrum above, this second species is likely to be a decomposition product due to reaction with atmosphere.<sup>†</sup> The broad doublet band in the NH region having the extrema  $\tilde{\nu} = 3186$  and 3146 cm<sup>-1</sup> is indicative of two different amino isomers. The relatively low resonance energy is indicative of hydrogen bonding.

<sup>†</sup>At present time, the local infrastructure at DTU Chemistry do not allow for strict inert montage of the sample for measurement.

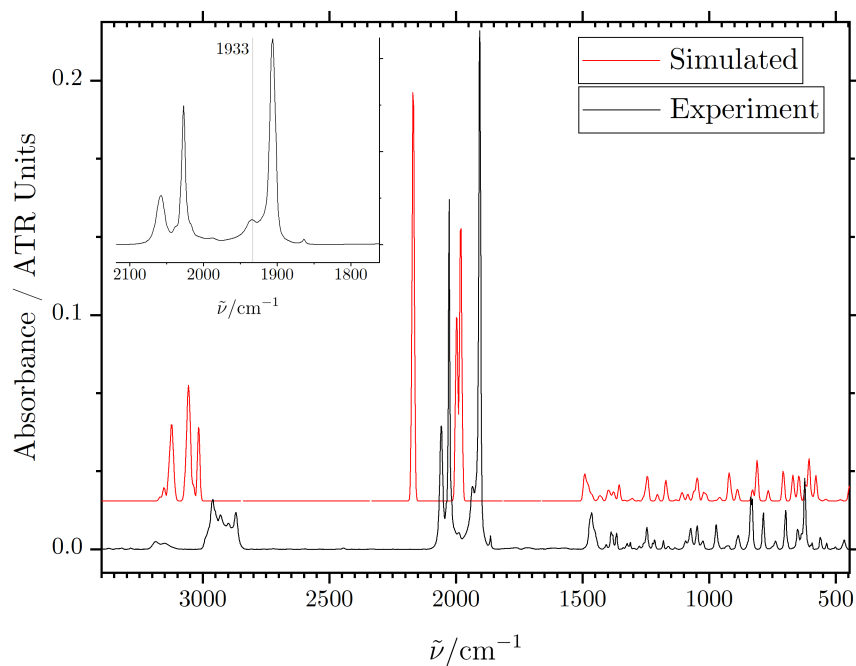
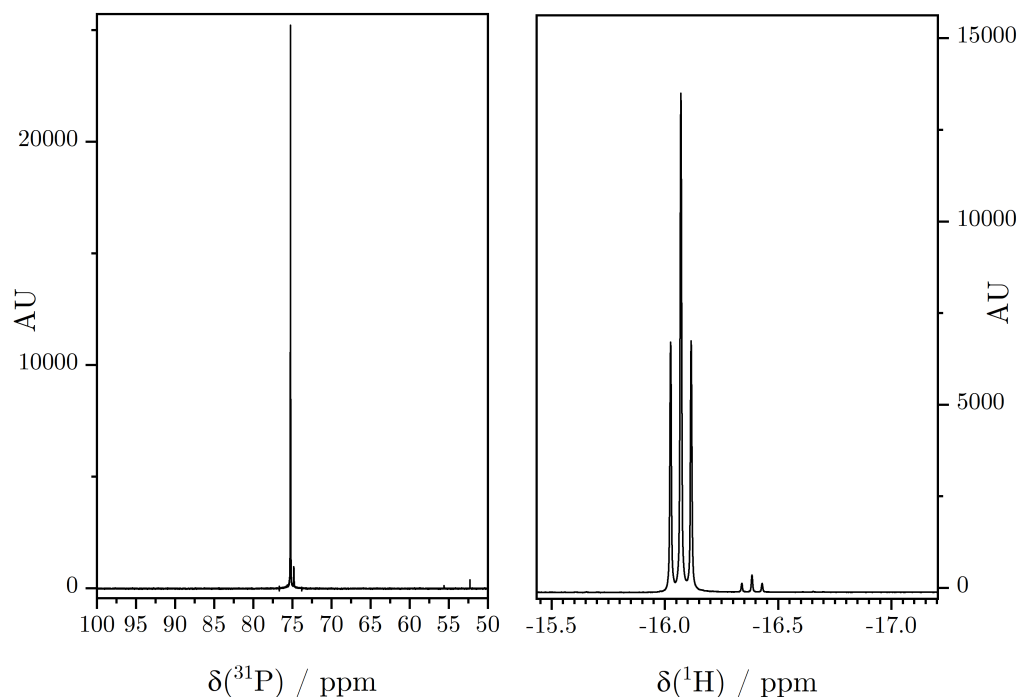


Figure 2.18: Infrared spectrum of compound (5).

Figure 2.19:  $^1\text{H}$ -decoupled  $^{31}\text{P}$ -NMR spectrum (left).  $^1\text{H}$ -NMR spectrum (right) in the hydride region of complex (5).

The  $^{31}\text{P}$ -NMR spectrum (Figure 2.19) shows a sharp singlet at 75.23 ppm. The singlet nature of the signal is expected from two magnetically equivalent phosphorus atoms. The  $^1\text{H}$ -NMR spectrum shows two characteristic triplets at  $-16.07$  and  $-16.38$  ppm

respectively. The two triplets arise from two different hydride ligands coupling to two equivalent phosphorus atoms and are ascribed to *syn-anti*-isomerism. The two triplets show slightly different coupling constants,  $J_{(-16.07)} = 18.1$  Hz and  $J_{(-16.38)} = 17.9$  Hz which express a slightly stronger coupling from one isomer hydride over the other.

### 2.2.6 (iPr<sub>2</sub>PNP)RuH(NCS/SCN)(CO) - (6)

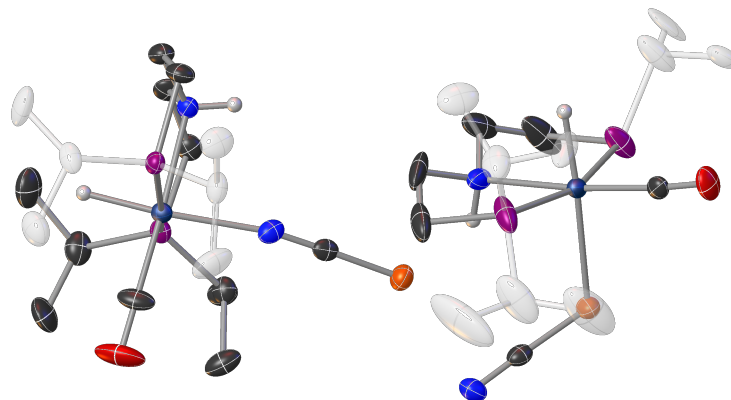


Figure 2.20: Crystal structure of the titled complex after IAM refinement. Hydrogens on all carbon atoms has been omitted and isopropyl substituents on P has been ghosted out for clarity. Plotted at 50% probability level.

As mentioned earlier, the reaction between the commercial complex (1a) and AgSCN or the reaction of (1) with [TBA]SCN yields a mixture of the corresponding isothiocyanato and thiocyanato complex. The two linkage isomers crystallise together in the triclinic space group  $P\bar{1}$ . Unfortunately, the data set obtained in this work is rather weak. That is, high resolution of 0.84 Å (in d-spacing), low signal-to-noise ratio ( $I/\sigma(I) = 10.0$ ) and a low redundancy indicated by  $R_{int} = 11.61\%$  indicates a poor crystal quality. Unfortunately, the crystallisation of the titled compound is difficult and time consuming. Crystals were obtained from a dilute acetonitrile solution by 1) standing at  $-30^\circ\text{C}$  for 30 days whereby a white fibrous product precipitated. 2) Transfer the cold suspension to a refrigerator and letting the sample stand at  $4^\circ\text{C}$  for an additional 30 days before the sample was 3) transferred back to the freezer and left for 30 days at  $-30^\circ\text{C}$  whereby few crystals formed among the fibrous material.

The isopropyl substituents (*cis* with respect to the hydride) on phosphorus of the thiocyanato complex show significant disorder over two positions. The two components in the disorder are related by rotation around the C-P bond axis. To obtain a better model, this disorder was modeled by splitting along the axis of the biggest atomic displacement parameters (ADPs) of each atom of the aforementioned groups followed by the proper rotation. The SADI restrain was applied on each group of atoms to assure equal C-P bond lengths within each group. For atoms sharing the same crystallographic sites the EADP constrain was applied to force equal ADPs. The inter molecular distance  $\text{HN}\cdots\text{S}$  (amine-*N*

to isothiocyanate-*S*) of 3.362 Å indicate only weak H-S interaction.

### Spectroscopic characterisation of (6)

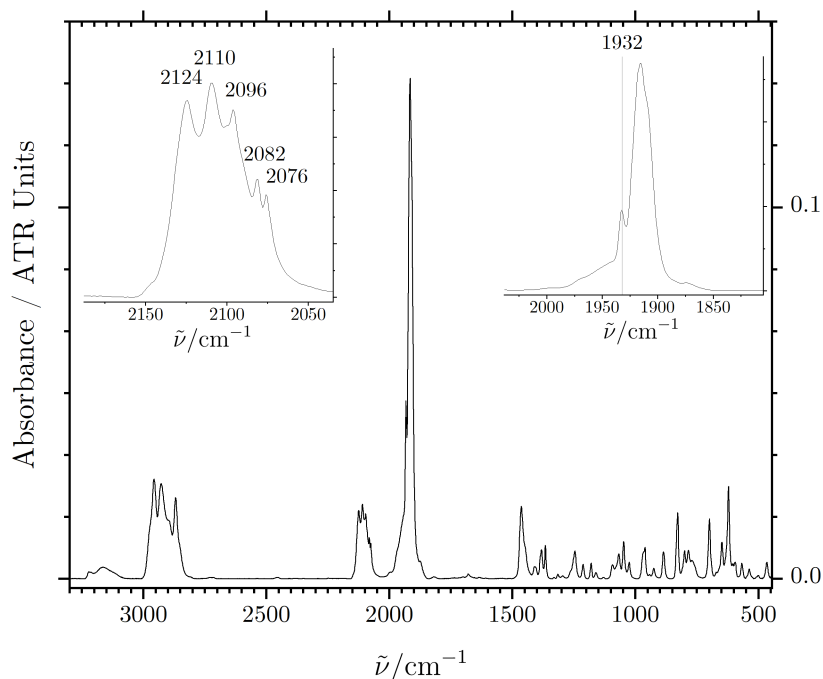


Figure 2.21: Infrared spectrum of compound mixture (6).

As can be seen from Figure 2.21, the product mixture obtained from the reaction between the commercial complex (1a) with AgSCN gives rise to a rather complex IR spectrum. The unsymmetrical nature of the  $\nu(\text{CO})$  stretching mode at  $1916\text{ cm}^{-1}$  is indicative of the presence of two chemically different CO ligands having  $\tilde{\nu}$  close, but not equal in energy. The  $\nu(\text{RuH})$  mode is observed as a sharp shoulder at  $1932\text{ cm}^{-1}$  (right insert) as expected *a priori*. In the region  $\tilde{\nu} = 2150 - 2050\text{ cm}^{-1}$  a broad feature composed of at least five absorptions is observed (left insert). This feature is most likely composed by the vibrational modes of the *S*- and *N*-bound SCN-ligand which are difficult to distinguish as the  $\nu(\text{CN})$  mode are very close in energy.<sup>186</sup> However, the *N*-bound isomer does in general have lower lying  $\nu(\text{CN})$  modes than the *S*-bound isomer.<sup>196</sup> As such, the two close absorptions at  $2082\text{ cm}^{-1}$  and  $2076\text{ cm}^{-1}$  may be ascribed to the *N*-bound isomer. This interpretation also seems in agreement with previously reported isothiocyanato complexes of ruthenium(II).<sup>197</sup> It would, however, be ambitious to assign all resonances to different linkage isomers without isotope labelling which is beyond the scope of this thesis.



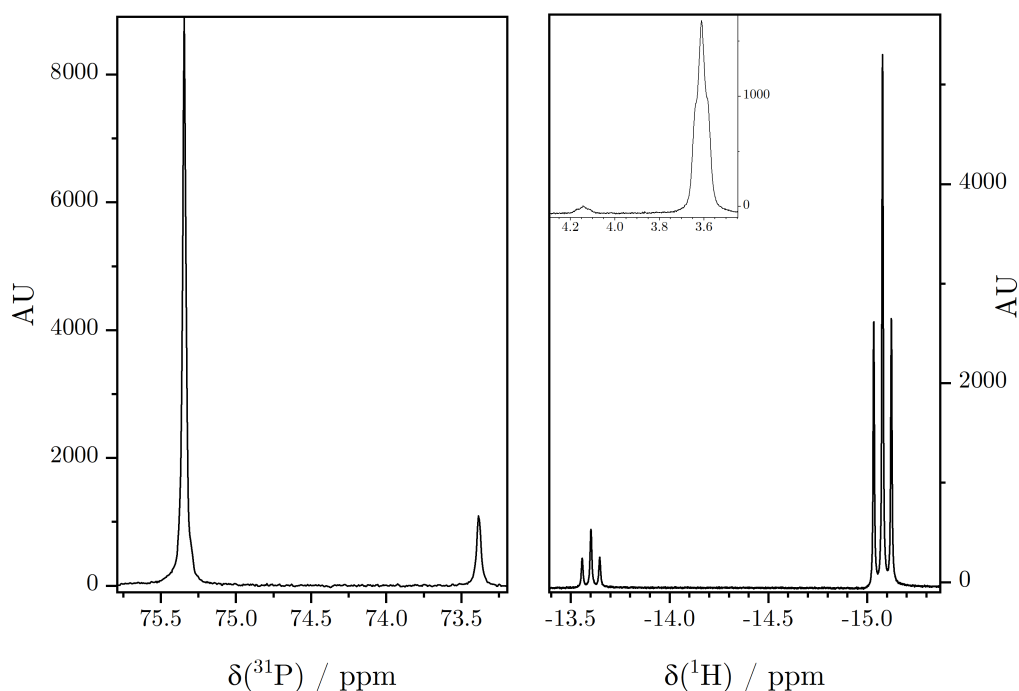


Figure 2.22:  $^1\text{H}$ -decoupled  $^{31}\text{P}$ -NMR spectrum (left).  $^1\text{H}$ -NMR spectrum (right) in the hydride region of complex mixture (6).

The two hydride signals in the  $^1\text{H}$ -NMR spectrum (Figure 2.22, right) appear at  $-13.60$  and  $-15.08$  ppm with  $J = 17.8$  and  $17.9$  Hz respectively. The insert reveals two different amine protons appearing at  $4.14$  ppm and  $3.61$  ppm as broad, overlapping triplets from coupling with the two magnetically equivalent, but diastereotopic,  $\alpha$ -methylene groups. The integral ratio in the  $^{31}\text{P}$ -NMR spectrum (Figure 2.22, left) of  $1 : 0.18$  is in magnitude comparable to the ratio obtained from the hydride peaks of  $1 : 0.16$ .<sup>†</sup>

## 2.3 Discussion and conclusions

As the *trans*-influence is an observed phenomenon mostly related to the ligand field  $\sigma$ -parameter of the ligand, it is interesting to compare the results outlined in the present chapter with the two extremes of *trans*-influence experienced by the hydrido ligand. That is, the ultimate weakening of the *trans*-influence experienced by the hydrido ligand in the present class of compound, can be regarded as the example where no *trans*-ligand is at place. On the other hand, one of the strongest *trans*-influencing ligands are the very strongly donating  $\sigma$ -only donors  $\text{H}^-$  and  $\text{H}_3\text{C}^-$  (methyl) ligands. As there is no data available for a methyl complex that would fall natural into this discussion, only the *trans*-dihydrido complex shown in Figure 2.23 will be of concern. This complex shows excellent catalytic activity in the dehydrogenation of aqueous isopropanol<sup>198</sup> highlighting

<sup>†</sup>Due to the Nuclear Overhauser Effect, NOE, the absolute values of the integrals in decoupled phosphorus- and proton NMR are not comparable. However, they should be in the same order of magnitude.

the possibly importance of the *trans*-influence. The data presented in this chapter is summarised in Table 2.10 together with relevant literature data and graphically in Figure 2.25. The mixture of linkage isomers, (6), has been left out from the discussion as it has not been possible to characterise the clean isomers. Unfortunately, no data on the vibrational structure of the five coordinate amidohydrido complex (that is  $X^- = \text{none}$ ) is reported in literature.

It is clear from the spectroscopic and crystallographic data that the *trans*-influence experienced by a hydrido ligand is a challenging task to unravel due to the difficulty in obtaining accurate data on bond distances. As such, conclusions about the *trans*-influence drawn on crystallographic models alone is a dangerous endeavor. IR- and NMR spectroscopy serve as excellent indicators for relative Ru-H bond lengths within a series of related complexes. Unfortunately, there is no obvious correlation between the crystallographically determined Ru-H bond lengths

and the spectroscopic data for the compounds in this work. However, some general observation can be made. It is noteworthy that the strongest down-field shift of the hydrido ligand is observed for  $X^- = \text{H}^-$ ,  $\text{CN}^-$ . In both cases the chemical shift is found above  $-10$  ppm. This indicates that cyanide is an appreciable  $\sigma$ -donor ligand compared to the other ligands presented here. This observation is also reflected in the surprisingly low energy of the  $\nu(\text{RuH})$  mode for the *trans*-cyanido complex which is even lower than the corresponding stretching mode for the *trans*-dihydrido species. This is strikingly surprising as this bathochromic shift indicates a weaker Ru-H bond strength for the cyanido complex than for the dihydrido complex, and as such, can be interpreted as the cyanido ligand have a significantly stronger *trans*-influence than the hydrido ligand. On the other hand, the  $\delta(\text{RuH})$  for the dihydrido complex is observed at lower field than the corresponding absorption for the cyanido complex indicative of a longer and thereby weaker Ru-H bond for the dihydrido complex than for the cyanido species. It is worth noticing, that the indicated high *trans*-influence for the cyanido ligand is perfectly in line with previous reports on octahedral Ru(II) and Os(II) complexes.<sup>199</sup>

Strikingly, the values of the  $\tilde{\nu}(\text{RuH})$  do not correlate with the bond distances obtained from the crystallographic experiments, regardless of the refinement method used. The azido complex exhibits a  $\nu(\text{RuH})$  mode at resonance frequency  $\tilde{\nu} = 1933 \text{ cm}^{-1}$  together with a bond length of  $1.548 \text{ \AA}$  (HAR) which is in contrast to the iodido complex which shows a higher energy Ru-H vibrational resonance but a slightly longer bond length (regardless of the crystallographic refinement method). In that regard, the longer R-H bond length is in line with the more positive chemical shift. On that note, the bromido complex exhibits a longer Ru-H bond length than the iodido complex, but a more negative chemical shift and a higher energy  $\nu(\text{RuH})$  mode. The longer bond length should give rise to a more negative chemical shift, which is also observed. However, the observation that the  $\nu(\text{RuH})$  vibration

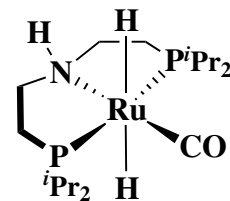


Figure 2.23: Dihydrido-carbonylruthenium(II).

mode appears at higher energy for the bromido species than for the iodido species suggests a longer bond length for the former, and, as such, is in contrast to the crystallographic model as well as the NMR data.

Reviewing the  $\delta(^{31}\text{P})$  it appears that this is the most coherent probe for the indirect analyses of the *trans*-influence in the molecules presented here. As  $\delta(^{31}\text{P})$  is sensitive to the electron density at the ruthenium center without being particularly sensitive to relativistic effects as is the hydrogen atom, the  $\delta(^{31}\text{P})$  may prove more reliable in comparison in structurally similar complexes. Following  $\delta(^{31}\text{P})$ , it appears that the pseudohalogens are more donating than the halogens. However, one should be careful with interpreting on  $\delta(^{31}\text{P})$  without separation of the ligand field  $e_\sigma$  and  $e_\pi$  parameters as the more low-field chemical shift is likely to arise from the  $\pi$ -donation of the halido ligand as shown in Figure 2.24 below.

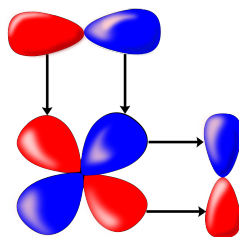
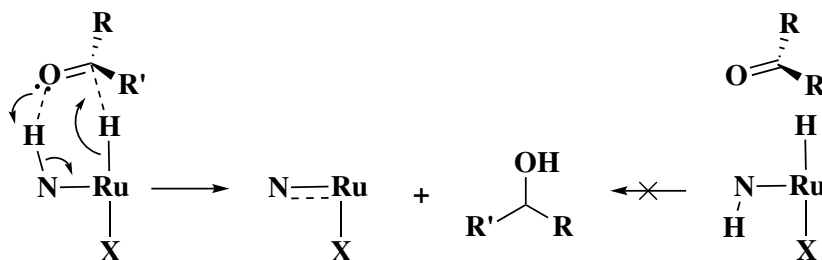


Figure 2.24:  $\pi$ -donation from an axial donor ligand, such as, halide, and  $\pi$ -acceptance from a equatorial ligand such as phosphine or carbonyl.

This picture seem to be supported by the observation that the  $\tilde{\nu}(\text{CO})$  energy follows the same general trend as  $\delta(^{31}\text{P})$ . In this view, it is clear that very strong *trans*  $\sigma$ -donors have a similar effect on both  $\delta(^{31}\text{P})$  and  $\tilde{\nu}(\text{CO})$ . As such, it is tempting to conclude that the cyanido ligand would be the most promising candidate for catalyst screening. On the other hand, as was shown by Guan *et al.* the *syn*-isomer is of crucial importance in Noyori type<sup>200,201</sup> catalysis as this is required according the established mechanism<sup>161,166,202–204</sup> schematised in Scheme 2.2. When the N-H proton is positioned *syn* to the hydride stabilising  $\text{O} \cdots \text{H}-\text{N}$  interaction occur and keeps the substrate in place. This interaction is not available in the *anti* conformation.



Scheme 2.2: Hydrogenation step in Noyori type hydrogenation of carbonyl derivatives showing the importance of *syn*-isomerism (left) for the reaction to proceed.

However, the isomerisation has been shown in some instances to be thermally accessible.<sup>205</sup> Unfortunately, the fact that the cyanido ligand is usually not considered labile might hamper the reaction. On the other hand, the robustness of the cyanido ligand may allow for the addition of strong base without the complex undergoing elimination of cyanide through a dissociative conjugate base mechanism. Alternatively, weak base would most likely be able to course some degree of isomerisation. Due to the strongly nucleophilic behavior of the cyanide ion and the general robustness of cyanide-metal bonds it may be possible to generate a *trans*-cyanido-hydrido complex analogous to the complexes presented in this chapter but deviating in the PNP backbone linkers such that the amine proton is tuned more labile (acidic). By changing the backbone from diethylene to phenylene-ethylene or diethylene, the acidity of the amine proton is expected to increase as stabilisation of the amido lone-pair can be obtained through aromatic conjugation. PNP complexes of the diphenylene type are known to be rather acidic at the amino moiety as is conveniently illustrated by the fact, that the majority of these complexes are isolated as both six-,<sup>206–208</sup> five-<sup>209–211</sup> and four-<sup>212–214</sup>coordinated amido-species. Only the azido complex exhibits the preferred *syn*-isomerism in the solid state and, as such, would be an interesting catalyst in hydrogenation reactions. In addition, the low  $\tilde{\nu}(\text{RuH})$  compared to the other halido/pseudo halido complexes indicates a weaker bond strength.

As communicated by Morris and co-workers<sup>103,104</sup> the asymmetric H-Ru-X vibrational mode could give qualitative insight into the hydricity of the hydrido ligand. Unfortunately, this highly interesting  $\nu(\text{RuH})$  mode has proven illusive in the present study and has not been observed neither experimentally nor computationally.

Table 2.10: Summary of spectral and geometric data for the complexes (2)-(5). Data obtained from literature is indicated by reference.

Trans X <sup>-</sup>	$\delta(\text{RuH})$ / ppm	$\nu(\text{Ru-H})$ / cm <sup>-1</sup>	d(Ru-H) / Å IAM	d(Ru-H) / Å HAR	$\nu(\text{CO})$ / cm <sup>-1</sup>	$\delta(^{31}\text{P})$ / ppm
none	-17.3 <sup>b161</sup>	—	1.536 <sup>159</sup>	—	1883 <sup>161</sup>	93.8 <sup>161</sup>
H <sup>-</sup>	-6.41 <sup>c215</sup>	1886 <sup>103</sup>	<i>syn</i> : 1.665 <sup>161</sup> <i>anti</i> : 1.659 <sup>161</sup>	—	1881 <sup>216</sup>	92.1 <sup>215</sup>
Cl <sup>-</sup>	-16.31 <sup>d</sup>	$\begin{cases} 1974^a \\ 1960^a \end{cases}$	<i>syn</i> : 1.550 <sup>161</sup> <i>anti</i> : 1.525 <sup>216</sup>	—	1911 <sup>a</sup>	74.78
Br <sup>-</sup>	-15.66 <sup>d</sup>	1971	1.558	1.614	1914	73.54
I <sup>-</sup>	-14.03 <sup>d</sup>	1956	1.495	1.561	1915	72.02
CN <sup>-</sup>	-9.60 <sup>d</sup>	1832	1.557	1.629	1918	78.41
N <sub>3</sub> <sup>-</sup>	-16.07 <sup>d</sup>	1933	1.491	1.548	1906	75.23

<sup>a</sup>R Wugt Larsen, *Personal communication*, November 25, 2021.

<sup>b</sup>NMR chemical shifts: recorded in THF-*d*<sub>8</sub>.

<sup>c</sup>NMR chemical shifts: recorded in C<sub>6</sub>D<sub>6</sub>.

<sup>d</sup>NMR chemical shifts: (this work) recorded in CD<sub>2</sub>Cl<sub>2</sub>.

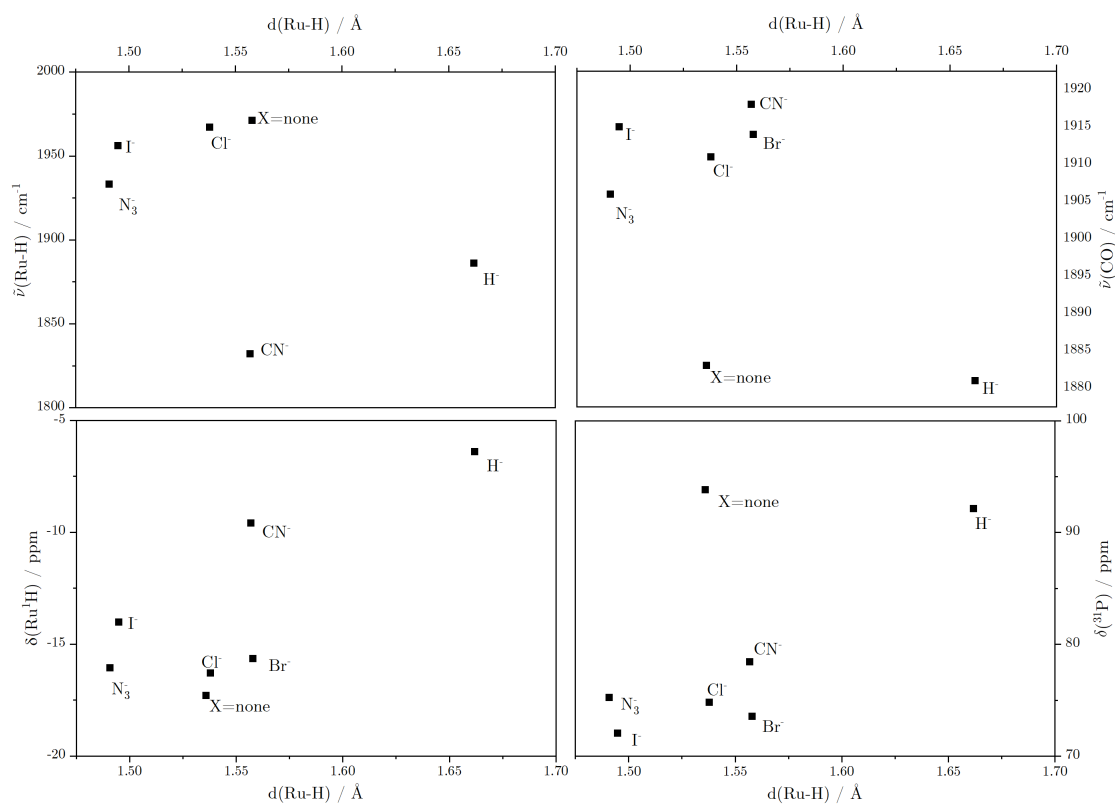


Figure 2.25: Vibrational frequencies and NMR chemical shifts presented in Table 2.10 plotted against the IAM-refined Ru-H distances.

## Chapter 3

# Characterisation and reactivity of PNP ruthenium nitrosyl complexes

The structural aspects of metal nitrosyl complexes have been recognised as diagnostic to the electronic structure of the ligand. As such, the M-N-O bond angle has been widely used to assess the electronic structure of the complex in question.<sup>8,217</sup> However, as much

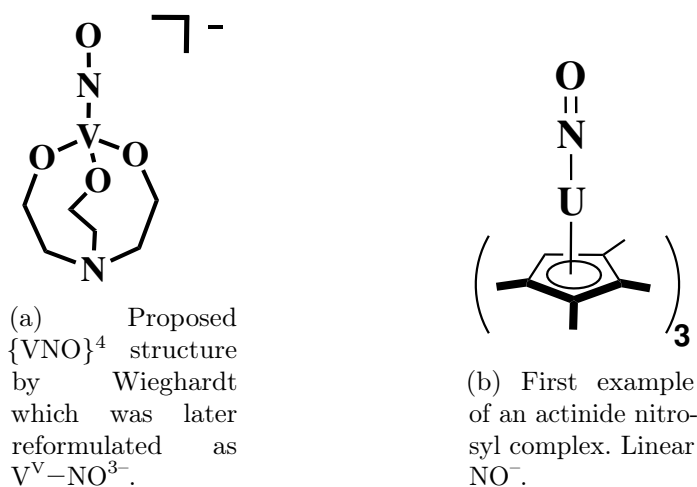
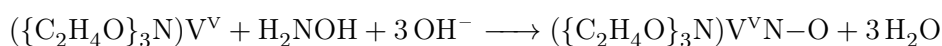


Figure 3.1: Schematic representation of the metal nitrosyl complexes bearing negatively charged NO ligand with linear coordination geometry.

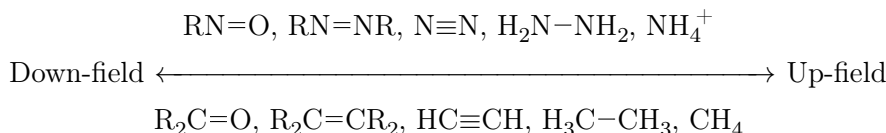
as this approach seems within reason for the bookkeeping of electrons and assignment of formal oxidation states of the central metal atom, the realistic appreciations are in some cases ambiguous. One of the more striking examples of misinterpretation of the metal oxidation state based on the M-N-O angle is the (2,2',2''-nitrilotriethanolato)vanadium(NO) complex in Figure 3.1a formed in the reaction between ammonium vanadate(V), 2,2',2''-nitrilotriethanol, hydroxylamine and potassium hydroxide in a reductive nitrosylation reaction:<sup>218</sup>



The product was initially formulated as a  $V^I\text{--NO}^+$  compound based on the linear V-N-O angle.<sup>219</sup> however, as it was that later proved, no redox reaction took place,<sup>220</sup> and the NO ligand in this case was best described as a triply deprotonated hydroxylamine, thus, the better description of this species is  $V^V\text{--NO}^{3-}$ . Another more recent example of oxidation state ambiguity in metal nitrosyl chemistry is shown in Figure 3.1b. This compound represents the first example of an actinide nitrosyl<sup>221</sup> complex and was achieved by direct nitrosylation of analogous  $(C_5Me_4H)_3U$  with gaseous NO. The U-N-O bond angle is linear as indicated, however the spectroscopic nature ( $\tilde{\nu}(\text{NO}) = 1439\text{ cm}^{-1}$ ) as well as reactivity with electrophiles were not in support of a  $U^{II}\text{--N}\equiv O^+$  formulation but an  $\text{NO}^-$  electronic structure was highly favored. Supported by DFT, it was argued that the linearity of the U-N-O entity was due to very strong  $U_{5f\pi} - \pi^*\text{NO}$  interactions effectively favourising the  $U\equiv^+N\text{--O}^-$  resonance structure. A similar case was reported by Meyer in 2019 for a trigonally coordinated iron nitrosyl that in its  $\{\text{FeNO}\}^6$  state exhibited a linear Fe-N-O angle (as expected) however, the linear angle was retained upon successive reduction:  $\{\text{FeNO}\}^6 \xrightarrow{e^-} \{\text{FeNO}\}^7 \xrightarrow{e^-} \{\text{FeNO}\}^8 \xrightarrow{e^-} \{\text{FeNO}\}^9$  and it was through extensive spectroscopic- and computational analysis concluded that for all  $\{\text{FeNO}\}^n$  ( $n > 6$ ) species the NO-ligand comprised a triplet electronic structure ( $\text{NO}^-$ ), and that the linear geometry most likely was steric in origin.<sup>222</sup> For these aforementioned examples of linear metal-nitroxylide bond angles, the crystal structures were all derived without any obvious disorder in the NO group, which is an important point when conclusions are drawn on the basis on the crystallographically derived M-N-O bond angle, as thermal motion of the O atom in the M-N-O fragment can, when not treated properly during refinement, provide significant errors in both bond angles and distances.<sup>223–226</sup>

### 3.1 Nitrogen NMR spectroscopy

Nitrogen NMR spectroscopy can provide valuable information about the M-N-O geometrical and electronic structure. Unfortunately, the most abundant isotope of nitrogen ( $^{14}\text{N}$ ) has a nuclear spin  $I = 1$  and thus its NMR spectra often suffer from quadrupolar broadening of the signals.<sup>227</sup> On the contrary,  $^{15}\text{N}$  is an  $I = \frac{1}{2}$ , and thus adequate for NMR spectroscopy. However, the low natural abundance often makes it necessary to isotopically enrich the sample,<sup>228</sup> which is rather costly. On the other hand, valuable information can be extracted from the  $^{15}\text{N}$  chemical shift as this is very sensitive to M-N-O bending and can change several hundred ppm and, as such, the  $^{15}\text{N}$  chemical shift have been used as diagnostic for the electronic charge at the ligand, thus, proved as a valuable tool in assignment of the true oxidation state of the metal.<sup>228–231</sup> As noted by Mason,<sup>232</sup> the chemical shift of nitrogen can qualitatively be compared to those for  $^{13}\text{C}$ :



It is immediately noticed, that double bonds are more deshielding than triple bonds which, in turn, are more deshielding than single bonds. Lone-pair carrying nitrogen atoms are exceedingly deshielded due to the fact, that these species have low-energy magnetic dipole-allowed  $n \rightarrow \pi^*$  transitions ( $n$  being the electronic ground state) and a greater degree of asymmetry of the nitrogen charge as compared to fully saturated or triply bonded species. The chemical shift dependence of asymmetry around the nucleus in question has also been noted in  $^{13}\text{C}$ -NMR.<sup>233</sup>

### 3.2 Vibrational spectroscopy of NO complexes

The bond length in the free NO molecule is 1.154 Å and the vibrational stretching frequency of  $\sim 1870\text{ cm}^{-1}$  which upon oxidation to  $\text{NO}^+$  changes to  $2377\text{ cm}^{-1}$  and upon reduction to  $\text{NO}^-$  falls to  $1470\text{ cm}^{-1}$ . These vibrational signatures are reflected in the expected bond orders in NO-redox reactions<sup>8,217</sup> and as such, the vibrational frequency is a valuable tool in the interpretation of the structure of metal nitrosyls.<sup>234</sup>

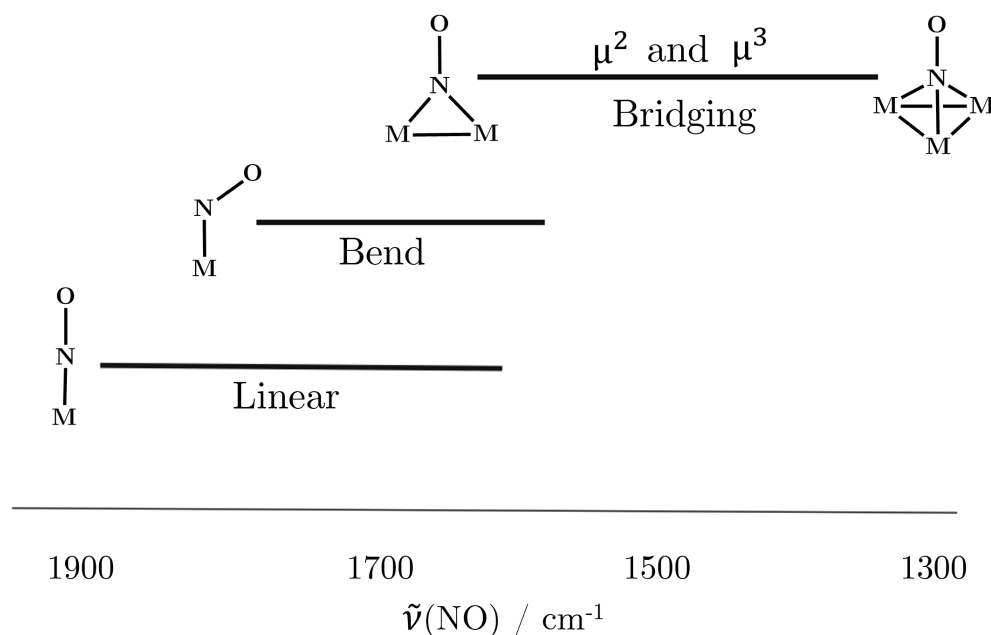


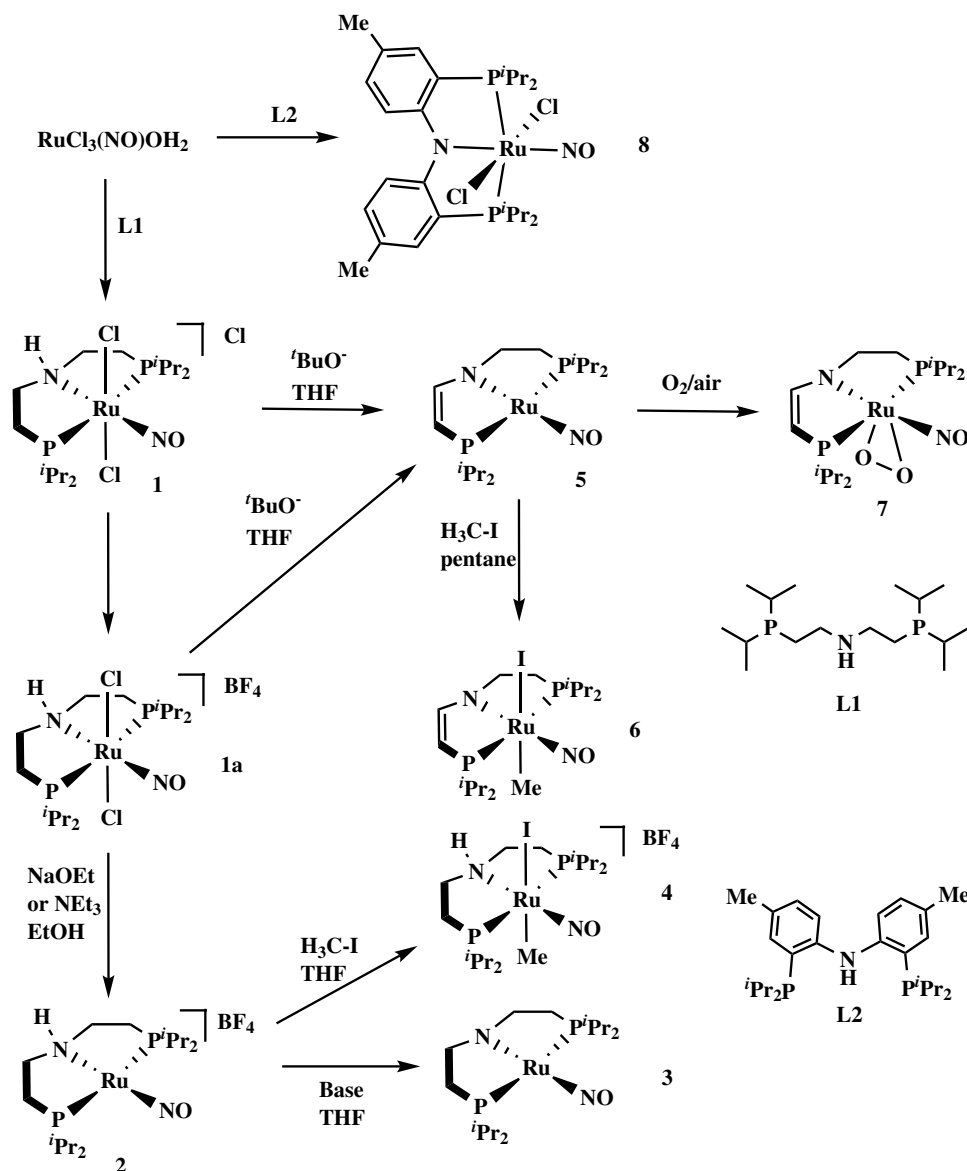
Figure 3.2: Vibrational stretching frequency ranges for the  $\nu(\text{NO})$  mode in transition metal nitrosyls. Adapted from Ref.<sup>8</sup>

However, as can be seen from Figure 3.2, the big overlap of bend and linear coordination modes of the M-N-O fragment are significantly overlapping and, as such, vibrational spectroscopy alone does not hold sufficient gravity for irrefutable conclusions about the structural characterisation.



### 3.3 Results and discussion

In this section, the physical and chemical reactivity of the new RuNO complexes will be presented. The oxidation states of these new species will be addressed based on the observed reactivity and spectroscopic characteristics as well as single-crystal X-ray diffraction. The main part of this work has revolved around the characterisation of the electronic structure of the complexes, and, as outlined above, the  $^{15}\text{N}$  chemical shift has proven a valuable tool. However, enrichment with  $^{15}\text{NO}$  is rather costly (1 g  $\text{Na}^{15}\text{NO}_2$ , 290 €, Sigma-Aldrich). An effort has therefore been done to obtain the  $^{15}\text{N}$  chemical shift at natural abundance through Hetero Multiple Bond Coherence (HMBC) NMR which utilises spin-polarisation from the  $^1\text{H}$  nucleus. This work has been done in collaboration with ph.d. Kasper Enemark-Rasmussen.

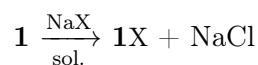


Scheme 3.1: Synthetic route for the nitrosyl complexes in this work.

Scheme 3.1 show the synthetic procedures of the compounds in this work. As will become apparent later, a number of additional complexes have been isolated and structurally characterised. Unfortunately, not all have been fully spectroscopically investigated for which reason this will be a part of future works. The large variety of complexes presented here have their offspring in the same commercially available substance:  $\text{RuCl}_3(\text{NO})\text{OH}_2$ . Although the compound is commercially distributed as a hydrate (water of crystallisation) the true formulation is more likely to be an aqua complex<sup>235</sup> as indicated in Scheme 3.1.

### 3.4 The parent complex **1** and **1a**

Even though these complexes make up for a certain part of Chapter 6, their brief inclusion in this chapter is merited as they serve as starting materials for the species described herein. The complex **1** is easily prepared simply by adding the free ligand, L1, in THF to a THF suspension of  $\text{RuCl}_3(\text{NO})(\text{OH}_2)$  under an inert atmosphere. By stirring at room temperature over night the complex can be filtered off as an air-stable pink powder. The complex is hydrophilic (but not hygroscopic) in the sense, that it is highly soluble in polar protic solvent and only sparingly soluble in aprotic polar solvents (eg acetonitrile). The solubility of the complex can be tuned by anion exchange:



Where  $\text{X/sol.} = \text{BF}_4^-/\text{H}_2\text{O}$ ,  $\text{BPh}_4^-/\text{THF}$ ,  $\text{BArF}/\text{Et}_2\text{O}$

As such, manipulations to the cation in **1** can take place in a large variety of solvents. Regarding the  $\text{BF}_4^-$  counter ion, the product **1a** is precipitating from the solvent phase whereas for the other anions listed above the complex salt need to be recovered from the organic phase.

### 3.5 Reactions of **1** and **1a**

In the pursue of catalytically active species in (de)hydrogenation reactions, the transfer hydrogenation of acetophenone in basic isopropanol was attempted\*. The complexes **1** and **1a** proved effective in this catalytic transformation as is explained in detail in Chapter 4. However, when substituting ethanol for isopropanol, the visual appearance of the reaction was no longer brownish red as in the case of isopropanol as solvent but turned intensely dark green and no catalytic activity was observed.

#### 3.5.1 Reaction with base in ethanol

A reaction was performed with 5 mg of **1** in  $\text{EtOH}/\text{Et}_3\text{N}$  in a J-Young NMR tube (Schlenk conditions) at 80 °C for 1 h. From the NMR spectrum it was concluded that basic ethanolic

---

\*A number of different bases was employed:  $\text{OH}^-$ ,  $^t\text{BuO}^-$ ,  $\text{EtO}^-$ ,  $\text{Et}_3\text{N}$

solutions reduces the compound under the formation of acetaldehyde (see NMR spectrum in Appendix C.16). As no paramagnetic broadening of the signals was observed in the spectra, the complex was assumed to undergo a 2-electron reduction. As can be seen in the  $^{31}\text{P}$ -NMR, the formation of a new product (74.9 ppm) happens already at room temperature along with other species. After 1 h the product distribution has converged into one product indicated by the singlet at 74.9 ppm (Figure 3.3).

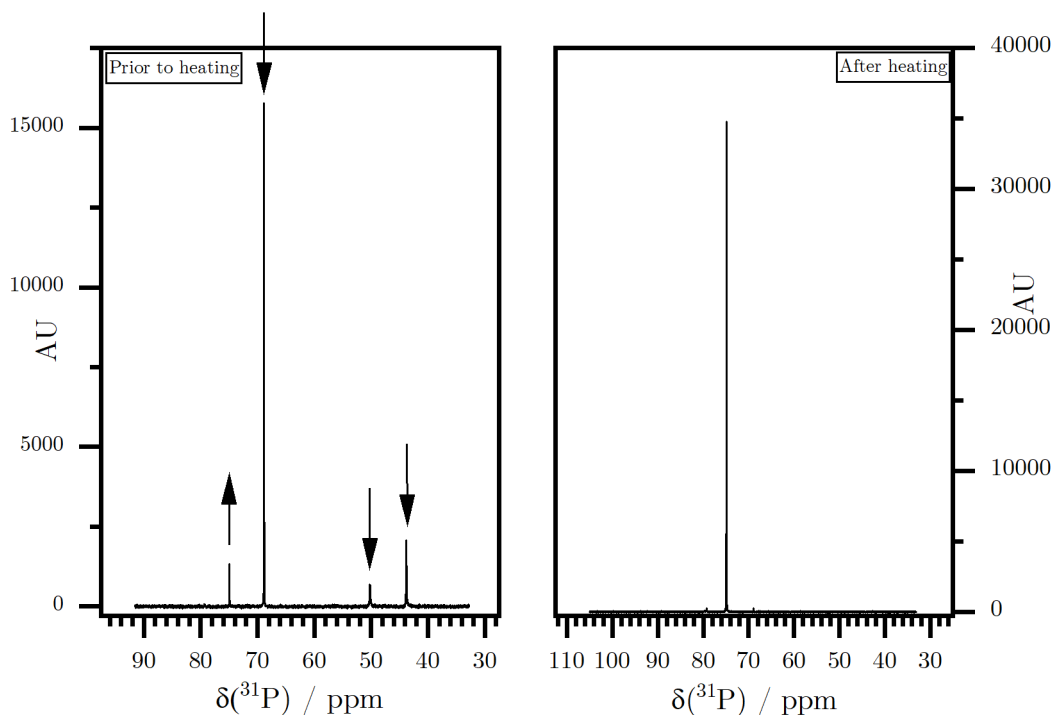


Figure 3.3:  $^1\text{H}$ -decoupled  $^{31}\text{P}$ -NMR spectrum of the mixture of **1** in ethanol/triethylamine mixture immediately prior to heating (left) show the distribution of species converts into one upon heating at  $80^\circ\text{C}$  for 1 h (right).

In the attempt to isolate the purportedly reduced species of **1**, the solvent was evaporated and toluene was added to dissolve the remnant for work-up. Interestingly, the solution changed colour immediately from dark green to yellow.  $^1\text{H}$ -NMR and  $^{31}\text{P}$ -NMR was measured on the yellow solution. The proton spectrum was particularly revealing as a hydrido-species was formed, indicated by the high-field triplet at  $-3.8$  ppm with  $J = 15.8$  Hz (*cis*- $^{31}\text{P}$  coupling<sup>161</sup>). To check the reversibility of this reaction, an excess of triethylamine was added to the yellow solution which immediately changed its colour back to intensely green. This indicates, qualitatively, that the formation of the yellow species from the green product obtained from the reduction of **1** is pH dependent. A similar qualitative analysis based on colour changes was taken out on complex **1a** which revealed the same behavior: The red starting complex reacts with basic ethanol to yield a green product that upon dissolution in toluene turns yellow which, again, upon reaction with excess  $\text{Et}_3\text{N}$  yields the same dark green colour as the initial reaction. Interestingly, upon exposure of the yellow intermediate solution to air, the starting material, **1/1a** was obtained as indicated

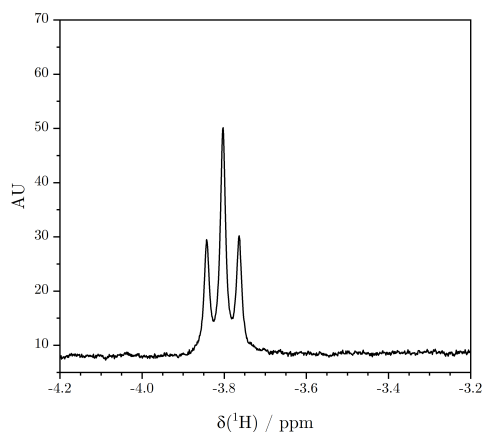


Figure 3.4:  $^1\text{H}$ -NMR spectrum shows the hydride signal from a generated hydrido species upon re-dissolving of the initially generated product mixture from the reaction in ethanolic triethylamine.

by single-crystal X-ray diffraction analysis.

In order to reveal the nature of the green complexes formed in the reaction of basic ethanol with **1** and **1a**, the reactions were performed on 8 mg **1** and **1a** in a set of J-Young tubes and treated with a 1:1 mixture (5 mL)  $\text{Et}_3\text{N}/\text{EtOH}$  and heated for 1 h at  $80^\circ\text{C}$  as described above. After the reaction mixtures were cooled to rt, the volatiles were removed *in vacuo* where after the J-Young tubes were submerged in a heat bath at  $80^\circ\text{C}$  and put under dynamic vacuum over night to sublime the triethylamine hydrochloride that supposedly had been formed during the reaction. Subsequently, the dark green residues were dissolved in THF inside an Ar filled glovebox and diethyl ether was allowed to diffuse into the solution at  $-30^\circ\text{C}$  whereby crystals formed during the course of 3 days. In the case of the reaction of **1** the resulting dark green crystals were rhombic in shape whereas for **1a** formed green rectangular plates. Both dark green complexes are extremely air sensitive both in the solid state and solution phase. The results from the single crystal X-rays analysis of the complexes is shown in Figure 3.5 below and shall hence forth be referenced as indicated in the caption.

On the basis of the detailed analysis outlined in Chapter 6 these complexes are concluded to comprise a ruthenium(0) central metal. As such, this will be denoted as a  $\{\text{RuNO}\}^8$  species according to the Enemark-Feltham nomenclature. This is in line with the linear Ru-N-O bond angle as well as the perfectly square planar geometry around the ruthenium atom as there are no observed tetrahedralisation of the angles which sums to  $360^\circ$  which can be concluded on the basis of the crystallographic model. No intermolecular close contacts are observed in the structure in Figure 3.5a. For complex **2** however, as indicated in Figure 3.5b, the  $\text{BF}_4^-$  counter ion reveal a moderate hydrogen bond to the PNP-amine moiety ( $\text{F}\cdots\text{N} = 2.945 \text{ \AA}$ ,  $\text{F}\cdots\text{H-N} = 2.041 \text{ \AA}$ ).

Based on the results of the crystallographic and chemical analysis it was suspected that the hydride signal was due to protonation of the complexes by the generated triethylamine

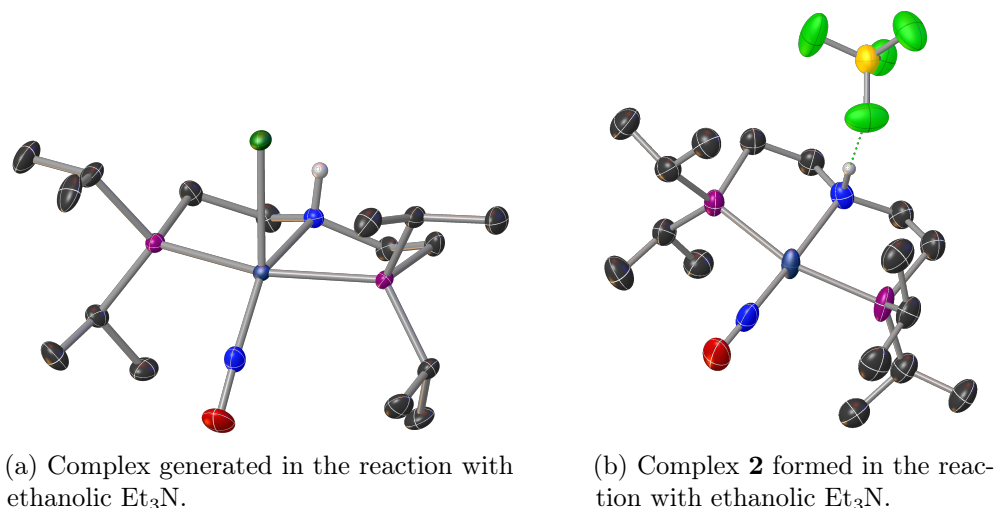
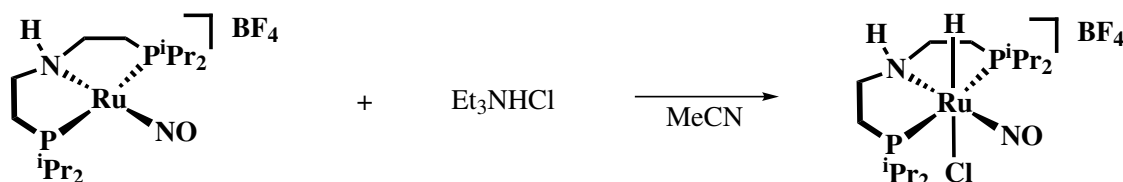


Figure 3.5: Dark green complexes formed in the reaction of **1** and **1a** respectively with ethanolic  $\text{Et}_3\text{N}$  at  $80^\circ\text{C}$  for 1 h. Hydrogens on all carbon atoms has been removed for clarity. Thermal ellipsoids are plotted at 50% probability level.

hydrochloride. As such, a reaction between **2** and triethylamine hydrochloride was expected form the corresponding chloridohydridoruthenium(II) complex. Indeed, this yellow species was generated according to Scheme 3.2. The scheme shows the generation of the chlorido-hydridoruthenium(II) complex through protonation of the metal ion (effectively, oxidative addition of hydrogen chloride).



Scheme 3.2: Reaction of complex **2** with the very weak acid, triethylamine hydrochloride, to yield a hydridochloridoruthenium(II) complex.

The  $^1\text{H}$ -NMR spectrum showing the characteristic hydride peaks is given in Figure 3.6 and by the presence of two triplets at  $-4.28$  and  $-4.71$  ppm respectively, with the former being the most significant, thereby allows for the irrefutable conclusion that a hydride species indeed has been formed in the reactions outlined in Scheme 3.2.

It is clear that the position of the peaks are not exactly at the same chemical shift as the products observed in the *in situ* generated complex in Figure 3.4. This may be explained by the presence of additional species with acid/base character which are expected to influence the NMR spectra as chemical shifts are known to be sensitive to pH changes.

Attempts to isolate the chloridohydrido complex in quantitative yields were made. The compound, however, was difficult to obtain in a crystalline state as, upon removal of the solvent, an oily residue was left. The oily nature of the compound was remained even when submitting it to slow precipitation with diethyl ether, toluene or saturated hydrocarbons. In order to furnish nucleation, different counter ions were used  $\text{BF}_4^-$ ,  $\text{BPh}_4^-$ ,  $\text{BArF}^-$ ,  $\text{Cl}^-$ .

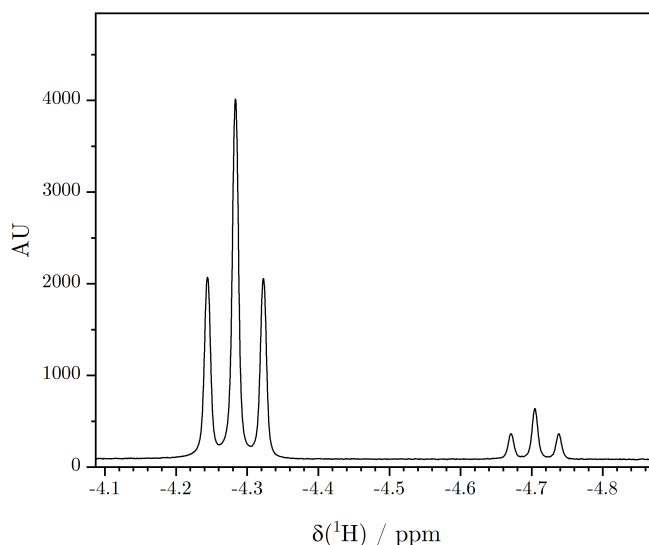


Figure 3.6: Hydride region of the reaction product from the reaction described in Scheme 3.2.

Only with use of chloride as counter ion crystal growth was successful, however only at low yields, 15 - 25% (see Appendix C).

### 3.5.2 Characterisation of $[(^i\text{Pr}_2\text{PNP})\text{RuClH}(\text{NO})]\text{Cl} \cdot \text{HCl}$

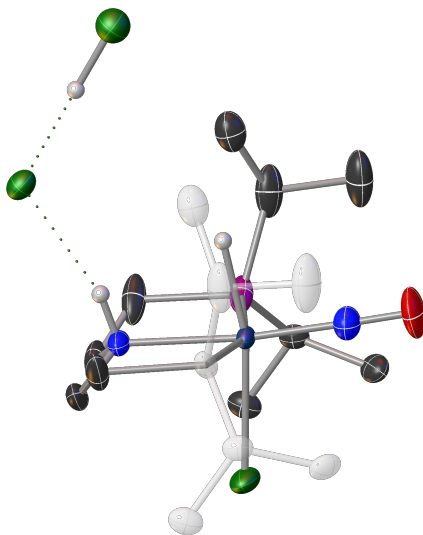


Figure 3.7: Crystal structure of the chloridohydridoruthenium(II) complex containing co-crystallised HCl. All hydrogens on carbon atoms have been omitted for clarity. For the same reason, two isopropyl groups are ghosted out. Thermal ellipsoids are plotted at 50% probability level.

The chloridohydrido complex shown in Figure 3.7 crystallises in the space group  $P2_1/m$  together with one molecule of hydrogen chloride per asymmetric unit. The cation belongs to the  $C_s$  point group and can be regarded as a distorted octahedron. The co-crystallised HCl is engaged in hydrogen bonding with the amine proton. The Ru-N-O bond angle of  $170.03^\circ$  and the short N-O bond length of  $1.148 \text{ \AA}$  is in line with an  $\text{N}\equiv\text{O}^+$  electronic

structure. This will render the ruthenium atom in the oxidation state +2. The Ru-H bond distance (IAM) of 1.715 Å is exceptionally long as compared to the carbonyl analogues outlined in Chapter 2.

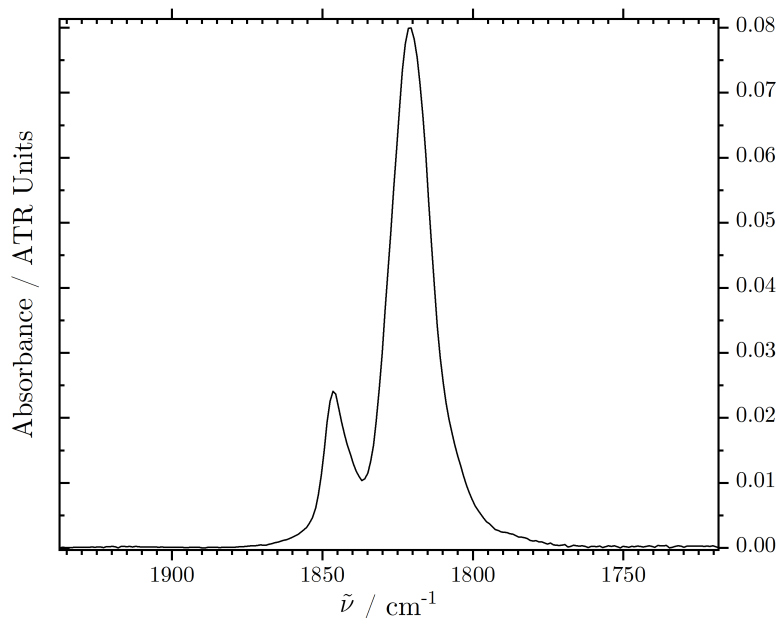


Figure 3.8: IR spectrum in the range of the  $\tilde{\nu}(\text{NO}) = 1821 \text{ cm}^{-1}$  and  $\tilde{\nu}(\text{Ru-H}) = 1847 \text{ cm}^{-1}$  modes of powdered crystals of chloridohydridoruthenium(II).

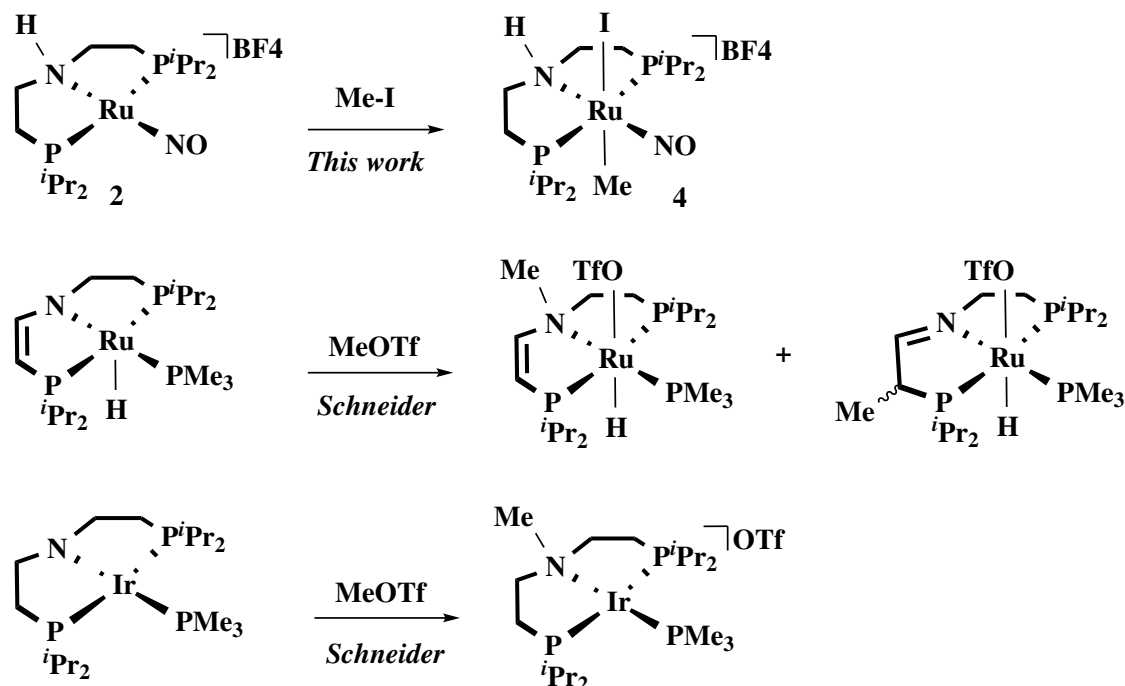
The long Ru-H distance is in line with the rather low-field  $\delta(\text{RuH})$  as found in the proton NMR spectrum. The IR spectrum shown in Figure 3.8 shows a very strong absorption at  $1821 \text{ cm}^{-1}$  which is characteristic to the  $\nu(\text{NO})$  stretching mode. The medium-to-strong absorption at  $1847 \text{ cm}^{-1}$  is assigned as  $\nu(\text{Ru-H})$  mode. This bathochromic shift (as compared to the carbonyl analogues) indicates a long and relatively weak Ru-H bond. The  $\nu(\text{NO})$  frequency as well as the Ru-NO and N-O bond distances is in line with previously reported  $\text{Ru}^{\text{II}}\text{-NO}^+$  complexes.<sup>236–238</sup>

Table 3.1: Summary of selected geometric parameters reflected in the asymmetric unit of the  $C_s$  symmetric molecule,  $[(^i\text{Pr}_2\text{PNP})\text{RuClH}(\text{NO})]\text{Cl} \cdot \text{HCl}$ .

Atom	Atom	Length / Å
Ru	P	2.382
Ru	H	1.72
Ru	Cl	2.485
Ru	N <sub>PNP</sub>	2.159
Ru	N(O)	1.744
N	O	1.148
		Angle / °
Ru-N-O		179.03

3.5.3 Reaction of **2** with iodomethane  $\longrightarrow$  **4**

The observation that protonation of the metal center occur upon reaction of **2** with the very weak acid, triethylamine hydrochloride ( $pK_a(\text{AH}) = 18.63$  in MeCN<sup>239</sup>) is indicative of a very electron rich ruthenium center. In comparison, isoelectronic iridium(I) PNP complexes show *N*-centered reactivity with strong electrophiles.<sup>240</sup> As such, it was inferred, that the complex **2** should be nucleophilic enough to furnish cleavage of weak carbon halide bonds via oxidative addition of the ruthenium center.



Scheme 3.3: **Top:** Reaction of complex **2** (this work) with iodomethane. **Mid:** Addition of methyl triflate across the amido-ruthenium(II) bond as well as across the C=C double bond. No change in formal oxidation state of the metal.<sup>205</sup> **Bottom:** Addition of methyl triflate across the amido-iridium(I) bond with no change in oxidation states.<sup>240</sup>

As outlined in Scheme 3.3, the complex **2** does indeed undergo oxidative addition with iodomethane, in contrast to the isoelectronic iridium case (Scheme 3.3 bottom) which does not undergo oxidative addition with strong electrophiles. This result indicates that **2** is a low valent ruthenium species with much of the electron density located on the metal center, despite being coordinated by the extreme  $\pi$ -acceptor, the  $\text{N}\equiv\text{O}^+$  ligand. The resulting iodidomethylruthenium(II) complex was characterised by multi-nuclear NMR spectroscopy which revealed the presence of isomers in solution by two weak high-field triplets ( $\text{Ru-CH}_3$ ) at 1.4 and -1.0 ppm with  $J(\text{C-P}) = 6.0, 6.1$  Hz respectively in the  $^{13}\text{C}$ -NMR spectrum. The  $^{31}\text{P}$ -NMR was also in support of the presence of different isomers (62.6 and 62 ppm respectively). The  $^{15}\text{N}$ -chemical shifts, obtained from HMBC experiments, were more sensitive at the PNP amino moiety with respect to isomerisation than was the N(O) chemical shift. As such, the  $^{15}\text{NH}$  chemical shift for isomer A is 54 ppm and 51.6 ppm for isomer B. The nitrogen chemical shift for the NO ligands are found at 369 ppm



and 370 ppm for isomer A and B respectively. The chemical shifts for the N(O) are both in agreement with a linear  $\text{N}\equiv\text{O}^+$  ligand electronic structure which was also indicated by the crystallographic model (*vide infra*).

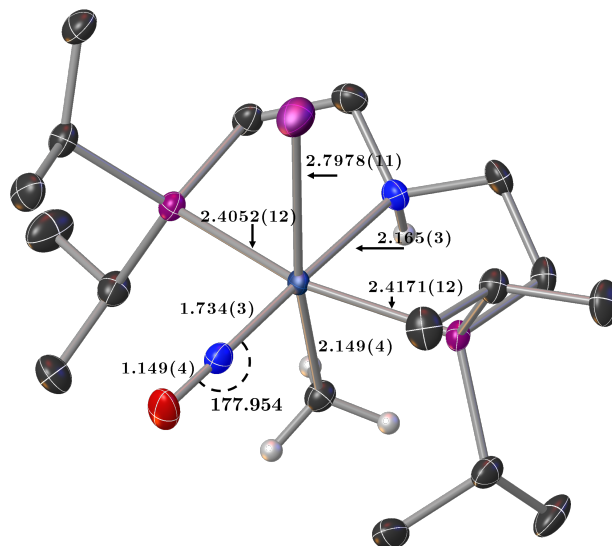


Figure 3.9: Crystal structure of the cation in **4**. All hydrogen atoms on carbon atoms associated with the PNP ligand is omitted for clarity. Thermal ellipsoids are plotted at 50% probability level.

The elemental analysis is perfectly in support of the presence of isomers (see C.1.5). The compound **4** crystallises in the space group  $P2_1/n$ . The global symmetry as well as the local symmetry around the ruthenium atom can only be regarded as  $C_1$ . The almost linear Ru-N-O angle ( $\sim 178^\circ$ ) as well as the very short N-O bond length of 1.149 Å are indicative of an  $\text{N}\equiv\text{O}^+$  triple bond. The triple bond character of the NO ligand is supported by high energy  $\nu(\text{NO})$  vibrational mode at  $1815\text{ cm}^{-1}$ . The characteristic  $\nu(\text{N-H})$  stretching mode is observed at  $3000\text{ cm}^{-1}$  with a corresponding rocking mode at  $1462\text{ cm}^{-1}$ . The large degree of coherence in the IR spectrum is indicative of a clean product.

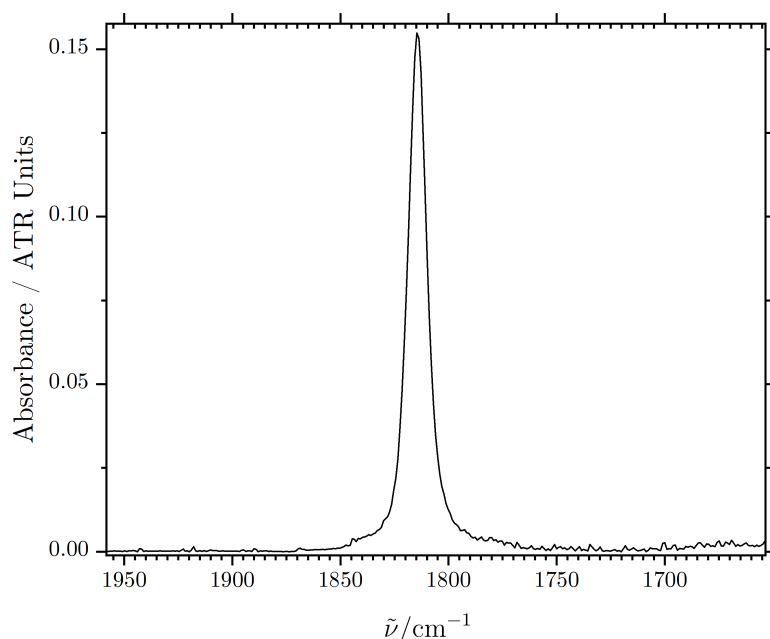


Figure 3.10: Infrared vibrational absorbance at  $1815\text{ cm}^{-1}$  related to the  $\nu(\text{NO})$  stretching mode.

#### 3.5.4 Reaction of **1**/**1a** with base in aprotic solvent $\rightarrow$ complex **5**

In the reaction of **1** or **1a** with excess strong base (alkoxides) in aprotic solvent, a forest green, extremely air sensitive complex is obtained. The  $^1\text{H}$ -NMR spectrum shown below shows two low-field doublets that both integrate to 0.5 indicative of that the two doublet is one signal from one proton with a  $J(\text{H-H}) = 5.6\text{ Hz}$  and  $J(\text{H-P}) = 45\text{ Hz}$ . The same  $J(\text{H-H}) = 5.6\text{ Hz}$  is found in the doublet of triplets at  $\sim 3.8 - 3.83\text{ ppm}$  (coupling symmetry) thus this is strongly indicating that this proton is bound at the  $\alpha$ -carbon (relative to one of the phosphorus atoms). This assignment is in line with previous works by Friedrich *et al.*<sup>205</sup> where a  $\text{C}=\text{C}$  double bond is present. As such, a  $J(\text{H-P}) = 2.6\text{ Hz}$  which is almost half of 5.6 and thereby makes it reasonable that the observed signal appears as two partially merged triplets. The  $^{31}\text{P}$ -NMR spectrum shows two roofing doublets in line with the phosphorus atoms being chemically nonequivalent ( $J(\text{P-P}) = 223\text{ Hz}$ ) and coordinated *trans* with respect to each other.

The  $\delta(^{15}\text{N}) = 163.9\text{ ppm}$  indicates that the amino moiety in the PNP ligand has undergone deprotonation to an amido species which is further supported by single-crystal X-ray analysis, *vide infra*. Crystals of quality suitable for X-ray diffraction were notoriously difficult to obtain due to the disadvantageous solubility profile exhibited by the complex. The complex possesses remarkably good solubility in the crystallographic oil (polybutenes), thus, the crystals have to be grown to a large size which makes the entire process very time consuming. The complex is extremely soluble in all common solvents (including pentane in which a homogeneous solution can be obtained by dissolving 70 mg of **5** in 0.1 ml pentane). The structure is square planar and, as such, a  $d^8$  electron configuration at the metal is expected. Under the strongly basic conditions employed in the synthesis, the amino group is deprotonated to form the amido species shown in Figure 3.12.

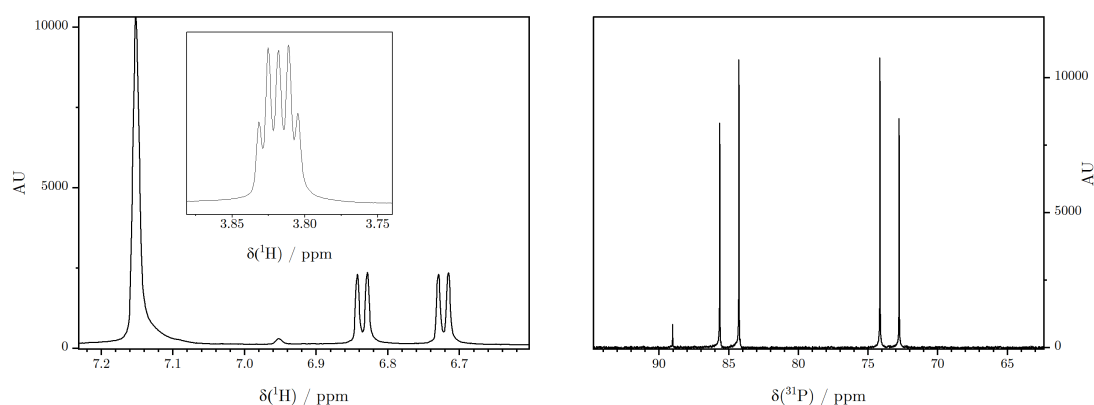


Figure 3.11: **Left:**  $^1\text{H}$ -NMR in the aromatic region showing a doublet of doublets as well as a merged doublet of triplets (insert). **Right:**  $^{31}\text{P}$ -NMR spectrum shows two doublets from chemically nonequivalent phosphine groups.

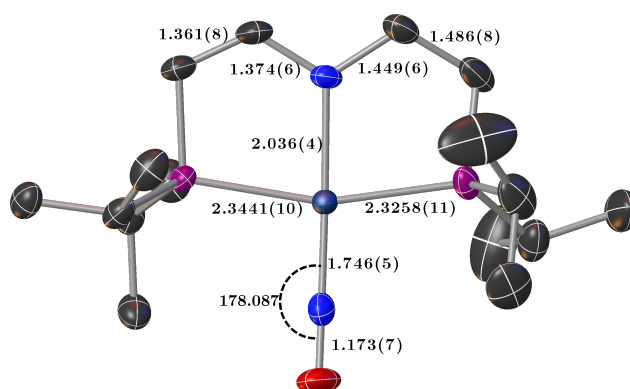


Figure 3.12: Square planar complex **5**. All hydrogen atoms have been omitted for clarity. Thermal ellipsoids are plotted at 50% probability level.

The complex crystallises in the  $P2_1$  space group and exhibits two independent molecules in the asymmetric unit where in one unit carbon atoms suffered from statistical disorder. The global symmetry is  $C_1$  whereas the local symmetry around the ruthenium center (with respect to the ligators) can be considered as  $C_{2v}$ . Crystals were obtained by storing a concentrated pentane solution at  $-30^\circ\text{C}$  for 2 months. The Ru-N-O bond angle is  $178.087^\circ$  and the short N-O bond distance of  $1.173 \text{ \AA}$  is in line with a formulation of  $\text{N}\equiv\text{O}^+$  nitrosonium ligand which, in turn, is in favour of the formulation of the titled compound to comprise a zero-valent ruthenium atom. The short bonding distance between the ruthenium central atom and the amido moiety of  $2.036 \text{ \AA}$  reveals a significant multiple bond character.<sup>241</sup> As can be seen in Figure 3.12, the ligand backbone is unsymmetrical with one C-C distance significantly shorter than the other. The carbon atoms having the shortest C-C distance possess planar conformation as would be expected for  $sp^2$  hybridised carbon atoms. The C-C distance of  $1.361 \text{ \AA}$  is in line with previously reported vinylene-ethylene-amido (PNP) pincer structures.<sup>242–245</sup>

The IR spectrum of **5** (Figure 3.13) show the strong, sharp absorption of the  $\nu(\text{NO})$

stretching mode at  $1691\text{ cm}^{-1}$  and the diagnostic C=C stretchings at  $\tilde{\nu} = 1532\text{ cm}^{-1}$  which is, not surprisingly, lower than free vinylamine ( $1668\text{ cm}^{-1}$ )<sup>246</sup> and the terminal C=C stretch in styrene. However, the frequency observed in Figure 3.13 is more close to the C–C ring stretch in styrene ( $1575\text{ cm}^{-1}$ ),<sup>247</sup> indicating that the bond is not a pure double bond but somewhere in between single and double which may be expected when in conjugation with an amido-ruthenium multiple bond and electron density is distributed into the vinylene moiety by resonance.

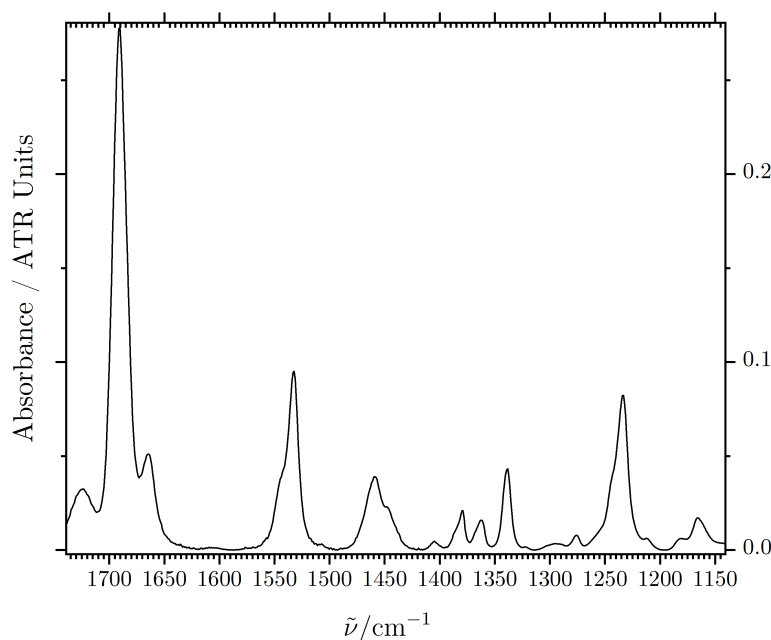


Figure 3.13: IR spectrum of **5** in the characteristic region of the diagnostic frequencies of the  $\nu(\text{NO})$  and  $\nu(\text{C}=\text{C})$  modes.

#### **O<sub>2</sub> activation: Complex **5** $\rightarrow$ **7****

As mentioned previously, complex **5** is extremely air sensitive and reacts instantaneously with both atmospheric air and pure dioxygen. Initial studies on the nature of the resulting red-brown compound formed in the reaction of **5** (in solution) with dioxygen were firstly undertaken by NMR spectroscopy. A solution of 8 mg of **5** in 0.4 mL  $\text{C}_6\text{D}_6$  was loaded into a J-Young NMR tube and frozen in an acetone/dry-ice cold bath before the NMR tube was evacuated and back-filled with  $\text{O}_2$  (CANgas, Sigma-Aldrich). The mixture was then quickly heated to approximately room temperature and a  $^1\text{H}$ -NMR and  $^{31}\text{P}$ -NMR spectrum were measured immediately (previous attempts on the synthesis and isolation of this species failed due to thermal instability).

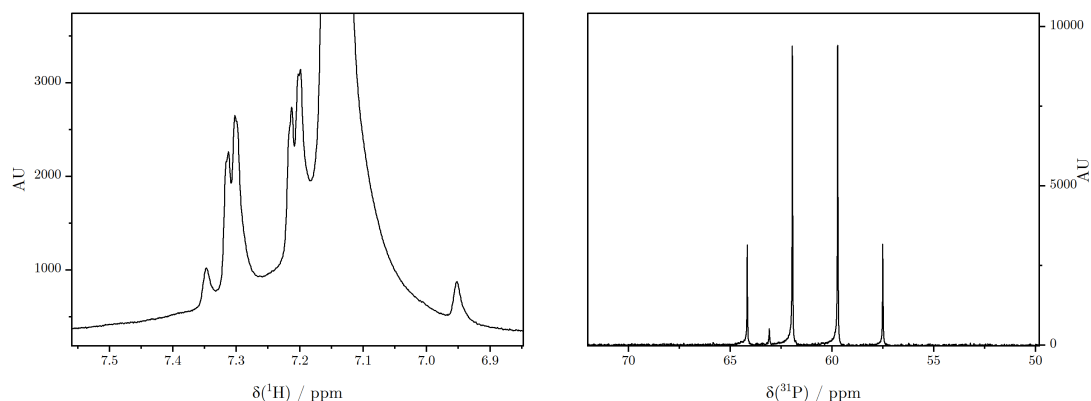


Figure 3.14: Left:  $^1\text{H}$ -NMR in the characteristic region (aromatic). Right: The full  $^{31}\text{P}$ -NMR spectrum.

The  $^1\text{H}$ -NMR in Figure 3.14 above shows the double doublet as was observed for complex **5** in Figure 3.11 and the  $^{31}\text{P}$ -NMR spectrum exhibits the roofing doublets as was also observed for complex **5**. Together, it can be concluded that the PNP-complex does not degrade structurally on exposure to  $\text{O}_2$ . The double doublet in the  $^1\text{H}$ -NMR spectrum is shifted down-field by  $\sim 0.5$  ppm with respect to **5**. The  $J(\text{H-H}) = 5.9$  Hz is slightly bigger than for **8** and the  $J(\text{H-P}) = 40.5$  Hz is slightly smaller. The signals in the  $^{31}\text{P}$ -NMR spectrum is shifted significantly up-field, indicative of less  $\pi$ -electron density around the P-nuclei as compared to **5** and the  $J(\text{P-P}) = 359$  Hz shows a stronger P-P interaction. These observations are in line with the interpretation of that the complex **5** on exposure to dioxygen undergoes oxidation without loss of its molecular integrity.

After measurement of the IR spectrum of **5**, the sample compartment was purged with atmospheric air for 3 min before re-measurement. After 3 min in air the spectra are almost identical but a low intensity band at  $850\text{ cm}^{-1}$  which is diagnostic for the presence of a side-on coordinate metal-peroxo species intensifies, *vide infra*.

### Characterisation of **7**

Due to the thermal instability of **7** it was difficult to obtain crystals of proper quality. A successful route was to mount a crystal of **5** on a cryo loop and monitor the reaction with air under a microscope. When the colour change of the crystal (dark green to brownish red) ceased, the crystal was mounted on the diffractometer under a cold (120 K) stream of  $\text{N}_2$ .

*Comparison with Vaska's and Milstein's complexes:* As this structure was obtained by aerial oxidation of a crystal of **5**, it is

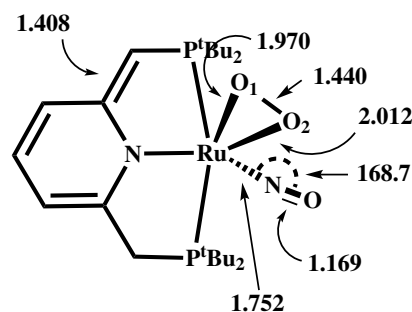


Figure 3.15: Schematic representation of the peroxo nitrosyl complex presented by Milstein and co-workers. All distances and angles are expressed in Ångström and degrees respectively.

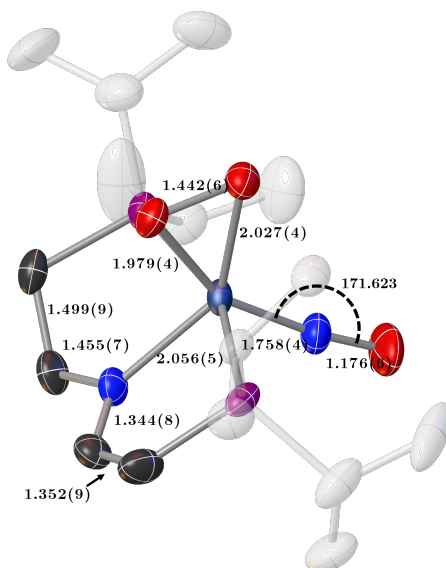
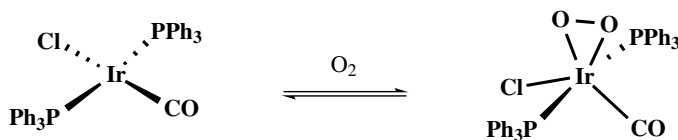


Figure 3.16: Crystal structure of complex **7** obtained from the solid-state-gas-phase-reaction between a single-crystal of **5** and atmospheric oxygen. Hydrogen on carbon atoms have been omitted for clarity and the isopropyl groups on phosphorus have been ghosted out. Thermal ellipsoids are plotted at 50% probability level.

tempting to conclude that the reaction proceeds faster than Vaska's complex which uptakes dioxygen relatively slowly.<sup>248</sup> On the contrary to Vaska's complex, the de-coordination of dioxygen from **7** could not be furnished by reduced pressure. In addition, it is interesting that the R-O(O) distances in Vaska's oxygenated complex are almost equivalent. The O-O bond length was initially reported to be 1.30 Å and thus, is more representative to superoxide,  $\text{O}_2^-$  than peroxide ( $\text{O}_2^{2-}$ ).<sup>249</sup> A re-determination of the dioxygen adduct of Vaska's complexes proved the initially determined O-O bond distance wrong and, as such, reported a new, more accurate O-O distance of 1.465 Å, which was significantly longer than previously reported and much closer to the formulation of a peroxide ligand and, in addition, a better agreement of the  $\nu(\text{O}_2)$  vibrational mode with a resonance energy of  $856\text{ cm}^{-1}$ .<sup>250</sup>



Scheme 3.4: Generation of iridium-peroxo species (right) from the reaction of Vaska's complex (left) with dioxygen.

The angle Ru-N-O of  $171.62^\circ$  in the peroxo complex, **7** is more close to linear than for the related complex in Figure 3.15 reported by Milstein, who reported a Ru-N-O angle of  $167.7^\circ$  in conjunction with a shorter N-O bond distance ( $1.169\text{ Å}$ ).<sup>251</sup> Interestingly, for the complex in Figure 3.15 the authors report a  $\tilde{\nu}(\text{O}_2) = 1021\text{ cm}^{-1}$  which is remarkably higher than the band energy of  $\tilde{\nu}(\text{O}_2) = 850\text{ cm}^{-1}$  observed in this work and for Vaska's dioxygen adduct.<sup>249,250</sup> Additionally, the higher  $\nu(\text{O}_2)$  absorption energy observed by

Milstein stands in contrast to the long O1-O2 bond distance of 1.440 Å (as compared to 1.442 Å /  $\tilde{\nu}(\text{O}_2) = 850 \text{ cm}^{-1}$  for complex **7**). As such, it is questionable whether this absorption is correctly assigned by Milstein. The  $\tilde{\nu}(\text{NO}) = 1721 \text{ cm}^{-1}$  in **7** is well in agreement with the resonance energy reported for the Milstein complex (1733  $\text{cm}^{-1}$ ) albeit slightly lower and thus, reflects the slight longer N-O bond length in **7** (1.176 Å) compared to the Milstein complex (1.169 Å). The C=C bond length of 1.352 Å in **7** is significantly shorter than the analogous bond in the Milstein complex of 1.408 Å and as such, reflects the more electron poor ligand backbone in **7**. The O2-Ru-N4 angle shown in Figure 3.17 is

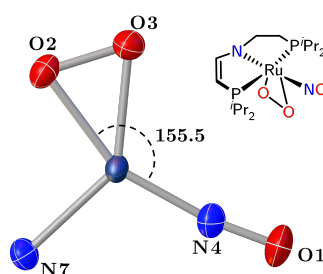
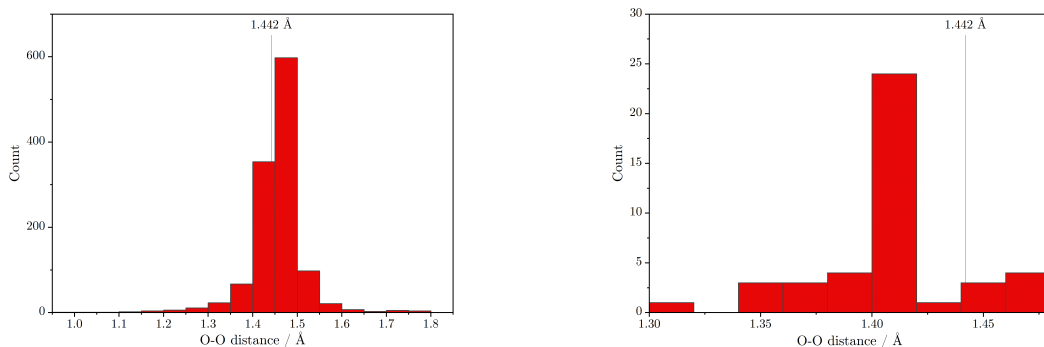


Figure 3.17: Show the basal plane for the distorted trigonal bipyramidal complex **7** and highlight the *trans* coordination of O2–NO.

similar to the one observed in Vaska's complex (155.7°).<sup>250</sup> On a related note, the Ir-O distances in Vaska's complex are close to equidistant which is reflected in the Cl-CO positional disorder observed in the crystal structure (Vaska's complex) as the lack of more pronounced  $\pi$ -donation from *one* oxygen atom do not make a preferred coordination site for the CO ligand. Complex **7**, depicted in Figure 3.16, resembles the coordination of a side-on bonded peroxo ligand and a close to linear Ru-N-O angle 171.6°. The two oxygen atoms in the peroxo ligand are chemically nonequivalent as is shown in the different Ru-O distances of 1.979 and 2.027 Å respectively and, as such, represents more multiple bond character for the former as was also observed in the chemically related complex reported by Milstein, shown in Figure 3.15. The O-O bond length in **7** is 1.442 Å which is only slightly shorter than the O-O bond length in sodium peroxide (1.49 Å).<sup>252</sup> The Ru-N-O angle (171.6°) is close to linear but slightly bent in comparison to what was found in **5** (178.1°) which also points towards a multiple bond character in the short Ru-O(O) bond length and that the less linear Ru-N-O angle is due to extended back bonding to the NO ligand even though the metal is oxidised to, formally, less electron-rich ruthenium(II).

As can be seen from the histogram below, the O-O distance in **7** falls within the expected range for crystallographically characterised transition metal peroxo species. With respect to ruthenium peroxo species (Figure 3.18b), the observed O-O bond distance is longer than the vast majority of examples indicating that **7** is more reducing than the average Ru-species in the formation of peroxo complexes.



(a) Statistics over O-O bond distances in transition metal peroxo complexes across the periodic table.

(b) Statistics over O-O bond distances in ruthenium peroxo complexes.

Figure 3.18: Statistical comparison of the O-O bond distances in peroxo ligands in (a) transition metal complexes across the periodic table and (b) Ru-peroxo complexes. Data is obtained from CCSD.

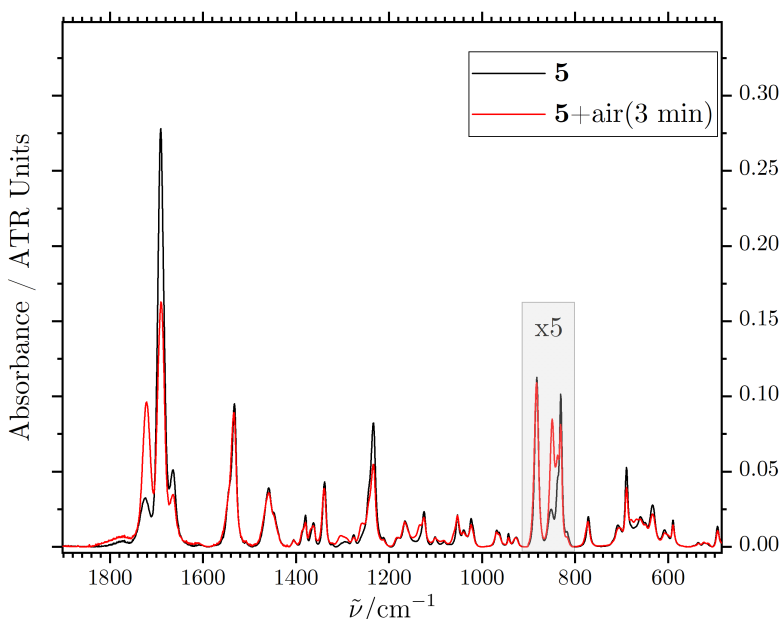


Figure 3.19: IR spectra **8** when in high-vacuum (black line) and after  $\sim 3$  min of venting the sample compartment with atmospheric oxygen. The bands at 900 to 800  $\text{cm}^{-1}$  have been scaled with a factor of 5 for clarity, showing the growth of the characteristic peak of a metal-peroxide.

Measuring a clean IR spectrum of **7** was, unfortunately, unfeasible due to the intrinsically thermal instability of the complex. However, by first measuring the IR spectrum of **5** and subsequently venting the sample compartment with atmospheric oxygen, it was possible to extract the characteristic resonances by comparing the two spectra. Figure 3.19 shows the IR spectrum of **5** before exposure to air (black line) and after  $\sim 3$  min atmospheric venting of the sample compartment. The band attributed to the  $\nu(\text{NO})$  mode at 1691  $\text{cm}^{-1}$  decreases in intensity while a new band increases in intensity at 1721  $\text{cm}^{-1}$ . Additionally, a band at 850  $\text{cm}^{-1}$  increase in intensity upon exposure to air which fits perfectly with the formation of a peroxo species ( $\tilde{\nu}([\text{O}-\text{O}]^{2-})$ ).



### 3.5.5 Reaction of **5** with electrophiles $\longrightarrow$ complex **6** and a diphenyltetratriazeno complex

The number of different functional groups presented in complex **5** (e.g. amide, vinylene, nitrosonium and low-valent ruthenium atom) is particularly interesting as they potentially give rise to a versatile reactivity profile. As drafted in Scheme 3.3, ligand centered reactivity with electrophiles have previously been demonstrated where methyl triflate was observed to add across the metal-amido bond as well as across the vinylene moiety in the PNP backbone. This observation was interpreted as the revelation of the chemical localisation of electrons which is especially interesting for the vinylene based PNP complex as electron delocalisation is expectedly more pronounced in this case. In this spirit, complex **5** in hexane was reacted with an excess of iodomethane (0.2 M in toluene, 3 equivalents). The solution changed colour immediately from green to purple and precipitation sat in during the addition. The purple product could easily be isolated by filtration and washing with hexane under ambient conditions.

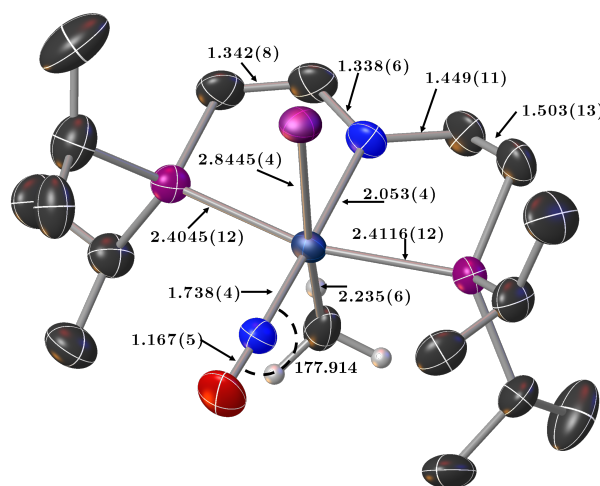
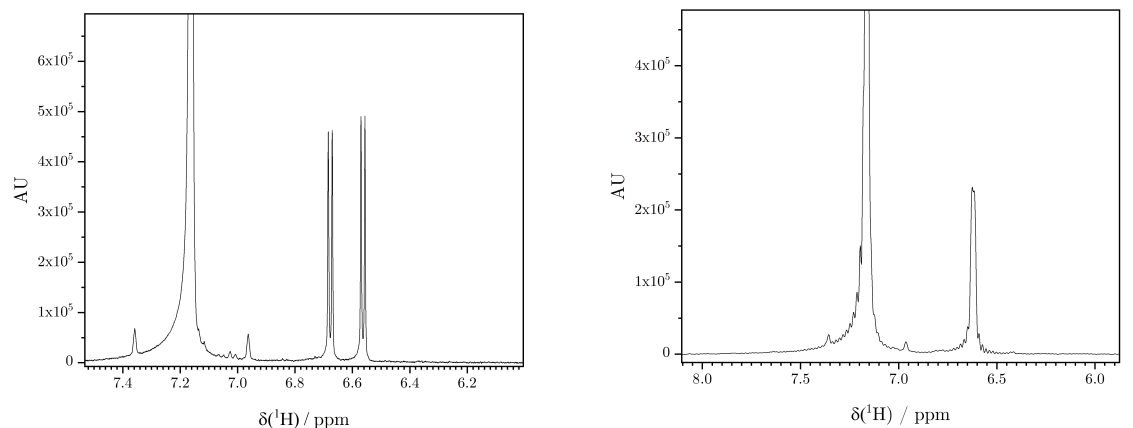


Figure 3.20: Crystal structure of complex **6**. Hydrogen on carbon atoms associated with the PNP ligand have been omitted for clarity. Thermal ellipsoids are plotted at 50% probability level.

Complex **6** shown in Figure 3.20 crystallise, in the *Pbca* space group and half of the PNP scaffold suffers from positional disorder which was modeled by splitting atoms along the largest ADPs and the SADI restrain was applied to assure same bond lengths between disordered parts. For atoms occupying the same crystallographic site, the EADP and RIGU constrains were applied to force identical and well behaving ADPs. The complex can be regarded as a distorted octahedron belonging to the  $C_1$  point group. The Ru-N-O bond angle of  $178^\circ$  and the short N-O bond length indicate an  $\text{N}\equiv\text{O}^+$  ligand electronic structure. The  $\text{N}_{\text{amido}}$ -Ru distance of 2.053 Å is close to but slightly shorter than the one observed for **7** (2.056 Å). Compared to **5**, the N-O distance is slightly shorter ( $\Delta = -0.006$  Å). The C=C-N bonds in **6** is significantly shorter than in the square planar ruthenium(0) complex, **5**. The Ru-CH<sub>3</sub> distance is significantly longer than in the aliphatic amino analogue, **4**.

Complex **6** shows the same spectral features of the unsaturated ligand backbone as **5**. As **6** is robust towards both thermal- and oxidative (aerial) decomposition, more elaborate NMR studies were conveniently undertaken. As the proof of that the double doublet in **5**, **6** and **7** the  $^1\text{H}$ -NMR spectrum is due to  $^1\text{H}$ - $^{31}\text{P}$  coupling, a  $^1\text{H}$ - $^{31}\text{P}$  decoupled proton spectrum was measured. As can be seen in Figure 3.21, the two doublet signals at  $\sim 5.6$ – $7.2$  ppm (Figure 3.21a) do indeed merge into one signal upon  $^1\text{H}$ - $^{31}\text{P}$  decoupling (Figure 3.21b). Unfortunately the band broadening is too severe to resolve any fine structure.



(a)  $^1\text{H}$ -NMR spectrum in the low-field region showing the double doublet signals from the  $\alpha$ -vinylene proton (wrt N).

(b)  $^{31}\text{P}$ -decoupled  $^1\text{H}$ -NMR spectrum in the region of the vinylene.

Figure 3.21:  $^1\text{H}$ - $^{31}\text{P}$  coupled  $^1\text{H}$ -NMR spectrum (a) reveals the double doublet signal from one proton merges into one broad signal in (b) upon  $^1\text{H}$ - $^{31}\text{P}$ -decoupling.

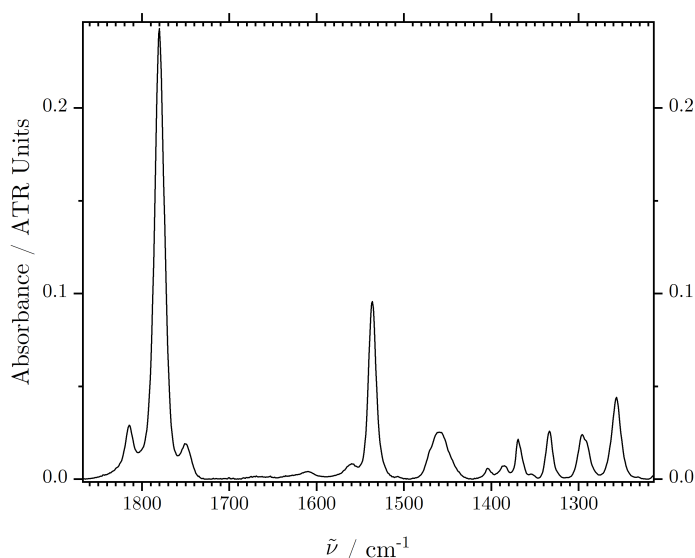


Figure 3.22: IR spectrum in the characteristic region of **6** showing the  $\nu(\text{NO})$  and  $\nu(\text{C}=\text{C})$  stretching modes.

The methyl-C signal in the  $^{13}\text{C}$ -NMR spectrum is found in the high-field region at 0.61 ppm as a triplet with a  $J(\text{C}-\text{P}) = 6.4$  Hz. The  $\delta^{13}\text{C}$  for the  $=\text{CH}-\text{N}$  group is found at significantly higher field (162.9 ppm) than the  $\text{P}-\text{CH}=\text{}$  signal which appear at 72.4 ppm.

The low-field  $\delta(^{15}\text{N}) = 154.5$  ppm is in line with the formulation of an amide nitrogen, as indicated by the crystallographic model. Additionally the linear Ru-N-O observed by X-ray diffraction analysis is supported in  $\delta(^{15}\text{NO}) = 382.2$  ppm.

The IR spectrum shows the sharp  $\nu(\text{NO})$  resonance at  $1780\text{ cm}^{-1}$  and thus, is bathochromic relative to the complex **4** and is in line with the stronger  $\pi$ -donation from the enamide group relatively to the aliphatic amino group. The characteristic C=C stretching mode at  $1532\text{ cm}^{-1}$  in **5** is in **6** observed at almost exactly the same frequency ( $1536\text{ cm}^{-1}$ ) which supports both the crystallographic interpretation as well as the NMR data in that the nucleophile (iodomethane) does indeed not add across the C=C bond in the ligand backbone.

### The crystal structure of a diphenyltetrazenido complex

Metal-imido species are interesting as they serve as a nitrene group source in catalytic amination of C-H bonds,<sup>253</sup> aziridination of olefins<sup>254</sup> and the fundamental understanding of metal-ligand multiple bonds.<sup>255</sup> As tetrazenido ligands are formed in cyclisation reactions of metal-imine complexes with organic azides<sup>256</sup> the fact that the titled compound is formed upon reaction of **5** with azidobenzene, points at a transient imido-species having been present in the reaction mixture. The majority of (the few) published structures on ruthenium imido complexes are usually in oxidation state  $\geq +4$ <sup>257–264</sup> whereas only a handful of examples are known for ruthenium(II)/(III).<sup>265–267</sup> The oxidation of ruthenium(0) PNP complexes with organic azides may prove as an effective route to new  $\text{Ru}^{\text{II}}$ -imido complexes in new coordination environments and geometries. Additionally, tetrazenidoruthenium(II) complexes can undergo light-induced ligand cleavage to yield a dimido species.<sup>255</sup> As such, the potential photo chemistry of this compound, *vide infra*, would be a natural outlook.

The complex crystallises in the  $P\bar{1}$  space group with one full molecule in the asymmetric unit. The bidentate tetrazenido ligand forces the nitrosyl ligand to coordinate on the axial axis relative to the equatorial plane spanned by the PNP ligand. This site of coordination is unique for the crystallographically characterised NO-species in this work. The Ru-N-O angle of  $\sim 172^\circ$  indicates an  $\text{N}\equiv\text{O}^+$  electronic structure which is supported by the short N-O bond length of  $1.166\text{ \AA}$ . The PNP(N)-Ru distance of  $2.0624\text{ \AA}$  is slightly longer than in the previous examples where the NO-ligand is coordinated *trans* to the amido moiety pointing at the NO-ligand being a slightly better  $\pi$ -acceptor than the  $\kappa^2\text{N}, \text{N}'$ -diphenyltetrazenido ligand. This view is also supported by the vinylene bond distances which are collectively longer than the corresponding bond lengths observed for the isoelectronic congeners, **7**, **6**, *vide supra*.

The phenyl rings are close to coplanar with a dihedral angle of  $7.47^\circ$ <sup>†</sup> and with the  $\text{N}_4$ -core. As such, a large degree of electron delocalisation in the tetrazenido ligand scaffold

<sup>†</sup>Left ring plane:  $0.758x + 0.073y + 0.649z + 10.549 = 0$

Right ring plane:  $0.838x + 0.070y + 0.542z + 10.620 = 0$

$\text{N}_4$ -core plane:  $0.536x + 0.190y + 0.823z + 9.958 = 0$

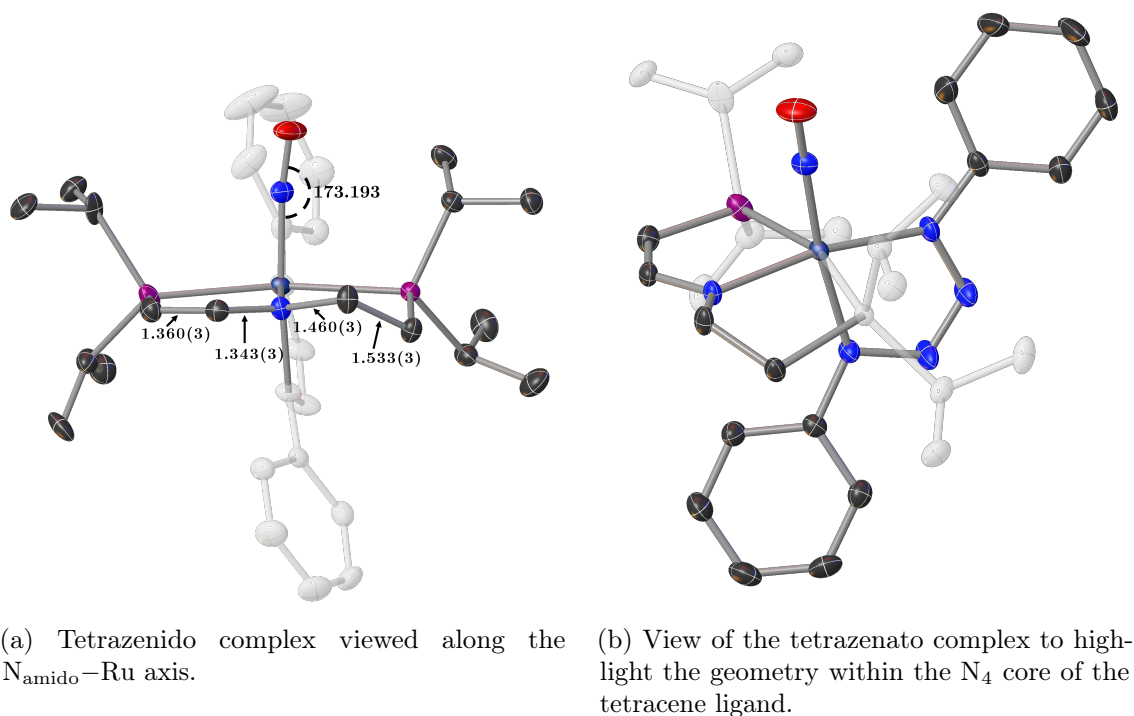
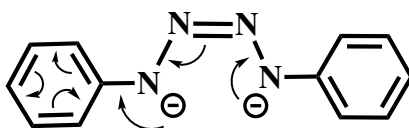


Figure 3.23: Crystal structure of the tetrazenido complex obtained from the reaction of **5** with azidobenzene. (a) (and b): Hydrogen atoms have been omitted for clarity. a): All atoms associated with the tetrazenido ligand is ghosted out for clarity. b): All carbon atoms on the P-ligators as well as the P-atom on the ethylene side of the PNP ligand are ghosted out for clarity.

is expected. In addition, the ring plane with N-coordination *trans*-NO (referred to as "left ring plane") is more close to planarity with the  $N_4$ -core (dihedral angle:  $17.50^\circ$ ) than the ring plane with N-coordination in the equatorial plane (referred to as "right ring plane") is (dihedral angle:  $24.64^\circ$ ). This difference in dihedral angles between the phenyl rings and the  $N_4$ -core of the tetrazenido ligand indicates the degree of delocalisation to the left phenyl ring (*trans*-NO) is more pronounced than to the right phenyl ring (*cis*-NO).<sup>268</sup> This interpretation is supported by the fact that the bond lengths of the tetrazenido ligand are not equal across the *local* (ligand) pseudo- $\sigma_v$  symmetry element. As can be seen in Figure 3.24, the N3-C and N3-N4 bond lengths are shorter than the N6-C and N6-N5 distances. Especially the shorter N3-C bond length is indicating a larger degree of double bond character than in the N6-C bond and, as such a smaller dihedral angle of the left phenyl ring plane and the  $N_4$ -plane would be expected.



Scheme 3.5: Schematic simplification of the electron delocalisation in the tetrazenido dianion through resonance structures.

As the  $\pi$ -system in the free tetrazenido dianion is expected to be delocalised over the entire molecule, the negative charges are somewhat delocalised according to the simplified

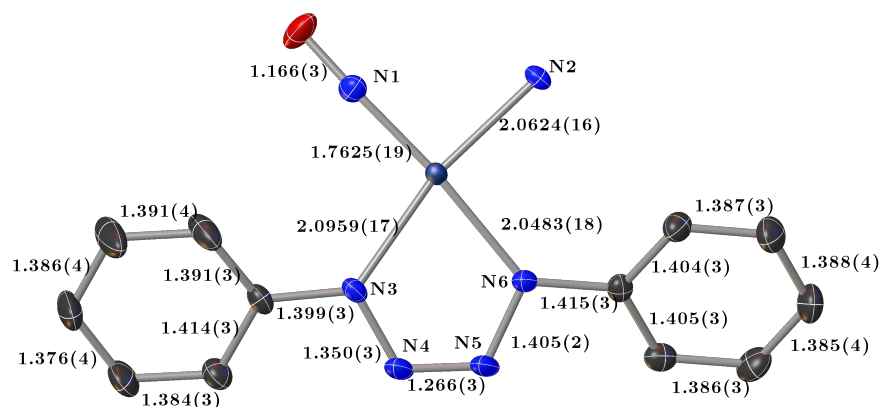
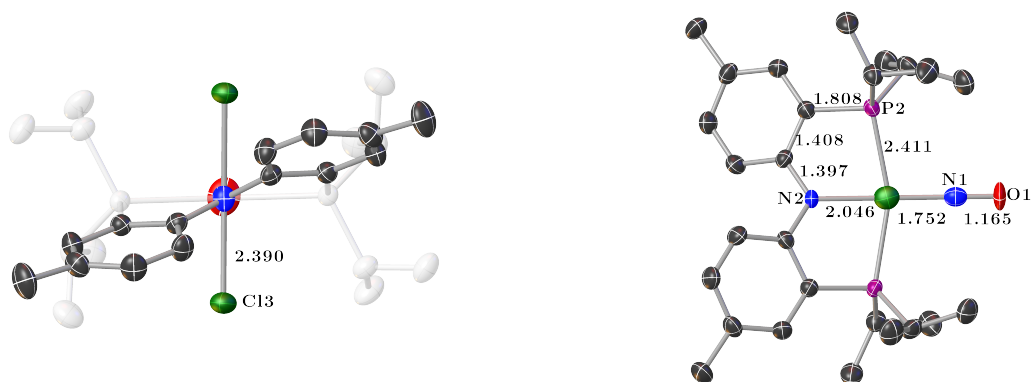


Figure 3.24: Geometry around the ruthenium atom and within the tetrazenido ligand showing the asymmetry across the  $N_4$ -core.

scheme above. However, upon coordination to a positively charged metal ion, the degree of delocalisation is expected to be diminished and differences in bond lengths between like atoms are observed. From the crystallographic model above, it is clear, that the resonance structure shown in Scheme 3.5 is having the most significant contribution to the overall ligand structure.

### 3.6 Diphenylene PNP-Ru(NO) - complex 8



(a) Crystal structure of complex **8** viewed along the crystallographic  $C_2$  axis. Phosphine groups have been ghosted out for clarity.

(b) Crystal structure of complex **8** viewed perpendicular to the crystallographic  $C_2$  axis showing selected bond distances in the asymmetric unit.

Figure 3.25: Crystal structure of the complex **8**. All hydrogens on carbon atoms have been omitted for clarity. Thermal ellipsoids are plotted 75% probability level.

The crystal structure of complex **8** is shown in Figure C.21. The complex possesses  $C_2$  symmetry with the molecular two-fold rotation axis parallel to the crystallographic  $C_2$  symmetry element which imposes perfectly linear Ru-N-O and N1-Ru-N2 bond angles of  $180^\circ$ . The titled complex represents the first example of a diphenylene based PNP ligand on 6-coordinated ruthenium atom where the phenylene backbone is not fused together

which allows for more flexibility. It is interesting to note that for all complexes exhibiting this diarylene pincer ligand, the backbone plane is not coplanar with the equatorial plane spanned by the PNP and NO ligands. This may be due to steric clash between the *ortho*-hydrogen atoms in the ring system as near-planar conformation can be reached by fusing the two ring systems together with a C<sub>1</sub> group between the C6 and C6' positions.<sup>269,270</sup> Also, a planar PNP-pincer backbone is exclusively observed for systems where no steric clash is possible as has extensively been demonstrated by the Schneider group.<sup>18,25,26,242,271,272</sup> The dihedral angle between the mean planes is defined by the Cl-Ru-N2<sup>‡</sup> atoms and the N2-C6-C6' atoms<sup>§</sup> is 60.38° which is in line with similar structures of d<sup>8</sup> complexes of the platinum group metals.<sup>273–280</sup> Not many d<sup>6</sup> complexes exhibiting this PNP ligand scaffold have been reported, however, examples of Ir<sup>III</sup>,<sup>206,207,281,282</sup> Mn<sup>I</sup>, Re<sup>I</sup>,<sup>208,283</sup> Co<sup>III</sup>,<sup>284</sup> Rh<sup>III</sup>,<sup>285</sup> are well known with examples of Ir being most abundant are known to literature.

Interestingly, this ligand scaffold is mainly associated with high oxidation state d<sup>0</sup> species of the early transition metals with Zr<sup>IV</sup>, Hf<sup>IV</sup>,<sup>286</sup> Nb<sup>IV/V</sup>,<sup>287,288</sup> Ti<sup>IV</sup>,<sup>289</sup> Ta<sup>V</sup>,<sup>290</sup> being only a small selection of examples.

A related 5-coordinated Ru<sup>II</sup>-H species is reported.<sup>211</sup> It is interesting, that for all of the above examples, the PNP ligand spontaneously deprotonates upon complexation and the corresponding amino moiety is only restored by treating the complex with strong acid.<sup>283</sup> This behavior reflects the expected stronger acidity of the amine as the nitrogen based lone-pair is in direct conjugation with the flanking aromatic systems. This assumption is well justified in the observed *pK<sub>a</sub>* values in DMSO of 25 and 44 for diphenylamine<sup>291</sup> and pyrrolidine<sup>292</sup> respectively. As such, decreased  $\pi$ -donation towards the ruthenium center is expected as the nitrogen lone-pair would be stabilised by interaction with the  $\pi$ -system of the aryl substituents. On the other hand, the N1-Ru bond distance of 2.046 Å is slightly shorter than the corresponding bond in complexes **6** (2.053 Å) and **7** (2.056 Å) thus, indicative of comparable donation. This observation points at the nitrogen lone-pair in **8** not engaging in the aromatic  $\pi$ -system to a significant degree but being more engaged in  $\pi$ -donation towards the ruthenium center. This is also substantiated by the fact that the two phenylene units are non-coplanar. The geometry around the PNP-nitrogen in all the enamido complexes is planar and linearly coordinating to the ruthenium center (as represented in Figure 3.23a) and, thus, is in optimal conformation with respect to  $\pi$ -donation. This is, as mentioned, not the case in this diphenylene amido ligand.

The IR spectrum of **8** (Figure 3.26) shows two intense absorbances at 1725 and 1458 cm<sup>-1</sup> with the latter being the most intense. The highest energy absorption at 1825 cm<sup>-1</sup> is assigned to the  $\nu(\text{NO})$  mode. This resonance energy is lower than the corresponding vibration frequency for the enamido complex, **6** ( $\tilde{\nu}$  = 1780 cm<sup>-1</sup>) and, as such, is in support of the interpretation that the amido moiety in complex **8** is more  $\pi$ -donating, despite the fact that the amido nitrogen is in direct conjugation with the two aromatic systems, as was

<sup>‡</sup>  $-0.586x + 0.810y - 12.076 = 0$

<sup>§</sup>  $0.448x + 0.894y + 15.006 = 0$

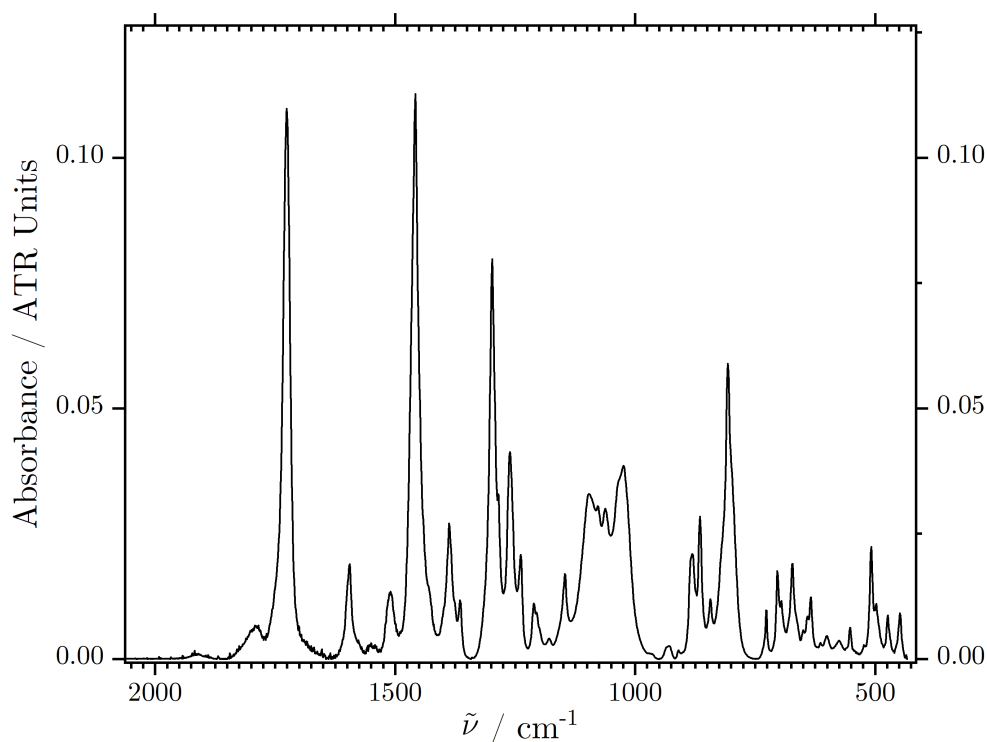


Figure 3.26: IR spectrum in the fingerprint region of complex **8** shows the strong absorption at  $1725\text{ cm}^{-1}$  as well as a another strong absorption at  $1458\text{ cm}^{-1}$  followed by a series of relatively strong bands associated with the aromatic rings.

understood on basis of the crystallographic model. Additionally, the spectrum clearly shows the intense bands in the region  $1460\text{ cm}^{-1}$  to  $1200\text{ cm}^{-1}$  associated with the aromatic rings.

The appearance of one singlet signal in the  $^{31}\text{P}$ -NMR spectrum supports the crystallographic model in which the phosphorus atoms are equivalent, thus, fluxionality in the solution phase does not impose magnetically non-equivalence with respect to the phosphine ligators.

### 3.7 Conclusions

Table 3.2 summarises the characteristic crystallographic and spectroscopic results outlined in this chapter. In addition, the structural similarities of the complexes **2** and **3** merit their inclusion in said table and, as such, some of their spectroscopic and crystallographic characteristics will be discussed in the light of the results presented throughout this chapter.

As mentioned previously, the geometry around the nitrosyl N atom is often used as a marker for the electronic structure of the ligand, and thus, the metal. As such, in the crystallography of such species, the M-N-O angle is often one of the first aspects of the geometry to be addressed. In this work, all proposed nitrosyl complexes have been characterised by single-crystal X-ray diffraction as well as IR- and multi-nuclear NMR

spectroscopy<sup>†</sup> and thus, provide high level details about the molecular structure and chemical behavior of said complexes. From the crystallographic models as well as the spectral characteristic of these complexes, it is possible to address the effective oxidation state of the ruthenium metal. As such, the complexes **1/1a**, **4**, **6** and **7** can all be regarded as ruthenium(II) complexes whereas **2**, **3** and **5** contains a ruthenium(0) centre. Interestingly, upon oxidation of complex **5** (enamido) to either **7** (peroxo) or **6** (iodido-methyl) the bond strength, indicated by the similar  $\nu(\text{C}=\text{C})$  resonance energy. This indicates that electronic delocalisation into the  $\text{C}=\text{C}$  double bond is, de facto, negligible in both Ru(0) and Ru(II) oxidation states of the enamido complexes. This interpretation contrasts the general understanding that ligand backbone dehydrogenation stabilises the amido lone-pair.<sup>241</sup> On the other hand, the amido-Ru distance clearly shows a strong influence of the vinyl entity: on going from **2** to **3** by simple deprotonation of the amine nitrogen the N-Ru distance decrease dramatically from 2.176 Å to 2.007 Å reflecting a significant double bond character. Upon dehydrogenation of the ligand backbone (that is going from **3** to **5**), the N-Ru distance increases significantly from 0.029 Å to 2.036 Å (please note that the oxidation state of ruthenium is invariant) thus a decrease in the amido  $\rightarrow$  Ru  $\pi$ -donation is expected, which is not reflected in  $\nu(\text{C}=\text{C})$ . In addition, the absorption energy of the  $\nu(\text{NO})$  mode reflects the N-Ru distances described above such that:  $\tilde{\nu}(\text{NO})$  increases in the order:

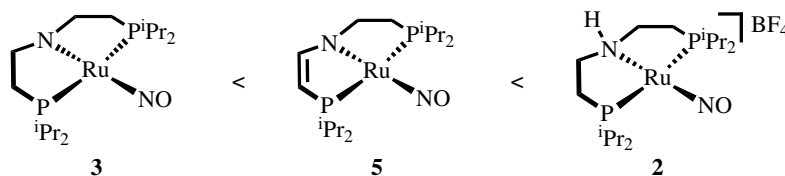


Figure 3.27: Schematic representation of the scale for increasing  $\nu(\text{NO})$  absorption energy among related square planar  $\text{Ru}^0$  complexes in this work.

This is expected on the basis of inferred  $\pi$ -donor strength of the amido nitrogen. On the contrary, the energy of the  $\nu(\text{C}=\text{C})$  mode does not serve as a reliable probe for the relative electron density of the central metal as small (but in contrast: significant) differences in the  $\text{C}=\text{C}$  bond length are not reflected in the IR vibrational frequency.

Unfortunately, it has not been possible to extract the  $^{15}\text{N}$  chemical shift for the NO ligand for all complexes with  $^1\text{H}-^{15}\text{N}$ -HMBC experiments however, for all of those complexes where possible (**1/1a**, **3**, **6**), the chemical shift value is in agreement with a linear  $\text{NO}^+$  ligand structure. On a different note, the  $\delta(^{15}\text{N})$  for the PNP ligand was obtained for all complexes (except **7**). These measurements show, that the magnitude of the value of  $\delta$  is diagnostic for coordinated amine vs coordinated amide with the former having values one order of magnitude larger than the latter.

In general, the NO vibrational frequencies measured in this work, are in the expected

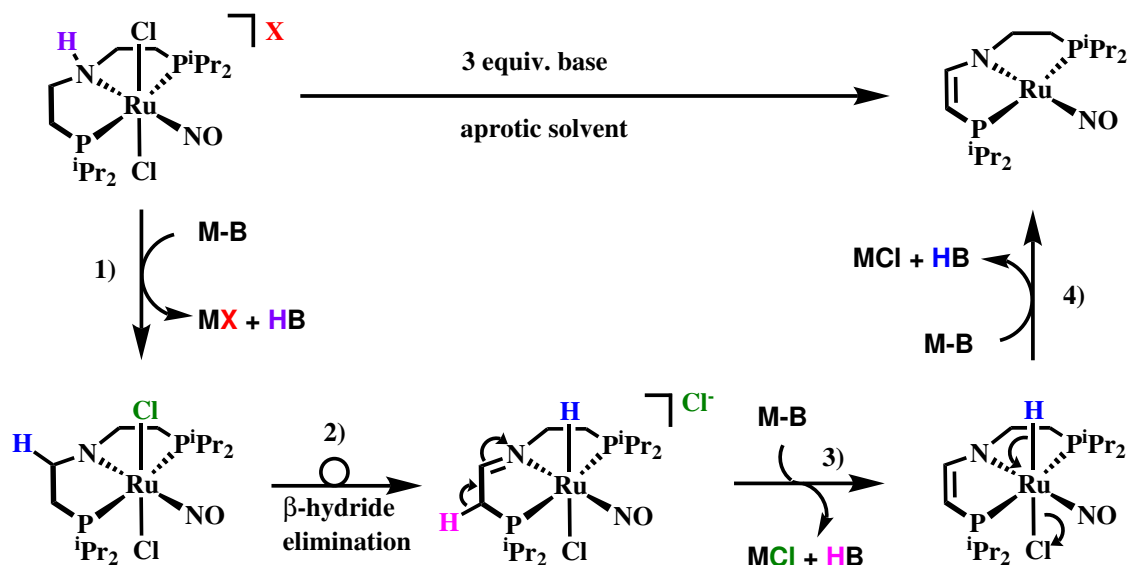
<sup>†</sup>Only the tetrazenido complex has been characterised by crystallography only.



range when compared to the solid phase structures. All NO frequencies of complexes of zero valent ruthenium are lower than for divalent ruthenium. It is noteworthy that the NO frequency in the diarylene complex, **8**, appears seemingly unaffected by the amido moiety in the *trans* position and the value ( $1825\text{ cm}^{-1}$ ) falls in between those for the parent complex, **1a**, and methyl complex, **4**, of  $1838\text{ cm}^{-1}$  and  $1815\text{ cm}^{-1}$  respectively. This result is highly surprising especially when considering the N-O bond length of  $1.166\text{ \AA}$  in the  $\text{Ru}^0$ -salt, **2**, which is comparable to  $1.167\text{ \AA}$  as observed in the enamido complex **6**. In this light, the high vibrational frequency observed for the diarylene species, **8**, may be due to protonation of the amido nitrogen by humid air. However, based on the fact that complexes comprising this ligand are almost exclusively isolated as amido species and protonation requires very strong acids (see discussion in Section 3.6), protonation by gaseous water at room temperature seem highly unlikely. Thus, it may be inferred that delocalisation of the nitrogen lone-pair is *not* distributed over *both* of the aryl ring systems at the same time.

The chlorido-hydrido complex presented in Section 3.5.2 exhibits a significantly long Ru-H bond length (IAM) which is surprising in the view of the fact that the relatively weak  $\sigma$ -donor in the *trans* position ( $\text{Cl}^-$ ) should not induce the hydride any significant hydricity as discussed in Chapter 2. The relatively low Ru-H vibrational frequency at  $1847\text{ cm}^{-1}$  is in support of the interpretation that the Ru-H distance must be rather long. Also, the long Ru-H distance is indicated by the comparably low-field hydride shift at  $-3.8\text{ ppm}$ . As was also described in Chapter 2, the M-H bond is very sensitive to, not only the *trans* ligand of which it is particularly sensitive, but also to the ligands residing in the equatorial plane. As such, PNP complexes of metal nitrosyls that exhibit a M-H bond can potentially be more finely tuned with respect to hydricity than the isoelectronic carbonyl congeners described in the aforementioned chapter.

Finally, formation of similar complexes to **5** is, to the extent of the knowledge of the author, unprecedented. The mechanism of formation is interesting as the reaction proceeds very fast (seconds) and represent a 2-electron reduction of the parent complex, **1/1a**, under seemingly redox-innocent conditions. It is known to literature, that imino ligands exhibit relatively acidic C-H bonds, and, thus can be deprotonated under the formation of the enamide.<sup>241,293</sup> As it was discussed in Section 3.5, the hydrido-chlorido complex is readily deprotonated at the metal and, as such, the metal undergoes a 2-electron reduction. In addition, a 6-coordinate enamido species (presumably ruthenium(II)) could be isolated from a reaction mixture with a 1:1 ratio of **1a** and  $\text{KO}^t\text{Bu}$  in THF. Unfortunately, the reaction product decomposes fast and is notoriously difficult to obtain in the solid state (see crystallographic model in Appendix C). The mechanism behind the formation of PNP-enamido complexes without change in metal oxidation state is known to literature.<sup>294</sup> Based on these observations, the mechanism for the formation of **5** is proposed in Scheme 3.6 below: 1) deprotonation of the amine moiety to yield a transient amido species. 2)  $\beta$ -hydride elimination from the amine  $\alpha$ -carbon, probably with prior dissociation of one of the chlorido

Scheme 3.6: Proposed mechanism for the formation of complex **5**.

ligands, results in a hydrido-chlorido imino complex of ruthenium(II). This is followed by 3), deprotonation of the imino- $\alpha$ -proton results in an enamido hydridochlorido ruthenium(II) complex that under, 4), deprotonation at the metal center undergo a 2-electron reduction with concomitant elimination of the chlorido ligand results in the formation of complex **5**. Based on the findings in this work, it is clear that it is not possible to irrefutably conclude whether the metal centered deprotonation happens before- or after deprotonation of the imino-PNP backbone.

Table 3.2: Summary of geometric and spectroscopic characteristics for the complexes **1a** - **8**.

Metric	1a	2	3	4	5	6	7	8
<b>Bond lengths / Å</b>								
N-O	1.134	1.179	1.187	1.149	1.173	1.167	1.176	1.166
Ru-NO	1.754	1.719	1.752	1.734	1.746	1.738	1.758	1.752
(PNP)N-Ru	2.150	2.176	2.007	2.165	2.036	2.053	2.056	2.046
X1-Ru	2.377	-	-	$\begin{cases} 2.798, \\ \text{X1=I} \end{cases}$	-	$\begin{cases} 2.844 \\ \text{(X1=I)} \end{cases}$	1.979	2.390
X2-Ru	2.366	-	-	$\begin{cases} 2.149, \\ \text{X2=Me} \end{cases}$	-	$\begin{cases} 2.235 \\ \text{(X2=Me)} \end{cases}$	2.027	2.390
HC=CH	-	-	-	-	1.361	1.342	1.352	-
N-(CH)2	-	-	-	-	1.374	1.338	1.344	1.397
N-(CH2)2	-	-	-	-	1.449	1.449	1.455	-
<b>Bond angles / °</b>								
Ru-N-O	178.04	177.56	179.86	177.95	178.09	177.92	171.62	180.00
N-Ru-NO	178.02	177.00	177.95	175.34	177.74	178.62	108.23	180.00
P-Ru-P	162.60	163.27	164.08	163.00	162.81	161.43	160.05	159.88
X1-Ru-X2	171.77	-	-	170.56	-	173.12	42.18	176.78
<b><math>\delta^{31}\text{P}</math> / ppm</b>								
P-(CH)2	-	-	-	-	73.5	64.6	58.6	56.3 <sup>a</sup>
P-(CH2)2	68.0	56.9	89.0	62.2b / 62.0c	84.9	69.5	63.1	-
<b><math>\delta^{15}\text{N}</math> / ppm</b>								
<sup>15</sup> NO	372	-	388.9	369 <sup>b</sup> / 370 <sup>c</sup>	-	382.2	-	-
P <sup>15</sup> NP	67.8	75.5	159.5	54 <sup>b</sup> / 51.6 <sup>c</sup>	163.9	154.5	-	144.6
<b><math>\tilde{\nu}</math> / cm<sup>-1</sup></b>								
$\nu(\text{NO})$	1838	1737	1666	1815	1690	1790	1721	1825
$\nu(\text{HC=CH})$	-	-	-	-	1533	1532	1533	1458

<sup>a</sup> Here the  $\delta(^{31}\text{P})$  represents the two equivalent phosphine groups on the arylene backbone of the PNP ligand.<sup>b</sup> chemical shift for isomer 1.<sup>c</sup> chemical shift for isomer 2.

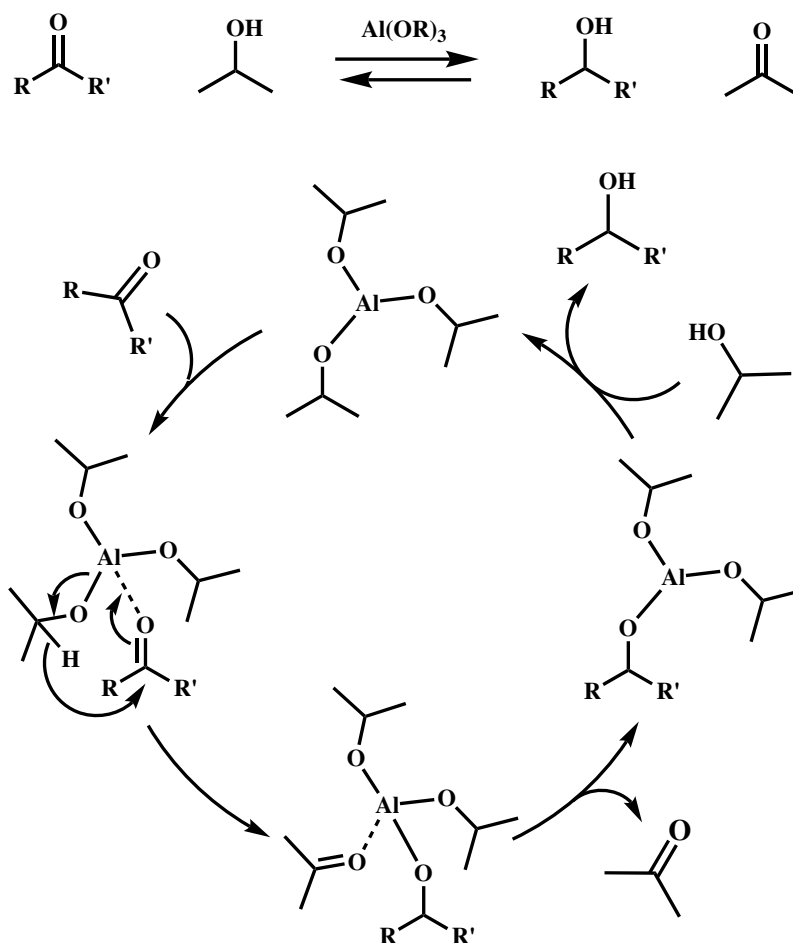
## Chapter 4

# Catalytic transfer hydrogenation

In comparison with heterogeneous catalysis, homogeneous catalysis has often proved inferior with respect to catalytic activity, stability and isolation and purification of the catalyst<sup>295</sup> which makes heterogeneous catalysis the most prominent in industrial applications. However, the Grubbs- and Schrock Ru/Mo-carbene systems for olefin metathesis reaction, Ziegler-Natta polymerisation, Noyori asymmetric hydrogenation, Knowles synthesis of the L-DOPA molecule used in the treatment of Parkinson's disease represent important examples of homogeneous catalytic processes that have found way to industry<sup>296-299</sup> and their importance have been cemented by the Nobel Committee.<sup>300-304</sup>

In the mid 20<sup>th</sup> century, Bradue and Lindstead<sup>305</sup> divided the term "hydrogen transfer" into three sub categories: (A) hydrogen migration (transfer within one molecule); (B) hydrogen disproportionation (transfer between identical donors and acceptors); (C) transfer-hydrogenation (TH) (transfer between unlike donors and acceptors) of which the last term is by far the most important and, thus, is also the main topic of the present chapter. The pioneering works of the 1960's and 1970's chemists developed ruthenium and iridium catalysed TH reactions and, as such, sparked the research in mid-to-late transition metal catalysis of the reduction of unsaturated ketones in the presence of isopropanol.<sup>306-310</sup> It was later found, that upon addition of NaOH as sacrificial agent, the rate of the TH reaction increased several orders of magnitude.<sup>311</sup>

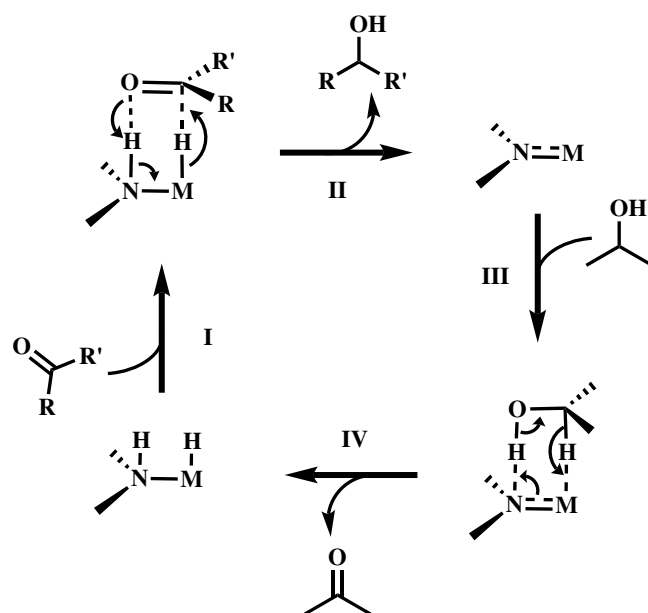
The most renowned TH reaction is probably the Meerwein-Ponndorf-Verley (MPV) reduction in which a ketone is reduced to its corresponding alcohol in conjunction with oxidation of the sacrificial alcohol that function as hydrogen donor as shown in Scheme 4.1<sup>312</sup> which, in turn, was the first TH reaction of carbonyl compounds and was traditionally catalysed by aluminium alkoxides.<sup>313</sup> The reverse reaction was studied by Oppenauer and, thus, called "Oppenauer oxidation".<sup>314,315</sup> Hydrogenation of polar bonds such as carbonyl groups in organic synthesis is industrially important and "green" approaches for such transformations are, thus, highly welcome.<sup>316</sup> Isopropanol has advantageous properties as hydrogen source in hydrogenation reactions such as it is stable, easy to handle as it is liquid at rt, environmentally benign, non-toxic and cheap. In addition, the dehydrogenated



Scheme 4.1: Meerwein-Ponndorf-Verley reaction mechanism.

side product, acetone, can be distilled off during the reaction thus, drag the chemical equilibrium towards product formation.

In these reactions, amine based ligands have proven especially useful in catalyst design.<sup>200,317,318</sup> In this regard, PNP pincer complexes have been a natural extension of the ligand library as they show high thermal/kinetic stability and easily tunable electronic- and geometrical structure<sup>27</sup> and is most often thought to operate through a so-called *outer-sphere* mechanism (not to confuse with electron transfer reactions)<sup>319,320</sup> as described schematically below (Scheme 4.2): Starting from an amino-hydrido species (I), a nucleophilic attack of the hydrido ligand to the carbonyl carbon atom on the substrate, as such, pre-coordination of the substrate in the second coordination sphere is followed by concerted<sup>321</sup> heterolytic (proton-hydride) hydrogen transfer from the metal complex to the substrate. The hydrogenated product is generated in step II. An amido complex which, in III, is hydrogenated by the sacrificial alcohol (here: isopropanol) through hydrogen bonding and C-H...M interaction followed by de-coordination of the generated acetone in IV convolutes the catalytic cycle. Similar metal-ligand-cooperation reactivity, through aromatisation-dearomatisation of pyridine based PNP pincer ligands, have been observed by Milstein and co-workers.<sup>322</sup>



Scheme 4.2: Simplified illustration of metal-ligand cooperation in transfer-hydrogenation catalysis.

As much as carbonyl complexes of ruthenium play a significant role in homogeneous catalysis, isoelectronic nitrosyl complexes have not yet benefitted from as much experimental or theoretical attention. In general, the role of transition metal nitrosyl complexes has, so far, held little interest in homogeneous catalysis despite the "catalytic" effect of NO in the historically important "lead chamber process" where  $\text{NO}_x$  oxidising  $\text{SO}_2$  to  $\text{SO}_3$  and  $\text{H}_2\text{SO}_4$  in moist air was recognised already in the mid 18<sup>th</sup> century.<sup>323,324</sup> Interestingly, ruthenium catalysts involving non-innocent ligands are no new phenomenon; however, the non-innocent ligands used are vastly represented by aromatic ligands such as 2,2':6',2''-terpyridine, catecholates and anthracenes<sup>325,326</sup> but the archetype of non-innocent ligands (read: nitrosyl) as ancillary ligand in catalytic systems are comparatively rare.

In this context, direct hydrogenation using nitrosyl complexes is more developed (albeit still in its infancy) than transfer hydrogenation systems. Works on the direct hydrogenation of imines using molybdenum complexes<sup>327</sup> have been reported but of more interest to the work presented in this thesis are the low valent  $d^6$  mono nitrosyl complexes of rhenium(I), shown in Figure 4.1. This class of complexes, which are isoelectronic to ruthenium(II) carbonyl compounds)

have shown effective in both dehydrogenation of aminoborane and transfer hydrogenation of olefins using aminoborane as hydrogen source.<sup>328,329</sup> The amount of pincer complexes of metal nitrosyls is surprisingly small and their synthesis and distinct physico-chemical properties are covered in a recent review by Doctorovich and co-workers.<sup>330</sup> Due

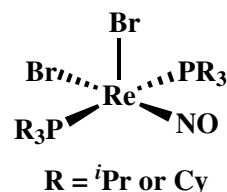


Figure 4.1: Berke's rhenium(I) complexes used in (de)hydrogenation reactions with amino borane as hydrogen source.

to the very small amount of pincer complexes exhibiting the metal-nitrosyl entity, the reports on their use in catalysis are naturally unexplored. However, chromium(I) and iron(I) complexes have shown useful in hydrosilylation of ketones and dehydrogenative reductive amination of alcohols respectively, as reported by Kirchner *et al.*<sup>331,332</sup> In addition, nitrosyl-cobalt(III) has been shown to work efficiently in alkene- and nitrile hydroboration.<sup>333,334</sup> It was in this context shown computationally that interconversion of nitrosyl geometry (linear  $\longleftrightarrow$  bend) was crucial for catalyst activity as was also shown experimentally for the non-pincer type complex  $\text{Re}(\text{H}_2)\text{I}_2(\text{PMe}_3)_2(\text{NO})$  and in this work coined as "the catalytic nitrosyl effect".<sup>335</sup>

Similar isoelectronic PNP pincer complexes exhibiting *trans*-dihydrido ligation as shown in Figure 4.2. This complex was reported by Chualet *et al.* and was tested in the catalytic transfer hydrogenation (TH) reaction of acetophenone and cyclohexanone using isopropanol as hydrogen source. Their findings showed that at catalyst loading of 4 mol% the conversion of acetophenone reached 50% in 1 h (unfortunately, the reaction temperature was not reported).

The poor activity was attributed to catalyst degradation caused by the solvent, isopropanol.

In the present work, catalytic activity of the  $[(^i\text{Pr}_2\text{PNP})\text{RuCl}_2(\text{NO})]\text{Cl}$  compound in TH reactions of acetophenone as benchmark substrate using isopropanol as hydrogen source will be presented. This work has been done in close collaboration with postdoc Dr Danielle Nielsen who is the *primus motor* of the catalytic studies. As such, selected results and not the full "catalytic picture" will be presented in this thesis.

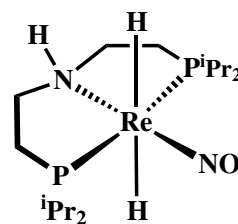


Figure 4.2: *Trans*-dihydrido nitrosyl complex of rhenium(I) used in catalytic TH of ketones with isopropanol as  $\text{H}_2$ -source.

## Results and discussion

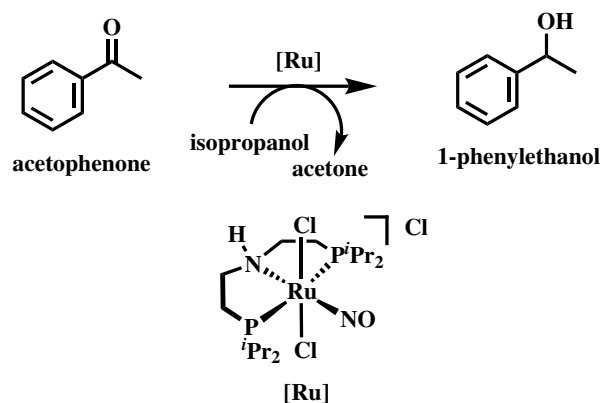


Figure 4.3: Representative reaction scheme for the TH reactions presented in this thesis.

Table 4.1 summarises the most important optimisation reactions. The reaction did not proceed without base. The transfer hydrogenation of acetophenone in isopropanol could be conducted at rt when using potassium KO<sup>*t*</sup>Bu. Albeit, a reaction time far beyond 4 h was needed to reach a conversion of 90%.

Table 4.1: Selected list of conditions used in the optimisation process using 1.3 mmol acetophenone and 3 mL isopropanol as solvent to 0.5 mole [Ru] relative to substrate.

Entry	Base (mol%)	Reaction time	Temperature	Conversion / %
1	LiOH (10)	3 h	rt	< 5
2	LiOH (10)	4 h	rt	< 5
3	KOH (10)	3 h	rt	< 5
4	LiO <sup><i>t</i></sup> Bu (10)	3 h	rt	< 5
5	KO <sup><i>t</i></sup> Bu (10)	2 h	rt	21
6	KO <sup><i>t</i></sup> Bu (10)	3 h	rt	28
7	KO <sup><i>t</i></sup> Bu (10)	4 h	rt	62
8	KO <sup><i>t</i></sup> Bu (10)	18 h	rt	90
9	KO <sup><i>t</i></sup> Bu (10)	90 min	90 °C	97
10	LiO <sup><i>t</i></sup> Bu (10)	90 min	90 °C	94
11	KOH (10)	90 min	90 °C	95
12	KOH (10)	30 min	90 °C	74
13	LiOH (10)	30 min	90 °C	33
14	NaOH (10)	30 min	90 °C	96
15	NaOH (10)	1 min	90 °C	49
16	NaOH (10)	5 min	90 °C	92
17	NaOH (5)	5 min	90 °C	70
18	NaOH(15)	5 min	90 °C	88
19	NaOH (20)	5 min	90 °C	90



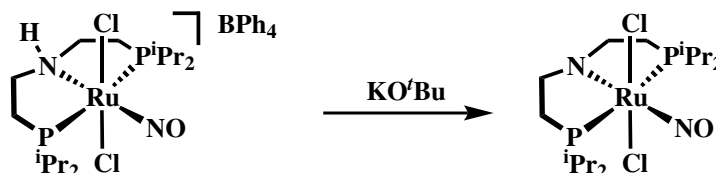
It is interesting to take note of that when using  $\text{LiO}^t\text{Bu}$  no significant reduction of acetophenone could be detected within 3 h reaction time as compared to 28% conversion when using  $\text{KO}^t\text{Bu}$  (Entry 4 and 6). Increasing the temperature to 90 °C conversion rates (90 min) and yields (94% and 97%) were significantly improved when using lithium- or potassium *tert*-butoxide respectively (Entry 9 and 10). Using KOH as base, similar conversions could be reached.

Interestingly, the high conversion reached by KOH and NaOH could not be matched when using LiOH. This points at the solubility of the alkali metal chloride supposedly formed in the reaction is having a negative impact on the reaction such that precipitation of KCl or NaCl function as beneficial for the TH reaction while having LiCl in solution is detrimental possibly because coordination-decoordination of chloride to the catalyst is a competing reaction generating catalytically inactive mono- and/or dichlorido complex(es). As can be seen in Table 4.1, NaOH gave the highest conversions. Even at only 1 min reaction time nearly half of the acetophenone was reduced. Increasing the amount of base did not provide any significant improvements on the conversion rate but decreasing the amount of base to 5 mol% (Entry 17) caused a decrease in conversion by more than 20%.

Table 4.2: Induction times. Conditions: 1.3 mmol acetophenone, 10 mol% NaOH, 15 min reaction time after added substrate. Temp: 90 °C.

Induction time / min	conversion / %
0	13
5	95
10	97

It was speculated whether the catalytically active species could be formed prior to reaction with the substrate and, as such improve the rate of the catalytic reaction. As such, by stirring the pre-catalyst and base in isopropanol at 90 °C for 0, 5 and 10 min respectively before adding the substrate it was found that an induction time to allow for the complex and base to react was indeed beneficial for the reaction rate, as can be seen in Table 4.2. The reaction between NaOH and [Ru] was not further investigated. That being said, based on other (to this unrelated) attempts to isolate the deprotonated species presumably formed when 1 equivalent of base reacted with the complex [Ru] might point at a metal alkoxide species.



Scheme 4.3: Schematic representation of the assumed reaction between the parent *trans*-dichlorido complex cation with 1 equiv. of non-coordinating base.

This reaction (Scheme 4.3) needs to be conducted under strict inert conditions and at −40 °C under which conditions a blood red solution forms. This solution changes colour to black along with dark brownish or black precipitate when allowed to warm to −15 °C. Attempts to isolate the blood red species as well as spectroscopic character-

isation was not successful due to its intrinsic instability. The instability of the blood red solution was interpreted as a consequence of high reactivity caused by a very chemically active amido lone pair. As such, degassed water (excess) was added to the cold reaction mixture whereby the colour changed to orange-yellow and a white precipitate formed. After cold filtration and vapour diffusion of hexane (rt) into the cold solution ( $-40^{\circ}\text{C}$ ) orange cuboid crystals were obtained. Unfortunately, these crystals were, as the initial red solution, thermally unstable and decomposed rapidly at rt. This made the harvesting and mounting especially challenging. Additionally, the crystal disintegrated during the measurement, thus, only a very weak dataset could be obtained. The dataset, allows for crystallographic interpretation but only at an indicative level. Figure 4.4 shows the weak crystallographic model obtained from the diffraction experiment. Unfortunately, only atoms heavier than nitrogen (besides the nitrosyl N atom) allowed for anisotropic refinement. The model complex is associated with the  $\text{BPh}_4^-$  anion (left out for clarity), thus, the white precipitation that was observed upon addition of water most likely consist of KCl. As illustrated in Figure 4.4, the N-H bond is elongated as a consequence of intramolecular hydrogen bonding with the hydroxido ligand and co-crystallised THF. The NO ligand is positioned *trans* to the hydroxido ligand, in accordance with stabilisation of  $\pi\text{O} \longrightarrow \pi\text{Ru}$  interaction. Given the weak nature of the dataset it is interesting that the N-H and O-H protons were directly observed in the difference Fourier map. This observation may point at the active species being a hydroxido species, or most likely, a mixture of isopropoxido and hydrixido species. It is, nevertheless, obvious, that more detailed studies need to be conducted to reveal the true identity of the catalytic species.

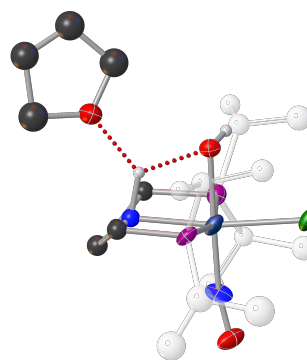


Figure 4.4: Crystallographic indication of a hydroxido species. The  $\text{BPh}_4^-$  counterion and all hydrogens on carbon atoms have been omitted for clarity. Thermal ellipsoids on Ru, (NO), Cl, O and P atoms are plotted at 30% probability level. All other atoms were refined isotropically.

#### 4.0.1 Aesthetic but arid: A *trans*-diacetato complex

As indicated *a priori*, the TH reaction presented in this work is dependent on the presence of base; However, the development of TH-catalysts and direct hydrogenation catalysts that are highly active without the addition of base have gained much attention in recent years.<sup>336–349</sup> In this spirit, the chlorido ligands associated with the pre-catalyst were exchanged with the basic acetate ligands. Dissociation of acetate ligands would then increase the pH of the reaction solution as if alkaline additives were added (albeit not to the same extent). Unfortunately, this complex was inactive both under additive-free conditions and when base was

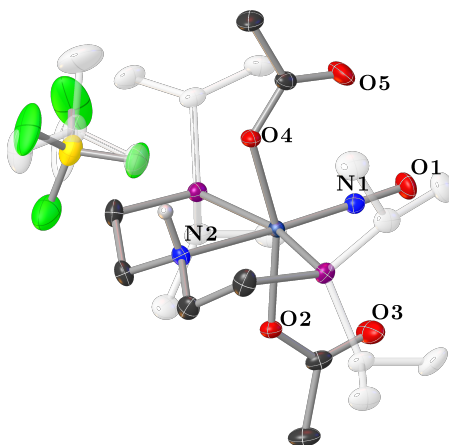


Figure 4.5: Crystal structure of the diacetato complex. Disorder in the anion and isopropyl substituents on phosphorus have been ghosted out and all hydrogens on carbon atoms have been omitted for clarity. Thermal ellipsoids are plotted at 50% probability level.

present.

The diacetato complex is shown in Figure 4.5 above. Unfortunately, the anion is disordered over two positions. The cation can be regarded as a geometrically distorted octahedral ruthenium complex. The two acetato ligands are coordinated *trans* with respect to one another. As such, the NO ligand and the PNP ligands constitute the basal plane. Both acetato ligands are coordinated in a mono-dentate manner and are almost equidistant to the central ruthenium atom (Ru-O4: 2.0497 Å; Ru-O2: 2.0443 Å). Both acetato ligands are co-linear with the NO ligand. The Ru-N-O bond angle of 178.84° is, thus, close to linear and, together with the very short N-O distance of 1.148 Å, is in agreement with an N≡O<sup>+</sup> ligand structure. The Ru-NO distance of 1.748 Å is in close agreement with the other Ru<sup>II</sup>-NO distances presented throughout this thesis. Unlike related mono-acetato- and formato complexes,<sup>161,350,351</sup> the carboxylate ligands presented here are not engaged in hydrogen bonding to the amine-proton which has been targeted as a detrimental interaction in dehydrogenation catalysis.<sup>352,353</sup>

Table 4.3: Self-diffusion coefficients (SDF) determined by DOSY NMR in THF at 25 °C.

Species	SDF / m <sup>2</sup> s <sup>-1</sup>
anion	8.61e <sup>-10</sup>
cation	8.57e <sup>-10</sup>
THF-d <sub>8</sub>	2.30e <sup>-9</sup>

To gain insight in whether the carboxylates were engaged in an intramolecular N-H...OAc interaction the diffusion constants for the cation and anion (in THF) was determined with DOSY NMR. It was hypothesised, that potential H-bonding to the amine via the carboxylates would cause different diffusion rates between the ion-pairs in solution, if the anion was responsible for the conformation of the carboxylates (read: N-H...F-BF<sub>3</sub> hydrogen bonding in the solid state). The calculated diffusion coefficients are given in Table 4.3. The diffusion coefficients for the ions are very similar with the cation having a slightly lower diffusion rate. This points towards a relatively high degree of co-diffusion/ion-pairing. The IR spectrum of the titled compound, shown in Figure 4.6 reveals the  $\nu(\text{NO})$  mode

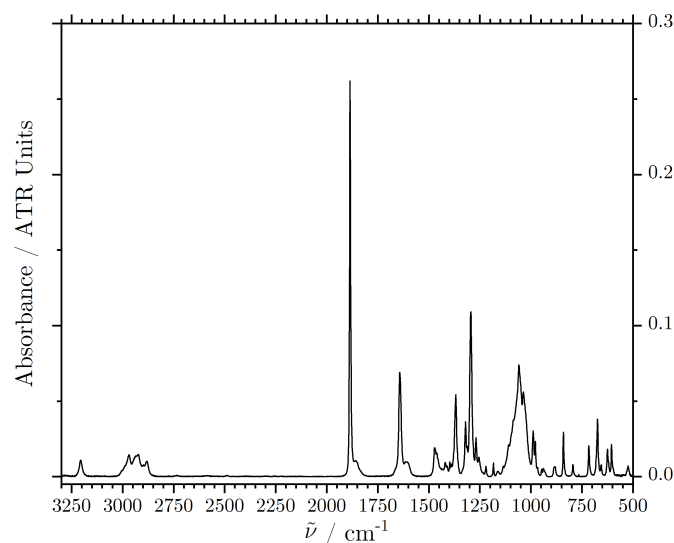


Figure 4.6: IR spectrum of the diacetato complex shown in Figure 4.5.

as a sharp, intense band at  $1886 \text{ cm}^{-1}$ . This high-energy absorption is in support of the interpretation of the crystallographic model of the NO ligand having a linear Ru-N-O with a significant  $\text{N}\equiv\text{O}$  triple bond character. The intense band at  $1642 \text{ cm}^{-1}$  is assigned to the  $\text{C}=\text{O}$  stretching mode which is  $58 \text{ cm}^{-1}$  higher than the corresponding absorption in sodium acetate.<sup>354</sup> The spectrum features the characteristic broad absorption from the  $\text{BF}_4^-$  counterion at  $1260 \text{ cm}^{-1} - 970 \text{ cm}^{-1}$  and the NH stretching mode at  $3207 \text{ cm}^{-1}$ . The very well-defined bands are in agreement with the sample being of high purity.

## 4.1 Conclusions

The catalytic activity of the chloride salt  $[(^i\text{Pr}_2\text{PNP})\text{RuCl}_2(\text{NO})]\text{Cl}$  in the reductive TH reaction of acetophenone using isopropanol as substrate has been demonstrated based on a selection of results. In respect, the author has chosen to leave out the greater substrate scope but it shall be mentioned that a plethora of ketones and aldehydes are currently being investigated, by Dr Danielle Nielsen, as substrates as well as many of the nitrosyl complexes being tested for catalytic activity with interesting results. It has been shown here, that the [Ru] catalyst exhibits excellent catalytic activity at low temperatures (rt to  $90^\circ$ ). Good conversion yields can be reached within few minutes by the application of NaOH as sacrificial agent. The reaction is sensitive to air and, hence, must be loaded and conducted under inert atmosphere. Crystallographic indications of the formation of highly unstable hydroxido species in degassed water point towards analogous alkoxido species playing a crucial role in the catalytic cycle (although more studies need to be conducted for irrefutable conclusions). Experiments aimed to test the longevity of the catalyst have not been undertaken but will serve as a natural outlook, as so, characterisation of the catalytically active species through stoichiometric studies is highly appealing. In an

attempt to design a catalyst which would reveal activity under additive-free conditions, a diacetato analogue of [Ru] ( $[(^1\text{Pr}_2\text{PNP})\text{Ru}(\text{OAc})_2(\text{NO})]\text{BF}_4$ ) was synthesised by simple chloride abstraction with silver(I) acetate in acetonitrile and characterised by single-crystal X-ray diffraction and IR spectroscopy. A satisfying level of purity was confirmed with elemental analysis and supported by IR spectroscopy. DOSY NMR revealed a large degree of co-diffusion of the ion pairs in the diacetato complex which indicates that the observed solid phase structure represents the main structure in the solution phase.

## Chapter 5

# The structure of the ruthenium-MACHO catalyst

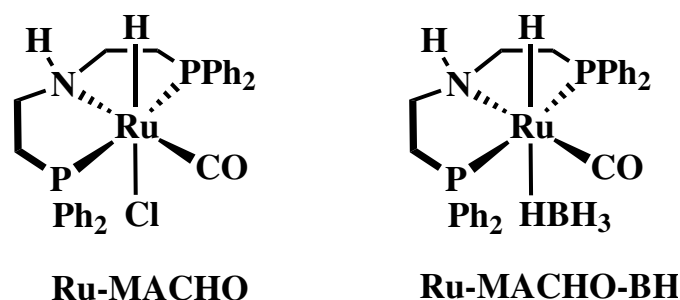


Figure 5.1: Structure of the Ru-MACHO and Ru-MACHO-BH catalysts.

The catalyst commercially known as "Ruthenium-MACHO", or just, "Ru-MACHO" and the related Ru-MACHO-BH (Figure 5.1), was first reported by the Takasago chemists Wataru Kuriyama and co-workers as highly active ruthenium based catalyst for ester reductions under mild reaction conditions.<sup>355</sup> Since then, a large number of reports on the catalytic versatility of these complexes have been communicated which includes hydrogenation of CO<sub>2</sub>,<sup>356–358</sup>  $\beta$ -methylation of alcohols,<sup>359</sup> acceptorless dehydrogenation of methanol,<sup>360</sup> cross-coupling of secondary alcohols to  $\alpha$ -substituted ketones<sup>361</sup>, hydrogenation of  $\alpha, \beta$ -unsaturated carbonyl compounds<sup>362</sup> and formation of  $\gamma$ -valerolactone from neat ethyl levulinate<sup>363</sup> and in reductive amination in isopropanol<sup>364</sup> is just a small representative of reactions where this class of compounds have been utilised as highly efficient catalysts. Despite the fact that the MACHO-systems presented in Scheme 5.1 above have been utilised to an extreme extent the in-depth characterisation of these systems remains. As is clear, the level of integrity of a compound is limited to the amount of characteristic data available. For those chemists who have worked with the Ru-MACHO system the distinct physical appearance of the off-white powder is striking: Sticky and non-crystalline (or extremely micro crystalline). This is in sharp contrast to the very well defined analogues that only differ in having isopropyl substituent on the P-ligands<sup>159,216</sup> which appear as

well defined, non-sticky and clearly crystalline products. Also, MACHO is not stable under basic conditions (under which the vast majority of reactions are conducted) and has been shown to decompose into several different compounds of which some do also show catalytic activity.<sup>244</sup> As such, it seems ambiguous to declare "Ru-MACHO a catalyst" the amount of characteristic data available do not hold sufficient gravity for irrefutable conclusions, hence, it is of great industrial and scientific interest to elucidate the structure of these catalysts as such species should be well-defined for accurate data acquisition on catalytic systems. In the following, spectroscopic characterisation of the Ru-MACHO compound as well as its crystal structure will be presented.

## 5.1 Results and discussion

In the work of identifying the optimal crystallisation conditions, it became clear, that the solubility profile of Ru-MACHO is highly disadvantageous as the compound is only little soluble in many common laboratory solvents such as alcohols, aromatics, THF and acetonitrile. This observation may hold relevance for catalytic systems conducted in these solvents as complex solubility is ought to influence catalytic activity. Upon dissolution of Ru-MACHO in chloroform the solution showed yellow discolouration, as opposed to all other solvents mentioned above. This led to the anticipation that Ru-MACHO undergoes reactions with chloroform. In this regard, the  $^1\text{H}$ -NMR spectra in  $\text{CDCl}_3$  was compared to the  $^1\text{H}$ -NMR in toluene- $d_8$  (where the solution remained colourless). Figure 5.2 shows

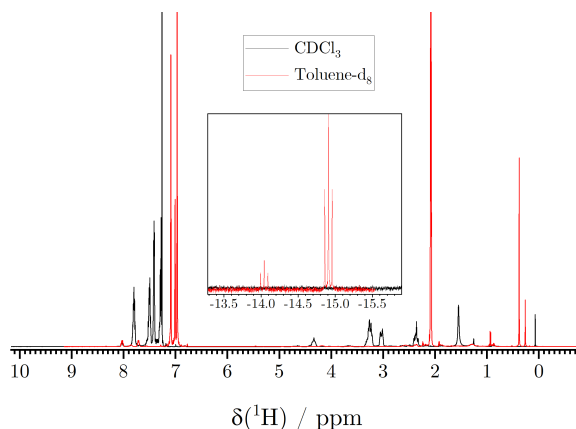


Figure 5.2: Overlay of the  $^1\text{H}$ -NMR spectra of Ru-MACHO measured in  $\text{CDCl}_3$  (black) and toluene- $d_8$  (red).

the difference between the  $^1\text{H}$ -NMR spectra of Ru-MACHO when measured in chloroform (black line) and in toluene (red line). Most importantly, the insert shows two hydride peaks as triplets at  $-14.04$  ppm and  $-14.91$  ppm with  $J = 20.1$  Hz and  $J = 19.8$  Hz respectively and in line with a statistical distribution of *syn* and *anti* isomers in solution and the hydrido ligands is coordinated mutually *cis* to the phosphine ligands. The figure clearly shows, that the hydrido entities being lost in chloroform thus pointing at this solvent not being chemically innocent towards the Ru-MACHO complex. It is interesting to note, that

the spectrum appears more coherent and ordered in chloroform as compared to toluene. This points at one major species being formed upon dissolution in chloroform. This is further supported by comparison with the  $^{31}\text{P}$ -NMR spectra (see Appendix E). The IR

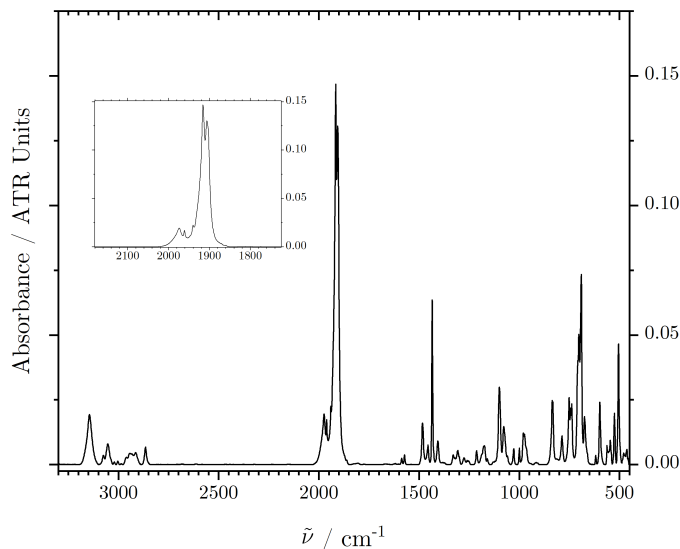


Figure 5.3: IR spectrum of the commercially available (Sigma-Aldrich) Ru-MACHO complex. The inset clearly show two different  $\nu(\text{CO})$  modes and at least two  $\nu(\text{Ru-H})$  modes.

spectrum of the Ru-MACHO complex is shown in Figure 5.3. Two strong absorption bands can be assigned to the  $\nu(\text{CO})$  stretching mode at 1915 and 1906  $\text{cm}^{-1}$  respectively as well as two bands may be assigned to the  $\nu(\text{RuH})$  mode at 1961 and 1974  $\text{cm}^{-1}$ . This observation suggests that more than one carbonyl and hydrido species may be represented in the powder. In addition, only one, sharp absorption appears for the N-H stretch 3144  $\text{cm}^{-1}$ . Two carbonyl stretching frequencies have previously been reported in works by Zhang *et al.*<sup>216</sup> They observed  $\tilde{\nu} = 1917$  and  $\tilde{\nu} = 1907$   $\text{cm}^{-1}$  respectively but only one Ru-H stretch at  $\tilde{\nu} = 1961$   $\text{cm}^{-1}$  and one N-H stretch at  $\tilde{\nu} = 3141$   $\text{cm}^{-1}$ . As such, the results presented here are in somewhat agreement with literature values despite of the fact, that two Ru-H frequencies are observed in this work.

### Decomposition product in chloroform

As it was shown above, the hydride signal disappears upon dissolution of Ru-MACHO in chloroform along with a colour change of the solution from colourless to bright yellow. Disappearance of the hydride signal is well in line with the common understanding that metal hydrides react with chlorinated solvents to give metal chloride species and (in case of chloroform) dichloromethane.<sup>365,366</sup> A crystal was grown from the chloroform reaction mixture by simply dissolution of  $\sim 25$  mg Ru-MACHO (Sigma-Aldrich) in 0.5 mL chloroform under ambient conditions. Diethyl ether was allowed to diffuse into the bright yellow solution at rt whereby high quality crystals suitable for single crystal X-ray diffraction could be harvested in a remarkably high yield of 86% thus reflecting high



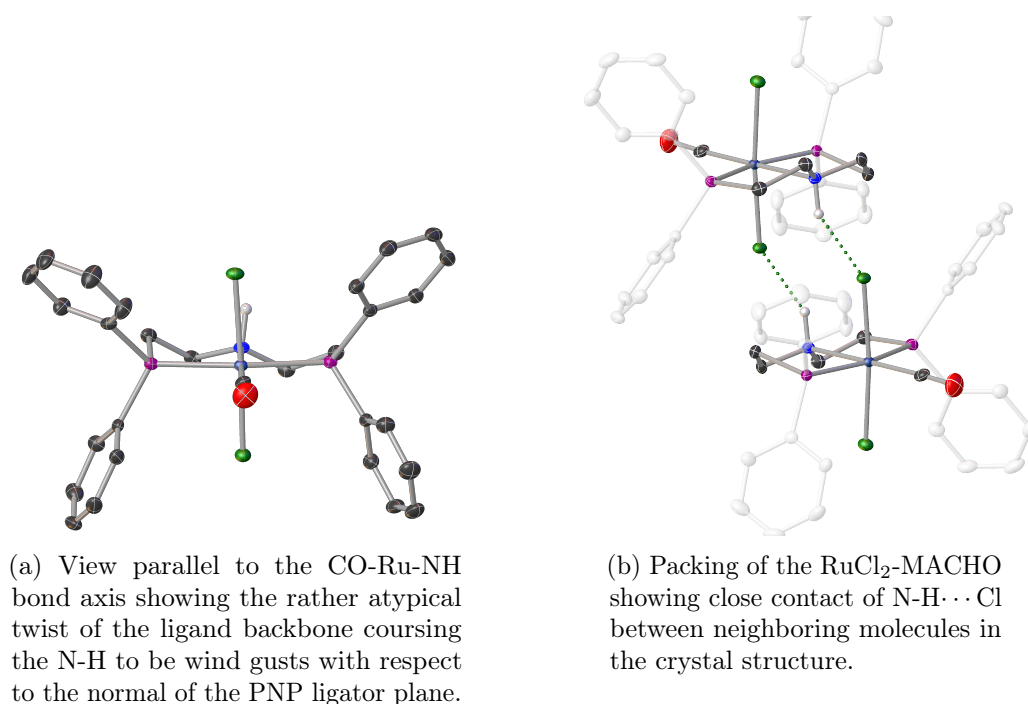


Figure 5.4: Crystal structure of the RuCl<sub>2</sub>-MACHO obtained from the reaction between commercial Ru-MACHO and chloroform under ambient conditions. All hydrogen atoms on carbon atoms have been omitted for clarity. Thermal ellipsoids are plotted at 50% probability level.

completeness of the reaction. The compound RuCl<sub>2</sub>-MACHO shown in Figure 5.4 above crystallises as yellow orthorhombic blocks in the space group  $P2_1/n$ . The Ru-C-O bond angle of  $176.1^\circ$  is close to linear and the very short C-O bond length (1.118 Å) indicate triple bond character. The Ru-Cl distances are almost identical with  $\text{Cl}_{syn} = 2.405 \text{ Å}$  and  $\text{Cl}_{anti} = 2.391 \text{ Å}$ . The Ru-P distances are also slightly different to one another: 2.3365 Å versus 2.3494 Å. As indicated in Figure 5.4a the ligand backbone is slightly twisted coursing the N-H bond to be skewed relative to the Ru-Cl axes. The Geometry can be regarded as a distorted octahedron. The symmetry can be regarded as  $C_s$ ; however, the tilted backbone effectively reduces the symmetry to  $C_1$ . The individual molecules in the crystal exhibit close contact with one another, as indicated in Figure 5.4b with the symmetry related distances of  $\text{Cl} \cdots \text{H-N} = 2.261$  ( $\text{Cl} \cdots \text{N(H)} = 3.149$ ).

### Structure of Ru-MACHO

Based on the results described above it was realised that a suitable crystal of the Ru-MACHO had to be grown from a more chemically inert solvent than chloroform (most likely any chlorinated solvent would have the same outcome). As mentioned, the solubility profile of Ru-MACHO in common innocent solvents are disadvantageous, that is, very low solubility. As there are no reports on Ru-MACHO reacting with dimethylsulfoxide (DMSO) this was chosen as the solvent as the complex shows good solubility in this solvent. Tests of precipitants (Et<sub>2</sub>O, dioxane, ethanol, methanol, *tert*-butylmethylether (TBME)) on a solutions of 10 mg complex in 0.3 mL solvent revealed Et<sub>2</sub>O and TBME as most effective.

TBME was chosen as precipitant in the following crystallisation experiment (isothermal distillation) to assure a slower diffusion rate as compared to Et<sub>2</sub>O and, theoretically, increase the possibility of successful nucleation. The successful crystallisation experiment was conducted as follows: 25 mg Ru-MACHO (Sigma-Aldrich) was dissolved in 0.7 mL DMSO under ambient conditions in a 4 mL glass vial. The vial containing the resulting clear, colourless solution was placed in a pool of 4 mL TBME in a 20 mL glass vial. The bigger vial was sealed with a teflon cap and left standing at rt for 2 weeks whereby small crystalites formed in the interphase of the solvent and the precipitant. To assure the integrity of the crystals upon further growing, the experiment was *carefully* cooled to 4 °C and left at this temperature for another week, where after high quality crystals could be harvested.

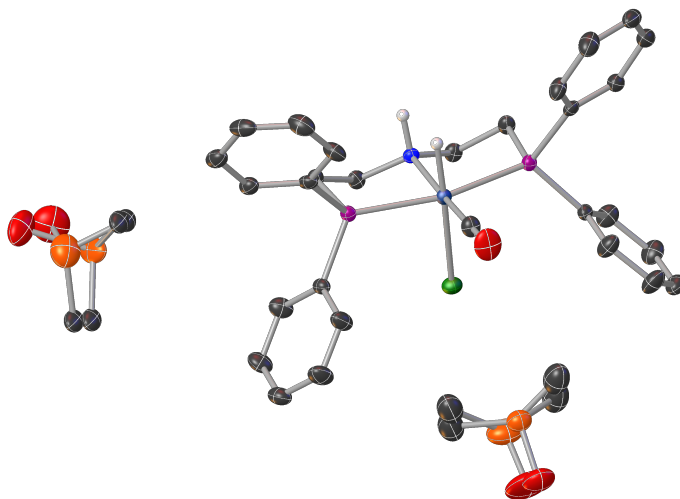


Figure 5.5: Crystal structure of the Ru-MACHO pre-catalyst showing significant disorder in the co-crystallised DMSO solvent. All hydrogens on carbon atoms have been omitted for clarity. Thermal ellipsoids are plotted at 50% probability level.

### Solution and refinement

Using Olex2,<sup>142</sup> the structure was solved with the SHELXT<sup>367</sup> structure solution program using Intrinsic Phasing and refined with the SHELXL<sup>368</sup> refinement package using Least Squares (LS) minimisation. As illustrated in Figure 5.5 the complex co-crystallises with two molecules of DMSO per formula unit (1.7 molecules DMSO per asymmetric unit) and, as such, obscures the model. However, a reasonable model as the one depicted in the figure above can be obtained by modeling of the solvent disorder. The solvent molecules were split over the two positions indicated by electron density peaks. The EADP constraint was applied to all atoms sharing the same crystallographic sites to assure same ADPs thereby reducing the size of the LS matrix used in the refinement. To further stabilise the LS refinement the RIGU and SADI restraints were applied to all parts related to the solvent of crystallisation to assure physically meaningful thermal motion and equalise bond distances between pairs of atoms related by different parts. The final model including solvent of

crystallisation converged to  $R_1 = 4.34\%$  and  $wR_2 = 12.22\%$  (all data).

To obtain a better model, a solvent mask was calculated using PLATON Squeeze<sup>369</sup> and 584 electrons were found in a volume of  $1516 \text{ \AA}^3$  in 1 void per unit cell. This is consistent with the presence of  $1.7[\text{C}_2\text{H}_6\text{SO}]$  per Asymmetric Unit which account for 571 electrons per unit cell. Excluding the structure factors related to the solvent voids the better model depicted in Figure 5.6 below was obtained. The solvent-free model converged

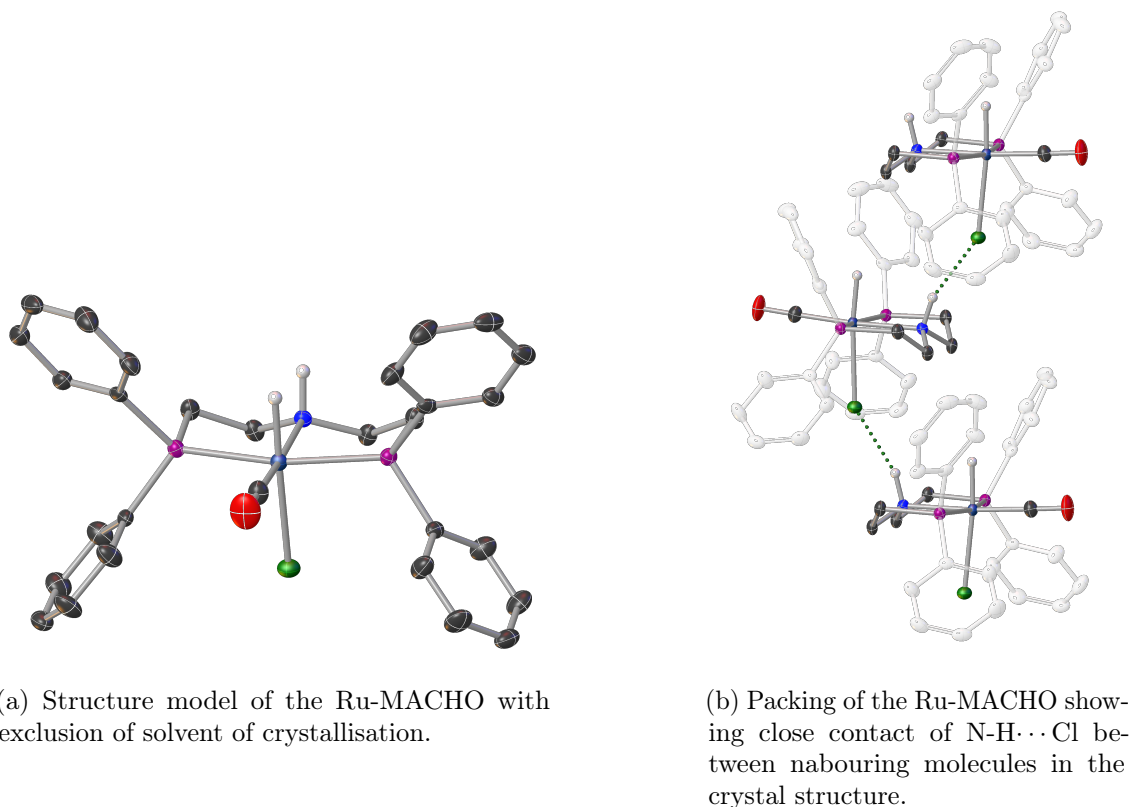


Figure 5.6: Crystal structure of the Ru-MACHO after solvent masking have been applied to the structure in Figure 5.5. All hydrogens on carbon atoms have been omitted for clarity. Thermal ellipsoids are plotted at 50% probability level.

to  $R_1 = 3.23\%$  and  $wR_2 = 7.56\%$  (all data) which indicates a significantly better model has been reached as compared to the "solvated" model. This also reflects that the model part related to the ruthenium complex is well defined and the disagreement between  $F_{\text{OBS}}$  and  $F_{\text{CALC}}$  in the initial model was mainly related to the presence of solvent. This was also hinted at by the small ADPs related to the complex which indicates a well-defined structure.

Table 2.1-2.10 summarises selected bond distances and angles for Ru-MACHO. The Ru-H bond length of  $1.45(3) \text{ \AA}$  is within the expected bond length of Ru-H compounds (see Chapter 2) however, significantly shorter than the  $(^i\text{Pr}_2\text{PNP})\text{RuHCl}(\text{CO})$  compound by  $0.1 \text{ \AA}$ . The short C-O bond distance of  $1.159 \text{ \AA}$  is in agreement with the interpretation of triple bond character. The long Ru-Cl bond length of  $2.5412 \text{ \AA}$  is in agreement with the large *trans*-influence exhibited by the hydrido ligand. The PNP bite angle of  $163.29^\circ$  is in line

Table 5.1: Selected bond lengths and angles for the Ru-MACHO complex.

Atom	Atom	Length/Å	Atom	Atom	Atom	Angle/°
Ru	H	1.45(3)	H	Ru	N	187.433
Ru	P	2.3214(5)	P	Ru	P <sup>1</sup>	163.29(3)
Ru	P <sup>1</sup>	2.3215(5)	P	Ru	Cl	90.934(14)
Ru	Cl	2.5411(8)	N	Ru	P	81.792(13)
Ru	N	2.196(2)	N	Ru	Cl	85.79(6)
Ru	C(O)	1.832(3)	O	C	Ru	179.0(3)
O	C(Ru)	1.159(3)				

<sup>1</sup>  $x, -\frac{3}{2}y, z$

with analogous structures of ruthenium(II) comprising this ligand.<sup>370–372</sup> By comparison with the RuCl<sub>2</sub>-MACHO, the P-Ru-P bite angle is significantly less, namely 103°. The apparently small bite angle in the RuCl<sub>2</sub>-MACHO complex is a direct consequence of the small twist exhibited by the ligand backbone. This is evident in the difference of the torsion angles P1-Ru-Cl-N and P2-Ru-Cl-N = 81.12° – (–82.31°) = 163.43° which is very close to the P-Ru-P angle observed in the model for Ru-MACHO.

## 5.2 Conclusions and outlook

The hitherto unknown crystal structure of the Ru-MACHO complex has been determined in great accuracy. However, the compound unfortunately co-crystallises with the solvent DMSO which was highly distorted. The distortion could be modeled to a satisfying level, although, a significantly better model was obtained by applying a solvent mask which could be done without harm to the complex model. The crystal structure revealed close contacts between the amine proton and chlorido ligands on neighboring molecules. This hydrogen bonding is found in both the RuCl<sub>2</sub>-MACHO and Ru-MACHO structure and may account for the molecular packing and, as such, stabilises the structure. In addition, depending on the strength of these intermolecular interactions, these may also account for the observed poor solubility in many common solvents, *vide infra*.

The reaction of Ru-MACHO with chloroform has been established to furnish the formation of RuCl<sub>2</sub>-MACHO via hydride/chloride exchange. RuCl<sub>2</sub>-MACHO has previously been prepared by same means albeit not in a quantitative yield.<sup>373</sup>

The findings in this work do not further an explanation of the fact that two  $\nu(\text{CO})$  bands and two  $\nu(\text{Ru-H})$  bands are found in the IR spectrum which strongly indicate the presence of structural isomers. A natural extension of this work is to obtain crystals of the titled compound without any solvent of crystallisation. In the successful case, the obtained model will have the sufficient quality to serve as model for the prediction of an accurate powder diffractogram that in comparison with the experimental powder-XRD will

reveal whether crystallographically different compounds (structure-isomers) are present in the sample. In addition, optimisation of the crystallisation protocol may furnish selective crystallisation of potential isomers.

As mentioned in the introduction, the Ru-MACHO-BH is at least equally used in catalytic reactions as is the Ru-MACHO, although its structure is unknown. Hence, extending the work presented here to the crystallographic characterisation of the Ru-MACHO-BH complex seems obvious and would indeed round off this work to a more appreciated completion.

## Chapter 6

# Intrinsic Geometric Distortion of 5-Coordinate Halido Complexes of Ruthenium(0)

This chapter (next page) is written as a draft for an ACS paper. Hence, the formatting of this chapter is different from the rest of this thesis. The present chapter describes the synthesis and analysis of new zero-valent ruthenium complexes which exhibits strongly distorted coordination geometries. Additionally, the exceedingly rare Ru(0)-halido bonds that are presented in these complexes have been analysed both spectroscopically as well as theoretically by means of DFT.

# Intrinsic Geometric Distortion of 5-Coordinate Halido Complexes of Ruthenium(0)

Mike S. B. Jørgensen, K. Enemark-Rasmussen, R. Wugt Larsen, and Martin Nielsen\*

Technical University of Denmark, 2800 Kgs. Lyngby, Denmark.

*Pincer complexes, PNP, nitrosyl, ruthenium nitrosyl, electronic structure, non-innocent ligands.*

**ABSTRACT:** We report the synthesis and analysis of the PNP-Ru halido nitrosyl complexes  $\{(\text{PNP})\text{RuX}(\text{NO})\}$  ( $\text{X} = \text{I}, \text{Br}, \text{Cl}$ ). These five-coordinated 18-electron  $\text{Ru}(0)$  compounds show substantial geometric deviation from literature-reported isoelectronic analogs. Instead of the typical square pyramidal or trigonal bipyramidal structures, they obtain Y-shaped distorted trigonal bipyramidal geometries, which is unusual for  $d^8$  complexes. Equally unusual, the  $\pi$ -donating ligand X and the PNP amine constitute the acute bond angle while the  $\pi$ -accepting NO resides in the third coordination site in the distorted trigonal plane. It is evident from SC-XRD, IR, and multinuclear NMR spectroscopies that the nature of the X ligand influences the degree of distortion, with the X-Ru-NH angle being. In supplement to the spectroscopic and crystallographic analyses, the nature of the rare X-Ru<sup>0</sup> bond is assessed by means of Natural Population Analysis and orbital interactions. The computational and spectroscopical results show a clear dependence of the  $\pi$ -donating capabilities as well as the electronegativity of the X ligand. Finally, DFT analysis of the hypothetical structures  $(\text{PNP})\text{RuF}(\text{NO})$  and  $(\text{PNP})\text{Ru}(\text{OMe})(\text{NO})$  at the BP86 and TPSSh level of theories corroborated our experimental findings.

## Introduction

Ruthenium(0) is dominated by derivatives of  $\text{Ru}_3\text{CO}_{12}$  and a number of arene/olefin species.<sup>1</sup> Only 27 structures on five coordinate ruthenium(0) compounds are described in the Cambridge crystallographic Structure Database (CCSD), and all show regular trigonal bipyramidal (TBP) or square pyramidal (SP) geometries as predicted by Hoffman.<sup>2</sup> Whereas isoelectronic rhodium(I) halido complexes are numerous,<sup>3</sup> only two ruthenium(0) halido complexes have been irrefutable structurally characterized (both 4-coordinate),<sup>4-7</sup> namely, the terminal chlorido complex  $\text{trans-}[\text{RuCl}(\text{NO})(\text{PR}_3)_2]$  by Werner<sup>4</sup> and the bridging iodido complex of mixed valent diruthenium  $(\text{C}_4\text{Ph}_4\text{COH})(\text{CO})_2\text{RuIRu}(\text{CO})_2(\text{C}_4\text{Ph}_4\text{CO})$  by Park et. al.<sup>5</sup>

Zero-valent ruthenium complexes have proven useful in a variety of catalytic transformations, such as oxidative coupling of alkenes,<sup>8</sup> hydrogenative cycloadditions,<sup>9</sup> cross-couplings of aniline derivatives<sup>10</sup> and [4+2] cycloadditions of acetylenic aldehydes with  $\alpha$ -ketols.<sup>11</sup>

On the other hand, transition metal nitrosyl complexes to date holds little merit in homogeneous catalysis. One possible explanation for the relatively unexplored catalytic activity of nitrosyl complexes may be due to the non-innocent nature of the NO-ligand as the NO moiety easily transforms between different electronic states.<sup>12,13</sup> These electronic states can be differentiated by the geometry around the nitrosyl N-atom, i.e. the higher electron density on the NO ligand (population of  $\pi^*$ -orbitals), the more the M-N-O angle deviates from 180°.<sup>14</sup> Controlled interconversion between bent and linear nitrosyl groups was shown by Berke to be

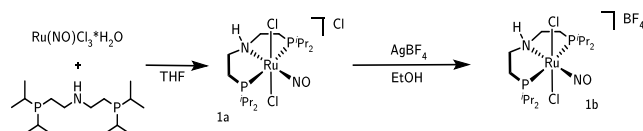
an effective tool in the fine-tuning of catalytic hydrogenation of alkenes using a  $\text{Re}(\text{I})$  mononitrosyl complex.<sup>15</sup> However, the nature of the NO ligand largely remains elusive.

Recently, Milstein showed examples of  $(\text{PNP})\text{Ru}(\text{NO})$  and  $(\text{PNN})\text{Ru}(\text{NO})$  complexes that that undergone 2-electron reduction in very mildly reductive to seemingly redox-neutral environment. The generated planar ruthenium species is indicative of a  $d^8$  electron configuration.<sup>16</sup>

The reactivity pattern mapped out by Milstein is in sharp contrast to the reactivities observed in this work. Unlike their work, all complexes presented here exhibit a close to linear nitrosyl coordination geometry, and a very acute X-Ru-NH angle and the N-Ru-NO angle deviate significantly from 180°. As such, these species 2-4 are highly distorted from both the TBP and SP structures that would be expected based on the normal behavior for  $\{\text{MNO}\}^8$  complexes, *vide infra*.<sup>2,13,17</sup>

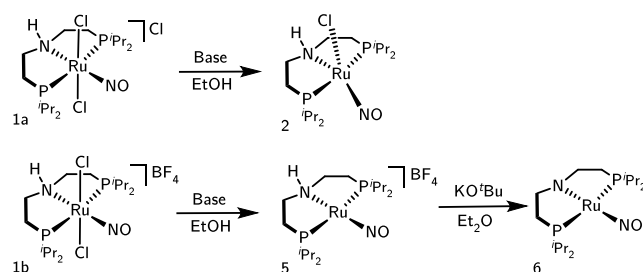
Herein we show that, by treating the octahedral dichlorido complex with chloride as counterion, **1a** (Scheme 1), with either be sodium ethoxide as indicated in Scheme 1, or triethylamine in analogy to the protocol by Milstein, the complex **2** can be crystallized from the mixture (Scheme 2). We do not observe any change in the oxidation state of the metal by interconversion between linear and bent nitrosyl coordination as all complexes presented in this work exhibits practically linear Ru-N-O angles.

### Scheme 1. Preparation of **1a** and **1b**.

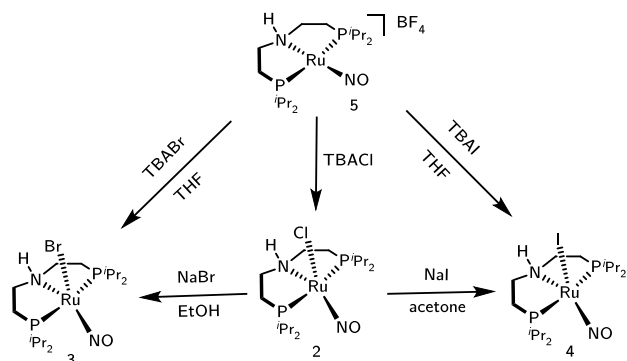


As outlined in Scheme 2, treating the parent dichlorido complex cation, but now with tetrafluoroborate as counterion, (complex **1b**) with basic ethanol in analogy to Milstein's protocol, the corresponding 16e square planar amino complex **5** is obtained. Whereas when chloride is the counterion (**1a**), the five-coordinate 18e complex **2** is isolated. By treating this chlorido species with NaBr or NaI, the geometrically distorted complexes **3** and **4** are generated and show similar geometry as the analogous chloride complex, **2**. These complexes can also be obtained by addition of tetrabutylammonium halide to the square planar amino complex salt, **5** (Scheme 3). By treating **5** with base the square planar amido complex **6** can be isolated from a diethyl ether solution.

### Scheme 2. Synthesis of **2**, **5**, and **6**.



### Scheme 3. Synthesis of **3** and **4** from **2** and **5**.



Herein, we present the crystal structures as well as the spectroscopic comportment of all complexes presented in Figure 2 and 3 and systematically discuss the nature of the unprecedented terminal Ru<sup>0</sup>-X bond and the electronic structure of these new five coordinated halido complexes supported by population analysis on the DFT level. We will in the following discussion aim for the creation of a coherent explanation about the nature of the intrinsic disorder exhibited by these compounds. For the sake of completeness, we have calculated the geometry on electronic structure of the hypothetical complexes for X=F and OMe and found that these computational results are in line with what can be expected from the structural and spectroscopic trends observed for complex **2-4**.

### Experimental Section

**General:** Ru(NO)Cl<sub>3</sub>·H<sub>2</sub>O and bis(2-diisopropylphosphinoethyl)amine were purchased from Strem Chemicals. NaBr and NaI were purchased from Merck Denmark. Deuterated solvents were purchased from Fluorochem. Ethanol, THF, diethyl ether and anhydrous acetone were purchased from VWR Denmark. Ethanol was dried by refluxing over magnesium/iodine under N<sub>2</sub> atmosphere overnight followed by trap-to-trap distillation followed by degassing by 3 cycles of freeze-pump-thaw and stored under N<sub>2</sub> over 3 Å molecular sieves (activated by microwave heating). Acetone was flushed with N<sub>2</sub> prior to use. THF and Et<sub>2</sub>O were dried over aluminum oxide, purged with N<sub>2</sub> and stored inside an Ar filled glovebox. All manipulations were conducted using standard Schlenk techniques unless otherwise stated.

[(PNP)RuCl<sub>2</sub>(NO)]Cl (**1a**): To the dark red suspension of 400 mg (1.57 mmol) Ru(NO)Cl<sub>3</sub>·H<sub>2</sub>O (0 °C) was added 500 mg (1.64 mmol) bis(2-diisopropylphosphinoethyl)amine in 15 mL THF via cannula transfer. After 15 min of stirring in the ice bath, the mixture was allowed to heat to rt followed by stirring overnight. The pink powdery product was filtered off under ambient conditions, washed with acetonitrile until colorless filtrate appeared, followed by washing with Et<sub>2</sub>O and dried in air. High quality single crystals were obtained by vapor diffusion of Et<sub>2</sub>O into a concentrated ethanolic solution of the compound at room temperature. Yield: 87% NMR DATA <sup>1</sup>H NMR (14.1 T MeOD-d<sub>3</sub>): δ/ppm 3.25 (m, NCH<sub>2</sub>a, 2H), 3.18 (m, NCH<sub>2</sub>b, 2H), 3.20 (m, iPr1-CH, 2H), 3.19 (m, iPr2-CH, 2H), 2.74 (m, P-CH<sub>2</sub>a, 2H), 2.18 (m, P-CH<sub>2</sub>b, 2H), 1.54 (m, iPr2-CH<sub>3</sub>2, 6H), 1.53 (m, iPr2-CH<sub>3</sub>1, 6H), 1.50 (m, iPr1-CH<sub>3</sub>2, 6H), 1.48 (m, iPr1-CH<sub>3</sub>1, 6H). <sup>13</sup>C NMR (18.8 T MeOD): δ/ppm 51.5 (t, <sup>2</sup>J(<sup>13</sup>C-<sup>31</sup>P) = 2.3 Hz, NCH<sub>2</sub>), 25.4 (t, <sup>1</sup>J(<sup>13</sup>C-<sup>31</sup>P) = 12.5 Hz, iPr1-CH), 24.8 (t, <sup>1</sup>J(<sup>13</sup>C-<sup>31</sup>P) = 12.0 Hz, PCH<sub>2</sub>), 22.9 (t, <sup>1</sup>J(<sup>13</sup>C-<sup>31</sup>P) = 11.4 Hz, iPr2-CH), 18.7 (s, iPr1-CH<sub>3</sub>1), 18.2 (s, iPr2-CH<sub>3</sub>1), 17.6 (s, iPr1-CH<sub>3</sub>2), 17.4 (s, iPr2-CH<sub>3</sub>2). <sup>31</sup>P NMR (14.1 T MeOD): δ/ppm 68.0. <sup>15</sup>N NMR (18.8 T MeOD): δ/ppm 373 (Ru-NO), 67.8 (Ru-NCH<sub>2</sub>).

Elemental analysis on basis of Cl<sub>16</sub>H<sub>37</sub>Cl<sub>3</sub>N<sub>2</sub>O<sub>2</sub>P<sub>2</sub>Ru:

Calc: C: 35.40 H: 6.87 N: 5.16

Found: C: 35.52 H: 6.96 N: 5.14

[(PNP)RuCl<sub>2</sub>(NO)]BF<sub>4</sub> (**1b**): Under ambient conditions, 185 mg (340.8 μmol) of **1a** was dissolved in 25 mL EtOH. To the red solution was added 66.34 mg AgBF<sub>4</sub> in 30 mL EtOH dropwise. A white precipitate of AgCl started to form immediately upon addition of the AgBF<sub>4</sub>. After the addition of AgBF<sub>4</sub>, the flask was closed and excluded from light by coverage with tin foil. The mixture was stirred at rt overnight. The white precipitate was filtered off on a glass filter funnel. The filtrate was concentrated under reduced pressure to half the volume and layered with twice the volume of Et<sub>2</sub>O whereupon standing at rt for 3 days high quality crystals suitable for X-ray diffraction were obtained. The crystals were collected by decanting off the mother liquor. The rest of the product was obtained by evaporating the volatiles under reduced pressure until precipitation set in followed by layering with diethyl ether. Combined yield (crystals): 70%.

NMR DATA <sup>1</sup>H NMR (14.1 T MeOD-d<sub>3</sub>): δ/ppm 3.25 (m, NCH<sub>2</sub>a, 2H), 3.18 (m, NCH<sub>2</sub>b, 2H), 3.20 (m, iPr1-CH, 2H), 3.19 (m, iPr2-CH, 2H), 2.74 (m, P-CH<sub>2</sub>a, 2H), 2.18 (m, P-CH<sub>2</sub>b, 2H),



1.54 (m, iPr2-CH<sub>3</sub>2, 6H), 1.53 (m, iPr2-CH<sub>3</sub>1, 6H), 1.50 (m, iPr1-CH<sub>3</sub>2, 6H), 1.48 (m, iPr1-CH<sub>3</sub>1, 6H). <sup>13</sup>C NMR (18.8 T MeOD): δ/ppm 51.5 (t, <sup>2</sup>J(<sup>13</sup>C-<sup>31</sup>P) = 2.3 Hz, NCH<sub>2</sub>), 25.4 (t, <sup>1</sup>J(<sup>13</sup>C-<sup>31</sup>P) = 12.5 Hz, iPr1-CH), 24.8 (t, <sup>1</sup>J(<sup>13</sup>C-<sup>31</sup>P) = 12.0 Hz, PCH<sub>2</sub>), 22.9 (t, <sup>1</sup>J(<sup>13</sup>C-<sup>31</sup>P) = 11.4 Hz, iPr2-CH), 18.7 (s, iPr1-CH<sub>3</sub>1), 18.2 (s, iPr2-CH<sub>3</sub>1), 17.6 (s, iPr1-CH<sub>3</sub>2), 17.4 (s, iPr2-CH<sub>3</sub>2). <sup>31</sup>P NMR (14.1 T MeOD): δ/ppm 68.2. <sup>15</sup>N NMR (18.8 T MeOD): δ/ppm 372 (Ru-NO), 68.0 (Ru-NCH<sub>2</sub>).

Elemental analysis on basis of C<sub>16</sub>H<sub>37</sub>BCl<sub>2</sub>F<sub>4</sub>N<sub>2</sub>OP<sub>2</sub>Ru:

Calc: C: 32.34 H: 6.28 N: 4.71

Found: C: 32.35 H: 6.41 N: 4.68

(PNP)RuCl(NO) (**2**): To a red ethanolic solution (1 mL) of 70 mg (129 μmol) of **1** was added 17.6 mg NaOEt in 3 mL EtOH whereby the solution darkened. The dark red solution was stirred at 50 °C for 2 h giving an intense dark green solution which was allowed to cool to rt before all volatiles were removed in vacuo. The crude product was extracted with three times 1.5 mL THF by filtering through cannula. The combined extracts were dried in vacuo yielding the pure product as a green solid. Further handling of the extremely air sensitive compound was done in a glovebox where the product was dissolved in THF and subsequently left in the freezer at -30 °C for 3 days whereafter the mother liquor was decanted off and the crystals were washed with cold THF. An additional batch of crystals was isolated by reducing the volume of the mother liquor until precipitation set in followed by storing at -30 °C, decanting and washing with cold THF. Yield (crystals): 45%. NMR DATA <sup>1</sup>H NMR (14.1 T C<sub>6</sub>D<sub>6</sub>): δ/ppm 3.05 (m, iPr1-CH, 2H), 2.44 (t, 3J = 11.6 Hz, NH, 1H), 2.28 (m, NCH<sub>2</sub>a, 2H), 2.13 (m, iPr2-CH, 2H), 2.09 (m, NCH<sub>2</sub>b, 2H), 1.62 (m, P-CH<sub>2</sub>, 4H), 1.69 (m, iPr1-CH<sub>3</sub>1, 6H), 1.18 (m, iPr1-CH<sub>3</sub>2, 6H), 1.15 (m, iPr2-CH<sub>3</sub>1, 6H), 1.06 (m, iPr2-CH<sub>3</sub>2, 6H). <sup>13</sup>C NMR (18.8 T C<sub>6</sub>D<sub>6</sub>): δ/ppm 53.7 (broad, NCH<sub>2</sub>), 28.7 (t, <sup>1</sup>J(<sup>13</sup>C-<sup>31</sup>P) = 9.5 Hz, PCH<sub>2</sub>), 26.5 (t, <sup>1</sup>J(<sup>13</sup>C-<sup>31</sup>P) = 8.8 Hz, iPr2-CH), 26.0 (t, <sup>1</sup>J(<sup>13</sup>C-<sup>31</sup>P) = 10.8 Hz, iPr1-CH), 21.0 (broad, iPr1-CH<sub>3</sub>1), 19.8 (broad, iPr2-CH<sub>3</sub>1), 17.3 (broad, iPr1-CH<sub>3</sub>2), 19.3 (broad, iPr2-CH<sub>3</sub>2). <sup>31</sup>P NMR (14.1 T C<sub>6</sub>D<sub>6</sub>): δ/ppm 71.2. <sup>15</sup>N NMR (18.8 T C<sub>6</sub>D<sub>6</sub>): δ/ppm 62.6 (Ru-NCH<sub>2</sub>).

(PNP)RuBr(NO) (**3**): In 3 mL EtOH was dissolved 120 mg (221 μmol) **1** and treated with 30 mg (442 μmol) NaOEt 5 mL EtOH. The resulting dark red solution was stirred at 50 °C for 2 h and subsequently allowed to cool to rt. The tempered solution was filtered via cannula into a Schlenk flask loaded with 68 mg (661 μmol) NaBr. The head space atmosphere was carefully removed, and the suspension was stirred at rt for 24 h. All volatiles were removed in vacuo and the product was extracted 3 times with 4 mL THF using cannula filtration. By evaporation of the combined extracts, the extremely air sensitive compound **3** could be isolated as a brownish powder. Inside an Ar filled glovebox, the product was dissolved in THF and layered with Et<sub>2</sub>O and left for crystallization at -30 °C for one week. The mother liquor was decanted off and the crystals were washed with cold THF. An additional amount of product was isolated by concentration until precipitation occurred followed by layering with Et<sub>2</sub>O and storing at -30 °C for one week. Yield (crystals): 51%. NMR DATA <sup>1</sup>H NMR (14.1 T C<sub>6</sub>D<sub>6</sub>): δ/ppm 3.18 (m, iPr1-CH, 2H), 2.51 (t, 3J = 11.6 Hz, NH, 1H), 2.31 (m, NCH<sub>2</sub>a, 2H), 2.15 (m, iPr2-CH, 2H), 2.03 (m, NCH<sub>2</sub>b, 2H), 1.72

(m, P-CH<sub>2</sub>a, 2H), 1.68 (m, iPr1-CH<sub>3</sub>1, 6H), 1.63 (m, P-CH<sub>2</sub>b, 2H), 1.35 (m, iPr1-CH<sub>3</sub>2, 6H), 1.17 (m, iPr2-CH<sub>3</sub>1, 6H), 1.05 (m, iPr2-CH<sub>3</sub>2, 6H). <sup>13</sup>C NMR (18.8 T C<sub>6</sub>D<sub>6</sub>): δ/ppm 54.0 (broad, NCH<sub>2</sub>), 29.0 (t, <sup>1</sup>J(<sup>13</sup>C-<sup>31</sup>P) = 9.5 Hz, PCH<sub>2</sub>), 27.0 (t, <sup>1</sup>J(<sup>13</sup>C-<sup>31</sup>P) = 8.8 Hz, iPr1-CH), 26.6 (t, <sup>1</sup>J(<sup>13</sup>C-<sup>31</sup>P) = 10.8 Hz, iPr2-CH), 21.0 (broad, iPr1-CH<sub>3</sub>1), 19.9 (broad, iPr2-CH<sub>3</sub>1), 19.6 (broad, iPr2-CH<sub>3</sub>2), 17.4 (broad, iPr1-CH<sub>3</sub>2). <sup>31</sup>P NMR (14.1 T C<sub>6</sub>D<sub>6</sub>): δ/ppm 70.1. <sup>15</sup>N NMR (18.8 T C<sub>6</sub>D<sub>6</sub>): δ/ppm 60.3 (Ru-NCH<sub>2</sub>).

(PNP)Ru(NO) (**4**): Dissolved in 3 mL acetone 50 mg (106 μmol) of **2** was resulting in an intensely green solution. Upon addition of 19 mg (127 μmol) NaI in 3 mL acetone, the green solution changed color instantly to purple. The purple solution was stirred at rt for 30 min before the solvent was removed in vacuo. The crude product was extracted with 3 times 1 mL THF via cannula filtration. By evaporation of the combined extracts the extremely air sensitive compound **4** could be isolated as a purple powder. Inside the glovebox, the product was dissolved in the minimum amount of THF and Et<sub>2</sub>O was diffused into the solution at -30 °C over the course of 10 days whereupon high quality crystals precipitated as black rhombic blocks. Yield (crystals): 45%. NMR DATA <sup>1</sup>H NMR (14.1 T Tol-d<sub>8</sub>): δ/ppm 3.29 (m, iPr1-CH, 2H), 2.65 (t, 3J = 11.6 Hz, NH, 1H), 2.50 (m, NCH<sub>2</sub>a, 2H), 2.23 (m, iPr2-CH, 2H), 2.00 (m, NCH<sub>2</sub>b, 2H), 1.91 (m, P-CH<sub>2</sub>a, 2H), 1.76 (m, P-CH<sub>2</sub>b, 2H), 1.66 (m, iPr1-CH<sub>3</sub>1, 6H), 1.19 (m, iPr1-CH<sub>3</sub>2, 6H), 1.13 (m, iPr2-CH<sub>3</sub>1, 6H), 1.09 (m, iPr2-CH<sub>3</sub>2, 6H). <sup>13</sup>C NMR (18.8 T Tol-d<sub>8</sub>): δ/ppm 54.4 (broad, NCH<sub>2</sub>), 29.5 (t, <sup>1</sup>J(<sup>13</sup>C-<sup>31</sup>P) = 10.4 Hz, PCH<sub>2</sub>), 29.3 (t, <sup>1</sup>J(<sup>13</sup>C-<sup>31</sup>P) = 11.8 Hz, iPr1-CH), 26.6 (t, <sup>1</sup>J(<sup>13</sup>C-<sup>31</sup>P) = 9.9 Hz, iPr2-CH), 20.9 (t, <sup>2</sup>J(<sup>13</sup>C-<sup>31</sup>P) = 3.1 Hz, iPr1-CH<sub>3</sub>1), 19.9 (broad, iPr2-CH<sub>3</sub>1), 19.8 (t, <sup>2</sup>J(<sup>13</sup>C-<sup>31</sup>P) = 1.0 Hz, iPr2-CH<sub>3</sub>2), 17.2 (t, <sup>2</sup>J(<sup>13</sup>C-<sup>31</sup>P) = 1.4 Hz, iPr1-CH<sub>3</sub>2). <sup>31</sup>P NMR (14.1 T Tol-d<sub>8</sub>): δ/ppm 69.1. <sup>15</sup>N NMR (18.8 T Tol-d<sub>8</sub>): δ/ppm 56.0 (Ru-NCH<sub>2</sub>).

[(PNP)RuNO]BF<sub>4</sub> (**5**): In 4 mL EtOH was 100 mg (168.3 μmol) of **1b** dissolved and slowly treated with 23 mg (336.6 μmol) NaOEt in 4 mL EtOH at rt. The resulting dark red solution was heated to 55 °C and stirred at this temperature for 1 h where after the dark green solution was allowed to cool to rt. All volatiles were removed in vacuo. The crude product was washed with small amounts of toluene until the filtrates were only slightly colored (green). The pure, extremely air sensitive product was transferred to an argon filled glove box where the product was dissolved in THF and layered with Et<sub>2</sub>O and left at -30 °C for 3 days. The mother liquor was decanted off and the high-quality crystals were dried in vacuo. An additional amount of product could be isolated by concentration of the mother liquor until precipitation followed by layering with Et<sub>2</sub>O and leaving the solution at -30 °C for 5 days. Combined yield (crystals): 65%.

NMR DATA <sup>1</sup>H NMR (14.1 T THF-d<sub>8</sub>): δ/ppm 2.99 (m, NCH<sub>2</sub>a, 2H), 2.78 (m, iPr2-CH, 2H), 2.87 (m, iPr1-CH, 2H), 2.49 (t, 3J = 11.6 Hz, NH, 1H), 2.99 (m, NCH<sub>2</sub>a, 2H), 2.78 (m, iPr2-CH, 2H), 2.60 (m, P-CH<sub>2</sub>a, 2H), 2.46 (m, P-CH<sub>2</sub>b, 2H), 2.21 (m, NCH<sub>2</sub>b, 2H), 1.54 (m, iPr1-CH<sub>3</sub>1, 6H), 1.52 (m, iPr2-CH<sub>3</sub>1, 6H), 1.50 (m, iPr2-CH<sub>3</sub>2, 6H), 1.46 (m, iPr1-CH<sub>3</sub>2, 6H). <sup>13</sup>C NMR (18.8 T THF-d<sub>8</sub>): δ/ppm 52.3 (dt, <sup>2</sup>J(<sup>13</sup>C-<sup>31</sup>P) = 4.7 Hz NCH<sub>2</sub>), 22.0 (t, <sup>1</sup>J(<sup>13</sup>C-<sup>31</sup>P) = 10.2 Hz, PCH<sub>2</sub>), 26.9 (t, <sup>1</sup>J(<sup>13</sup>C-<sup>31</sup>P) = 11.4 Hz, iPr1-CH), 26.0 (t, <sup>1</sup>J(<sup>13</sup>C-<sup>31</sup>P) = 12.8 Hz, iPr2-CH), 19.2 (t, <sup>2</sup>J(<sup>13</sup>C-<sup>31</sup>P) = 2.3 Hz, iPr2-CH<sub>3</sub>2), 18.8 (t<sup>2</sup>J(<sup>13</sup>C-<sup>31</sup>P) =

2.1 Hz,  $iPr1-CH_32$ ), 18.3 (broad  $iPr1-CH_31$ ). 18.1 (broad,  $iPr2-CH_31$ ).  $^{31}P$  NMR (14.1 T THF- $d_8$ ):  $\delta/ppm$  75.5.  $^{15}N$  NMR (18.8 T THF- $d_8$ ):  $\delta/ppm$  56.9 (Ru-NCH2).

(PNP)RuNO (**6**): In 10 mL Et<sub>2</sub>O, was 100 mg (191.1  $\mu$ mol) of **5** and 21.5 mg KO<sup>t</sup>Bu (191.6  $\mu$ mol) suspended. The resulting dark red suspension was stirred at rt for 1 h and the mixture was subsequently filtered through a plug of Celite. The filtrate was evaporated in vacuo until dryness whereby the product was isolated as a reddish black powder. Single crystals suitable for X-ray diffraction analysis were obtained by saturating a mixture of Et<sub>2</sub>O and pentane (1:1) with the titled compound and leaving the solution at -30 °C for ~25 days. Yield (crystals): 30%

NMR DATA  $^1H$  NMR (14.1 T C<sub>6</sub>D<sub>6</sub>):  $\delta/ppm$  2.95 (m, NCH<sub>2</sub>, 4H), 2.20 (m,  $iPr1-CH1$ , 4H), 1.86 (m, P-CH<sub>2</sub>, 4H), 1.34 (m,  $iPr-CH_31$ , 12H), 1.21 (m,  $iPr-CH_32$ , 12H).  $^{13}C$  NMR (18.8 T C<sub>6</sub>D<sub>6</sub>):  $\delta/ppm$  61.2 (t,  $^1J(^{13}C-^{31}P) = 8.3$  NCH<sub>2</sub>), 26.4 (t,  $^1J(^{13}C-^{31}P) = 10.7$  Hz,  $iPr1-CH$ ), 24.1 (t,  $^1J(^{13}C-^{31}P) = 9.5$  Hz, PCH<sub>2</sub>), 19.7 t,  $^2J(^{13}C-^{31}P) = 3$  Hz  $iPr-CH_31$ ), 18.4 (broad,  $iPr-CH_32$ ).  $^{31}P$  NMR (14.1 T C<sub>6</sub>D<sub>6</sub>):  $\delta/ppm$  89.0.  $^{15}N$  NMR (18.8 T C<sub>6</sub>D<sub>6</sub>):  $\delta/ppm$  388.9 (Ru-NO), 159.5 (Ru-NCH2).

### Computational details

All calculations were performed using the Turbomole software, version 7.0.<sup>18</sup> All energies were converged to 10<sup>-6</sup> atomic units using the identity approximation to speed up calculations.<sup>19</sup> Geometry-optimized structures and energies were calculated using the BP86<sup>20,21</sup> and the hybrid TPSSH<sup>22</sup> functional with def2-SVP and def2-TZVPP basis sets respectively<sup>23</sup>. The effective core potential (ECP) approximation was used to account for the 28 inner core electrons of the Ru and I atoms.<sup>24,25</sup> All vibrational frequencies were calculated under the harmonic oscillator approximation.

### X-ray Crystallography

**General:** All crystal batches for X-ray diffraction analysis were immersed in polybutene oil (Aldrich, >90%) as protection against air. A suitable crystal was harvested with a MiTeGen cryo loop and mounted on a goniometer attached to a SuperNova Dual Source CCD-diffractometer. Data was collected at 120 K using CuK $\alpha$  radiation (**1b**, **2**, **5**, **6**) or Mo K $\alpha$  (**1a**, **3**, **4**). Using Olex2,<sup>26</sup> all structures were solved using SHELXT<sup>27</sup> structure solution program using Intrinsic Phasing and refined with SHELXL<sup>28</sup> refinement package using Least Squares minimization.

### Results and discussion

Crystals of **2** exhibit two independent molecules in the asymmetric unit. Refinement of all compounds proceeded smoothly using anisotropic thermal parameters for all non-hydrogen atoms. All hydrogen atoms could be observed in the difference Fourier map and placed in idealized positions in the subsequent least-square refinements. Complexes **1a** (supporting info) and **1b** crystallizes in the orthorhombic space groups P2<sub>1</sub>/c **1a** and Pbc<sub>a</sub> **1b** respectively with one formula unit presented in the asymmetric unit. The complex cation resembles a slightly distorted octahedral geometry with the PNP ligand meridionally coordinated with the NO ligand trans to the PNP amino moiety. As such, the chlorido ligands are coordinated trans to one another with an  $\angle(Cl-$

Ru-Cl) = 171.773<sup>o</sup>. The chlorido ligands are almost equidistantly arranged from the Ru center of 2.377 and 2.366 Å, respectively, with the chlorido ligand *syn* to the amine proton possessing the longer bond length. The Ru-N-O bond angle of 178<sup>o</sup> and the very short N-O bond distance of 1.134 Å are indicative of an N $\equiv$ O<sup>+</sup> ligand structure. Structural parameters are summarized in Table 1. In both **1a** and **1b**, the anion is involved in hydrogen bonding to the amine proton. The complexes **2-4** are all close to isostructural, and complexes **3** and **4** are isomorphous with their cell constants matching almost exactly. Complex **2**, however, differs in the regard that the cell dimensions are almost doubled and thereby reflects that the asymmetric unit is composed by two independent molecules with slightly different geometrical parameters. To exclude a wrongly assigned space group, a search for missing symmetry as well as twinning were performed with PLATON.<sup>29,30</sup> However, no additional symmetry elements nor twinning components were detected. A crystal from a new synthesis batch crystallized by diffusion of Et<sub>2</sub>O into a THF solution of the complex at -30 °C was measured independently and still two molecules per asymmetric unit were detected. A third crystal from a third crystal batch was measured using CuK $\alpha$  radiation and revealed the same results as described above. As such, we are confident that the assignment of the orthorhombic space group P2<sub>1</sub>/n is correct. In addition, seen as complex **2** is isostructural with **3** and **4**, which also crystallize in said space group this assignment for complex **2** seems justifiable. Interestingly, for all complexes **2-4**, the halido ligand tilts strongly towards the amino moiety as pointed out in Figure 2.

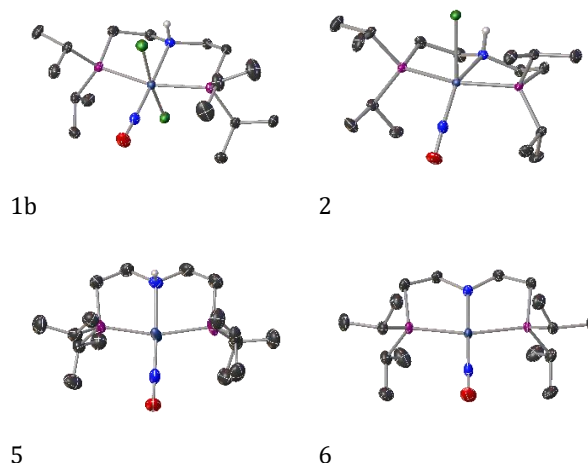
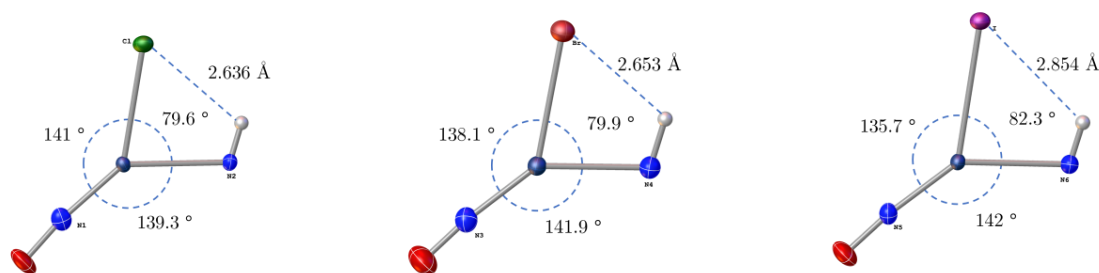


**Figure 1.** ORTEP representations of the complexes **1b**, **2**, **5**, **6**. Thermal ellipsoids are plotted at 50% probability level. All hydrogens on carbon atoms and counterions for **1b** and **5** are omitted for clarity. As there is no obvious geometrical difference between **1a** and **1b**, the model of the highest quality (**1b**) is presented here. See supporting info for representations of **1a**, **3** and **4**.

**Table 1. Selected experimental and calculated (harmonic approximation) geometries, vibrational NO frequencies and experimental NMR data. Experimental data is expressed in bold. “*Syn*” and “*anti*” refer to the orientation with respect to the amine proton.**

Measure	1a	2	3	4	5	6	X=F	X=OMe
$\nu(\text{NO}) / \text{cm}^{-1}$								
exp.	<b>1838</b>	<b>1630</b>	<b>1643</b>	<b>1646</b>	<b>1737</b>	<b>1666</b>	-	-
calc.	-	1752	1756	1762	1867	1784	1741	1720
Ru-X / Å								
exp.	<i>syn</i> : 2.377 <i>anti</i> : 2.366	<b>2.5523</b>	<b>2.698</b>	<b>2.8637</b>	-	-	-	-
calc.	-	2.5767	2.725	2.9211	-	-	2.1796	2.1742
Ru-NO / Å								
exp.	<b>1.7536</b>	<b>1.727</b>	<b>1.752</b>	<b>1.737</b>	<b>1.719</b>	<b>1.752</b>	-	-
calc.	-	1.734	1.734	1.735	1.727	1.750	1.7282	1.7329
N-O / Å								
exp.	<b>1.134</b>	<b>1.191</b>	<b>1.173</b>	<b>1.185</b>	<b>1.172</b>	<b>1.187</b>	-	-
calc.	-	1.195	1.194	1.193	1.174	1.191	1.198	1.200
HN-Ru / Å								
exp.	<b>2.150</b>	<b>2.221</b>	<b>2.225</b>	<b>2.235</b>	<b>2.176</b>	<b>2.007</b>	-	-
calc.	-	2.285	2.289	2.291	2.197	2.019	2.276	2.314
Ru-N-O / deg								
exp.	<b>178.039</b>	<b>172.9</b>	<b>174.28</b>	<b>174.2</b>	<b>177.56</b>	<b>179.89</b>	-	-
calc.	-	179.3	178.38	177.0	178.43	176.49	176.09	177.92
X-Ru-NO / deg								
exp.	<i>syn</i> : 92.665 <i>anti</i> : 85.724	<b>79.62</b>	<b>79.95</b>	<b>82.33</b>	-	-	-	-
calc.	-	74.15	75.71	77.75	-	-	67.691	66.827
HN-Ru-X / deg								
exp.	<i>syn</i> : 86.164 <i>anti</i> : 85.724	<b>97.616</b>	<b>79.945</b>	<b>82.328</b>	-	-	-	-
calc.	-	74.153	75.712	77.754	-	-	67.691	66.827
<b>NMR <math>\delta</math> / ppm:</b>								
$^{15}\text{N}$ amine	<b>67.8</b>	<b>62.6</b>	<b>60.3</b>	<b>56.0</b>	<b>75.5</b>	<b>159.5</b>	-	-
$^{31}\text{P}$	<b>68.0</b>	<b>71.2</b>	<b>70.1</b>	<b>69.1</b>	<b>56.9</b>	<b>89.0</b>	-	-
$^1\text{H}$ -N	-	<b>2.44</b>	<b>2.51</b>	<b>2.65</b>	<b>2.49</b>	-	-	-



Compound 2 (green = X = Cl)

Compound 3 (brown = X = Br)

Compound 4 (magenta = X = I)

Figure 2. View perpendicular to the  $\sigma_v$  molecular symmetry element of the complexes 2 – 4 reveal the strong X $\cdots$ HN interaction and displacement of the halido ligand towards the amine moiety.

Table 2. Van der Waals radii for the hydrogen atom and the halides (X) and their sums.

Element	VdW radius / Å	VdW(H+X) / Å
H	1.10	–
Cl	1.75	2.85
Br	1.83	2.93
I	1.98	3.08

Table 3. Electronegativity ( $\chi$ ) of the X atoms and their differences.

Element	$\chi$	$-\Delta\chi$
Cl	2.83	–
Br	2.74	0.09
I	2.21	0.53

This tilting gives rise to moderately strong N-H $\cdots$ X interactions as the X-H(N) distance is significantly shorter than the sum of the Van der Waals radii which is illustrated in Table 2. Alongside the halido ligand being dragged towards the amido group, the linear NO-ligand is pushed below the basal plane which in complexes **1a/1b**, **5** and **6** is spanned by the NO-ligand and the PNP motif. In general, 5-coordinate {MNO}<sup>8</sup> complexes are known to adopt the TBP or SP geometries.<sup>2,31,32</sup> Additionally, the Ru-Cl bond distance in **2** is as much as 0.219 Å longer than in square planar four coordinate 16e complex *trans*-Ru(NO)Cl(P<sup>*i*</sup>Pr)<sub>3</sub>,<sup>4</sup> indicative of a larger electron density around the ruthenium atom in **2**. It is noticeable that the greatest difference in electronegativity among Cl, Br and I that is, between Br and I (see Table 3) is reflected in the geometrical distortion of the complexes. However, the tendency is inverted with respect to the Ru-N-O angle and the N-O bond distance (Table 2 and 3).

Complex **5** crystallizes in the orthorhombic space group P2<sub>1</sub>/c with one formula unit per asymmetric unit. The ruthenium atom is planar coordinated with the BF<sub>4</sub><sup>–</sup> anion being responsible for hydrogen bonding to the amine proton. The short Ru-NO bond distance of 1.719 Å and the elongation of the N-O bond (compared to **1a** and **1b**) witness a pronounced multiple bond character, consistent with significant  $\pi_{\text{Ru}} \rightarrow \pi_{\text{NO}}^*$  backdonation. Additionally, the Ru-NO bond length of 1.719 Å is close to the one observed for **2** (1.727 Å) but slightly longer than the 1.706 Å displayed by the analogous compound (II in Scheme 1) presented by Milstein.<sup>16</sup> Interestingly, the N-O bond distance (1.179 Å) is comparable to the 1.185 Å observed in complex **4**,

and the Ru-NH distance is significantly shorter than in **2-4**. This indicates a stronger donation from the PNP amine moiety in this species upon removal of the halido ligand. Thereby, no change in the formal oxidation state is interpreted, as is also indicated by no linear  $\rightarrow$  bend transition of the NO stereochemistry.

Complex **6** crystallizes in the triclinic space group P $\bar{1}$  with two independent molecules in the asymmetric unit having slightly different geometrical parameters. To exclude wrong space group assignment, the same analysis was performed as for **2**. As such, the parent space group assignment seems justifiable. As **5**, complex **6** exhibits planar coordination geometry with a linear Ru-N-O (179.86°) bond angle and N-Ru-N angle of 177.95° together with a (PNP)N-Ru distance of 2.007 Å. This very short distance indicates that a significant electron density is donated towards the ruthenium center from the amido ligand upon deprotonation of the amine in support of the push-pull principle that stabilizes the  $\pi_{\text{amido}}^* \rightarrow \pi_{\text{Ru}}$  interaction.<sup>33,34</sup>

The observed <sup>15</sup>N chemical shifts for the PNP amine corroborate the relative strength of the HN $\rightarrow$ Ru donation for **2-6** as indicated by the determined crystal structures. Complex **6**, which shows the shortest HN-Ru distance, exhibits a high chemical shift of 159.5 ppm which is in the same range, albeit lower, as some carbonylhydrido complexes of ruthenium(II).<sup>35</sup> This confirms a strong N  $\rightarrow$  Ru donation, and a corresponding large degree of deshielding at the nitrogen nucleus. This agrees with the interpretation of a significant Ru=N double bond character. For complex **5**, the amine <sup>15</sup>N chemical shift is observed at 75 ppm, which indicates a weaker HN-Ru coordination compared to **6**, in agreement with the determined N-Ru distances. The amines in the halido complexes **2-4** exhibit even lower <sup>15</sup>N chemical shifts, indicating that the X-Ru coordination is preferential to the HN-Ru coordination. Considering only the donor

strength of the halide and corresponding X-Ru distance, one should expect  $^{15}\text{N}$  coordination shift in the order  $\Delta 2 > \Delta 3 > \Delta 4$ .

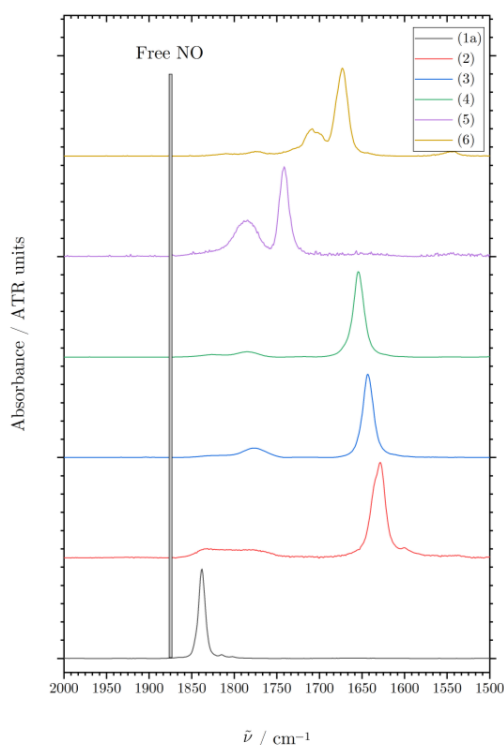


**Figure 3.** IR spectra showing the NO resonance energies for the complexes presented in this work.

However, the opposite trend is observed, which indicates that pronounced N-X electrostatic interactions contribute to the electronic shielding of the amine nucleus. The more electronegative Cl<sup>-</sup> thus deshields the N nucleus to a higher degree than Br<sup>-</sup> and I<sup>-</sup>. Comparing the  $^1\text{H}$  chemical shifts of the amine proton for complexes **2-5** shows very little effect of both the halide coordination as well as the nature of the halide. This contrasts with the proposed strong X $\cdots$ HN interaction, which would be expected to result in a significant deshielding of the hydrogen nucleus and correspondingly a large observed chemical shift. However, the low-viscosity solvents used for the NMR analysis could result in fast reorientation of the halide, and thus, in effect reduce the X $\cdots$ HN interaction. For complex **1a**, **1b** and **6** it is possible to extract the  $^{15}\text{N}$  chemical shift for the nitroso group from the  $^1\text{H}$ - $^{15}\text{N}$  HMBC experiment. In all three cases a long-range  $4J(^1\text{H}\text{-}^{15}\text{N})$  coupling between N-CH<sub>2</sub>a and NO is observed and are all in line with the interpretation of linearly coordinated NO ligands<sup>36</sup>. This coupling is not observed for the halido complexes nor complex **5**.

As indicated in Figure 3, **1a** has the NO stretching frequency at 1839 cm<sup>-1</sup> which correlates well with an NO bond order of 3 indicative of a singlet electronic configuration<sup>37</sup> in agreement with no observed paramagnetism in the NMR spectra. Conclusively, the solid state structure together with the spectroscopic nature of this compound is in strong agreement with the formulation of a ruthenium(II) central ion, coordinated by an NO<sup>+</sup> nitrosonium ligand. This interpretation is supported by the geometry around the Ru-NO bond that was observed in the crystal structure of **1a/b**, where the RuNO entity showed a linear Ru-N-O bond angle as well as a very short N-O bond length of

1.134 Å. In the 4-coordinated amido complex **6**, the ruthenium atom is in perfectly planar coordination geometry as revealed by the sum of coordination bond angles (360°), thus, the nitrosyl ligand is in the optimal coordinate set for accepting  $\pi$ -density from the ruthenium metal. The vibrational N-O resonance lies 71 cm<sup>-1</sup> below that of the analogous amino complex **5** (Table 1 and Figure 3) and the Ru-NH bonding distance is reduced to only 2.07 Å. These results reveal a strong electron donation from the amido group towards the ruthenium center upon deprotonation of the amino moiety.

However, even when the nitrosyl is positioned in the optimal position for  $\pi$ -acceptance in a push-pull synergetic fashion with the strongly  $\pi$ -donating amido moiety in the trans-position,<sup>33</sup> the stretching frequency is significantly higher than for the complexes **2-4**. The intriguing geometry exhibited by these compounds is indicatively a result of the strongly  $\pi$ -acidic NO ligand being positioned in such a way that maximum  $\pi$ Ru-density can be distributed onto the NO ligand when being in the trans-position to the potential  $\pi$ -donor. Table 3 lists the electronegativity for the free halide atoms (Cl, Br, I). The magnitude in difference appears to be reflected in the magnitude of the HN-Ru-X angle and it may be inferred that the stronger the HN $\cdots$ X interaction the more favorable the geometrical distortion observed for **2-4** becomes. With this observation in hand, characterization of the analogous fluorido complex is highly immersing as the highly electronegative fluorine atom is likely to induce even smaller HN-Ru-F and wider F-Ru-NO angles, respectively.

No low valent (oxidation state less than +2) fluorido species of ruthenium exists, and even ruthenium(II) mononuclear terminal fluorido complexes remain elusive. Hence, such species would be of high interests on its own merit. Preparation of this fluorido species is ongoing.

It is clear from the bathochromic shift of the NO bond vibration frequency of compound **2-4** when compared to **1** (see Table 1 and Figure 3) that a large amount of electron density has accumulated on the NO ligand which is expected from the reductive reaction conditions in the synthesis of **2**. Interestingly, the NO vibration frequency of **2-4** increases with decreasing electronegativity of the X-ligand (although the shift on going from **3** to **4** may be considered negligible), thus indicating that electron density accumulation on the NO ligand increases the more linear the X-Ru-NO angle and, as such, optimizes the geometry for  $\pi$ -electron interactions across the metal center. The upfield shift in the chemical shift for the PNP amine moiety in  $^{15}\text{N}$ -HMBC NMR do also show that the electron density at the metal center increases in line with the observations indicated by the IR spectra.

To exclude that the observed geometry exhibited by **2-4** were due to simple packing effects that were not obviously observable in the solid-state models, the geometries were calculated (no constraints) and they were all satisfactory reproduced. To exclude steric effects from the isopropyl substituents on the phosphorus atoms, these substituents were changed to methyl groups and re-optimized for **4**. Again, the geometric parameters around the ruthenium atom were reproduced to a satisfying level. The observed NO ligand stretching band origins in the range of 1630 to 1836 cm<sup>-1</sup> for the series of complexes **1a,b - 6** reveal a rather large span of complexation spectral red-shifts (~40 to ~245 cm<sup>-1</sup>) relative to the unbound NO molecule. In the simple harmonic oscillator approximation, these complexation bathochromic shifts relative to the bond origin of 1875 cm<sup>-1</sup> for



an unbound NO molecule indicate significantly smaller force constants for the intramolecular N-O bonds upon complexation e.g., ~5% reduction of the force constant for **1**, ~15% for **5**, ~20% for **6** and ~25% for **2-4** relative to the N-O bond lengths following the reverse order.

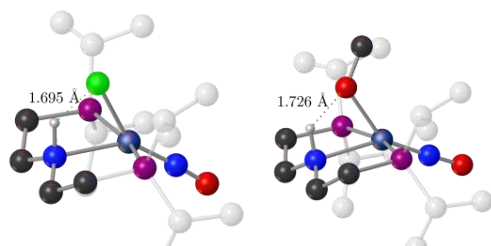


**Figure 2.** Structures as depicted by DFT of the fluorido- and methoxido complexes. Hydrogens on carbon atoms have been removed- and isopropyl substituents have been ghosted out for clarity.

The condensed phase structures and spectroscopic trends of the complexes **2-6** as well as the hypothetical complexes where  $X = F, OMe$  (methoxide) were investigated with DFT methods to gain further insight in the origin of the geometric distortions observed for **2**, **3** and **4**. Selected geometric parameters are summarized a priori in Table 1 together with the calculated N-O vibration frequencies. The trends conform satisfactory with experiments. As predicted by the discussion above, the structures of  $X = F$  or  $OMe$  as calculated by DFT do indeed show much stronger intramolecular hydrogen bonding than the experimentally determined halido complexes.

The trend in stretching frequency for the NO ligand is in line with previously reported results on the nature of the Ru-X bond when using carbonyl as the ligand reference.<sup>38</sup> Thus, we present here in support an analogous scale based on ruthenium(0) with nitrosyl as the “reporter”-ligand for the very rare ruthenium(0)-X bond. As outlined above, all data (experimental and computational) points towards the distortion being of electronic origin with the  $\pi$ -donor ability of the X-ligand being of paramount importance. As can be expected from electronegativity arguments, the Ru<sup>0</sup>-X bond becomes more ionic when ascending the halide group. This was confirmed by natural population analysis. Notably, the Ru-OMe bond is more ionic in character than is the Ru-F bond. In addition, the charge on the NO ligand decreases (more negative) in the order  $I^- < Br^- < Cl^- < F^- < MeO^-$  as would be expected based on the  $\pi$ -donor strength of these ligands and is in line with previously published results on the nature of the Ru<sup>II</sup>-X bond.<sup>39,40</sup> This indicates that the ligand field  $\sigma_X$  parameter is less significant than the ligand field  $\pi_X$  parameter.

For the sake of convenience, we will in the following discussion on the orbital interactions responsible for the observations outlined so far, align the Ru-NO bond along the coordinate z-axis as represented in Figure 4. The highly distorted trigonal bipyramidal structure shown in complex **2-4** can be explained by two different push-pull situations stabilizing antibonding interactions between the ruthenium atom and the PNP-amine and chlorido moieties. It is generally accepted that by having a  $\pi$ -acidic ligand in the equatorial plane closing the angle in the trans position to this ligand will stabilize the  $2 \times \sigma_L \rightarrow \sigma_{Ru}$  interactions<sup>17,40,41</sup> as schematically depicted in Figure 4 (left). However only by invoking  $\pi$ -interaction. The only orbital of appro-

prate symmetry available is the  $d_{xz}$  orbital. It is clear from Figure 4 (right) that the more linear the Cl-Ru-NO angle, the better the  $\pi$ -interaction between the chlorido- and nitrosyl ligand across the metal center and vice versa. As such, when descending the halide group and the angle  $\alpha$  opens, the  $X\pi \rightarrow \pi^*Ru$  interaction becomes worse and therefore less electron density is distributed into the  $\pi^*NO$ . As a result, the vibration frequency, and the Ru-NO bond distance increase. An orbital plot (supporting info) supports this simple view.

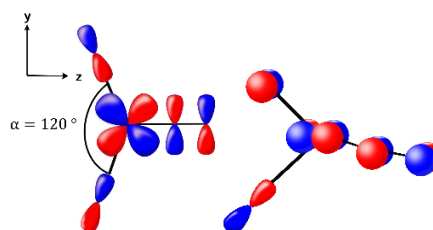


**Figure 3.** Orbital interactions in the complexes **2-4** giving rise to the acute angle trans to the linear NO ligand.

## ASSOCIATED CONTENT

Technical details about infrared and NMR measurements as well as computational details can be found in the supplementary information. This material is available free of charge via the Internet at <http://pubs.acs.org>.

## AUTHOR INFORMATION

### Corresponding Author

Martin Nielsen - Technical University of Denmark, 2800 Kgs. Lyngby, Denmark; Email: [marnie@kemi.dtu.dk](mailto:marnie@kemi.dtu.dk)

### Author Contributions

The manuscript was written through contributions of all authors. / All authors have given approval to the final version of the manuscript. / ‡These authors contributed equally. (match statement to author names with a symbol)

### Funding Sources

This work was supported by a research grant from VILLUM FONDEN (19049).

### Notes

Any additional relevant notes should be placed here.

## ACKNOWLEDGMENT

We gratefully thanks to Assoc. Prof. Susanne Lis Mossin and Dr. Mariusz Kubus for valuable discussions.

## REFERENCES

- (1) Bennett, M. A. Recent Advances in the Chemistry of Arene Complexes of Ruthenium(0) and Ruthenium(II). *Coordination Chemistry Reviews* **1997**, *166* (II), 225–254. [https://doi.org/10.1016/S0010-8545\(97\)00024-6](https://doi.org/10.1016/S0010-8545(97)00024-6).
- (2) Hoffmann, R.; Chen, M. M. L.; Elian, M. Pentacoordinate Nitrosyls. *Inorganic Chemistry* **1974**, *13* (11), 2666–2675. <https://doi.org/10.1021/ic50141a024>.
- (3) Medici, S.; Peana, M.; Pelucelli, A.; Zoroddu, M. A. Rh(I) Complexes in Catalysis: A Five-Year Trend. *Molecules* **2021**, *26* (9), 2553. <https://doi.org/10.3390/molecules26092553>.
- (4) Flügel, R.; Windmüller, B.; Gevert, O.; Werner, H. Synthesis, Molecular Structure and Reactions of Stable Square-Planar 16-Electron Ruthenium(0) Complexes: Trans-[RuCl(NO)(PR<sub>3</sub>)<sub>2</sub>]. *Chemische Berichte* **1996**, *129* (9), 1007–1013. <https://doi.org/10.1002/cber.19961290906>.
- (5) Do, Y.; Ko, S.-B.; Hwang, I.-C.; Lee, K.-E.; Lee, S. W.; Park, J. Formation of an Iodide-Bridged Diruthenium Complex from [(η<sup>5</sup>-Ph<sub>4</sub>C<sub>4</sub>COH)(CO)<sub>2</sub>RuI] and [(Ph<sub>4</sub>C<sub>4</sub>CO)(CO)<sub>2</sub>Ru]<sub>2</sub>: An Efficient Catalyst for Alcohol Oxidation with Ag<sub>2</sub>O. *Organometallics* **2009**, *28* (15), 4624–4627. <https://doi.org/10.1021/om9003434>.
- (6) Hall, D.; Williamson, R. D. Iodocarbonylbis(Triphenylphosphine)Nitrosylruthenium(0). *Crystal Structure Communications* **1974**, *3* (2), 327–230.
- (7) Bottomley, F. Nitrosyl Complexes of Ruthenium. *Coordination Chemistry Reviews* **1978**, *26* (1), 7–32. [https://doi.org/10.1016/S0010-8545\(00\)82063-9](https://doi.org/10.1016/S0010-8545(00)82063-9).
- (8) Hirano, M.; Komiya, S. Oxidative Coupling Reactions at Ruthenium(0) and Their Applications to Catalytic Homo- and Cross-Dimerizations. *Coordination Chemistry Reviews* **2016**, *314*, 182–200. <https://doi.org/10.1016/j.ccr.2015.07.008>.
- (9) Sato, H.; Fukaya, K.; Poudel, B. S.; Krische, M. J. Diols as Dienophiles: Bridged Carbocycles via Ruthenium(0)-Catalyzed Transfer Hydrogenative Cycloadditions of Cyclohexadiene or Norbornadiene. *Angewandte Chemie International Edition* **2017**, *56* (46), 14667–14671. <https://doi.org/10.1002/anie.201708189>.
- (10) Zhao, Q.; Zhang, J.; Szostak, M. Ruthenium(0)-Catalyzed Cross-Coupling of Anilines with Organoboranes by Selective Carbon–Nitrogen Cleavage. *ACS Catalysis* **2019**, *9* (9), 8171–8177. <https://doi.org/10.1021/acscatal.9b02440>.
- (11) Saxena, A.; Perez, F.; Krische, M. J. Ruthenium(0)-Catalyzed [4+2] Cycloaddition of Acetylenic Aldehydes with α-Ketols: Convergent Construction of Angucycline Ring Systems. *Angewandte Chemie* **2016**, *128* (4), 1515–1519. <https://doi.org/10.1002/ange.201509646>.
- (12) Jørgensen, C. K. *Oxidation Numbers and Oxidation States*; Springer Berlin Heidelberg: Berlin, Heidelberg, 1969. <https://doi.org/10.1007/978-3-642-87758-2>.
- (13) Feltham, R. D.; Enemark, J. H. *Topics in Inorganic and Organometallic Stereochemistry*; Geoffroy, G. L., Ed.; Topics in Stereochemistry; John Wiley & Sons, Inc.: Hoboken, NJ, USA, 1981. <https://doi.org/10.1002/9780470147214>.
- (14) Mingos, D. M. P. *Nitrosyl Complexes in Inorganic Chemistry, Biochemistry and Medicine I*; Mingos, D. M. P., Ed.; Structure and Bonding; Springer Berlin Heidelberg: Berlin, Heidelberg, 2014; Vol. 153. <https://doi.org/10.1007/978-3-642-41187-8>.
- (15) Jiang, Y.; Schirmer, B.; Blaque, O.; Fox, T.; Grimme, S.; Berke, H. The “Catalytic Nitrosyl Effect”: NO Bending Boosting the Efficiency of Ruthenium Based Alkene Hydrogenations. *Journal of the American Chemical Society* **2013**, *135* (10), 4088–4102. <https://doi.org/10.1021/ja400135d>.
- (16) Fogler, E.; Iron, M. A.; Zhang, J.; Ben-David, Y.; Diskin-Posner, Y.; Leitus, G.; Shimon, L. J. W.; Milstein, D. Ru(0) and Ru(II) Nitrosyl Pincer Complexes: Structure, Reactivity, and Catalytic Activity. *Inorganic Chemistry* **2013**, *52* (19), 11469–11479. <https://doi.org/10.1021/ic401780p>.
- (17) Enemark, J. H.; Feltham, R. D. Principles of Structure, Bonding, and Reactivity for Metal Nitrosyl Complexes. *Coordination Chemistry Reviews* **1974**, *13* (4), 339–406. [https://doi.org/10.1016/S0010-8545\(00\)80259-3](https://doi.org/10.1016/S0010-8545(00)80259-3).
- (18) Ahlrichs, R.; Bär, M.; Häser, M.; Horn, H.; Kölmel, C. Electronic Structure Calculations on Workstation Computers: The Program System Turbomole. *Chemical Physics Letters* **1989**, *162* (3), 165–169. [https://doi.org/10.1016/0009-2614\(89\)85118-8](https://doi.org/10.1016/0009-2614(89)85118-8).
- (19) Sierka, M.; Hogeckamp, A.; Ahlrichs, R. Fast Evaluation of the Coulomb Potential for Electron Densities Using Multipole Accelerated Resolution of Identity Approximation. *The Journal of Chemical Physics* **2003**, *118* (20), 9136–9148. <https://doi.org/10.1063/1.1567253>.

- (20) Perdew, J. P. Erratum: Density-Functional Approximation for the Correlation Energy of the Inhomogeneous Electron Gas. *Physical Review B* **1986**, *34* (10), 7406–7406. <https://doi.org/10.1103/PhysRevB.34.7406>.
- (21) Becke, A. D. Density-Functional Exchange-Energy Approximation with Correct Asymptotic Behavior. *Physical Review A* **1988**, *38* (6), 3098–3100. <https://doi.org/10.1103/PhysRevA.38.3098>.
- (22) Staroverov, V. N.; Scuseria, G. E.; Tao, J.; Perdew, J. P. Comparative Assessment of a New Nonempirical Density Functional: Molecules and Hydrogen-Bonded Complexes. *The Journal of Chemical Physics* **2003**, *119* (23), 12129–12137. <https://doi.org/10.1063/1.1626543>.
- (23) Weigend, F.; Ahlrichs, R. Balanced Basis Sets of Split Valence, Triple Zeta Valence and Quadruple Zeta Valence Quality for H to Rn: Design and Assessment of Accuracy. *Physical Chemistry Chemical Physics* **2005**, *7* (18), 3297. <https://doi.org/10.1039/b508541a>.
- (24) Andrae, D.; Haeussermann, U.; Dolg, M.; Stoll, H.; Preuss, H. Energy-Adjusted ab Initio Pseudopotentials for the Second and Third Row Transition Elements. *Theoretica Chimica Acta* **1990**, *77* (2), 123–141. <https://doi.org/10.1007/BF01114537>.
- (25) Peterson, K. A.; Figgen, D.; Goll, E.; Stoll, H.; Dolg, M. Systematically Convergent Basis Sets with Relativistic Pseudopotentials. II. Small-Core Pseudopotentials and Correlation Consistent Basis Sets for the Post- d Group 16–18 Elements. *The Journal of Chemical Physics* **2003**, *119* (21), 11113–11123. <https://doi.org/10.1063/1.1622924>.
- (26) Dolomanov, O. v.; Bourhis, L. J.; Gildea, R. J.; Howard, J. A. K.; Puschmann, H. OLEX2 : A Complete Structure Solution, Refinement and Analysis Program. *Journal of Applied Crystallography* **2009**, *42* (2), 339–341. <https://doi.org/10.1107/S0021889808042726>.
- (27) Sheldrick, G. M. SHELXT – Integrated Space-Group and Crystal-Structure Determination. *Acta Crystallographica Section A Foundations and Advances* **2015**, *71* (1), 3–8. <https://doi.org/10.1107/S2053273314026370>.
- (28) Sheldrick, G. M. Crystal Structure Refinement with SHELXL. *Acta Crystallogr. Sect. C Struct. Chem.* **2015**, *71* (1), 3–8. <https://doi.org/10.1107/S2053229614024218>.
- (29) Spek, A. L. Structure Validation in Chemical Crystallography. *Acta Crystallographica Section D Biological Crystallography* **2009**, *65* (2), 148–155. <https://doi.org/10.1107/S090744490804362X>.
- (30) Spek, A. L. Single-Crystal Structure Validation with the Program PLATON. *Journal of Applied Crystallography* **2003**, *36* (1), 7–13. <https://doi.org/10.1107/S0021889802022112>.
- (31) Enemark, J. H.; Feltham, R. D. Stereochemical Control of Valence. III. {CoNO}8 [Cobalt Mononitrosyl] Group in Ligand Fields of C<sub>4v</sub>, C<sub>2v</sub>, and C<sub>s</sub> Symmetry. *Journal of the American Chemical Society* **1974**, *96* (15), 5004–5005. <https://doi.org/10.1021/ja00822a058>.
- (32) Enemark, J. H.; Feltham, R. D. Stereochemical Control of Valence. II. Behavior of the {MNO}n [Metal Mononitrosyl] Group in Ligand Fields. *Journal of the American Chemical Society* **1974**, *96* (15), 5002–5004. <https://doi.org/10.1021/ja00822a057>.
- (33) Schneider, S.; Meiners, J.; Askevold, B. Cooperative Aliphatic PNP Amido Pincer Ligands – Versatile Building Blocks for Coordination Chemistry and Catalysis. *European Journal of Inorganic Chemistry* **2012**, *2012* (3), 412–429. <https://doi.org/10.1002/ejic.201100880>.
- (34) Rawat, K. S.; Pathak, B. Aliphatic Mn-PNP Complexes for the CO<sub>2</sub> Hydrogenation Reaction: A Base Free Mechanism. *Catalysis Science and Technology* **2017**, *7* (15), 3234–3242. <https://doi.org/10.1039/c7cy00737j>.
- (35) Zhang, L.; Nguyen, D. H.; Raffa, G.; Trivelli, X.; Capet, F.; Desset, S.; Paul, S.; Dumeignil, F.; Gauvin, R. M. Catalytic Conversion of Alcohols into Carboxylic Acid Salts in Water: Scope, Recycling, and Mechanistic Insights. *ChemSusChem* **2016**, *9* (12), 1413–1423. <https://doi.org/10.1002/cssc.201600243>.
- (36) Mason, J.; Larkworthy, L. F.; Moore, E. A. Nitrogen NMR Spectroscopy of Metal Nitrosyls and Related Compounds. *Chemical Reviews* **2002**, *102* (4), 913–934. <https://doi.org/10.1021/cr000075l>.
- (37) Schreiner, A. F.; Lin, S. W.; Hauser, P. J.; Hopcus, E. A.; Hamm, D. J.; Gunter, J. D. Chemistry and Optical Properties of 4d and 5d Transition Metals. III. Chemistry and Electronic Structures of Ruthenium Acidonitrosylamines, [Ru(NH<sub>3</sub>)<sub>4</sub>(NO)(L)]Q<sup>+</sup>1a. *Inorganic Chemistry* **1972**, *11* (4), 880–888. <https://doi.org/10.1021/ic50110a047>.
- (38) Coleman, K. S.; Fawcett, J.; Holloway, J. H.; Hope, E. G.; Russell, D. R. Air-Stable Ruthenium(II) and Osmium(II) Fluoride Complexes. Crystal Structures of [OC-6-13][MF<sub>2</sub>(CO)<sub>2</sub>(PR<sub>3</sub>)<sub>2</sub>] [M = Ru, PR<sub>3</sub> = PEtPh<sub>2</sub>; M = Os, PR<sub>3</sub> = PPh<sub>3</sub> or P(C<sub>6</sub>H<sub>11</sub>)<sub>3</sub>]. *Journal of the Chemical Society, Dalton Transactions* **1997**, *2* (19), 3557–3562. <https://doi.org/10.1039/a702142i>.



- (39) Ogasawara, M.; Huang, D.; Streib, W. E.; Huffman, J. C.; Gallego-Planas, N.; Maseras, F.; Eisenstein, O.; Caulton, K. G. RuX(CO)(NO)L<sub>2</sub> and Ru(CO)(NO)L<sub>2</sub> + : Ru(0) or Ru(II) or In Between? *Journal of the American Chemical Society* **1997**, *119* (37), 8642–8651. <https://doi.org/10.1021/ja970563j>.
- (40) Poulton, J. T.; Sigalas, M. P.; Folting, K.; Streib, W. E.; Eisenstein, O.; Caulton, K. G. RuHX(CO)(PR<sub>3</sub>)<sub>2</sub>: Can .Nu.CO Be a Probe for the Nature of the Ru-X Bond? *Inorganic Chemistry* **1994**, *33* (7), 1476–1485. <https://doi.org/10.1021/ic00085a043>.
- (41) Jean, Y.; Eisenstein, O. Ligand Dependent Nature of Three Possible Shapes for a D<sub>6</sub> Pentacoordinated Complex. *Polyhedron* **1988**, *7* (5), 405–407. [https://doi.org/10.1016/S0277-5387\(00\)80491-X](https://doi.org/10.1016/S0277-5387(00)80491-X).

## Chapter 7

# General conclusions and perspectives

This PhD project has been concerned about investigating the creation of new methods for the rational design of novel complexes with potential catalytic activity in mainly (de)hydrogenation reactions. This work has revolved around carbonyl hydrido species as well as nitrosyl species comprising ruthenium as the central metal ion. Through the study, a series of related carbonyl hydrido species was synthesised and characterised with multinuclear NMR spectroscopy, IR spectroscopy and single-crystal X-ray diffraction. The utility of the relatively new method of Hirschfeld refinement was evaluated in relation to the determination of the solid phase structures of well defined hydrido species. This was an attempt to disclose a more accurate protocol for the determination of the Ru-H bond distance and link it to the spectroscopic features of the Ru-H entity as well as the hydricity of the complexes under investigation. Unfortunately, a general trend between the spectroscopic nature of the Ru-H bond and the observed bond distances as obtained via the traditional IAM modeling or the Hirschfeld refinement could not be elucidated. So far, no catalytic screening of these new hydrido carbonyl complexes has been conducted. Thus, catalyst screening in (de)hydrogenation reactions under base-free conditions appears as an obvious outlook.

A series of new nitrosyl complexes has been synthesised and characterised by means of multinuclear NMR- and IR spectroscopy and single-crystal X-ray diffraction. However, not all of the crystallographically characterised compounds were spectroscopically scrutinised.

Some of the pentacoordinated nitrosyl complexes presented in this thesis show peculiar geometries that have not previously been observed for any low-valent complex of ruthenium. In addition to the observed geometries for these compounds, rare Ru-halide bonds were structurally and spectroscopically characterised. Also, Density Functional Theory was employed to gain insights into the nature of these rare bonds and coordination geometries. A natural extension of this work would comprise the preparation and characterisation of analogous complexes with strong  $\pi$ -donors and  $\sigma$ -only donors at the apical coordination site. Minimisation of the electrostatic interaction between the amine moiety and the apical

ligand through alkylation of the amino entity would likely disclose the extend of electrostatic stabilisation of the peculiar structures observed in this study.

All nitrosyl complexes in this thesis can be described with the Enemark-Feltham notation as either octahedral  $\{\text{RuNO}\}^6$  or tetra- to pentacoordinate  $\{\text{RuNO}\}^8$ . All  $\{\text{RuNO}\}^8$  complexes presented in this work are notoriously air sensitive and must be stored and handled under strictly inert conditions.

As it was disclosed during the reactivity studies of these new complexes, some  $\{\text{RuNO}\}^8$  species undergo oxidative addition reactions with protons and methyl iodide. As this points towards a very electron-rich metal, it may be worth to screen these complexes as potential catalysts in direct hydrogenation reactions of polar bonds such as carbonyl derivatives or even  $\text{CO}_2$  employing molecular hydrogen. It was investigated whether these complexes formed hydrido species under an atmosphere (1 bar) of hydrogen. No reaction was observed in this regard. However, it can not be ruled out, that these species will form hydrido species under elevated pressures of hydrogen, that could serve as potential hydrogenation catalysts.

The isolation of a tetrazenido-ruthenium(II) complex is interesting as it points towards a low- to intermediate-valent imido-ruthenium species having been transiently present. Isolation of such species would allow for characterisation of the bond between low-valent metals and strong  $\pi$ -donors. This metal-ligand combination is peculiar as repulsive filled-filled orbital interactions are expected to be significant. Thus, a low-valent ruthenium-imido species is expected to be highly reactive. As such, this species is interesting as potential catalyst in direct amidation reactions.

The parent nitrosyl complex,  $[(^i\text{Pr}_2\text{PNP})\text{RuCl}_2(\text{NO})]\text{Cl}$  has shown excellent catalytic activity in the transfer hydrogenation of acetophenone using isopropanol as hydrogen source. Currently, the catalytic activity of this complex towards transfer hydrogenation of a bigger scope of ketones and aldehydes is undertaken at different levels in the Martin Nielsen group. Additionally, the complex is currently screened for catalytic hydrogenation of olefins which already shows promising results.

The solid phase structure of the commercially available complex Ru-MACHO was irrefutably consolidated. This complex is a well-known and highly utilised (de)hydrogenation catalyst on both laboratory and industrial scale. As such, the structure of this compound should be of high interest in the field of homogeneous catalysis. The data obtained in this work does not furnish an explanation as to why the spectroscopic nature of the commercially available product points at a mixture of structural isomers presented in the product. Further analyses are needed to conclude the true composition of the commercial powder. Naturally, structure of the equally elusive and important analogue, Ru-MACHO-BH, needs to be established in future works.

Furthermore, a clean and convenient methodology for the preparation (hydride-chloride exchange with chloroform) of the *trans*-(PNP) $\text{RuCl}_2(\text{CO})$  analogue of the Ru-MACHO

complex was established, along with the high quality crystal structure of the respective dichlorido complex. The same reactivity is likely to be exhibited by the well established isopropyl analogue, ( $^i\text{Pr}_2\text{PNP}$ )RuClH(CO), thus, providing a potentially general methodology for the selective synthesis of chlorido complexes from commercially available species.

Hopefully, these works can contribute to a better understanding of future catalyst designs as well as motivate more research into the intriguing M-H bond. Even though ruthenium nitrosyl complexes are highly represented in literature, many aspects of how the nitrosyl ligand affects the reactivity of ruthenium complexes still needs to be illuminated. Hopefully, the new Ru<sup>0</sup> halido compound presented in this work might spike a renewed interest in the fundamental properties of M-H bonding modes.

# Bibliography

- [1] McCleverty, J. A. *Chem. Rev.* **2004**, *104*, 403–418.
- [2] Hoffmann, R.; Chen, M. M.; Elian, M. *Inorg. Chem.* **1974**, *13*, 2666–2675.
- [3] Gray, H. B.; Bernal, I.; Billig, E. *J. Am. Chem. Soc.* **1962**, *84*, 3404–3405.
- [4] Elian, M.; Hoffmann, R. *Inorg. Chem.* **1975**, *14*, 1058–1076.
- [5] Eisenberg, R.; Pierpont, C. G. *J. Am. Chem. Soc.* **1971**, *93*, 4905–4907.
- [6] Baranovskii, V. I.; Sizova, O. V. *Theor. Exp. Chem.* **1975**, *9*, 630–632.
- [7] Enemark, J. H.; Feltham, R. D.; Riker-Nappier, J.; Bizot, K. F. *Inorg. Chem.* **1975**, *14*, 624–632.
- [8] Mingos, D. M. P. In *Nitrosyl Complexes in Inorganic Chemistry, Biochemistry and Medicine I*; Mingos, D. M. P., Ed.; Structure and Bonding; Springer Berlin Heidelberg: Berlin, Heidelberg, 2014; Vol. 153; pp 1–260.
- [9] van Koten, G. *Pure Appl. Chem.* **1989**, *61*, 1681–1694.
- [10] Grove, D. M.; Van Koten, G.; Zoet, R.; Murrall, N. W.; Welch, A. J. *J. Am. Chem. Soc.* **1983**, *105*, 1379–1380.
- [11] Albrecht, M.; van Koten, G. *Angew. Chem. Int. Ed.* **2001**, *40*, 3750–3781.
- [12] Moulton, C. J.; Shaw, B. L. *J. Chem. Soc., Dalt. Trans.* **1976**, 1020–1024.
- [13] Van Koten, G.; Gossage, R. A. In *The Privileged Pincer-Metal Platform: Coordination Chemistry & Applications*; van Koten, G., Gossage, R. A., Eds.; Topics in Organometallic Chemistry; Springer International Publishing: Cham, 2016; Vol. 54; pp 1–369.
- [14] Plietker, B. In *Organometallic Pincer Chemistry*; van Koten, G., Milstein, D., Eds.; Topics in Organometallic Chemistry; Springer Berlin Heidelberg: Berlin, Heidelberg, 2013; Vol. 40.
- [15] Choi, J.; MacArthur, A. H.; Brookhart, M.; Goldman, A. S. *Chem. Rev.* **2011**, *111*, 1761–1779.

- [16] O'Reilly, M. E.; Veige, A. S. *Chem. Soc. Rev.* **2014**, *43*, 6325–6369.
- [17] Schluschaß, B.; Abbenseth, J.; Demeshko, S.; Finger, M.; Franke, A.; Herwig, C.; Würtele, C.; Ivanovic-Burmazovic, I.; Limberg, C.; Telser, J.; Schneider, S. *Chem. Sci.* **2019**, *10*, 10275–10282.
- [18] Abbenseth, J.; Bete, S. C.; Finger, M.; Volkmann, C.; Würtele, C.; Schneider, S. *Organometallics* **2018**, *37*, 802–811.
- [19] Ashida, Y.; Arashiba, K.; Nakajima, K.; Nishibayashi, Y. *Nature* **2019**, *568*, 536–540.
- [20] Nielsen, M. *Environ. Chem. Lett.* **2016**, *14*, 359–365.
- [21] Gravogl, L.; Heinemann, F. W.; Munz, D.; Meyer, K. *Inorg. Chem.* **2020**, *59*, 5632–5645.
- [22] Alig, L.; Eisenlohr, K. A.; Zelenkova, Y.; Rosendahl, S.; Herbst-Irmer, R.; Demeshko, S.; Holthausen, M. C.; Schneider, S. *Angew. Chem. Int. Ed.* **2022**, *61*, 1–5.
- [23] Gunanathan, C.; Milstein, D. *Science* **2013**, *341*, 1761–1779.
- [24] Delony, D.; Kinauer, M.; Diefenbach, M.; Demeshko, S.; Würtele, C.; Holthausen, M. C.; Schneider, S. *Angew. Chem. Int. Ed.* **2019**, *58*, 10971–10974.
- [25] Kinauer, M.; Diefenbach, M.; Bamberger, H.; Demeshko, S.; Reijerse, E. J.; Volkmann, C.; Würtele, C.; van Slageren, J.; de Bruin, B.; Holthausen, M. C.; Schneider, S. *Chem. Sci.* **2018**, *9*, 4325–4332.
- [26] Sun, J.; Abbenseth, J.; Verplancke, H.; Diefenbach, M.; de Bruin, B.; Hunger, D.; Würtele, C.; van Slageren, J.; Holthausen, M. C.; Schneider, S. *Nat. Chem.* **2020**, *12*, 1054–1059.
- [27] Piccirilli, L.; Lobo Justo Pinheiro, D.; Nielsen, M. *Catalysts* **2020**, *10*, 773.
- [28] Gunanathan, C.; Ben-David, Y.; Milstein, D. *Science* **2007**, *317*, 790–792.
- [29] Alig, L.; Fritz, M.; Schneider, S. *Chem. Rev.* **2019**, *119*, 2681–2751.
- [30] Su, F. M.; Cooper, C.; Geib, S. J.; Rheingold, A. L.; Mayer, J. M. *J. Am. Chem. Soc.* **1986**, *108*, 3545–3547.
- [31] Hillhouse, G. L.; Haymore, B. L. *J. Organomet. Chem.* **1978**, *162*, C23–C26.
- [32] Mazzotta, M. G.; Pichaandi, K. R.; Fanwick, P. E.; Abu-Omar, M. M. *Angew. Chem. Int. Ed.* **2014**, *53*, 8320–8322.

- [33] Gold, V., Ed. *IUPAC Compend. Chem. Terminol.*, 2nd ed.; International Union of Pure and Applied Chemistry (IUPAC): Research Triangle Park, NC, 2019; Vol. 1307; p 4328.
- [34] Moss, G. P.; Smith, P. A. S.; Tavernier, D. *Pure Appl. Chem.* **1995**, *67*, 1307–1375.
- [35] Cornils, B.; Herrmann, W. A.; Beller, M.; Paciello, R. In *Applied Homogeneous Catalysis with Organometallic Compounds*, 3rd ed.; Cornils, B., Herrmann, W. A., Beller, M., Paciello, R., Eds.; Wiley: Weinheim, 2017.
- [36] Mond, L.; Langer, C.; Quincke, F. *J. Chem. Soc., Trans.* **1890**, *57*, 749–753.
- [37] Mond, L.; Langer, C. *J. Chem. Soc., Trans.* **1891**, *59*, 1090–1093.
- [38] Brunet, J. J. *Chem. Rev.* **1990**, *90*, 1041–1059.
- [39] Rushman, P.; Van Buuren, G. N.; Shiralian, M.; Pomeroy, R. K. *Organometallics* **1983**, *2*, 693–694.
- [40] Mond, R. L.; Wallis, A. E. *J. Chem. Soc., Trans.* **1922**, *121*, 29–32.
- [41] Mond, L.; Hirtz, H.; Cowap, M. D. *J. Chem. Soc., Trans.* **1910**, *97*, 798–810.
- [42] Collman, J. P. *Acc. Chem. Res.* **1975**, *8*, 342–347.
- [43] Frenking, G.; Loschen, C.; Krapp, A.; Fau, S.; Strauss, S. H. *J. Comput. Chem.* **2007**, *28*, 117–126.
- [44] Huzinaga, S.; Miyoshi, E.; Sekiya, M. *J. Comput. Chem.* **1993**, *14*, 1440–1445.
- [45] Bagnoli, F.; Amico, D. B. D.; Calderazzo, F.; Englert, U.; Marchetti, F.; Herberich, G. E.; Pasqualetti, N.; Ramello, S. *J. Chem. Soc. Dalt. Trans.* **1996**, 4317.
- [46] Wisniak, J. *Educ. Química* **2015**, *26*, 57–65.
- [47] Goldman, A. S.; Krogh-Jespersen, K. *J. Am. Chem. Soc.* **1996**, *118*, 12159–12166.
- [48] Lupinetti, A. J.; Fau, S.; Frenking, G.; Strauss, S. H. *J. Phys. Chem. A* **1997**, *101*, 9551–9559.
- [49] Willner, H.; Aubke, F. *Organometallics* **2003**, *22*, 3612–3633.
- [50] Van der Maelen, J. F. *Organometallics* **2020**, *39*, 132–141.
- [51] Lomont, J. P.; Nguyen, S. C.; Harris, C. B. *J. Phys. Chem. A* **2013**, *117*, 2317–2324.
- [52] Frenking, G.; Fernández, I.; Holzmann, N.; Pan, S.; Krossing, I.; Zhou, M. *JACS Au* **2021**, *1*, 623–645.

- [53] Radius, U.; Bickelhaupt, F. M.; Ehlers, A. W.; Goldberg, N.; Hoffmann, R. *Inorg. Chem.* **1998**, *37*, 1080–1090.
- [54] Poulton, J. T.; Sigalas, M. P.; Folting, K.; Streib, W. E.; Eisenstein, O.; Caulton, K. G. *Inorg. Chem.* **1994**, *33*, 1476–1485.
- [55] Poulton, J. T.; Folting, K.; Streib, W. E.; Caulton, K. G. *Inorg. Chem.* **1992**, *31*, 3190–3191.
- [56] Ford, P. C. *Acc. Chem. Res.* **1981**, *14*, 31–37.
- [57] Schaper, L.; Herrmann, W. A.; Kühn, F. E. *Applied Homogeneous Catalysis with Organometallic Compounds*; Wiley, 2017; Vol. 3; pp 1689–1698.
- [58] Herrmann, W. A. *J. Organomet. Chem.* **1990**, *383*, 21–44.
- [59] Hieber, W.; Leutert, F. *Z. Anorg. Allg. Chem.* **1932**, *204*, 145–164.
- [60] Hieber, W.; Vetter, H. *Z. Anorg. Allg. Chem.* **1933**, *212*, 145–168.
- [61] Willner, H.; Bodenbinder, M.; Bröchler, R.; Hwang, G.; Rettig, S. J.; Trotter, J.; von Ahsen, B.; Westphal, U.; Jonas, V.; Thiel, W.; Aubke, F. *J. Am. Chem. Soc.* **2001**, *123*, 588–602.
- [62] Anderson, G. K.; Cross, R. J. *Acc. Chem. Res.* **1984**, *17*, 67–74.
- [63] Wink, D. A.; Kasprzak, K. S.; Maragos, C. M.; Elespuru, R. K.; Misra, M.; Dunams, T. M.; Cebula, T. A.; Koch, W. H.; Andrews, A. W.; Allen, J. S.; Keefer, L. K. *Science* **1991**, *254*, 1001–1003.
- [64] Koshland, D. E. *Science* **1992**, *258*, 1861–1861.
- [65] Culotta, E.; Koshland, D. E. *Science* **1992**, *258*, 1862–1865.
- [66] Lowenstein, C. J. *Proc. Nat. Acad. Sci.* **1999**, *96*, 10953–10954.
- [67] Pilegaard, K. *Philos. Trans. R. Soc. B Biol. Sci.* **2013**, *368*, 20130126.
- [68] Noxon, J. F. *Geophys. Res. Lett.* **1976**, *3*, 463–465.
- [69] Wanat, A.; Schnepf, T.; Stochel, G.; van Eldik, R.; Bill, E.; Wieghardt, K. *Inorg. Chem.* **2002**, *41*, 4–10.
- [70] Conradie, J.; Hopmann, K. H.; Ghosh, A. *J. Phys. Chem. B* **2010**, *114*, 8517–8524.
- [71] Monsch, G.; Klüfers, P. *Angew. Chem. Int. Ed.* **2019**, *58*, 8566–8571.
- [72] Huber, K. P.; Herzberg, G. In *Molecular Spectra and Molecular Structure*; 1., Ed.; Springer US: Boston, MA, 1979.



- [73] Enemark, J. H.; Feltham, R. D. *Proc. Nat. Acad. Sci.* **1972**, *69*, 3534–3536.
- [74] Abraham, P.; Lockwood, A.; Patka, J.; Rabinovich, M.; Sutherland, J.; Chester, K. *Toxicol. Cyanides Cyanogens*; John Wiley & Sons, Ltd: Chichester, UK, 2016; pp 129–150.
- [75] Jørgensen, C. K. *Oxidation Numbers and Oxidation States*; Springer Berlin Heidelberg: Berlin, Heidelberg, 1969.
- [76] Enemark, J.; Feltham, R. *Coord. Chem. Rev.* **1974**, *13*, 339–406.
- [77] Miessler, G. L.; Tarr, D. A. *Inorganic Chemistry*, 3rd ed.; Prentice-Hall: New Jersey, 1998; p 462.
- [78] Lewis, J.; Irving, R.; Wilkinson, G. *J. Inorg. Nucl. Chem.* **1958**, *7*, 32–37.
- [79] Enemark, J. H.; Feltham, R. D. *J. Am. Chem. Soc.* **1974**, *96*, 5002–5004.
- [80] Enemark, J. H.; Feltham, R. D. *J. Am. Chem. Soc.* **1974**, *96*, 5004–5005.
- [81] Kubota, M.; Phillips, D. A. *J. Am. Chem. Soc.* **1975**, *97*, 5637–5638.
- [82] Grundy, K. R.; Reed, C. A.; Roper, W. R. *J. Chem. Soc. D Chem. Commun.* **1970**, 1501.
- [83] La Monica, G.; Freni, M.; Cenini, S. *J. Organomet. Chem.* **1974**, *71*, 57–64.
- [84] Bottomley, F.; Brooks, W. V. F.; Clarkson, S. G.; Tong, S.-B. *J. Chem. Soc. Chem. Commun.* **1973**, 919.
- [85] Videla, M.; Jacinto, J. S.; Baggio, R.; Garland, M. T.; Singh, P.; Kaim, W.; Slep, L. D.; Olabe, J. A. *Inorg. Chem.* **2006**, *45*, 8608–8617.
- [86] Sauaia, M. G.; Da Silva, R. S. *Transit. Met. Chem.* **2003**, *28*, 254–259.
- [87] Gutiérrez, M. M.; Olabe, J. A.; Amorebieta, V. T. *Eur. J. Inorg. Chem.* **2012**, *2012*, 4433–4438.
- [88] Maciejowska, I.; Stasicka, Z.; Stochel, G.; van Eldik, R. *J. Chem. Soc. Dalton Trans.* **1999**, 3643–3649.
- [89] Johnson, M. D.; Wilkins, R. G. *Inorg. Chem.* **1984**, *23*, 231–235.
- [90] Wright, A. M.; Zaman, H. T.; Wu, G.; Hayton, T. W. *Inorg. Chem.* **2014**, *53*, 3108–3116.
- [91] Kura, S.; Kuwata, S.; Ikariya, T. *Angew. Chem. Int. Ed.* **2005**, *44*, 6406–6409.
- [92] Souza, M. L.; Roveda, A. C.; Pereira, J. C. M.; Franco, D. W. *Coord. Chem. Rev.* **2016**, *306*, 615–627.

- [93] Sharp, W. B.; Legzdins, P.; Patrick, B. O. *J. Am. Chem. Soc.* **2001**, *123*, 8143–8144.
- [94] Gavriluta, A.; Claiser, N.; Kuhn, P.; Novitchi, G.; Tommasino, J. B.; Iasco, O.; Druta, V.; Arion, V. B.; Luneau, D. *Eur. J. Inorg. Chem.* **2015**, *2015*, 1616–1624.
- [95] Haymore, B. L.; Huffman, J. C.; Butler, N. E. *Inorg. Chem.* **1983**, *22*, 168–170.
- [96] Cormary, B.; Malfant, I.; Buron-Le Cointe, M.; Toupet, L.; Delley, B.; Schaniel, D.; Mockus, N.; Woike, T.; Fejfarová, K.; Petříček, V.; Dušek, M. *Acta Crystallogr. Sect. B Struct. Sci.* **2009**, *65*, 612–623.
- [97] Fomitchev, D. V.; Furlani, T. R.; Coppens, P. *Inorg. Chem.* **1998**, *37*, 1519–1526.
- [98] Carducci, M. D.; Pressprich, M. R.; Coppens, P. *J. Am. Chem. Soc.* **1997**, *119*, 2669–2678.
- [99] Kim, C.; Novozhilova, I.; Goodman, M. S.; Bagley, K. A.; Coppens, P. *Inorg. Chem.* **2000**, *39*, 5791–5795.
- [100] Woike, T.; Kirchner, W.; Schetter, G.; Barthel, T.; Hyung-sang, K.; Haussühl, S. *Opt. Commun.* **1994**, *106*, 6–10.
- [101] Coppens, P.; Novozhilova, I.; Kovalevsky, A. *Chem. Rev.* **2002**, *102*, 861–884.
- [102] Moore, D. S.; Robinson, S. D. *Chem. Soc. Rev.* **1983**, *12*, 415–452.
- [103] Schnieders, D.; Tsui, B. T.; Sung, M. M.; Bortolus, M. R.; Schrobilgen, G. J.; Neugebauer, J.; Morris, R. H. *Inorg. Chem.* **2019**, *58*, 12467–12479.
- [104] Morris, R. H. *Inorg. Chem.* **2018**, *57*, 13809–13821.
- [105] Alderden, R. A.; Hall, M. D.; Hambley, T. W. *J. Chem. Educ.* **2006**, *83*, 728.
- [106] Basolo, F.; Pearson, R. G. *Prog. Inorg. Chem.* **1962**, *4*, 381–453.
- [107] Pidcock, A.; Richards, R. E.; Venanzi, L. M. *J. Chem. Soc. A* **1966**, 1707–1710.
- [108] See, R. F.; Kozina, D. *J. Coord. Chem.* **2013**, *66*, 490–500.
- [109] Burdett, J. K.; Albright, T. A. *Inorg. Chem.* **1979**, *18*, 2112–2120.
- [110] Pinter, B.; Van Speybroeck, V.; Waroquier, M.; Geerlings, P.; De Proft, F. *Phys. Chem. Chem. Phys.* **2013**, *15*, 17354.
- [111] Bhagan, S.; Wayland, B. B. *Inorg. Chem.* **2011**, *50*, 11011–11020.
- [112] Buckingham, A. D.; Stephens, P. J. *J. Chem. Soc.* **1964**, 2747.
- [113] Ruiz-Morales, Y.; Schreckenbach, G.; Ziegler, T. *Organometallics* **1996**, *15*, 3920–3923.

- [114] Cuesta, I. G.; De Merás, A. S.; Pelloni, S.; Lazzeretti, P. *J. Comput. Chem.* **2009**, *30*, 551–564.
- [115] Kaupp, M.; Malkina, O. L.; Malkin, V. G.; Pyykkö, P. *Chem. - A Eur. J.* **1998**, *4*, 118–126.
- [116] Xue, Z.-L.; Cook, T. M.; Lamb, A. C. *J. Organomet. Chem.* **2017**, *852*, 74–93.
- [117] Hrobárik, P.; Hrobáriková, V.; Meier, F.; Repiský, M.; Komorovský, S.; Kaupp, M. *J. Phys. Chem. A* **2011**, *115*, 5654–5659.
- [118] Vicha, J.; Novotný, J.; Komorovsky, S.; Straka, M.; Kaupp, M.; Marek, R. *Chem. Rev.* **2020**, *120*, 7065–7103.
- [119] Häller, L. J. L.; Mas-Marzá, E.; Cybulski, M. K.; Sanguramath, R. A.; Macgregor, S. A.; Mahon, M. F.; Raynaud, C.; Russell, C. A.; Whittlesey, M. K. *Dalt. Trans.* **2017**, *46*, 2861–2873.
- [120] Greif, A. H.; Hrobárik, P.; Hrobáriková, V.; Arbuznikov, A. V.; Autschbach, J.; Kaupp, M. *Inorg. Chem.* **2015**, *54*, 7199–7208.
- [121] Olgemöller, B.; Beck, W. *Inorg. Chem.* **1983**, *22*, 997–998.
- [122] Abrahams, S. C.; Ginsberg, A. P.; Knox, K. *Inorg. Chem.* **1964**, *3*, 558–567.
- [123] Bonhomme, F.; Stetson, N.; Yvon, K.; Fischer, P.; Hewat, A. *J. Alloys Compd.* **1993**, *200*, 65–68.
- [124] Morris, R. H. *Encycl. Inorg. Bioinorg. Chem.*; John Wiley & Sons, Ltd: Chichester, UK, 2018; pp 1–12.
- [125] Pearson, R. G. *Chem. Rev.* **1985**, *85*, 41–49.
- [126] Landau, S. E.; Groh, K. E.; Lough, A. J.; Morris, R. H. *Inorg. Chem.* **2002**, *41*, 2995–3007.
- [127] Abdur-Rashid, K.; Fong, T. P.; Greaves, B.; Gusev, D. G.; Hinman, J. G.; Landau, S. E.; Lough, A. J.; Morris, R. H. *J. Am. Chem. Soc.* **2000**, *122*, 9155–9171.
- [128] Sowa, J. R.; Zanutti, V.; Angelici, R. J. *Inorg. Chem.* **1991**, *30*, 4108–4110.
- [129] Wang, D.; Angelici, R. J. *J. Am. Chem. Soc.* **1996**, *118*, 935–942.
- [130] Labinger, J. A.; Komadina, K. H. *J. Organomet. Chem.* **1978**, *155*, C25–C28.
- [131] Brereton, K. R.; Smith, N. E.; Hazari, N.; Miller, A. J. *Chem. Soc. Rev.* **2020**, *49*, 7929–7948.

- [132] Wiedner, E. S.; Chambers, M. B.; Pitman, C. L.; Bullock, R. M.; Miller, A. J.; Appel, A. M. *Chem. Rev.* **2016**, *116*, 8655–8692.
- [133] Brereton, K. R.; Jadrich, C. N.; Stratakes, B. M.; Miller, A. J. M. *Organometallics* **2019**, *38*, 3104–3110.
- [134] Kumar, A.; Semwal, S.; Choudhury, J. *Chem. – A Eur. J.* **2021**, *27*, 5842–5857.
- [135] Li, W.; Huang, M.; Liu, J.; Huang, Y.-L.; Lan, X.-B.; Ye, Z.; Zhao, C.; Liu, Y.; Ke, Z. *ACS Catal.* **2021**, *11*, 10377–10382.
- [136] Jing, Y.; Ye, Z.; Su, J.; Feng, Y.; Qu, L.-B.; Liu, Y.; Ke, Z. *Catal. Sci. Technol.* **2020**, *10*, 5443–5447.
- [137] Cugny, J.; Schmale, H. W.; Fox, T.; Blacque, O.; Alfonso, M.; Berke, H. *Eur. J. Inorg. Chem.* **2006**, *2006*, 540–552.
- [138] La Placa, S. J.; Hamilton, W. C.; Ibers, J. A.; Davison, A. *Inorg. Chem.* **1969**, *8*, 1928–1935.
- [139] Fugel, M.; Jayatilaka, D.; Hupf, E.; Overgaard, J.; Hathwar, V. R.; Macchi, P.; Turner, M. J.; Howard, J. A. K.; Dolomanov, O. V.; Puschmann, H.; Iversen, B. B.; Bürgi, H.-B.; Grabowsky, S. *IUCrJ* **2018**, *5*, 32–44.
- [140] Compton, A. H. *Nature* **1915**, *95*, 343–344.
- [141] Kleemiss, F. *et al. Chem. Sci.* **2021**, *12*, 1675–1692.
- [142] Dolomanov, O. V.; Bourhis, L. J.; Gildea, R. J.; Howard, J. A. K.; Puschmann, H. *J. Appl. Crystallogr.* **2009**, *42*, 339–341.
- [143] Wieduwilt, E. K.; Macetti, G.; Malaspina, L. A.; Jayatilaka, D.; Grabowsky, S.; Genoni, A. *J. Mol. Struct.* **2020**, *1209*, 127934.
- [144] Gibson, D. H.; Pariya, C.; Mashuta, M. S. *Organometallics* **2004**, *23*, 2510–2513.
- [145] Yi, C. S.; Lee, D. W.; He, Z.; Rheingold, A. L.; Lam, K.-C.; Concolino, T. E. *Organometallics* **2000**, *19*, 2909–2915.
- [146] Sivakumar, V.; Nethaji, M.; Jagirdar, B. R.; Mathew, N. *Synth. React. Inorganic, Met. Nano-Metal Chem.* **2007**, *37*, 677–684.
- [147] Siedle, A. R.; Newmark, R. A.; Pignolet, L. H. *Inorg. Chem.* **1986**, *25*, 1345–1351.
- [148] Lindner, E.; Pautz, S.; Fawzi, R.; Steimann, M. *Organometallics* **1998**, *17*, 3006–3014.
- [149] Ghosh, P.; Panda, S.; Banerjee, S.; Lahiri, G. K. *Inorg. Chem.* **2017**, *56*, 10735–10747.
- [150] Maroń, A. M.; Małecki, J. G. *Polyhedron* **2015**, *85*, 549–559.

- [151] Han, S.-H.; Sung, K.-M.; Huh, S.; Jun, M.-J.; Whang, D.; Kim, K. *Polyhedron* **1996**, *15*, 3811–3820.
- [152] Reguillo, R.; Grellier, M.; Vautravers, N.; Vendier, L.; Sabo-Etienne, S. *J. Am. Chem. Soc.* **2010**, *132*, 7854–7855.
- [153] Chen, X.; Xue, P.; Sung, H. H. Y.; Williams, I. D.; Peruzzini, M.; Bianchini, C.; Jia, G. *Organometallics* **2005**, *24*, 4330–4332.
- [154] Filonenko, G. A.; Cosimi, E.; Lefort, L.; Conley, M. P.; Copéret, C.; Lutz, M.; Hensen, E. J. M.; Pidko, E. A. *ACS Catal.* **2014**, *4*, 2667–2671.
- [155] Sgro, M. J.; Stephan, D. W. *Dalt. Trans.* **2013**, *42*, 10460.
- [156] de Boer, S. Y.; Korstanje, T. J.; La Rooij, S. R.; Kox, R.; Reek, J. N. H.; van der Vlugt, J. I. *Organometallics* **2017**, *36*, 1541–1549.
- [157] Luconi, L.; Demirci, U. B.; Peruzzini, M.; Giambastiani, G.; Rossin, A. *Sustain. Energy Fuels* **2019**, *3*, 2583–2596.
- [158] Hernández-Juárez, M.; López-Serrano, J.; Lara, P.; Morales-Cerón, J. P.; Vaquero, M.; Álvarez, E.; Salazar, V.; Suárez, A. *Chem. - A Eur. J.* **2015**, *21*, 7540–7555.
- [159] Zhang, L.; Nguyen, D. H.; Raffa, G.; Trivelli, X.; Capet, F.; Desset, S.; Paul, S.; Dumeignil, F.; Gauvin, R. M. *ChemSusChem* **2016**, *9*, 1413–1423.
- [160] Mantina, M.; Chamberlin, A. C.; Valero, R.; Cramer, C. J.; Truhlar, D. G. *J. Phys. Chem. A* **2009**, *113*, 5806–5812.
- [161] Alberico, E.; Lennox, A. J. J.; Vogt, L. K.; Jiao, H.; Baumann, W.; Drexler, H.-J.; Nielsen, M.; Spannenberg, A.; Checinski, M. P.; Junge, H.; Beller, M. *J. Am. Chem. Soc.* **2016**, *138*, 14890–14904.
- [162] Wu, A.; Patrick, B. O.; James, B. R. *Inorg. Chem. Commun.* **2012**, *24*, 11–15.
- [163] Sun, Y.; Koehler, C.; Tan, R.; Annibale, V. T.; Song, D. *Chem. Commun.* **2011**, *47*, 8349.
- [164] Sola, E.; García-Camprubí, A.; Andrés, J. L.; Martín, M.; Plou, P. *J. Am. Chem. Soc.* **2010**, *132*, 9111–9121.
- [165] Gorgas, N.; Kirchner, K. *Acc. Chem. Res.* **2018**, *51*.
- [166] Dai, H.; Li, W.; Krause, J. A.; Guan, H. *Inorg. Chem.* **2021**, *60*, 6521–6535.
- [167] Chakraborty, S.; Leitun, G.; Milstein, D. *Angew. Chem. Int. Ed.* **2017**, *56*, 2074–2078.
- [168] Langer, R.; Leitun, G.; Ben-David, Y.; Milstein, D. *Angew. Chem. Int. Ed.* **2011**, *50*, 2120–2124.

- [169] Gorgas, N.; Stöger, B.; Veiros, L. F.; Pittenauer, E.; Allmaier, G.; Kirchner, K. *Organometallics* **2014**, *33*, 6905–6914.
- [170] Mazza, S.; Scopelliti, R.; Hu, X. *Organometallics* **2015**, *34*, 1538–1545.
- [171] Choualeb, A.; Lough, A. J.; Gusev, D. G. *Organometallics* **2007**, *26*, 3509–3515.
- [172] Salem, H.; Shimon, L. J. W.; Diskin-Posner, Y.; Leitun, G.; Ben-David, Y.; Milstein, D. *Organometallics* **2009**, *28*, 4791–4806.
- [173] Liao, Q.; Cavaillé, A.; Saffon-Merceron, N.; Mézailles, N. *Angew. Chem. Int. Ed.* **2016**, *55*, 11212–11216.
- [174] Fryzuk, M. D.; MacNeil, P. A.; Rettig, S. J. *J. Am. Chem. Soc.* **1987**, *109*, 2803–2812.
- [175] Raynal, M.; Pattacini, R.; Cazin, C. S. J.; Vallée, C.; Olivier-Bourbigou, H.; Braunschtein, P. *Organometallics* **2009**, *28*, 4028–4047.
- [176] Joost, M.; Alcaraz, G.; Vendier, L.; Poblador-Bahamonde, A.; Clot, E.; Sabo-Etienne, S. *Dalt. Trans.* **2013**, *42*, 776–781.
- [177] Almeida, S. S.; Guedes da Silva, M. C.; Jerzykiewicz, L. B.; Sobota, P.; Pombeiro, A. J. *Inorganica Chim. Acta* **2003**, *356*, 259–266.
- [178] Swartz, B. D.; Brennessel, W. W.; Jones, W. D. *Organometallics* **2011**, *30*, 1523–1529.
- [179] Erhardt, S.; Grushin, V. V.; Kilpatrick, A. H.; Macgregor, S. A.; Marshall, W. J.; Roe, D. C. *J. Am. Chem. Soc.* **2008**, *130*, 4828–4845.
- [180] Partl, G. J.; Nussbaumer, F.; Schuh, W.; Kopacka, H.; Wurst, K.; Peringer, P. *Acta Crystallogr. Sect. E Crystallogr. Commun.* **2019**, *75*, 75–80.
- [181] Leroi, G. E.; Klemperer, W. *J. Chem. Phys.* **1961**, *35*, 774–775.
- [182] Shen, C.; Yu, F.; Chu, W.-K.; Xiang, J.; Tan, P.; Luo, Y.; Feng, H.; Guo, Z.-Q.; Leung, C.-F.; Lau, T.-C. *RSC Adv.* **2016**, *6*, 87389–87399.
- [183] Philippopoulos, A. I.; Terzis, A.; Raptopoulou, C. P.; Catalano, V. J.; Falaras, P. *Eur. J. Inorg. Chem.* **2007**, *2007*, 5633–5644.
- [184] Ngo, D. X.; Del Ciello, S. A.; Barth, A. T.; Hadt, R. G.; Grubbs, R. H.; Gray, H. B.; McNicholas, B. J. *Inorg. Chem.* **2020**, *59*, 9594–9604.
- [185] Wang, Y.; Zhu, X.; Sheng, T.; Wu, X. *New J. Chem.* **2018**, *42*, 9051–9057.
- [186] Maroń, A. M.; Małecki, J. G. *Polyhedron* **2015**, *85*, 549–559.
- [187] Małecki, J. G.; Maroń, A. *Transit. Met. Chem.* **2013**, *38*, 133–142.

- [188] Maroń, A.; Małecki, J. G. *Transit. Met. Chem.* **2013**, *38*, 419–428.
- [189] Walker, I.; Strähle, J. *Z. Anorg. Allg. Chem.* **1983**, *506*, 13–21.
- [190] Fraser, R. T. M. *Anal. Chem.* **1959**, *31*, 1602–1603.
- [191] Schweitzer, D. *Croat. Chem. Acta* **2001**, *74*, 415–418.
- [192] Hansen, H. D.; Maitra, K.; Nelson, J. H. *Inorg. Chem.* **1999**, *38*, 2150–2156.
- [193] Che, C.-M.; Lai, T.-F.; Lau, K.; Mak, T. C. W. *J. Chem. Soc. Dalt. Trans.* **1988**, 239.
- [194] Nongbri, S. L.; Das, B.; Rao, K. M. *J. Organomet. Chem.* **2009**, *694*, 3881–3891.
- [195] Makino, M.; Ishizuka, T.; Ohzu, S.; Hua, J.; Kotani, H.; Kojima, T. *Inorg. Chem.* **2013**, *52*, 5507–5514.
- [196] Nakamoto, K. *Infrared and Raman Spectra of Inorganic and Coordination Compounds*; John Wiley & Sons, Inc.: Hoboken, NJ, USA, 2008.
- [197] Małecki, J. *Polyhedron* **2010**, *29*, 2489–2497.
- [198] Nielsen, M.; Kammer, A.; Cozzula, D.; Junge, H.; Gladiali, S.; Beller, M. *Angew. Chem. Int. Ed.* **2011**, *50*, 9593–9597.
- [199] Chatt, J.; Hayter, R. G. *J. Chem. Soc.* **1961**, 5507.
- [200] Jia, W.; Chen, X.; Guo, R.; Sui-Seng, C.; Amoroso, D.; Lough, A. J.; Abdur-Rashid, K. *J. Chem. Soc. Dalt. Trans.* **2009**, *2*, 8301–8307.
- [201] Morris, R. H. *Chem. Rec.* **2016**, *16*, 2644–2658.
- [202] Morris, R. H. *Chem. Rev.* **2016**, *116*, 8588–8654.
- [203] Gusev, D. G. *ACS Catal.* **2016**, *6*, 6967–6981.
- [204] Abdur-Rashid, K.; Clapham, S. E.; Hadzovic, A.; Harvey, J. N.; Lough, A. J.; Morris, R. H. *J. Am. Chem. Soc.* **2002**, *124*, 15104–15118.
- [205] Friedrich, A.; Drees, M.; Käss, M.; Herdtweck, E.; Schneider, S. *Inorg. Chem.* **2010**, *49*, 5482–5494.
- [206] Melnick, J. G.; Radosevich, A. T.; Villagrán, D.; Nocera, D. G. *Chem. Commun.* **2010**, *46*, 79–81.
- [207] Romero, P. E.; Whited, M. T.; Grubbs, R. H. *Organometallics* **2008**, *27*, 3422–3429.
- [208] Bacciu, D.; Chen, C.-H.; Surawatanawong, P.; Foxman, B. M.; Ozerov, O. V. *Inorg. Chem.* **2010**, *49*, 5328–5334.

- [209] Fout, A. R.; Basuli, F.; Fan, H.; Tomaszewski, J.; Huffman, J. C.; Baik, M.-H.; Mindiola, D. J. *Angew. Chem. Int. Ed.* **2006**, *45*, 3291–3295.
- [210] MacBeth, C. E.; Harkins, S. B.; Peters, J. C. *Can. J. Chem.* **2005**, *83*, 332–340.
- [211] Çelenligil-Çetin, R.; Watson, L. A.; Guo, C.; Foxman, B. M.; Ozerov, O. V. *Organometallics* **2005**, *24*, 186–189.
- [212] Yoo, C.; Lee, Y. *Inorg. Chem. Front.* **2016**, *3*, 849–855.
- [213] Davidson, J. J.; DeMott, J. C.; Douvris, C.; Fafard, C. M.; Bhuvanesh, N.; Chen, C.-H.; Herbert, D. E.; Lee, C.-I.; McCulloch, B. J.; Foxman, B. M.; Ozerov, O. V. *Inorg. Chem.* **2015**, *54*, 2916–2935.
- [214] Kosanovich, A. J.; Shih, W.-C.; Ozerov, O. V. *J. Organomet. Chem.* **2019**, *897*, 1–6.
- [215] Bertoli, M.; Choualeb, A.; Lough, A. J.; Moore, B.; Spasyuk, D.; Gusev, D. G. *Organometallics* **2011**, *30*, 3479–3482.
- [216] Zhang, L.; Raffa, G.; Nguyen, D. H.; Swesi, Y.; Corbel-Demailly, L.; Capet, F.; Trivelli, X.; Desset, S.; Paul, S.; Paul, J. F.; Fongarland, P.; Dumeignil, F.; Gauvin, R. M. *J. Catal.* **2016**, *340*, 331–343.
- [217] Ford, P. C.; Lorkovic, I. M. *Chem. Rev.* **2002**, *102*, 993–1018.
- [218] Wieghardt, K.; Quilitzsch, U. *Z NATURFORSCH B* **1981**, *36*, 683–686.
- [219] Wieghardt, K.; Kleine-Boymann, M.; Swiridoff, W.; Nuber, B.; Weiss, J. *J. Chem. Soc., Dalt. Trans.* **1985**, 2493–2497.
- [220] Ampßler, T.; Monsch, G.; Popp, J.; Riggermann, T.; Salvador, P.; Schröder, D.; Klüfers, P. *Angew. Chem. Int. Ed.* **2020**, *59*, 12381–12386.
- [221] Siladke, N. A.; Meihaus, K. R.; Ziller, J. W.; Fang, M.; Furche, F.; Long, J. R.; Evans, W. J. *J. Am. Chem. Soc.* **2012**, *134*, 1243–1249.
- [222] Keilwerth, M.; Hohenberger, J.; Heinemann, F. W.; Sutter, J.; Scheurer, A.; Fang, H.; Bill, E.; Neese, F.; Ye, S.; Meyer, K. *J. Am. Chem. Soc.* **2019**, *141*, 17217–17235.
- [223] Feltham, R. D.; Enemark, J. H. In *Topics in Inorganic and Organometallic Stereochemistry*; Geoffroy, G. L., Ed.; Topics in Stereochemistry; John Wiley & Sons, Inc.: Hoboken, NJ, USA, 1981; pp 155–215.
- [224] Johnson, P. L.; Enemark, J. H.; Feltham, R. D.; Swedo, K. B. *Inorg. Chem.* **1976**, *15*, 2989–2993.
- [225] Pratt, C. S.; Coyle, B. A.; Ibers, J. A. *J. Chem. Soc. A* **1971**, 2146.
- [226] Scheidt, W. R.; Piciulo, P. L. *J. Am. Chem. Soc.* **1976**, *98*, 1913–1919.



- [227] Bultitude, J.; Larkworthy, L. F.; Mason, J.; Povey, D. C.; Sandell, B. *Inorg. Chem.* **1984**, *23*, 3629–3633.
- [228] Mason, J.; Larkworthy, L. F.; Moore, E. A. *Chem. Rev.* **2002**, *102*, 913–934.
- [229] Bell, L. K.; Mingos, D. M. P.; Tew, D. G.; Larkworthy, L. F.; Sandell, B.; Povey, D. C.; Mason, J. *J. Chem. Soc. Chem. Commun.* **1983**, 125–126.
- [230] Mason, J.; Mingos, D. M. P.; Schaefer, J.; Sherman, D.; Stejskal, E. O. *J. Chem. Soc. Chem. Commun.* **1985**, 444.
- [231] Gaviglio, C.; Ben-David, Y.; Shimon, L. J. W.; Doctorovich, F.; Milstein, D. *Organometallics* **2009**, *28*, 1917–1926.
- [232] Mason, J. *Chem. Rev.* **1981**, *81*, 205–227.
- [233] Pople, J. A. *Discuss. Faraday Soc.* **1962**, *34*, 7.
- [234] De La Cruz, C.; Sheppard, N. *Spectrochim. Acta Part A Mol. Biomol. Spectrosc.* **2011**, *78*, 7–28.
- [235] Fairy, M. B.; Irving, R. J. *J. Chem. Soc. A* **1966**, *11*, 475.
- [236] Fogler, E.; Iron, M. A.; Zhang, J.; Ben-David, Y.; Diskin-Posner, Y.; Leitun, G.; Shimon, L. J.; Milstein, D. *Inorg. Chem.* **2013**, *52*, 11469–11479.
- [237] Serli, B.; Zangrando, E.; Iengo, E.; Alessio, E. *Inorganica Chim. Acta* **2002**, *339*, 265–272.
- [238] Kimura, T.; Sakurai, T.; Shima, M.; Togano, T.; Mukaida, M.; Nomura, T. *Inorganica Chim. Acta* **1983**, *69*, 135–140.
- [239] Kütt, A.; Selberg, S.; Kaljurand, I.; Tshepelevitsh, S.; Heering, A.; Darnell, A.; Kaupmees, K.; Piirsalu, M.; Leito, I. *Tetrahedron Lett.* **2018**, *59*, 3738–3748.
- [240] Askevold, B.; Friedrich, A.; Buchner, M. R.; Lewall, B.; Filippou, A. C.; Herdtweck, E.; Schneider, S. *J. Organomet. Chem.* **2013**, *744*, 35–40.
- [241] Schneider, S.; Meiners, J.; Askevold, B. *Eur. J. Inorg. Chem.* **2012**, *2012*, 412–429.
- [242] Bruch, Q. J.; Lindley, B. M.; Askevold, B.; Schneider, S.; Miller, A. J. *Inorg. Chem.* **2018**, *57*, 1964–1975.
- [243] Wellala, N. P. N.; Luebking, J. D.; Krause, J. A.; Guan, H. *ACS Omega* **2018**, *3*, 4986–5001.
- [244] Anaby, A.; Schelwies, M.; Schwaben, J.; Rominger, F.; Hashmi, A. S. K.; Schaub, T. *Organometallics* **2018**, *37*, 2193–2201.

- [245] Lagaditis, P. O.; Schluschaß, B.; Demeshko, S.; Würtele, C.; Schneider, S. *Inorg. Chem.* **2016**, *55*, 4529–4536.
- [246] Hamada, Y.; Tsuboi, M.; Matsuzawa, T.; Yamanouchi, K.; Kuchitsu, K.; Koga, Y.; Kondo, S. *J. Mol. Spectrosc.* **1984**, *105*, 453–464.
- [247] Choi, C. H.; Kertesz, M. *J. Phys. Chem. A* **1997**, *101*, 3823–3831.
- [248] Vaska, L. *Science* **1963**, *140*, 809–810.
- [249] La Placa, S. J.; Ibers, J. A. *J. Am. Chem. Soc.* **1965**, *87*, 2581–2586.
- [250] Lebel, H.; Ladjel, C.; Bélanger-Gariépy, F.; Schaper, F. *J. Organomet. Chem.* **2008**, *693*, 2645–2648.
- [251] Fogler, E.; Efremenko, I.; Gargir, M.; Leitus, G.; Diskin-Posner, Y.; Ben-David, Y.; Martin, J. M.; Milstein, D. *Inorg. Chem.* **2015**, *54*, 2253–2263.
- [252] Tallman, R. L.; Margrave, J. L.; Bailey, S. W. *J. Am. Chem. Soc.* **1957**, *79*, 2979–2980.
- [253] Baek, Y.; Betley, T. A. *J. Am. Chem. Soc.* **2019**, *141*, 7797–7806.
- [254] Amisial, L. T. D.; Dai, X.; Kinney, R. A.; Krishnaswamy, A.; Warren, T. H. *Inorg. Chem.* **2004**, *43*, 6537–6539.
- [255] Aldrich, K. E.; Fales, B. S.; Singh, A. K.; Staples, R. J.; Levine, B. G.; McCracken, J.; Smith, M. R.; Odom, A. L. *Inorg. Chem.* **2019**, *58*, 11699–11715.
- [256] Vaddypally, S.; McKendry, I. G.; Tomlinson, W.; Hooper, J. P.; Zdilla, M. J. *Chem. – A Eur. J.* **2016**, *22*, 10548–10557.
- [257] Park, J. Y.; Kim, Y.; Bae, D. Y.; Rhee, Y. H.; Park, J. *Organometallics* **2017**, *36*, 3471–3476.
- [258] Law, S.-M.; Chen, D.; Chan, S. L.-F.; Guan, X.; Tsui, W.-M.; Huang, J.-S.; Zhu, N.; Che, C.-M. *Chem. – A Eur. J.* **2014**, *20*, 11035–11047.
- [259] Intrieri, D.; Caselli, A.; Ragaini, F.; Macchi, P.; Casati, N.; Gallo, E. *Eur. J. Inorg. Chem.* **2012**, *2012*, 569–580.
- [260] Fantauzzi, S.; Gallo, E.; Caselli, A.; Ragaini, F.; Casati, N.; Macchi, P.; Cenini, S. *Chem. Commun.* **2009**, 3952.
- [261] Risse, J.; Dutta, B.; Solari, E.; Scopelliti, R.; Severin, K. *Z. Anorg. Allg. Chem.* **2014**, *640*, 1322–1329.
- [262] Aldrich, K. E.; Odom, A. L. *Chem. Commun.* **2019**, *55*, 4403–4406.

- [263] Danopoulos, A. A.; Wilkinson, G.; Hussain-Bates, B.; Hursthouse, M. B. *Polyhedron* **1992**, *11*, 2961–2964.
- [264] Shing, K.-P.; Wan, Q.; Chang, X.-Y.; Che, C.-M. *Chem. Commun.* **2020**, *56*, 4428–4431.
- [265] Singh, A. K.; Levine, B. G.; Staples, R. J.; Odom, A. L. *Chem. Commun.* **2013**, *49*, 10799.
- [266] Takaoka, A.; Gerber, L. C. H.; Peters, J. C. *Angew. Chem. Int. Ed.* **2010**, *49*, 4088–4091.
- [267] Walstrom, A. N.; Fullmer, B. C.; Fan, H.; Pink, M.; Buschhorn, D. T.; Caulton, K. G. *Inorg. Chem.* **2008**, *47*, 9002–9009.
- [268] Miller, G. A.; Lee, S. W.; Trogler, W. C. *Organometallics* **1989**, *8*, 738–744.
- [269] Daw, P.; Kumar, A.; Espinosa-Jalapa, N. A.; Diskin-Posner, Y.; Ben-David, Y.; Milstein, D. *ACS Catal.* **2018**, *8*, 7734–7741.
- [270] Mo, Z.; Shima, T.; Hou, Z. *Angew. Chem. Int. Ed.* **2020**, *59*, 8635–8644.
- [271] Abbenseth, J.; Finger, M.; Würtele, C.; Kasanmascheff, M.; Schneider, S. *Inorg. Chem. Front.* **2016**, *3*, 469–477.
- [272] Schneck, F.; Finger, M.; Tromp, M.; Schneider, S. *Chem. - A Eur. J.* **2017**, *23*, 33–37.
- [273] Hung, Y.-T.; Chen, M.-T.; Huang, M.-H.; Kao, T.-Y.; Liu, Y.-S.; Liang, L.-C. *Inorg. Chem. Front.* **2014**, *1*, 405.
- [274] Yu, C.-H.; Zhu, C.; Ji, X.; Hu, W.; Xie, H.; Bhuvanesh, N.; Fang, L.; Ozerov, O. V. *Inorg. Chem. Front.* **2020**, *7*, 4357–4366.
- [275] Huang, M.-H.; Liang, L.-C. *Organometallics* **2004**, *23*, 2813–2816.
- [276] Liang, L.-C.; Chien, P.-S.; Huang, Y.-L. *J. Am. Chem. Soc.* **2006**, *128*, 15562–15563.
- [277] Liang, L.-C.; Chien, P.-S.; Lin, J.-M.; Huang, M.-H.; Huang, Y.-L.; Liao, J.-H. *Organometallics* **2006**, *25*, 1399–1411.
- [278] Liang, L.-C.; Hung, Y.-T.; Huang, Y.-L.; Chien, P.-S.; Lee, P.-Y.; Chen, W.-C. *Organometallics* **2012**, *31*, 700–708.
- [279] Huang, M.; Lee, W.; Zou, X.; Lee, C.; Hong, S.; Liang, L. *Applied Organometallic Chemistry* **2021**, *35*, 1–11.
- [280] Liang, L.-C.; Lin, J.-M.; Lee, W.-Y. *Chem. Commun.* **2005**, 2462.

- [281] Whited, M. T.; Zhu, Y.; Timpa, S. D.; Chen, C.-H.; Foxman, B. M.; Ozerov, O. V.; Grubbs, R. H. *Organometallics* **2009**, *28*, 4560–4570.
- [282] Whited, M. T.; Grubbs, R. H. *Organometallics* **2008**, *27*, 5737–5740.
- [283] Radosevich, A. T.; Melnick, J. G.; Stoian, S. A.; Bacciu, D.; Chen, C.-H.; Foxman, B. M.; Ozerov, O. V.; Nocera, D. G. *Inorg. Chem.* **2009**, *48*, 9214–9221.
- [284] Foley, B. J.; Palit, C. M.; Bhuvanesh, N.; Zhou, J.; Ozerov, O. V. *Chem. Sci.* **2020**, *11*, 6075–6084.
- [285] Zhu, Y.; Smith, D. A.; Herbert, D. E.; Gatard, S.; Ozerov, O. V. *Chem. Commun.* **2012**, *48*, 218–220.
- [286] Liang, L.-C.; Chien, P.-S.; Hsiao, Y.-C.; Li, C.-W.; Chang, C.-H. *J. Organomet. Chem.* **2011**, *696*, 3961–3965.
- [287] Kilgore, U. J.; Yang, X.; Tomaszewski, J.; Huffman, J. C.; Mindiola, D. J. *Inorg. Chem.* **2006**, *45*, 10712–10721.
- [288] Kurogi, T.; Carroll, P. J.; Mindiola, D. J. *J. Am. Chem. Soc.* **2016**, *138*, 4306–4309.
- [289] Bailey, B. C.; Fout, A. R.; Fan, H.; Tomaszewski, J.; Huffman, J. C.; Mindiola, D. J. *Angew. Chem. Int. Ed.* **2007**, *46*, 8246–8249.
- [290] Kurogi, T.; Manor, B. C.; Carroll, P. J.; Mindiola, D. J. *Polyhedron* **2017**, *125*, 80–85.
- [291] Bordwell, F. G.; Branca, J. C.; Hughes, D. L.; Olmstead, W. N. *J. Org. Chem.* **1980**, *45*, 3305–3313.
- [292] Bordwell, F. G.; Drucker, G. E.; Fried, H. E. *J. Org. Chem.* **1981**, *46*, 632–635.
- [293] Lagaditis, P. O.; Lough, A. J.; Morris, R. H. *J. Am. Chem. Soc.* **2011**, *133*, 9662–9665.
- [294] Käck, M.; Friedrich, A.; Drees, M.; Schneider, S. *Angew. Chem.* **2009**, *121*, 922–924.
- [295] Cui, X.; Li, W.; Ryabchuk, P.; Junge, K.; Beller, M. *Nat. Catal.* **2018**, *1*, 385–397.
- [296] Britovsek, G. J. P.; Gibson, V. C.; Wass, D. F. *Angew. Chem. Int. Ed.* **1999**, *38*, 428–447.
- [297] Trnka, T. M.; Grubbs, R. H. *Acc. Chem. Res.* **2001**, *34*, 18–29.
- [298] Dub, P. A.; Gordon, J. C. *Nat. Rev. Chem.* **2018**, *2*, 396–408.
- [299] Yun, O. *Proc. Nat. Acad. Sci.* **2005**, *102*, 16913–16915.
- [300] Shamiri, A.; Chakrabarti, M.; Jahan, S.; Hussain, M.; Kaminsky, W.; Aravind, P.; Yehye, W. *Materials (Basel)*. **2014**, *7*, 5069–5108.

- [301] Grubbs, R. H. *Adv. Synth. Catal.* **2007**, *349*, 34–40.
- [302] Schrock, R. R. *Adv. Synth. Catal.* **2007**, *349*, 41–53.
- [303] Noyori, R. *Adv. Synth. Catal.* **2003**, *345*, 15–32.
- [304] Knowles, W. S. *Adv. Synth. Catal.* **2003**, *345*, 3–13.
- [305] Braude, E. A.; Linstead, R. P. *J. Chem. Soc.* **1954**, 3544.
- [306] Hadad, Y.; Husbands, J.; Henbest, H.; Mitchell, T. *Proc. Chem. Soc. London* **1964**, 361.
- [307] Trocha-Grimshaw, J.; Henbest, H. B. *Chem. Commun. (London)* **1967**, 544–544.
- [308] McPartlin, M.; Mason, R. *Chem. Commun. (London)* **1967**, 545–546.
- [309] Sasson, Y.; Blum, J. *Tetrahedron Lett.* **1971**, *12*, 2167–2170.
- [310] Sasson, Y.; Blum, J. *J. Org. Chem.* **1975**, *40*, 1887–1896.
- [311] Chowdhury, R. L.; Bäckvall, J.-E. *J. Chem. Soc., Chem. Commun.* **1991**, *43*, 1063–1064.
- [312] Cohen, R.; Graves, C. R.; Nguyen, S. T.; Martin, J. M. L.; Ratner, M. A. *J. Am. Chem. Soc.* **2004**, *126*, 14796–14803.
- [313] Meerwein, H.; Schmidt, R. *Justus Liebig's Ann. Chem.* **1925**, *444*, 221–238.
- [314] Oppenauer, R. V. *Recl. des Trav. Chim. des Pays-Bas* **2010**, *56*, 137–144.
- [315] de Graauw, C. F.; Peters, J. A.; van Bekkum, H.; Huskens, J. *Synthesis (Stuttg.)* **1994**, *1994*, 1007–1017.
- [316] Constable, D. J. C.; Dunn, P. J.; Hayler, J. D.; Humphrey, G. R.; Leazer, Jr., J. L.; Linderman, R. J.; Lorenz, K.; Manley, J.; Pearlman, B. A.; Wells, A.; Zaks, A.; Zhang, T. Y. *Green Chem.* **2007**, *9*, 411–420.
- [317] Noyori, R.; Hashiguchi, S. *Acc. Chem. Res.* **1997**, *30*, 97–102.
- [318] Sui-Seng, C.; Freutel, F.; Lough, A. J.; Morris, R. H. *Angew. Chem. Int. Ed.* **2008**, *47*, 940–943.
- [319] Khusnutdinova, J. R.; Milstein, D. *Angew. Chem. Int. Ed.* **2015**, *54*, 12236–12273.
- [320] Eisenstein, O.; Crabtree, R. H. *New J. Chem.* **2013**, *37*, 21–27.
- [321] Casey, C. P.; Singer, S. W.; Powell, D. R.; Hayashi, R. K.; Kavana, M. *J. Am. Chem. Soc.* **2001**, *123*, 1090–1100.
- [322] Milstein, D. *Topics in Catalysis* **2010**, *53*, 915–923.

- [323] Billinger, R. D.; Rose, A. *J. Chem. Educ.* **1930**, *7*, 1138.
- [324] Smith, H. A. *J. Chem. Educ.* **1937**, *14*, 479.
- [325] Boyer, J. L.; Rochford, J.; Tsai, M.-K.; Muckerman, J. T.; Fujita, E. *Coord. Chem. Rev.* **2010**, *254*, 309–330.
- [326] Luca, O. R.; Crabtree, R. H. *Chem. Soc. Rev.* **2013**, *42*, 1440–1459.
- [327] Dybov, A.; Blacque, O.; Berke, H. *Eur. J. Inorg. Chem.* **2011**, *2011*, 652–659.
- [328] Jiang, Y.; Blacque, O.; Fox, T.; Frech, C. M.; Berke, H. *Organometallics* **2009**, *28*, 5493–5504.
- [329] Jiang, Y.; Berke, H. *Chem. Commun.* **2007**, 3571.
- [330] Gallego, C. M.; Mazzeo, A.; Gaviglio, C.; Pellegrino, J.; Doctorovich, F. *Eur. J. Inorg. Chem.* **2021**, *2021*, 4712–4730.
- [331] Himmelbauer, D.; Stöger, B.; Veiros, L. F.; Pignitter, M.; Kirchner, K. *Organometallics* **2019**, *38*, 4669–4678.
- [332] Pecak, J.; Stöger, B.; Mastalir, M.; Veiros, L. F.; Ferreira, L. P.; Pignitter, M.; Linert, W.; Kirchner, K. *Inorg. Chem.* **2019**, *58*, 4641–4646.
- [333] Pecak, J.; Eder, W.; Stöger, B.; Realista, S.; Martinho, P. N.; Calhorda, M. J.; Linert, W.; Kirchner, K. *Organometallics* **2020**, *39*, 2594–2601.
- [334] Pecak, J.; Fleissner, S.; Veiros, L. F.; Pittenauer, E.; Stöger, B.; Kirchner, K. *Organometallics* **2021**, *40*, 278–285.
- [335] Jiang, Y.; Schirmer, B.; Blacque, O.; Fox, T.; Grimme, S.; Berke, H. *J. Am. Chem. Soc.* **2013**, *135*, 4088–4102.
- [336] Ruff, A.; Kirby, C.; Chan, B. C.; O'Connor, A. R. *Organometallics* **2016**, *35*, 327–335.
- [337] Weber, S.; Veiros, L. F.; Kirchner, K. *Adv. Synth. Catal.* **2019**, *361*, 5412–5420.
- [338] Wang, R.; Han, X.; Xu, J.; Liu, P.; Li, F. *J. Org. Chem.* **2020**, *85*, 2242–2249.
- [339] Sánchez, P.; Hernández-Juárez, M.; Rendón, N.; López-Serrano, J.; Álvarez, E.; Paneque, M.; Suárez, A. *Organometallics* **2021**, *40*, 1314–1327.
- [340] Lu, S.-M.; Wang, Z.; Li, J.; Xiao, J.; Li, C. *Green Chem.* **2016**, *18*, 4553–4558.
- [341] Farrar-Tobar, R. A.; Wei, Z.; Jiao, H.; Hinze, S.; de Vries, J. G. *Chem. - A Eur. J.* **2018**, *24*, 2725–2734.
- [342] Rawat, K. S.; Pathak, B. *J. Chem. Sci.* **2018**, *130*, 65.

- [343] Farrar-Tobar, R. A.; Wozniak, B.; Savini, A.; Hinze, S.; Tin, S.; de Vries, J. G. *Angew. Chem. Int. Ed.* **2019**, *58*, 1129–1133.
- [344] Wang, Y.; Yang, G.; Xie, F.; Zhang, W. *Org. Lett.* **2018**, *20*, 6135–6139.
- [345] Soltani, O.; Ariger, M. A.; Vázquez-Villa, H.; Carreira, E. M. *Org. Lett.* **2010**, *12*, 2893–2895.
- [346] Elliott, A. G.; Green, A. G.; Diaconescu, P. L. *Dalt. Trans.* **2012**, *41*, 7852.
- [347] Brewster, T. P.; Rezayee, N. M.; Culakova, Z.; Sanford, M. S.; Goldberg, K. I. *ACS Catal.* **2016**, *6*, 3113–3117.
- [348] Satheesh, C.; Sathish Kumar, P. N.; Kumara, P. R.; Karvembu, R.; Hosamani, A.; Nethaji, M. *Applied Organometallic Chemistry* **2019**, *33*, 1–10.
- [349] Navarro, M.; Smith, C. A.; Albrecht, M. *Inorg. Chem.* **2017**, *56*, 11688–11701.
- [350] Zhang, Y.; MacIntosh, A. D.; Wong, J. L.; Bielinski, E. A.; Williard, P. G.; Mercado, B. Q.; Hazari, N.; Bernskoetter, W. H. *Chem. Sci.* **2015**, *6*, 4291–4299.
- [351] Smith, N. E.; Bernskoetter, W. H.; Hazari, N.; Mercado, B. Q. *Organometallics* **2017**, *36*, 3995–4004.
- [352] Bielinski, E. A.; Lagaditis, P. O.; Zhang, Y.; Mercado, B. Q.; Würtele, C.; Bernskoetter, W. H.; Hazari, N.; Schneider, S. *J. Am. Chem. Soc.* **2014**, *136*, 10234–10237.
- [353] Bielinski, E. A.; Förster, M.; Zhang, Y.; Bernskoetter, W. H.; Hazari, N.; Holthausen, M. C. *ACS Catal.* **2015**, *5*, 2404–2415.
- [354] Noma, H.; Miwa, Y.; Yokoyama, I.; Machida, K. *J. Mol. Struct.* **1991**, *242*, 207–219.
- [355] Kuriyama, W.; Matsumoto, T.; Ogata, O.; Ino, Y.; Aoki, K.; Tanaka, S.; Ishida, K.; Kobayashi, T.; Sayo, N.; Saito, T. *Org. Process Res. Dev.* **2012**, *16*, 166–171.
- [356] Kothandaraman, J.; Goeppert, A.; Czaun, M.; Olah, G. A.; Prakash, G. K. S. *J. Am. Chem. Soc.* **2016**, *138*, 778–781.
- [357] Kar, S.; Goeppert, A.; Prakash, G. K. S. *J. Am. Chem. Soc.* **2019**, *141*, 12518–12521.
- [358] Yang, J.; Pell, A. J.; Hedin, N.; Lyubartsev, A. *Mol. Catal.* **2021**, *506*, 111544.
- [359] Kaithal, A.; Schmitz, M.; Hölscher, M.; Leitner, W. *ChemCatChem* **2019**, *11*, 5287–5291.
- [360] Kaithal, A.; Chatterjee, B.; Werlé, C.; Leitner, W. *Angew. Chem. Int. Ed.* **2021**, *60*, 26500–26505.
- [361] Thiagarajan, S.; Gunanathan, C. *J. Am. Chem. Soc.* **2019**, *141*, 3822–3827.

- [362] Padmanaban, S.; Gunasekar, G. H.; Yoon, S. *Inorg. Chem.* **2021**, *60*, 6881–6888.
- [363] Padilla, R.; Jørgensen, M. S. B.; Paixão, M. W.; Nielsen, M. *Green Chem.* **2019**, *21*, 5195–5200.
- [364] Pinheiro, D.; Nielsen, M. *Catalysts* **2021**, *11*, 558.
- [365] Wailes, P.; Weigold, H. *J. Organomet. Chem.* **1970**, *24*, 405–411.
- [366] Chatt, J. *Science* **1968**, *160*, 723–729.
- [367] Sheldrick, G. M. *Acta Crystallogr. Sect. C Struct. Chem.* **2015**, *71*, 3–8.
- [368] Sheldrick, G. M. *Acta Crystallogr. Sect. A Found. Adv.* **2015**, *71*, 3–8.
- [369] Spek, A. L. *Acta Crystallogr. Sect. C Struct. Chem.* **2015**, *71*, 9–18.
- [370] Anzellotti, A.; Briceño, A.; Delgado, G.; Díaz de Delgado, G.; Fontal, B. *Acta Crystallogr. Sect. C Cryst. Struct. Commun.* **2002**, *58*, m355–m357.
- [371] Chauvier, C.; Imberdis, A.; Thuéry, P.; Cantat, T. *Angew. Chem. Int. Ed.* **2020**, *59*, 14019–14023.
- [372] Ogata, O.; Nara, H.; Fujiwhara, M.; Matsumura, K.; Kayaki, Y. *Org. Lett.* **2018**, *20*, 3866–3870.
- [373] Kothandaraman, J.; Czaun, M.; Goeppert, A.; Haiges, R.; Jones, J.-P.; May, R. B.; Prakash, G. K. S.; Olah, G. A. *ChemSusChem* **2015**, *8*, 1442–1451.
- [374] Ahlrichs, R.; Bär, M.; Häser, M.; Horn, H.; Kölmel, C. *Chem. Phys. Lett.* **1989**, *162*, 165–169.
- [375] Sierka, M.; Hogekamp, A.; Ahlrichs, R. *J. Chem. Phys.* **2003**, *118*, 9136–9148.
- [376] Perdew, J. P.; Burke, K.; Ernzerhof, M. *Phys. Rev. Lett.* **1996**, *77*, 3865–3868.
- [377] Weigend, F.; Ahlrichs, R. *Phys. Chem. Chem. Phys.* **2005**, *7*, 3297.
- [378] Andrae, D.; Haeussermann, U.; Dolg, M.; Stoll, H.; Preuss, H. *Theor. Chim. Acta* **1990**, *77*, 123–141.
- [379] Peterson, K. A.; Figgen, D.; Goll, E.; Stoll, H.; Dolg, M. *J. Chem. Phys.* **2003**, *119*, 11113–11123.
- [380] Pollak, P.; Weigend, F. *J. Chem. Theory Comput.* **2017**, *13*, 3696–3705.
- [381] Stejskal, E. O.; Tanner, J. E. *J. Chem. Phys.* **1965**, *42*, 288–292.



## Appendix A

# General Instrumentation

### Elemental analysis

Elemental analyses were acquired by the Micro analytical Laboratory at the Department of Chemistry, University of Copenhagen on a Thermo Fischer FlashEA 1112 analyser. All handling was conducted under ambient conditions.

### Attenuated-Total-Reflection Fourier Transform Infrared Spectroscopy

The attenuated-total-Reflectance (ATR) Fourier Transform infrared (FTIR) spectra were recorded on a VERTEX 80 vacuum FTIR spectrometer from Bruker Optics GmbH. The FTIR spectrometer was equipped with a Ge on KBr beam splitter, a liquid nitrogen cooled HgCdTe detector, a thermal global radiation source and a single-reflection germanium ATR accessory (IRIS) from PIKE Technologies Inc. Small traces of residual water vapor absorption from the interferometer were subtracted and the resulting absorption spectra were corrected for minor baseline drifts. Subsequently, extended ATR corrections were applied to account for the wavelength-dependent penetration depth of the infrared probe beam into the solid samples.

### NMR spectroscopy

NMR spectra have been measured on either an AVANCEIII-HD (Bruker) spectrometer operating at 14.1 T or an AVANCEIII (Bruker) spectrometer operating at 18.8 T. The system at 14.1 T was equipped with a 5 mm BBFO probe. The system at 18.8 T was equipped with a 5 mm TCI CryoProbe.

### Single-Crystal X-ray diffraction

All crystal batches were immersed in polybutene oil (Aldrich, > 90%) as protection against air. A suitable crystal was harvested with a MiTeGen cryo loop and mounted on a goniometer attached to a SuperNova Dual Source CCD-diffractometer. Data were collected at 120 K using Cu K $\alpha$  radiation or Mo K $\alpha$  with CrysAlisPro 1.171.41.110a (Rigaku Oxford

Diffraction, 2021) empirical absorption correction using spherical harmonics, implemented in SCALE3 ABSPACK scaling algorithm. Using Olex2<sup>142</sup> all structures were solved using SHELXT<sup>368</sup> structure solution program using Intrinsic Phasing and refined with SHELXL refinement package<sup>367</sup> using Least Squares minimization.

## Appendix B

Samples for elemental analysis of (1) and (6) had disintegrated into a dark powder upon arrival.

### B.1 General synthesis protocol for (2)-(6)

All manipulations were conducted under inert atmosphere using standard Schlenk- or glove-box techniques unless otherwise stated. All solvents were dried over activated aluminium oxide using an inert<sup>®</sup> solvent purification system (SPS).

A solution of (1) (Strem Chemicals) was prepared by treating 75 mg (159  $\mu$ moles) in 2 mL acetonitrile (VWR Denmark) via drop wise addition of 40 mg (159  $\mu$ moles) AgPF<sub>6</sub> (Merck) in 3 mL acetonitrile. The resulting suspension was stirred for 4 h in the dark at rt before the precipitated AgCl was filtered off. To the filtrate was added drop wise the appropriate tetrabutylammonium halide/pseudohalide (Sigma Aldrich) salt in equimolar amount in 2 mL acetonitrile following by stirring overnight.

**Special to (2):**

After stirring with bromide, the reaction mixture was concentrated to half the volume and left for crystallisation at  $-30^{\circ}\text{C}$  overnight the product could be collected as colourless/off-white crystals. An additional batch of crystals was obtained by repeated concentration/crystallisation as described above.

Combined yield: 75%

Elemental analysis on basis of  $\text{C}_{17}\text{H}_{38}\text{BrNOP}_2\text{Ru}$ :

Calculated: C: 39.62 H: 7.43 N: 2.72

Found: C: 39.64 H: 7.45 N: 2.91

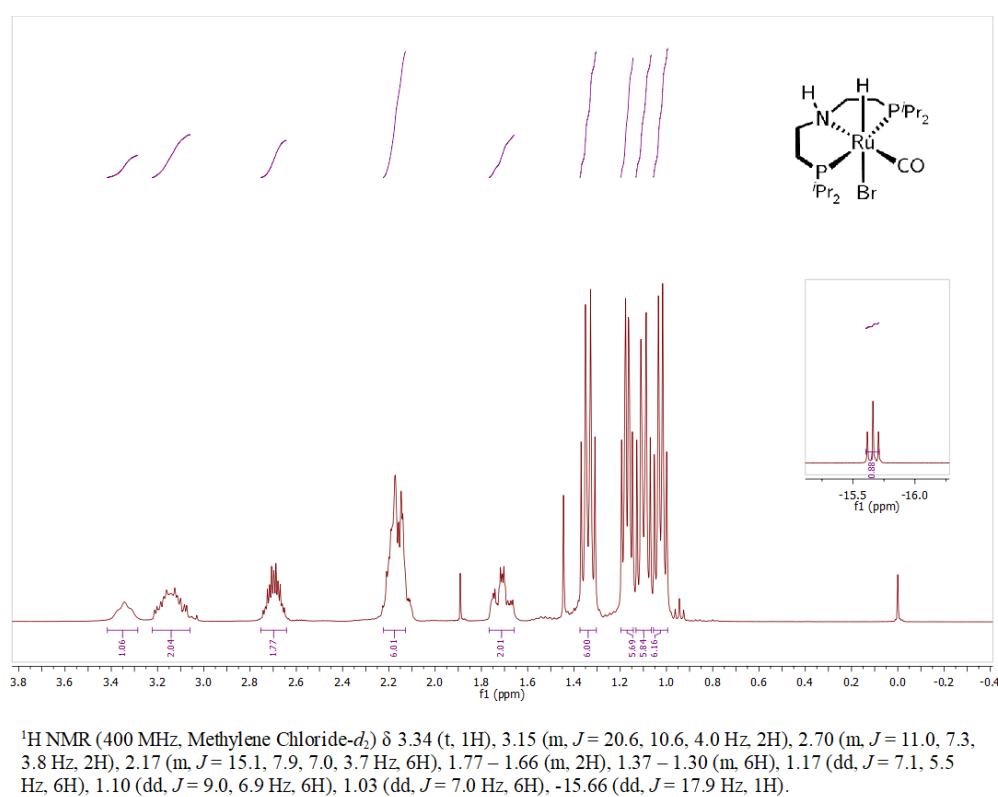


Figure B.1:  $^1\text{H-NMR}$  spectrum of (2). Referenced against TMS.

**Special to (3)**

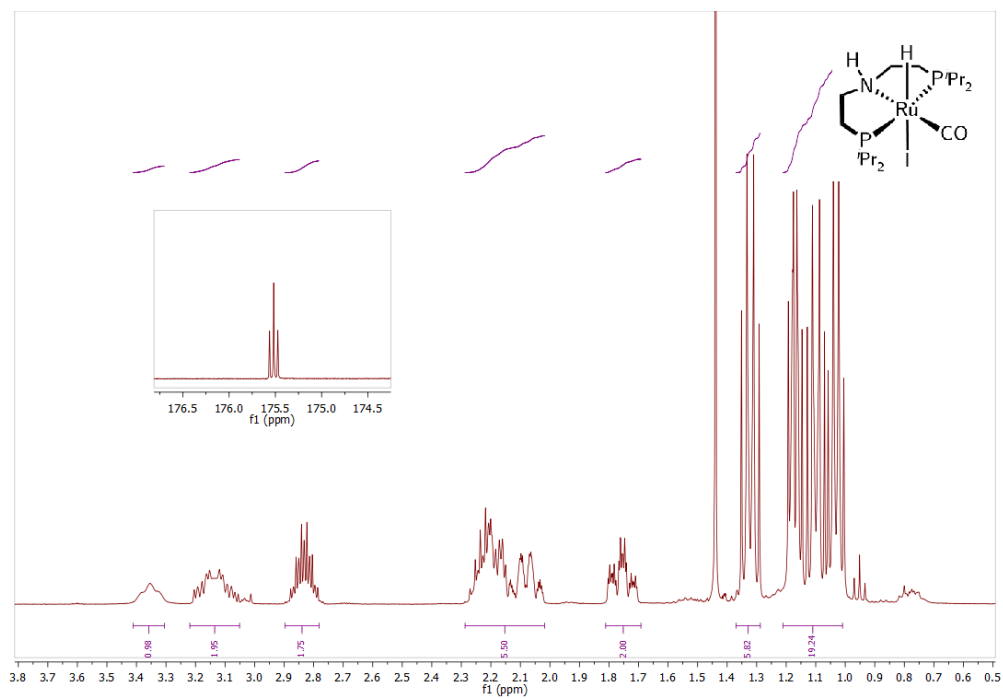
The freshly prepared and filtrated solution of (1) was evaporated until near dryness. The residue was suspended in a 4:1 (5 mL) solvent mixture of  $\text{Et}_2\text{O}$  and THF and stirred at rt overnight. The mixture was filtered and the filtrate was left for crystallisation at  $-30^{\circ}\text{C}$  overnight. The mother liquor was decanted off and the fibrous white product was washed with cold  $\text{Et}_2\text{O}$  and dried *in vacuo*.

Yield: 70%

Elemental analysis on basis of  $\text{C}_{17}\text{H}_{38}\text{INOP}_2\text{Ru}$ :

Calculated: C: 36.31 H: 6.81 N: 2.49

Found: C: 36.32 H: 6.86 N: 2.73



$^1\text{H}$  NMR (400 MHz, Methylene Chloride- $d_2$ )  $\delta$  3.35 (t, 1H), 3.22 – 3.05 (m, 2H), 2.83 (m,  $J = 11.0, 7.3, 3.6$  Hz, 2H), 2.29 – 2.02 (m, 5H), 1.75 (m,  $J = 14.2, 5.5, 2.1$  Hz, 2H), 1.37 – 1.29 (m, 6H), 1.21 – 1.01 (m, 19H), -14.02 (t,  $J = 18.0$  Hz, 1H).

Figure B.2:  $^1\text{H}$ -NMR spectrum of (3). Referenced against TMS.

**Special to (4):**

During the dropwise addition of tetrabutylammonium cyanide the product will precipitate out as a colourless powder. Decanting off the mother liquor and washing with cold acetonitrile followed by drying *in vacuo* gives the product as a white powder.

Yield: 80%

Elemental analysis on basis of  $C_{18}H_{38}N_2OP_2Ru$ :

Calculated: C: 46.84 H: 8.30 N: 6.07

Found: C: 45.75 H: 8.13 N: 5.81

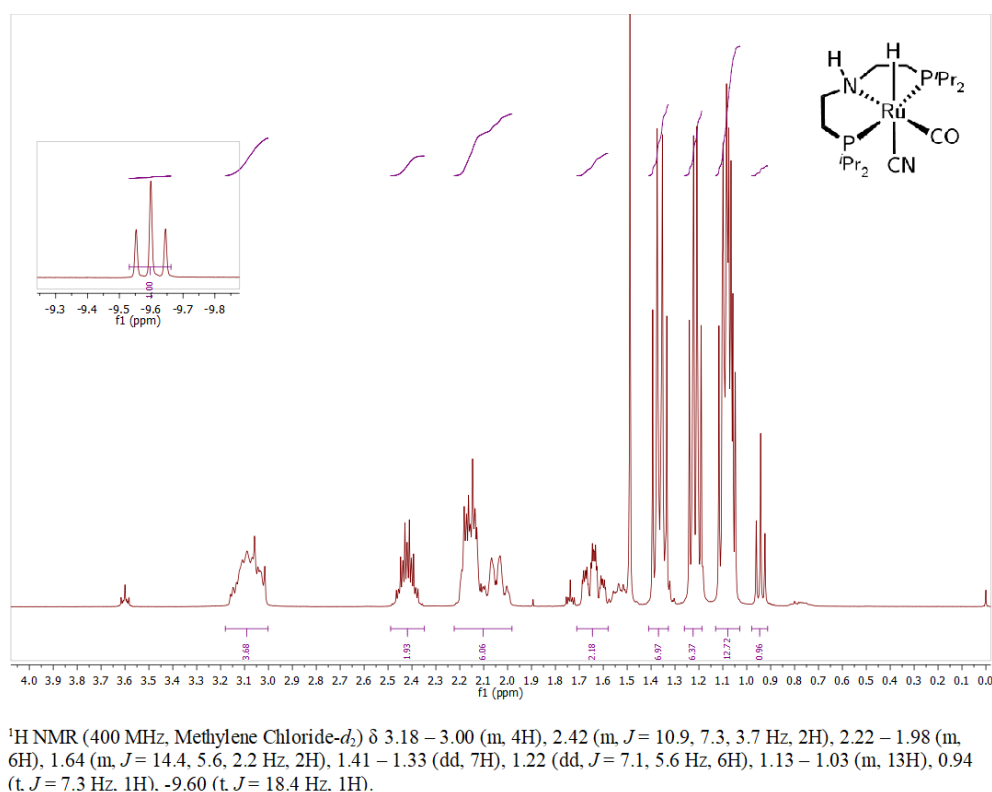


Figure B.3:  $^1H$ -NMR spectrum of (4). Referenced against TMS.

**Special to (5):**

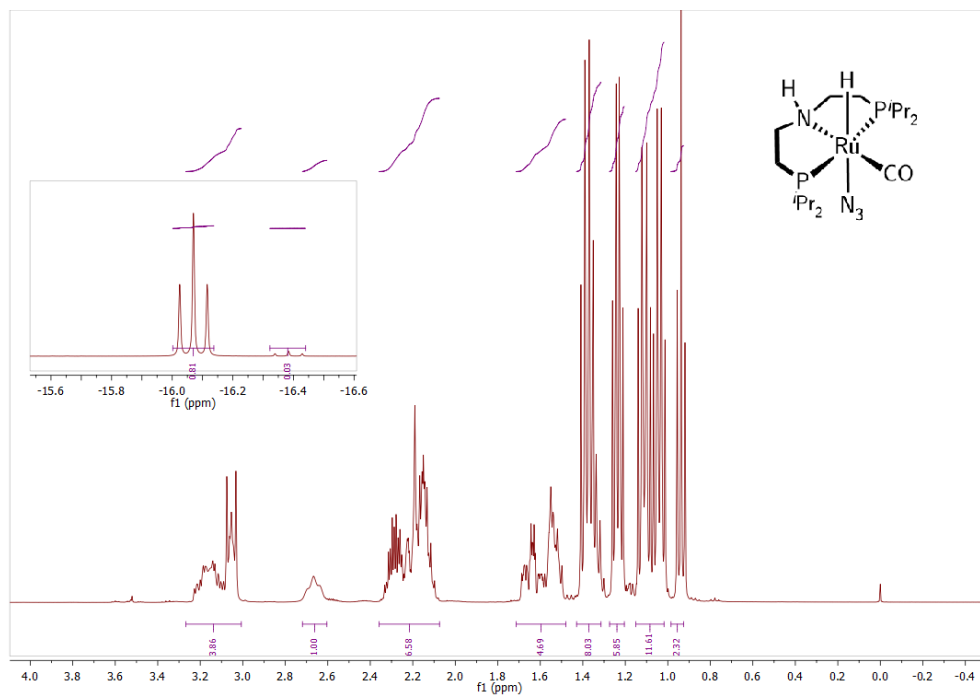
The compound could be isolated by evaporation of the solvent followed by extraction with toluene and filtration through a plug of celite. The combined extracts were evaporated until near dryness followed by dissolution in just the right amount of THF. The solution was left at  $-30^{\circ}\text{C}$  for 2 days whereby crystals of the product could be collected. An additional amount of product was obtained by concentration to half the volume followed by crystallisation as described above. The combined batches were washed with  $\text{Et}_2\text{O}$  and dried *in vacuo*.

Yield: 45%

Elemental analysis on basis of  $\text{C}_{17}\text{H}_{38}\text{N}_4\text{OP}_2\text{Ru}$ :

Calculated: C: 42.76 H: 8.02 N: 11.73

Found: C: 43.23 H: 8.09 N: 11.45



$^1\text{H}$  NMR (400 MHz, Methylene Chloride- $d_2$ )  $\delta$  3.27 – 3.01 (m, 4H), 2.72 – 2.60 (t, 1H), 2.36 – 2.07 (m, 7H), 1.71 – 1.48 (m, 5H), 1.36 (m,  $J = 14.9, 13.4, 7.4$  Hz, 8H), 1.24 (m,  $J = 7.1, 5.6$  Hz, 6H), 1.15 – 1.02 (m, 12H), 0.95 (m,  $J = 7.3$  Hz, 2H), -16.07 (t,  $J = 18.1$  Hz, 1H), -16.38 (t,  $J = 17.9$  Hz, 0H).

Figure B.4:  $^1\text{H}$ -NMR spectrum of (5). Referenced against TMS.

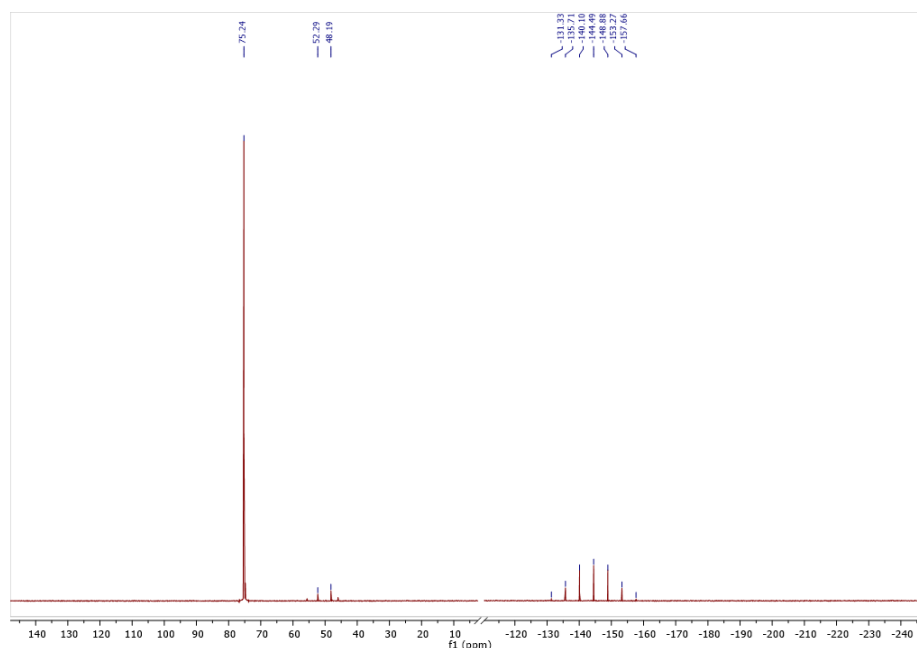


Figure B.5:  $^{31}\text{P}$ -NMR spectrum of (5). As evident by the septet at  $-157.66$  to  $-131.33$  ppm the sample still contains  $[\text{TBA}]\text{PF}_6$ .

### Special to (6):

The linkage-isomer mixture (6) can be obtained analogous to (4). However, the following protocol yielded better results: The complex (1a) was stirred in THF together with  $\text{AgSCN}$  in 3% excess in the dark over night. The resulting suspension was filtered through a plug of celite. The product was isolated by evaporation of volatiles *in vacuo*.

Yield: 77%

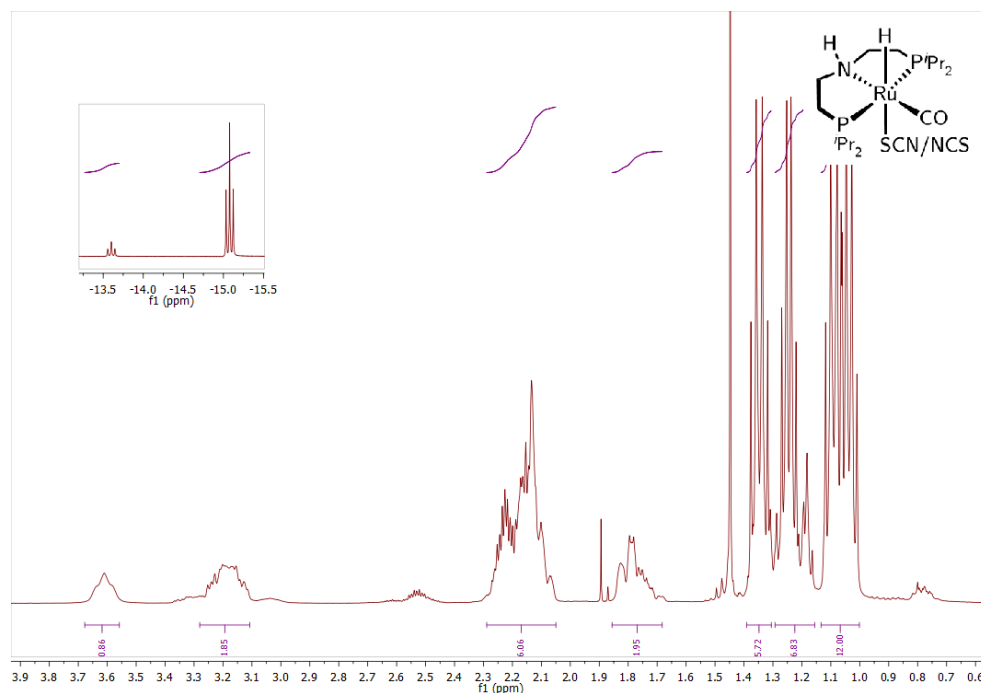
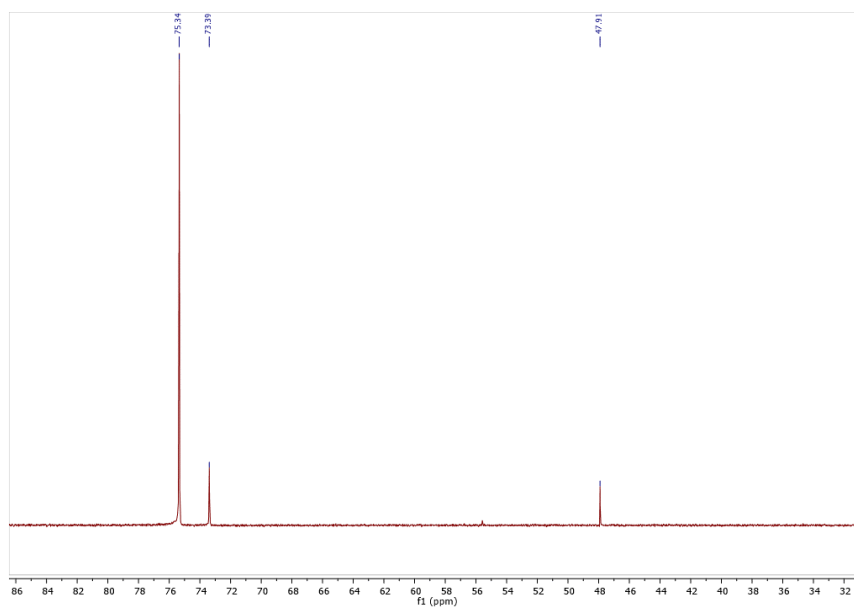
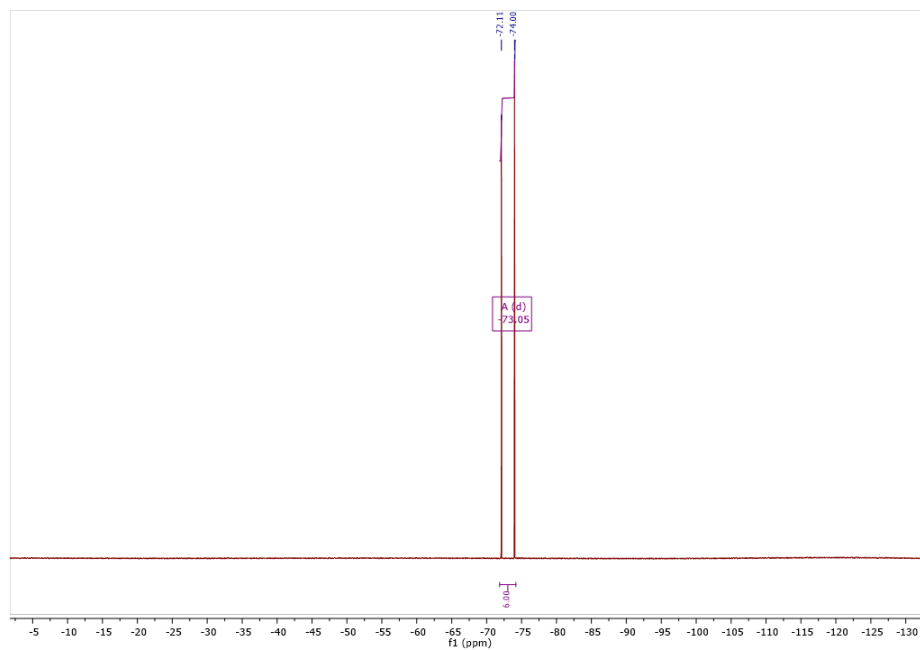


Figure B.6:  $^1\text{H}$ -NMR spectrum of (6). Referenced against TMS.



Figure B.7:  $^{31}\text{P}$ -NMR spectrum of (6).

### B.1.1 NMR spectroscopy of (1)

Figure B.8:  $^{19}\text{F}$ -NMR spectrum of (1) in  $\text{CD}_2\text{Cl}_2$ . Showing the characteristic doublet of the  $\text{PF}_6^-$  anion.

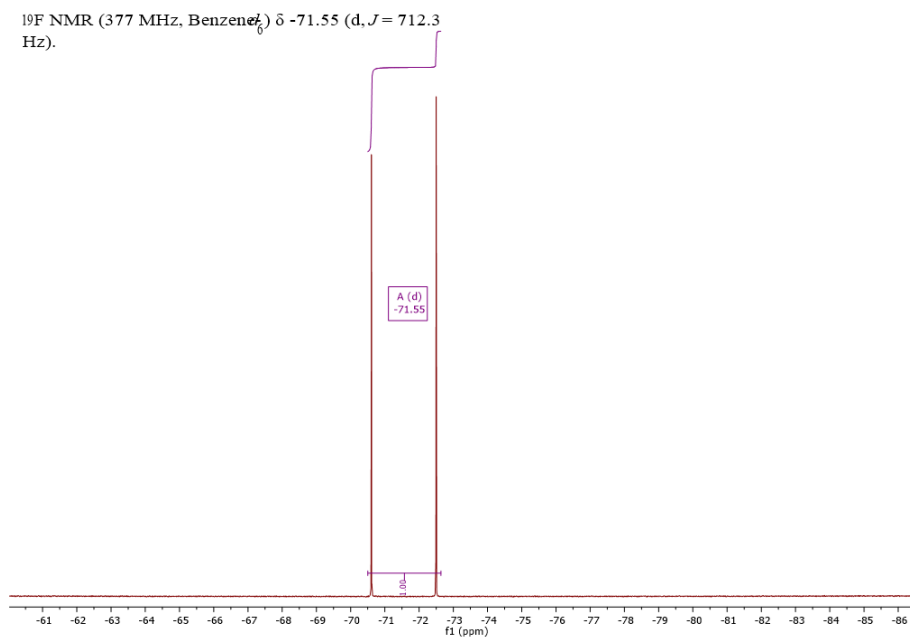


Figure B.9:  $^{19}\text{F}$ -NMR spectrum of (1) in  $\text{C}_6\text{D}_6$ . Showing the characteristic doublet of the  $\text{PF}_6^-$  anion.

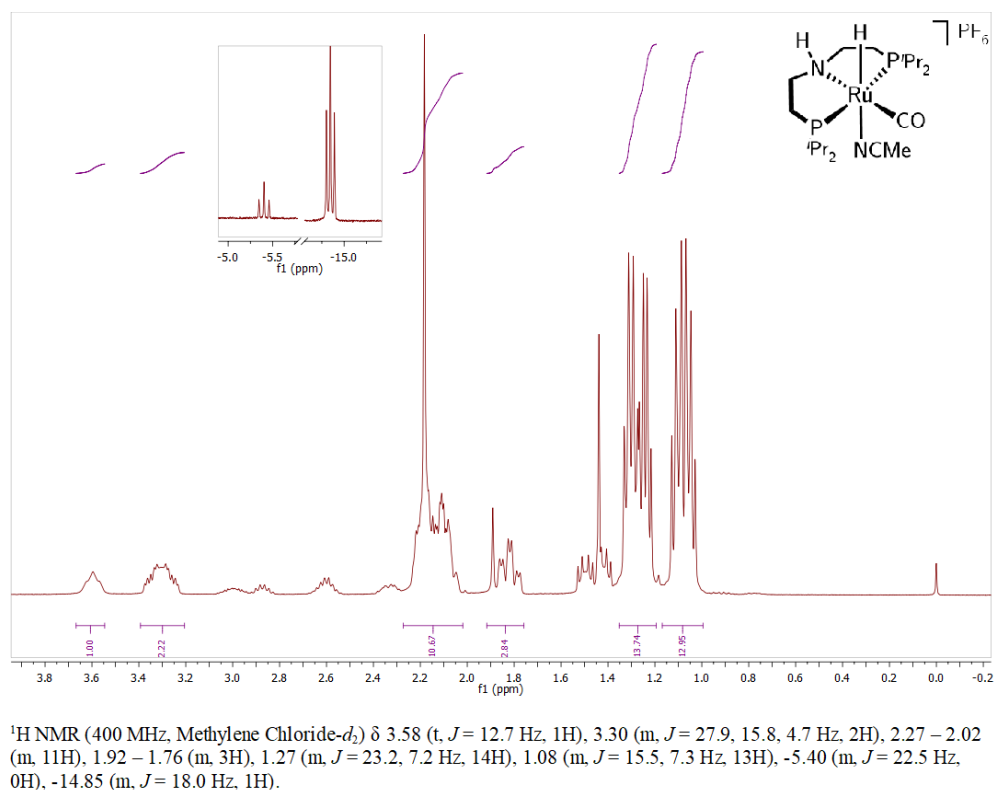
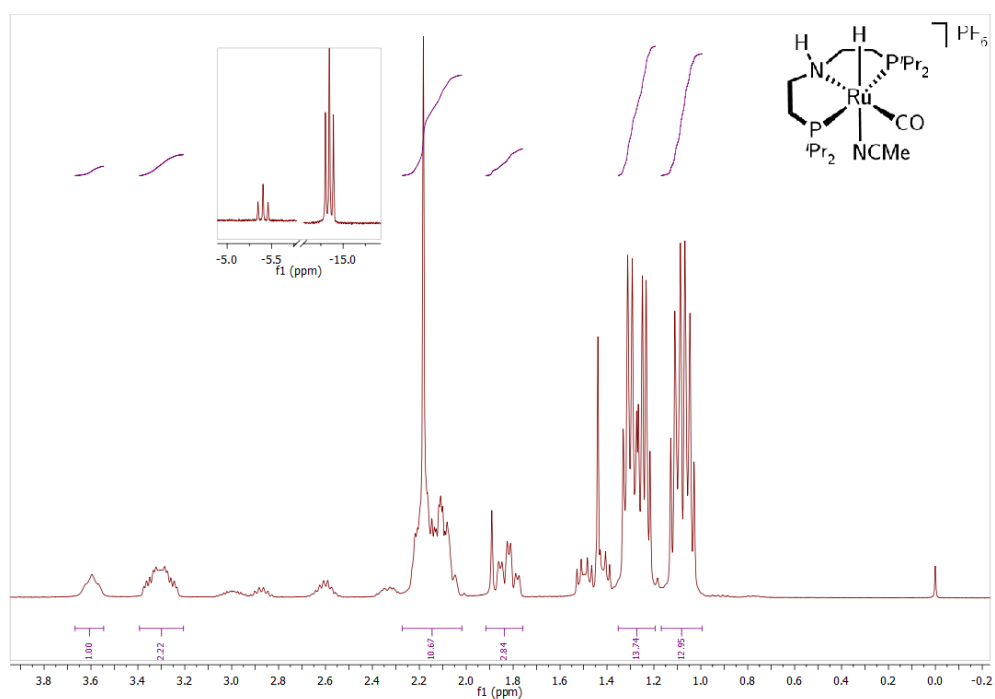


Figure B.10:  $^1\text{H}$ -NMR spectrum of (1) in  $\text{CD}_2\text{Cl}_2$ .



$^1\text{H}$  NMR (400 MHz, Methylene Chloride- $d_2$ )  $\delta$  3.58 (t,  $J = 12.7$  Hz, 1H), 3.30 (m,  $J = 27.9, 15.8, 4.7$  Hz, 2H), 2.27 – 2.02 (m, 11H), 1.92 – 1.76 (m, 3H), 1.27 (m,  $J = 23.2, 7.2$  Hz, 14H), 1.08 (m,  $J = 15.5, 7.3$  Hz, 13H), -5.40 (m,  $J = 22.5$  Hz, 0H), -14.85 (m,  $J = 18.0$  Hz, 1H).

Figure B.11:  $^1\text{H}$ -NMR spectrum of (1) in  $\text{C}_6\text{D}_6$ .

## B.2 Computational details

All calculations were performed using the Turbomole software, version 7.0.<sup>374</sup> All energies were converged to  $10^{-6}$  atomic units using the identity approximation to speed up calculations.<sup>375</sup> Geometry optimised structures were calculated using the GGA functional PBE<sup>376</sup> with def2-TZVP basis set.<sup>377</sup> The effective core potential (ECP) approximation<sup>378,379</sup> was used to account for the 28 inner core electrons of the Ru and I atoms. In the case of complex (4) the geometry optimisation converged to a saddle point. This was remedied by increasing the integration grid from m3 to m5 and using a less strict convergence criterium of  $10^{-5}$ .

Hirschfeld refinements were performed at the all electron 2-component triple- $\zeta$  level of theory (x2c-def2-TZVPall)<sup>380</sup> in conjunction with the PBE functional as above.

## B.3 Crystallographic details

Table B.1: Crystallographic experimental and refinement (IAM) details.

	(1)	(2)	(3)	(4)	(5)	(6)
Empirical formula	$C_{19}H_{41}F_6N_2OP_3Ru$	$C_{17}H_{38}BrNOP_2Ru$	$C_{21}H_{48}INO_2P_2Ru$	$C_{17}H_{38}N_2OP_2Ru$	$C_{17}H_{38}N_4OP_2Ru$	$C_{18}H_{38}N_2OP_2RuS$
Formula weight	621.53	515.42	636.54	461.53	477.54	493.59
Temperature/K	120.00(10)	119.99(10)	120.00(10)	120.00(11)	120.02(10)	120.00(10)
Crystal system	orthorhombic	monoclinic	monoclinic	monoclinic	triclinic	triclinic
Space group	$Pnma$	$P2_1/n$	$P2_1/m$	$P2_1/n$	$P\bar{1}$	$P\bar{1}$
a/Å	13.69330(10)	8.0822(2)	7.5925(2)	8.0839(2)	8.1578(3)	7.8955(3)
b/Å	13.16000(10)	13.8938(4)	13.2353(4)	13.9215(4)	11.5684(4)	15.7121(6)
c/Å	15.60600(10)	19.6587(5)	13.9591(4)	19.5012(5)	12.9734(4)	19.6257(8)
$\alpha/^\circ$	90	90	90	90	77.162(3)	101.722(3)
$\beta/^\circ$	90	93.764(2)	98.261(3)	93.483(3)	86.697(3)	94.083(3)
$\gamma/^\circ$	90	90	90	90	72.799(3)	96.574(3)
Volume/Å <sup>3</sup>	2812.26(3)	2202.76(10)	1388.18(7)	2190.60(11)	1140.30(7)	2357.02(16)
Z	5	6	4	5	1	6
$\rho_{\text{calc}}/\text{cm}^3$	1.468	1.554	1.523	1.399	1.391	1.387
$\mu/\text{mm}^{-1}$	6.616	2.675	1.808	0.870	0.840	0.898
F(000)	1280.0	1056.0	645.3	968.0	500.0	1029.0
Crystal size/mm <sup>3</sup>	? × ? × ?	? × ? × ?	? × ? × ?	? × ? × ?	? × ? × ?	? × ? × ?
Radiation	Cu K $\alpha$ ( $\lambda = 1.54184$ )	Mo K $\alpha$ ( $\lambda = 0.71073$ )	Mo K $\alpha$ ( $\lambda = 0.71073$ )	Mo K $\alpha$ ( $\lambda = 0.71073$ )	Mo K $\alpha$ ( $\lambda = 0.71073$ )	Mo K $\alpha$ ( $\lambda = 0.71073$ )
2 $\theta$ range for data collection/ $^\circ$	8.59 to 153.208	6.888 to 59.33	6.66 to 59.4	6.928 to 59.486	6.442 to 75.458	6.38 to 50.052
Index ranges	-16 $\leq h \leq 17$ , -16 $\leq k \leq 16$ , -14 $\leq l \leq 19$	-11 $\leq h \leq 10$ , -18 $\leq k \leq 19$ , -26 $\leq l \leq 26$	-10 $\leq h \leq 10$ , -18 $\leq h \leq 18$ , -19 $\leq h \leq 19$	-10 $\leq h \leq 11$ , -17 $\leq h \leq 11$ , -27 $\leq h \leq 24$	-13 $\leq h \leq 13$ , -18 $\leq h \leq 19$ , -22 $\leq h \leq 22$	-9 $\leq h \leq$ , -18 $\leq h \leq 18$ , -23 $\leq h \leq 23$
Reflections collected	27558	41748	27064	20282	23222	45614
Independent reflections	3087 ( $R_{\text{int}} = 0.0375$ , $R_{\text{sigma}} = 0.0167$ )	5777 ( $R_{\text{int}} = 0.0356$ , $R_{\text{sigma}} = 0.0236$ )	3853 ( $R_{\text{int}} = 0.0362$ , $R_{\text{sigma}} = 0.0254$ )	5489 ( $R_{\text{int}} = 0.0391$ , $R_{\text{sigma}} = 0.0432$ )	11541 ( $R_{\text{int}} = 0.0440$ , $R_{\text{sigma}} = 0.0754$ )	8309 ( $R_{\text{int}} = 0.1152$ , $R_{\text{sigma}} = 0.0996$ )
Data/restraints/parameters	3087/104/198	5777/0/220	3853/0/151	5489/0/229	11541/0/238	8309/17/520
Goodness-of-fit on F <sup>2</sup>	1.043	1.046	1.048	1.082	1.087	1.040
Final R indexes ( $I \geq 2\sigma(I)$ )	$R_1 = 0.0222$ , $wR_2 = 0.0559$	$R_1 = 0.0197$ , $wR_2 = 0.0397$	$R_1 = 0.0229$ , $wR_2 = 0.0423$	$R_1 = 0.0297$ , $wR_2 = 0.0557$	$R_1 = 0.0418$ , $wR_2 = 0.0682$	$R_1 = 0.0498$ , $wR_2 = 0.0859$
Final R indexes (all data)	$R_1 = 0.0231$ , $wR_2 = 0.0567$	$R_1 = 0.0242$ , $wR_2 = 0.0412$	$R_1 = 0.0289$ , $wR_2 = 0.0448$	$R_1 = 0.0406$ , $wR_2 = 0.0618$	$R_1 = 0.0590$ , $wR_2 = 0.0787$	$R_1 = 0.0893$ , $wR_2 = 0.1009$
Largest diff. peak/hole / e Å <sup>-3</sup>	0.56/-0.46	0.45/-0.38	0.67/-0.60	0.57/-0.39	1.53/-1.08	1.35/-0.51

Table B.2: Crystallographic experimental and Hirschfeld atom refinement details for the complexes (2)-(5).

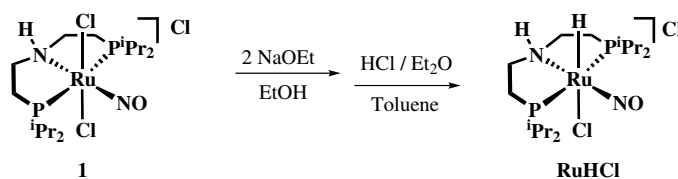
	(2)	(3)	(4)	(5)
Empirical formula	$C_{17}H_{38}BrNOP_2Ru$	$C_{17}H_{38}INOP_2Ru$	$C_{18}H_{38}N_2OP_2Ru$	$C_{17}H_{38}N_4OP_2Ru$
Formula weight	515.42	562.42	461.53	477.54
Temperature/K	119.99(10)	120.00(10)	120.00(11)	120.02(10)
Crystal system	monoclinic	monoclinic	monoclinic	triclinic
Space group	$P2_1/n$	$P2_1/m$	$P2_1/n$	$P\bar{1}$
a/Å	8.0822(2)	7.5925(2)	8.0839(2)	8.1578(3)
b/Å	13.8938(4)	13.2353(4)	13.9215(4)	11.5684(4)
c/Å	19.6587(5)	13.9591(4)	19.5012(5)	12.9734(4)
$\alpha/^\circ$	90	90	90	77.162(3)
$\beta/^\circ$	93.764(2)	98.261(3)	93.483(3)	86.697(3)
$\gamma/^\circ$	90	90	90	72.799(3)
Volume/Å <sup>3</sup>	2202.76(10)	1388.18(7)	2190.60(11)	1140.30(7)
Z	6	4	5	1
$\rho_{calc} g/cm^3$	1.554	1.346	1.399	1.391
$\mu/mm^{-1}$	2.675	1.795	0.870	0.840
F(000)	1051.3	560.2	964.1	497.6
Crystal size/mm <sup>3</sup>	? $\times$ ? $\times$ ?	? $\times$ ? $\times$ ?	? $\times$ ? $\times$ ?	? $\times$ ? $\times$ ?
Radiation	Mo K $\alpha$ ( $\lambda = 0.71073$ )	Mo K $\alpha$ ( $\lambda = 0.71073$ )	Mo K $\alpha$ ( $\lambda = 0.71073$ )	Mo K $\alpha$ ( $\lambda = 0.71073$ )
2 $\Theta$ range for data collection/ $^\circ$	6.88 to 59.32	6.66 to 59.4	6.92 to 59.48	6.442 to 75.458
Index ranges	$-11 \leq h \leq 10$ , $-18 \leq k \leq 19$ , $-26 \leq l \leq 26$	$-10 \leq h \leq 10$ , $-18 \leq h \leq 18$ , $-19 \leq h \leq 19$	$-10 \leq h \leq 11$ , $-17 \leq h \leq 11$ , $-27 \leq h \leq 24$	$-13 \leq h \leq 13$ , $-18 \leq h \leq 19$ , $-22 \leq h \leq 22$
Reflections collected	41748	27064	20282	23222
Independent reflections	5777 ( $R_{int} = 0.0356$ , $R_{sigma} = 0.0236$ )	3853 ( $R_{int} = 0.0362$ , $R_{sigma} = 0.0254$ )	5489 ( $R_{int} = 0.0391$ , $R_{sigma} = 0.0432$ )	11541 ( $R_{int} = 0.0440$ , $R_{sigma} = 0.0755$ )
Data/restraints/parameters	5777/0/550	3853/0/283	5489/0/559	11541/21/563
Goodness-of-fit on $F^2$	1.088	1.062	1.086	1.045
Final R indexes ( $I \geq 2\sigma(I)$ )	$R_1 = 0.0161$ , $wR_2 = 0.0242$	$R_1 = 0.0198$ , $wR_2 = 0.0376$	$R_1 = 0.0257$ , $wR_2 = 0.0350$	$R_1 = 0.0398$ , $wR_2 = 0.0500$
Final R indexes (all data)	$R_1 = 0.0205$ , $wR_2 = 0.0253$	$R_1 = 0.0245$ , $wR_2 = 0.0391$	$R_1 = 0.0366$ , $wR_2 = 0.0399$	$R_1 = 0.0570$ , $wR_2 = 0.0570$
Largest diff. peak/hole / e Å <sup>-3</sup>	0.43/-0.34	0.61/-0.44	0.68/-0.46	1.57/-1.29

# Appendix C

## C.1 Experimentals

The experimental procedures for complexes **1** and **1a** can be found in Chapter 6. All manipulations were conducted under nitrogen or argon atmosphere using standard Schlenk- or glovebox techniques, unless otherwise stated. Ethanol (VWR Denmark) was dried by refluxing over Mg/I<sub>2</sub> under nitrogen overnight and subsequently degassed by 3 cycles of freeze-pump-thaw and stored over 3 Å molecular sieves. Hydrocarbons were purchased from VWR Denmark and dried over Na/K alloy followed by trap-to-trap distillation and degassing by 3 cycles of freeze-pump-thaw and then stored over 3 Å molecular sieves under N<sub>2</sub> atmosphere. HCl/Et<sub>2</sub>O solution was purchased from Sigma-Aldrich. THF, acetonitrile and toluene (VWR Denmark) were flushed with N<sub>2</sub> and stored over activated aluminium oxide for drying. Deuterated solvents were purchased from Fluorochem. NaOEt was purchased from TCI Chemicals. Complex **2** was synthesised according to the procedure outlined in Chapter 6.

### C.1.1 Synthesis and spectroscopy of [(<sup>i</sup>Pr<sub>2</sub>PNP)RuClH(NO)]Cl · HCl



In a Schlenk flask 100 mg (184 μmoles) of **1** was stirred together with 25 mg (368.42 μmoles) of NaOEt in 10 mL ethanol at 50 °C for 30 min and resulting green mixture was allowed to cool to room temperature. The volatiles were removed *in vacuo* and the dark residue was extracted with toluene (~3 × 5 mL). To the combined extracts was added 0.37 mL HCl/Et<sub>2</sub>O (Sigma-Aldrich: 1 M) drop wise while stirring whereby a powder precipitated. The mixture was stirred at room temperature for 1 h before the ether was distilled off. The dark solution was heated to 110 °C and filtered hot through a cannula. The filtrate was left at room temperature for 3 days whereby crystals suitable for single-crystal X-ray diffraction could be harvested. An additional amount of crystals could be obtained by

leaving the mother liquor at  $-30^{\circ}\text{C}$  over night to give a combined yield of 25%.

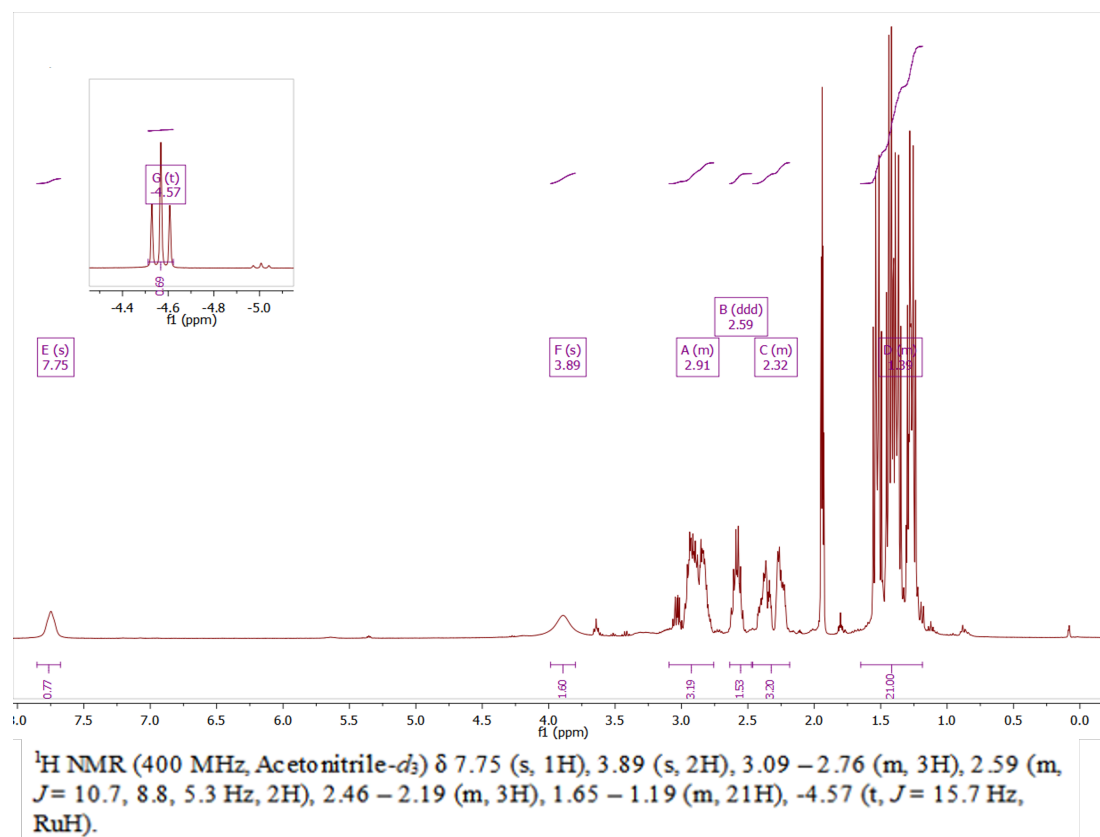


Figure C.1:  $^1\text{H}$ -NMR spectrum of the crystals obtained for  $\text{RuClH}$ . A rather much lowfield shifted amine proton, indicates extensive hydrogen bonding as revealed in the crystal structure which contains co-crystallised  $\text{HCl}$ . As such, it is expected that the spectrum is influenced by the pH being different from neutral.

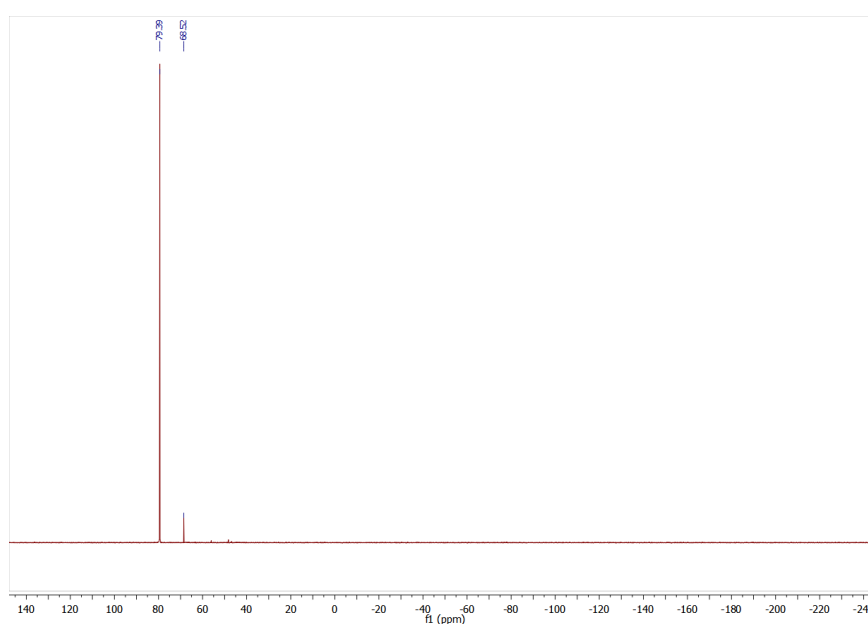


Figure C.2:  $^{31}\text{P}$ -NMR spectrum of the crystals obtained for  $\text{RuClH}$ .



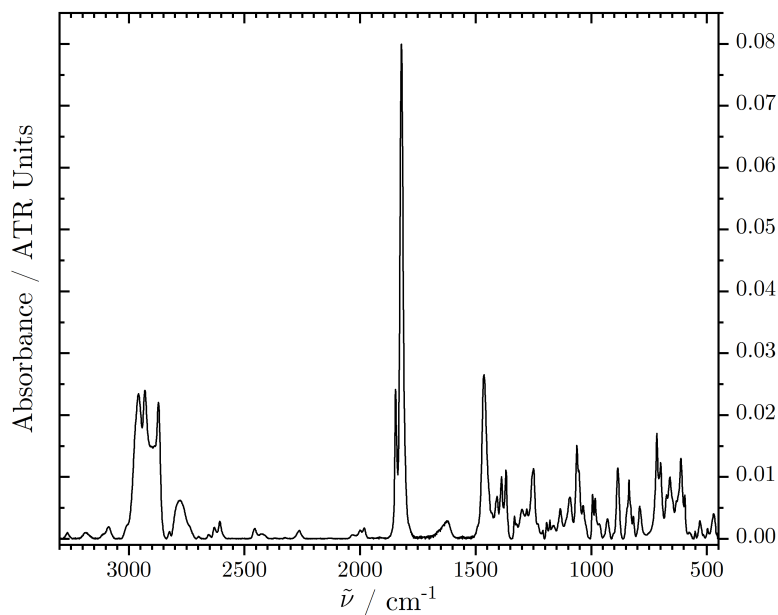
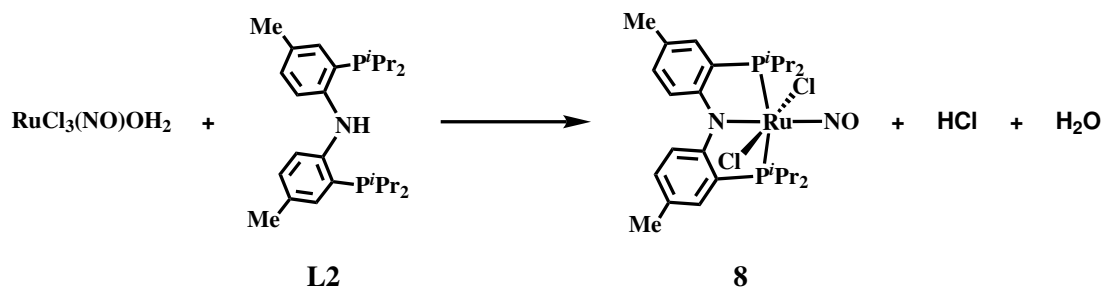


Figure C.3: IR spectrum of powderised crystals of  $[(i\text{Pr}_2\text{PNP})\text{RuClH}(\text{NO})]\text{Cl} \cdot \text{HCl}$ .

### C.1.2 Synthesis of complex 8



To a stirred solution of 100 mg (233  $\mu\text{moles}$ ) L2 in 4 mL THF was added 56.6 mg (222  $\mu\text{moles}$ ) of solid  $\text{RuCl}_3(\text{NO})(\text{OH}_2)$  whereby the colour of the liquid phase turned blue. The mixture was stirred at room temperature over night before the blue suspension was filtered and the dark blue product was washed with  $3 \times 1\text{mL}$  cold diethyl ether. Single crystals suitable for X-ray diffraction were obtained by leaving a saturated (rt) solution of the titled complex in diethyl ether at  $-30^\circ\text{C}$  for 3 days. Yield: 69%

Elemental analysis on basis of  $\text{C}_{26}\text{H}_{40}\text{Cl}_2\text{N}_2\text{OP}_2\text{Ru}$ :

Calculated: C: 49.53 H: 6.39 N: 4.44

Found: C: 47.47 H: 6.61 N: 3.96

Table C.1: NMR chemical shift assignment of complex **8**. NMR experiments (600 MHz, C<sub>2</sub>D<sub>2</sub>) and assignments have been conducted by the NMR Center at the Technical University of Denmark; experimentalist: PhD Kasper Enemark-Rasmussen.

$\delta(^{13}\text{C})$ / ppm	$\delta(^1\text{H})$ / ppm	Assignment	$J(^{13}\text{C} - ^{31}\text{P})$
17.7	1.31	iPr-CH <sub>3</sub>	s (broad)
24.9	3.1	iPr-CH	t, 12.9
19.6	2.3	Phe-Me	s (broad)
131.1	6.97	Phe-C5	t, 6.0
130.7	7.14	Phe-C3	s
115.4	7.26	Phe-C6	s
127.1	-	Phe-4 (-Me)	t, 3.8
123.3	-	Phe-5 (-P)	t, 3.5
158.7	-	Phe-6 (-N)	t, 11
56.3 ( <sup>31</sup> P)		Ru-P	
144.6 ( <sup>15</sup> N)		N	

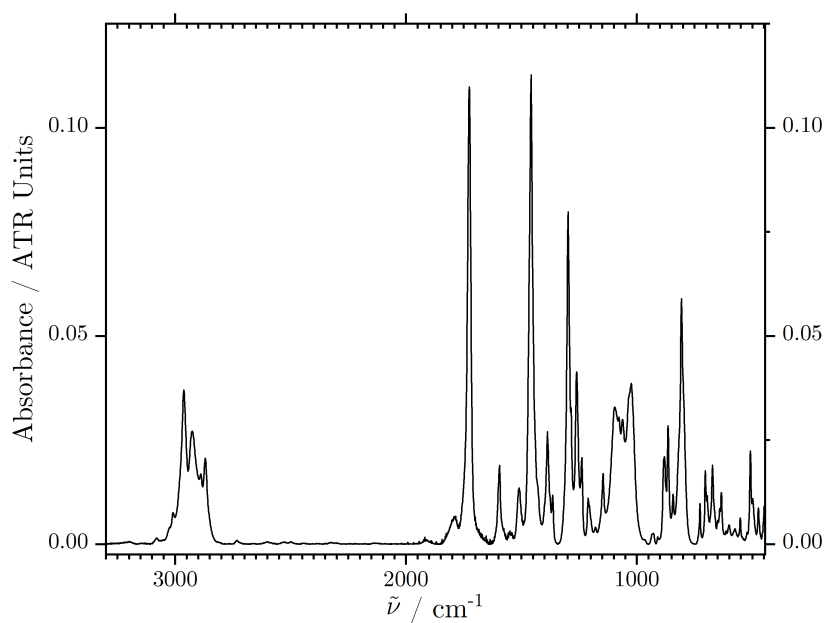
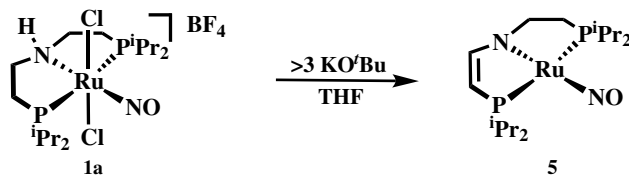


Figure C.4: IR spectrum of complex **8**.

C.1.3 Synthesis of (*i*Pr<sub>2</sub>PNP)Ru(NO), **5**

To a stirred solution of 100 mg (168  $\mu$ mol) **1a** in THF was added, at rt, 66 mg (589  $\mu$ mol) potassium *tert*-butoxide. After 30 min stirring, the intensely green suspension was concentrated *in vacuo* until dryness and the green product was extracted with hexane (filtered through cannula) until colourless extract. The clean product was isolated by evaporation of the solvent.

Yield: 65%.

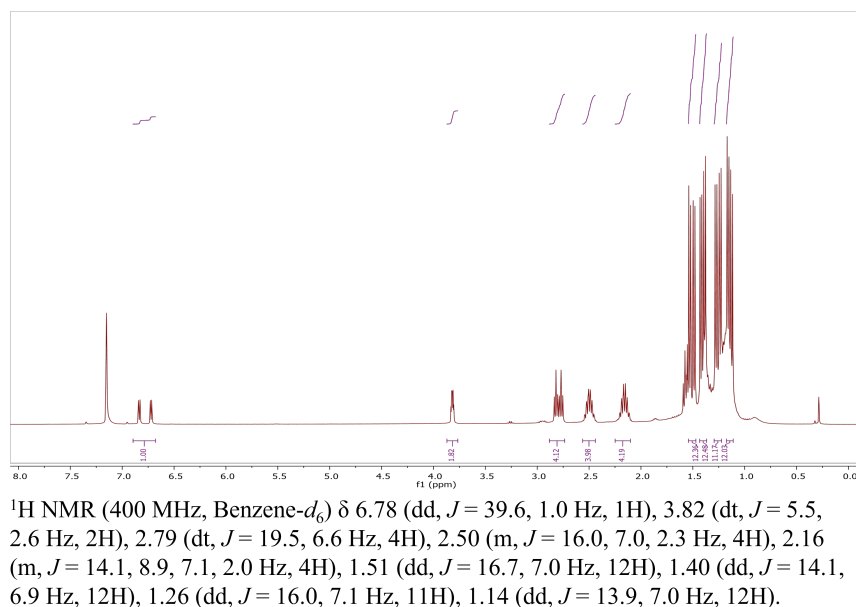


Figure C.5: <sup>1</sup>H-NMR spectrum of the complex **5**.

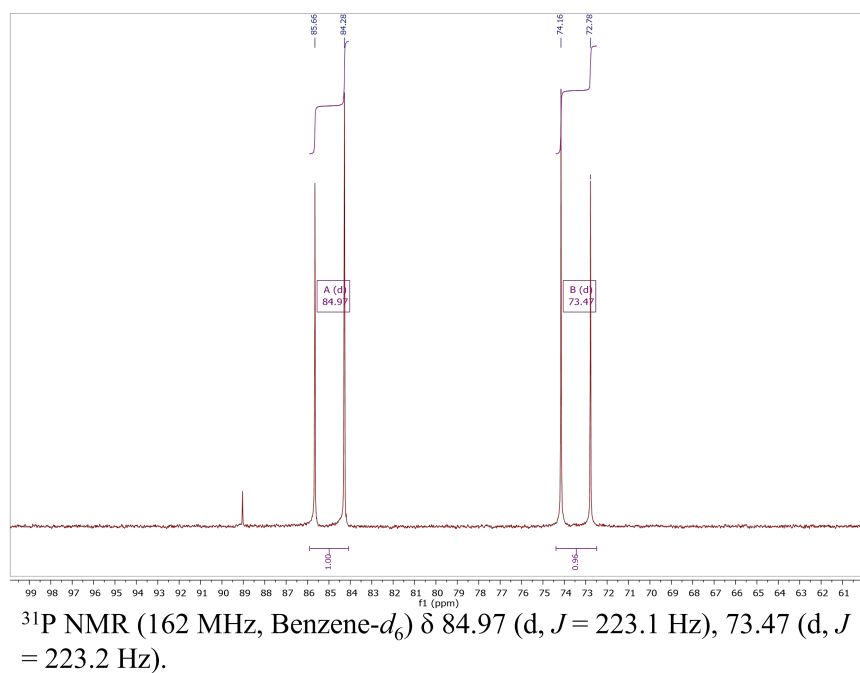
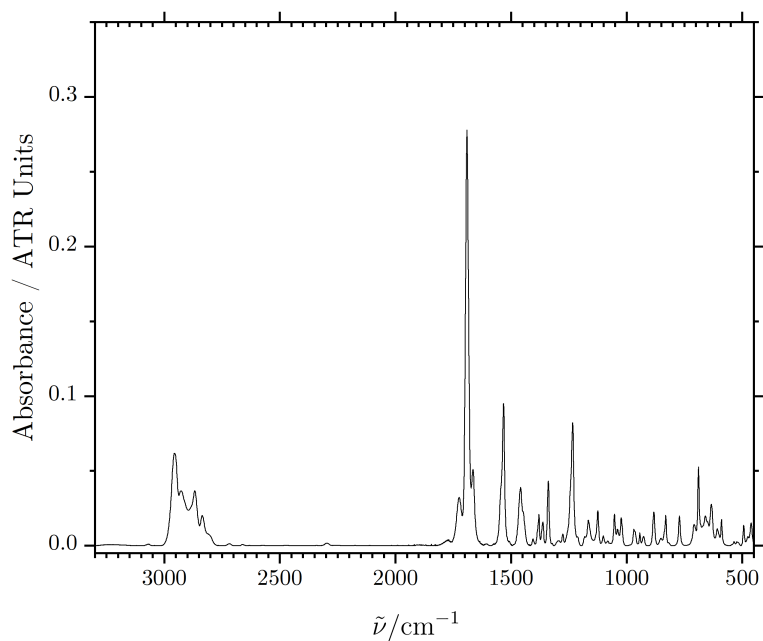
Figure C.6:  $^{31}\text{P}$ -NMR spectrum of the complex **5**.Figure C.7: IR spectrum of the complex **5**.

Table C.2: NMR chemical shift assignment of complex **5**. "=" indicates the "side" of the PNP ligand with  $sp^2$  carbons. NMR experiments (600 MHz,  $C_6D_6$ ) and assignments have been conducted by the NMR Center at the Technical University of Denmark; experimentalist: PhD Kasper Enemark-Rasmussen.

Complex <b>5</b>			
$\delta(^{13}C)$ / ppm	$\delta(^1H)$ / ppm	Assignment	$J(^{13}C - ^{31}P)$
18.6	1.13	iPr-CH <sub>3</sub>	<1
18.6	1.40	iPr-CH <sub>3</sub> (=)	<1
19.6	1.26	iPr-CH <sub>3</sub>	d, 5.7
19.8	1.51	iPr-CH <sub>3</sub> (=)	d, 6.5
24.0	1.59	P-CH <sub>2</sub>	d, 19.3
25.6	2.50	iPr-CH (=)	d, 25.2
26.1	2.16	iPr-CH	d, 20.7
57.1	2.79	N-CH <sub>2</sub>	dd, 9.8/2.3
74.6	3.82	PCH=	d, 38
168.2	6.79	NCH=	dd, 24.3/3.8
73.5 ( $^{31}P$ )	-	Ru-P (=)	d, 223 (P-P)
84.9 ( $^{31}P$ )	-	Ru-P	d, 223 (P-P)
163.9 ( $^{15}N$ )	-	Ru-N	

Reaction of **5** with O<sub>2</sub>

See main text for experimental procedure.

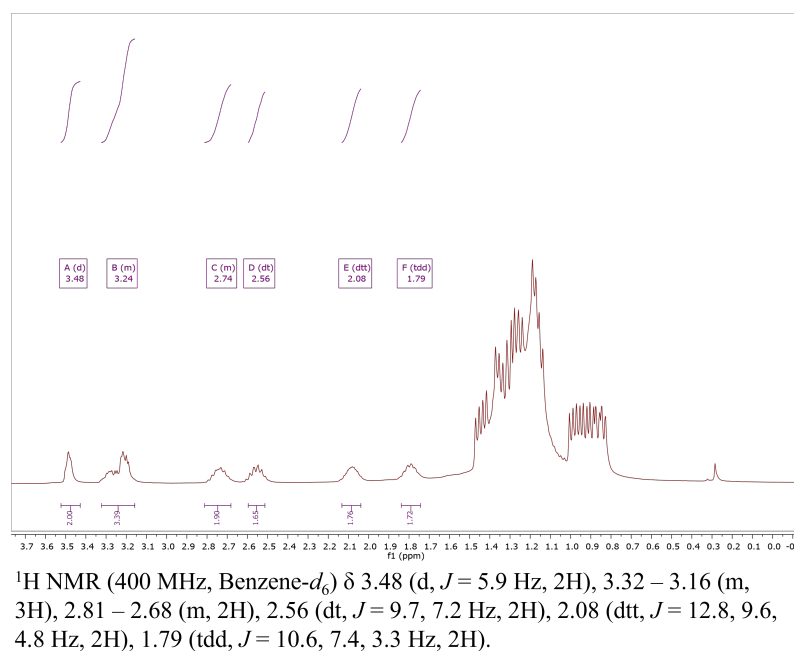


Figure C.8: <sup>1</sup>H-NMR spectrum of a C<sub>6</sub>D<sub>6</sub> solution of **5** under an atmosphere of O<sub>2</sub>.

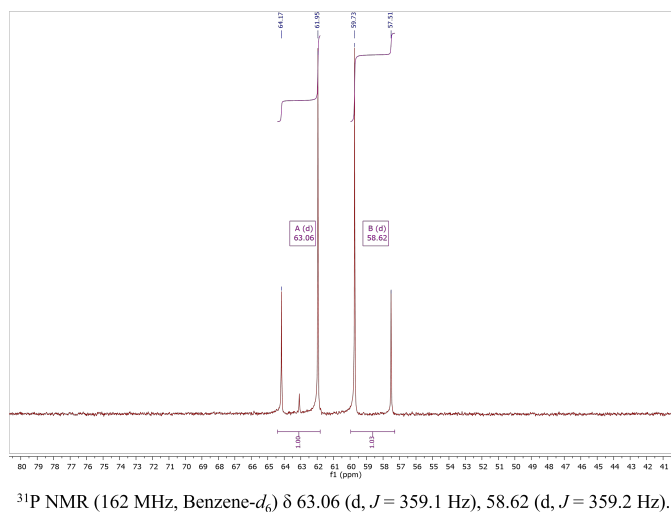
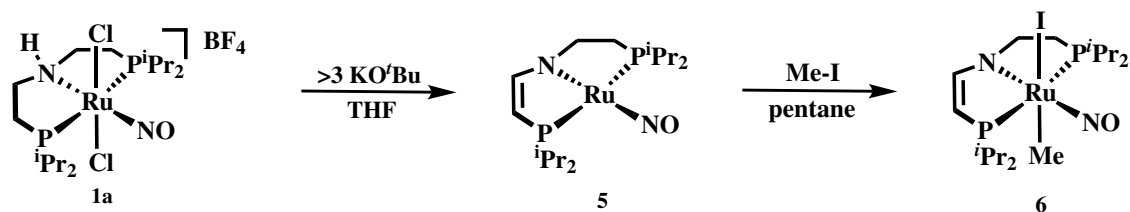


Figure C.9: <sup>31</sup>P-NMR spectrum of a C<sub>6</sub>D<sub>6</sub> solution of **5** under an atmosphere of O<sub>2</sub>.

C.1.4 Synthesis of **6**

At rt 100 mg (197  $\mu\text{moles}$ ) of **1a** together in THF was stirred with 77.4 mg (690  $\mu\text{moles}$ ) potassium *tert*-butoxide. All volatiles were removed *in vacuo* after 10 min stirring and the intermediate product (**5**) was extracted with pentane until colourless filtrate (cannula filtration). To the deep green pentane solution was added 3 mL iodomethane (Sigma-Aldrich) solution (0.2 M in toluene) whereby the solution changed colour to purple and precipitation of **6** was observed. Volatiles were removed *in vacuo* and the remnant was washed in a cold mixture of diethyl ether and toluene (1:1). Yield: 60%.

Elemental analysis on basis of  $\text{C}_{17}\text{H}_{37}\text{IN}_2\text{OP}_2\text{Ru}$ :

Calculated: C: 35.48 H: 6.48 N: 4.87

Found: C: 35.45 H: 6.60 N: 4.77

Single-crystals suitable for X-ray diffraction were obtained by slow evaporation at 4 °C of a dilute solution of the complex in acetone.

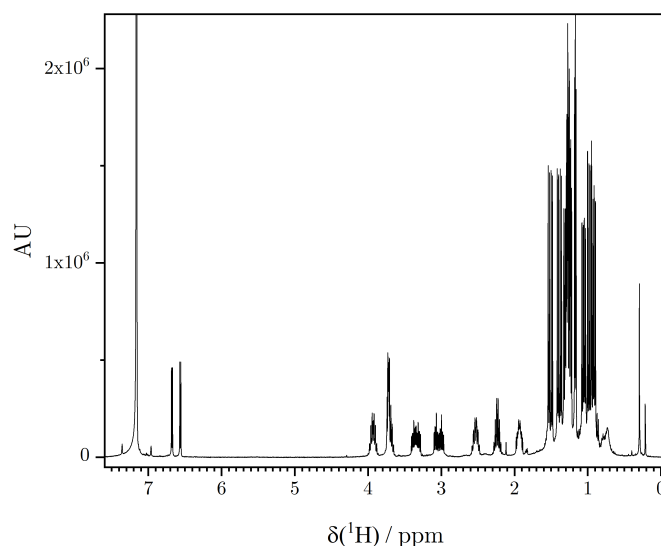


Figure C.10:  $^1\text{H}$ -NMR spectrum (400 MHz) of a  $\text{C}_6\text{D}_6$  solution of **6**.

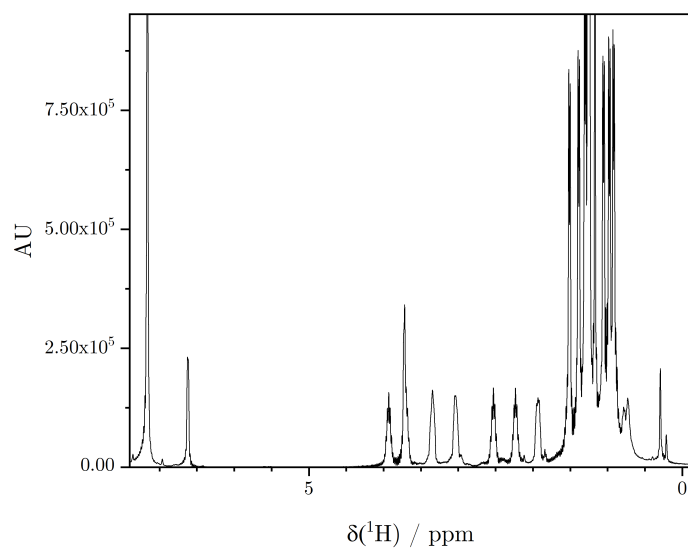


Figure C.11:  $^1\text{H}$ -NMR spectrum (400 MHz) of a  $\text{C}_6\text{D}_6$  solution of **6**.  $^1\text{H}$ - $^{31}\text{P}$  decoupled.

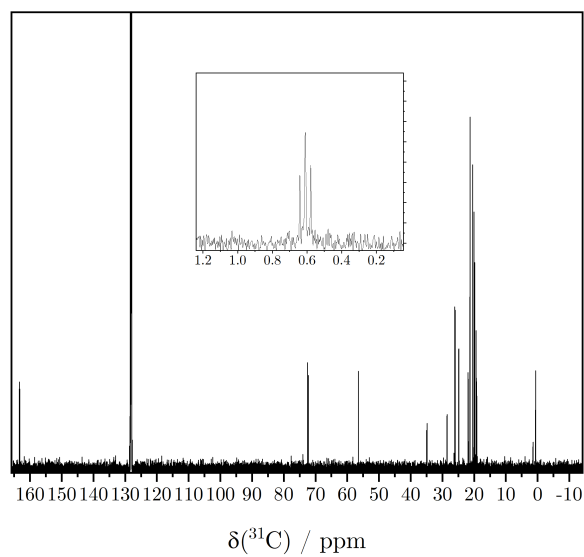


Figure C.12:  $^{13}\text{C}$ -NMR spectrum (800 MHz) of a  $\text{C}_6\text{D}_6$  solution of **6**.



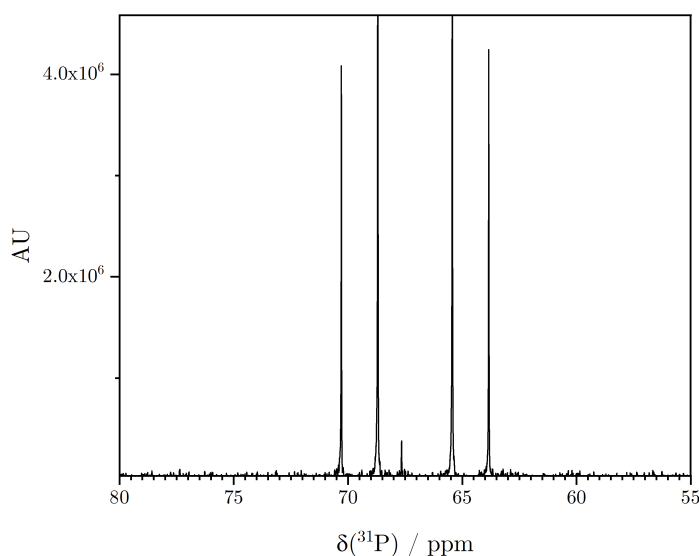
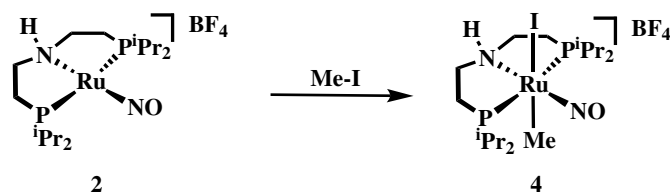


Figure C.13:  $^{31}\text{P}$ -NMR spectrum (400 MHz) of a  $\text{C}_6\text{D}_6$  solution of **6**.

Table C.3: NMR chemical shift assignment of complex **6**. NMR experiments ( $\text{C}_6\text{D}_6$ ) and assignments have been conducted by the NMR Center at the Technical University of Denmark; experimentalist: PhD Kasper Enemark-Rasmussen.

Complex <b>6</b>			
$\delta(^{13}\text{C})$ / ppm	$\delta(^1\text{H})$ / ppm	Assignment	$J(^{13}\text{C}-^{31}\text{P})$
0.61	1.17	Ru-CH <sub>3</sub>	t, 6.4
19.2	1.05	i-Pr(c) CH <sub>3</sub>	dd, 2.1 ; 4.6
19.3	1.30	i-Pr(d) CH <sub>3</sub>	dd, 2.7 ; 5.2
19.4	0.93	i-Pr(a) CH <sub>3</sub>	t, 1.8
19.8	1.39	i-Pr(c) CH <sub>3</sub>	d, 1.7
20.1	0.98	i-Pr(a) CH <sub>3</sub>	s
20.44	1.25	i-Pr(b) CH <sub>3</sub>	d, 1.7
20.45	1.52	i-Pr(d) CH <sub>3</sub>	t, 1.7
21.3	1.27	i-Pr(b) CH <sub>3</sub>	s
21.9	2.24	i-Pr(a) CH	dd, 1 ; 19.3
24.9	2.53	i-Pr(b) CH	d, 25.8
26.1	1.29/1.94	P-CH <sub>2</sub>	d, 23.2
28.5	3.69	i-Pr(c) CH	dd, 1.9 ; 22.0
34.91	3.92	i-Pr(d) CH	dd, 2.4 ; 29.1
56.5	3.03/3.34	N-CH <sub>2</sub>	dd, 1.8 ; 6.5
72.4	3.74	P-CH=	dd, 1.3 ; 47.8
162.9	6.62	=CH-N	dd, 3.3 ; 20.2
69.5 ( $^{31}\text{P}$ )	-		
64.6 ( $^{31}\text{P}$ )	-		
154.5 ( $^{15}\text{N}$ )	N		
382.2 ( $^{15}\text{N}$ )	NO	Ru-NO	

C.1.5 Synthesis of **4**

A Schlenk flask was loaded with 50 mg (96  $\mu$ moles) of **2** which was dissolved in 5 mL THF. At room temperature was added 2.4 mL 0.2 M iodomethane in toluene. The mixture was stirred at room temperature for 30 min after which the solvent was removed *in vacuo*. The resulting ocre coloured product was washed successively with toluene and diethyl ether. The product was then re-crystallised from hot toluene. Yield: 45%.

Elemental analysis on basis of  $\text{C}_{17}\text{H}_{40}\text{BF}_4\text{IN}_2\text{OP}_2\text{Ru}$ :

Calculated: C: 30.69 H: 6.06 N: 4.21

Found: C: 30.34 H: 6.10 N: 4.16

Crystals suitable for X-ray diffraction were obtained by diffusion of diethyl ether into THF solution of the complex.

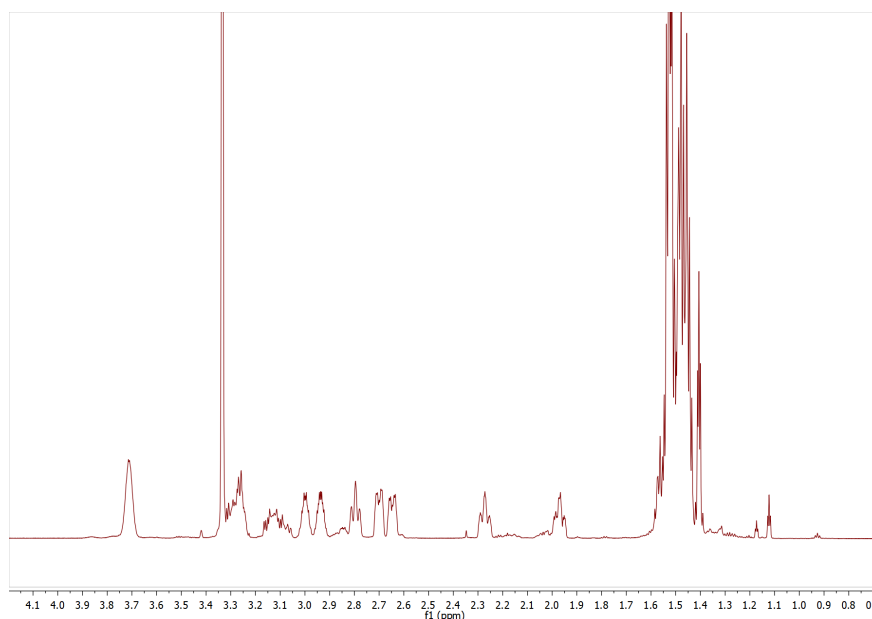


Figure C.14:  $^1\text{H}$ -NMR spectrum (600 MHz, methanol- $d_4$ ) of the iodidomethyl complex **4** revealing different isomers are present in solution.

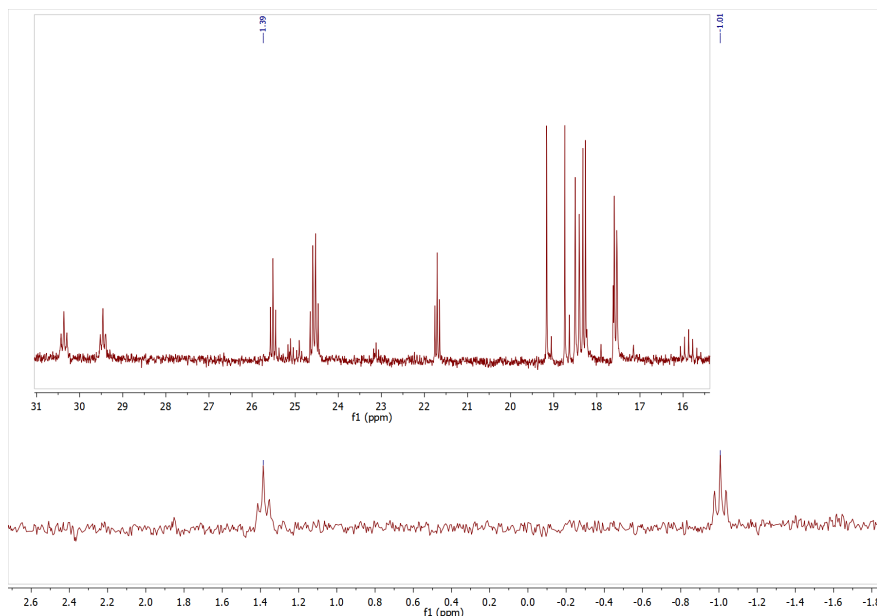


Figure C.15:  $^{13}\text{C}$ -NMR spectrum (150 MHz, methanol- $d_4$ ) of the iodidomethyl complex **4** revealing different isomers are present in solution with two characteristic triplets at 1.39 and -1.01 ppm respectively.

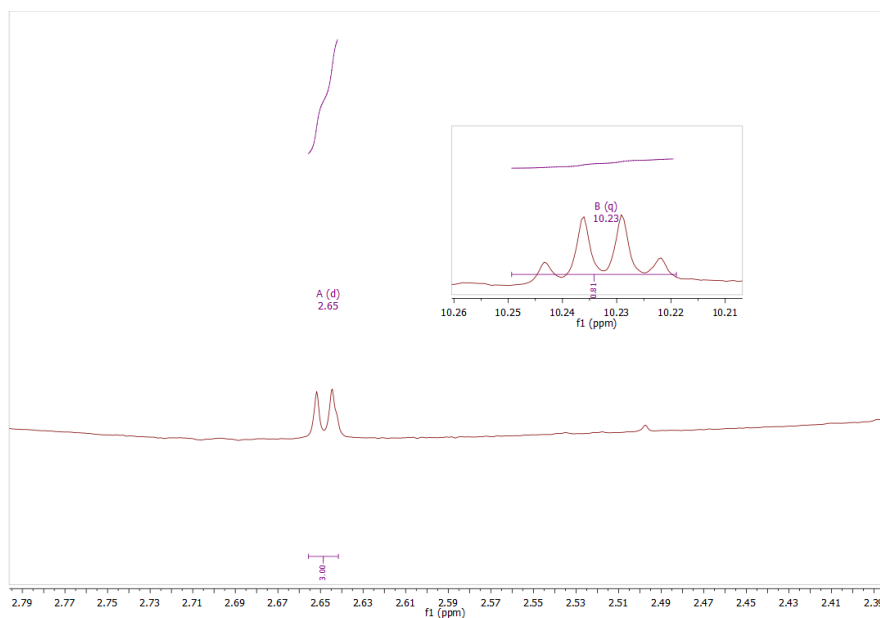
Table C.5: Assignment of isomer B observed for complex **4**. NMR experiments (600 MHz, methanol- $d_4$ ) and assignments have been conducted by the NMR Center at the Technical University of Denmark; experimentalist: PhD Kasper Enemark-Rasmussen.

Isomer B			
$\delta(^{13}\text{C})$ / ppm	$\delta(^1\text{H})$ / ppm	Assignment	$J(^{13}\text{C}-^{31}\text{P})$
1.4	1.45	Ru-CH <sub>3</sub>	t, 6.0
		CH <sub>3</sub>	
18.7	1.48	CH <sub>3</sub>	s
17.6		CH <sub>3</sub>	s
18.2		CH <sub>3</sub>	s
21.7	3.0	P-CH	t, 11.0
30.3	3.70	P-CH	t, 12.5
25.6	2.70/2.27	P-CH <sub>2</sub>	t, 12.0
50.7	3.12/2.79	N-CH <sub>2</sub>	t, 2.9
62.0 ( $^{31}\text{P}$ )		Ru-P	
51.6 ( $^{15}\text{N}$ )		NH	
370 ( $^{15}\text{N}$ )		NO	

Table C.4: Assignment of isomer A observed for complex **4**. NMR experiments (600 MHz, methanol- $d_4$ ) and assignments has been conducted by the NMR Center at the Technical University of Denmark; experimentalist: PhD Kasper Enemark-Rasmussen.

Isomer A			
$\delta(^{13}\text{C})$ / ppm	$\delta(^1\text{H})$ / ppm	Assignment	$J(^{13}\text{C} - ^{31}\text{P})$
-1.0	1.40	Ru-CH <sub>3</sub>	t, 6.1
17.53		CH <sub>3</sub>	s
		CH <sub>3</sub>	s
18.4		CH <sub>3</sub>	s
19.2	1.44	CH <sub>3</sub>	s
24.9	2.93	P-CH	t, 11.6
29.4	3.72	P-CH	t, 11.7
24.5	2.64/1.96	P-CH <sub>2</sub>	t, 11.7
52.8	3.27/3.25	N-CH <sub>2</sub>	t, 3.1
62.2 ( $^{31}\text{P}$ )		Ru-P	
54 ( $^{15}\text{N}$ )		NH	
369 ( $^{15}\text{N}$ )		NO	

## C.2 Miscellaneous spectral information



$^1\text{H}$  NMR (400 MHz, Benzene- $d_6$ )  $\delta$  10.23 (q,  $J = 2.8$  Hz, 1H), 2.65 (d,  $J = 2.9$  Hz, 3H).

Figure C.16:  $^1\text{H}$ -NMR spectrum of the mixture of **1** in ethanol/triethylamine mixture after heating for 1 h at 80 °C showing signals of generated acetaldehyde at 10.23 ppm (q,  $J = 2.8$  Hz) and 2.65 ppm (d,  $J = 2.9$  Hz). Referenced against benzene- $d_6$ .

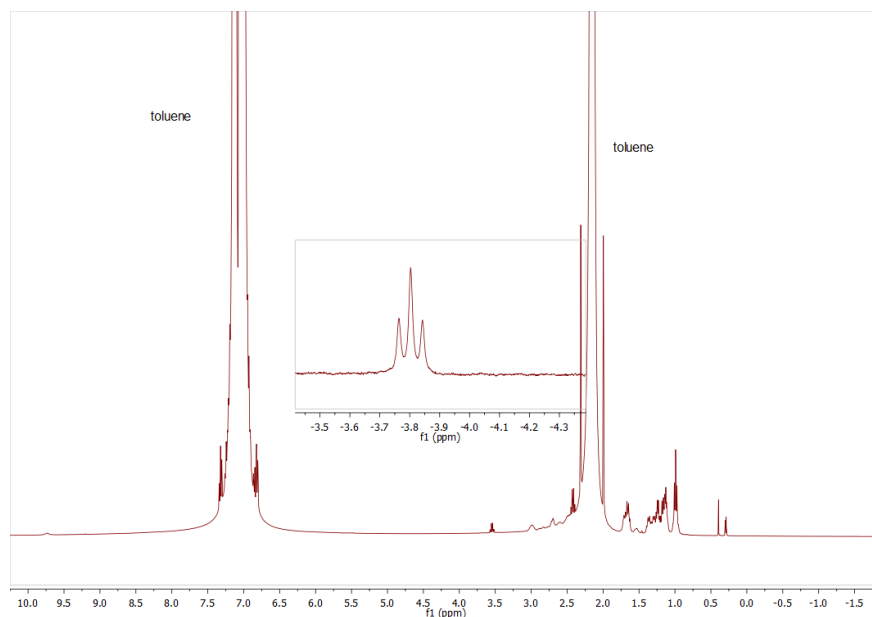


Figure C.17:  $^1\text{H}$ -NMR spectrum of the reaction mixture after **1** was heated to  $80^\circ\text{C}$  for 30 min in ethanolic triethylamine, followed by evaporation of volatiles followed by addition of toluene- $d_8$  reveals the characteristic triplet signal at -3.8 ppm of one hydride coordinates *cis* to two P atoms ( $J = 15.8\text{ Hz}$ ).

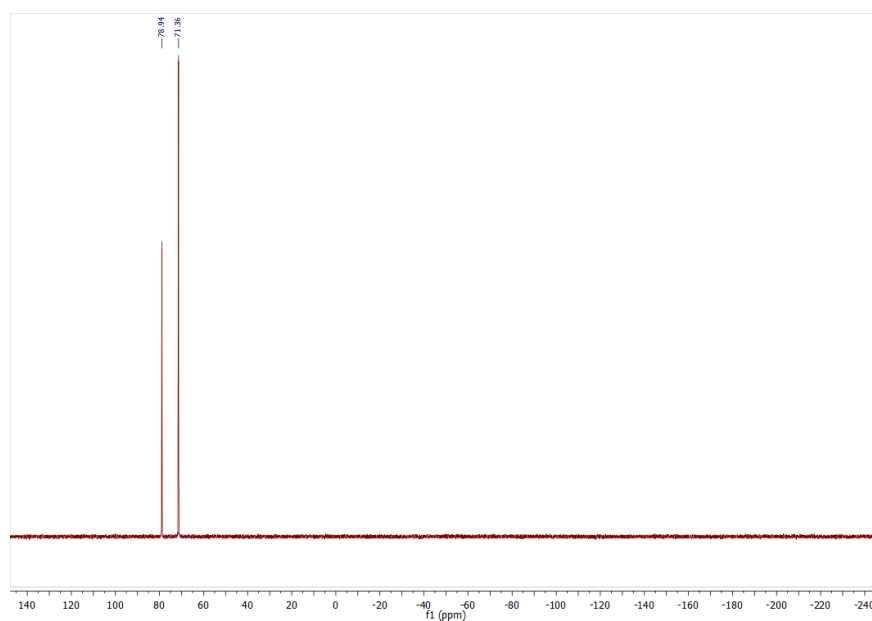
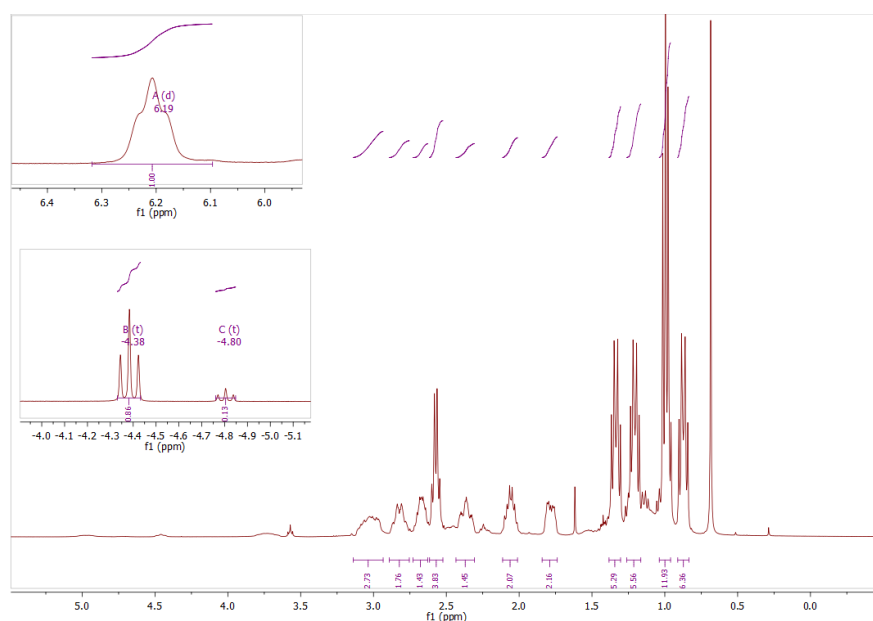
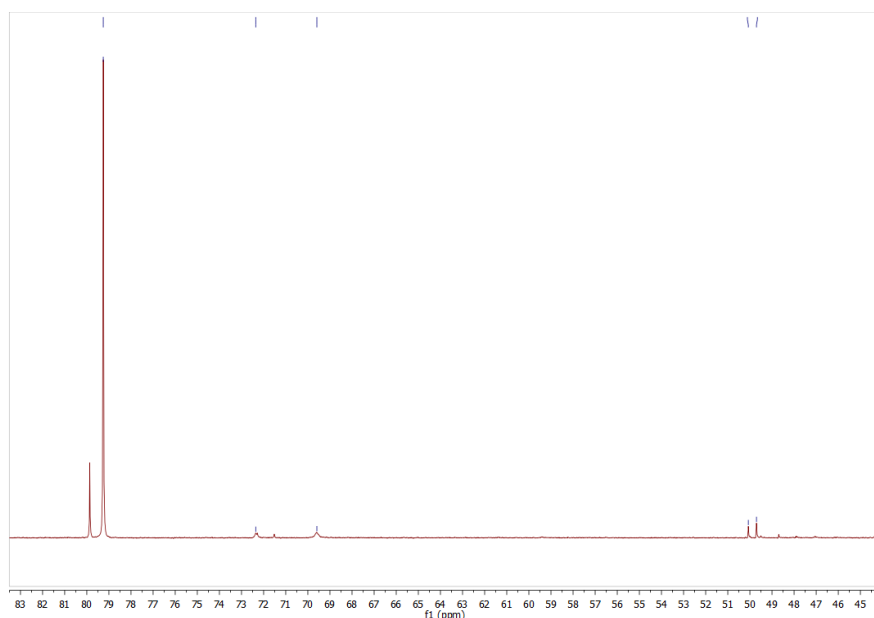


Figure C.18:  $^{31}\text{P}$ -NMR spectrum (162 MHz) of the product mixture after **1** was heating to  $80^\circ\text{C}$  for 30 min in ethanolic triethylamine, followed by evaporation of volatiles followed by addition of toluene- $d_8$  shows two main products at 78.94 ppm and 71.36 ppm.



$^1\text{H}$  NMR (400 MHz, Benzene- $d_6$ )  $\delta$  6.19 (t,  $J$  = 11.5 Hz, 1H), 3.14 – 2.93 (m, 3H), 2.82 (m,  $J$  = 10.8, 3.2 Hz, 2H), 2.73 – 2.63 (m, 1H), 2.57 (m,  $J$  = 7.3 Hz, 4H), 2.36 (m,  $J$  = 14.4, 5.8, 2.7 Hz, 1H), 2.11 – 2.01 (m, 2H), 1.78 (m,  $J$  = 14.9, 4.5 Hz, 2H), 1.38 – 1.30 (m, 5H), 1.26 – 1.16 (m, 6H), 1.00 (m,  $J$  = 7.3 Hz, 12H), 0.91 – 0.83 (m, 6H), -4.38 (t,  $J$  = 15.7 Hz, 1H), -4.80 (t,  $J$  = 13.5 Hz, 0H).

Figure C.19:  $^1\text{H}$ -NMR spectrum of the product mixture from the reaction between **2** and triethylamine hydrochloride. The spectrum contains small amounts of residual triethylamine hydrochloride as well as other unidentified products.



$^{31}\text{P}$  NMR (162 MHz, Benzene- $d_6$ )  $\delta$  79.25, 72.36, 69.59, 50.07, 49.70.

Figure C.20:  $^{31}\text{P}$ -NMR spectrum (162 MHz) of the product mixture from the reaction of **2** with triethylamine hydrochloride. The spectrum reveals additional products that remain unidentified.

### C.3 Crystal structure of a 6-coordinate enamido-ruthenium(II) complex

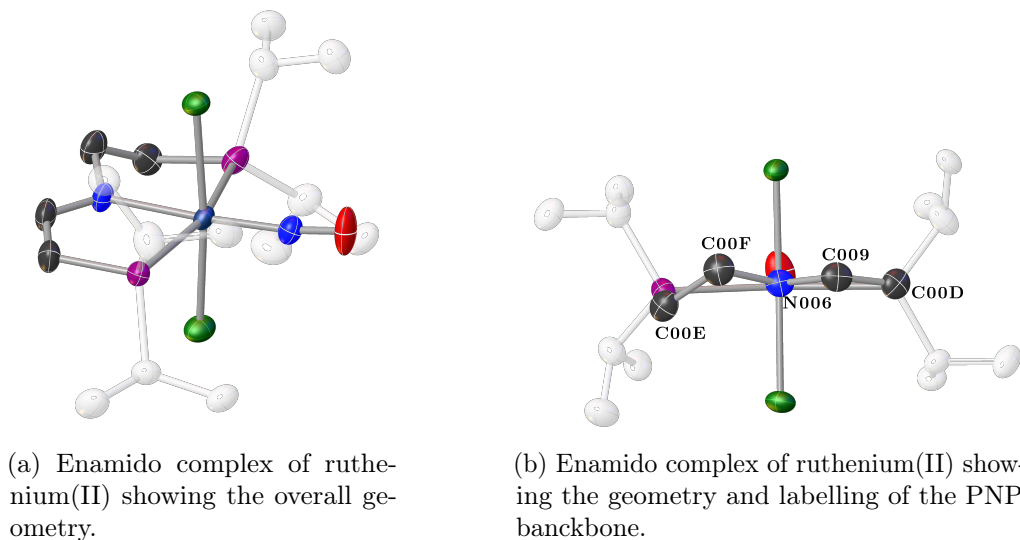


Figure C.21: 6-coordinate enamido complex of ruthenium(II) formed in the reaction of *tert*-butoxide and **1/1a** (1:1) in aprotic solvent. All hydrogens on carbon atoms have been omitted and the isopropyls on phosphorus have been ghosted out for clarity. Thermal ellipsoids are plotted at 35% probability level.

Table C.6: Selected geometrical data.

Atom	Atom	Length / Å	Atom	Atom	Atom	Angle / °
Ru	Cl02	2.3970(11)	O	N007	Ru	172.1(4)
Ru	P03	2.3973(12)	P03	Ru	P05	163.24(4)
Ru	Cl04	2.3806(12)	Cl04	Ru	Cl02	173.89(4)
Ru	P05	2.4130(13)	Cl04	Ru	P03	88.90(4)
Ru	N006	2.039(4)	N007	Ru	N006	175.61(18)
Ru	N007	1.757(4)	C009	N006	Ru	119.5(3)
N007	O	1.158(5)	C009	N006	C00F	119.6(4)
N006	C009	1.344(7)	C00F	N006	Ru	118.8(3)
C009	C00D	1.357(8)	N006	C009	C00D	124.5(5)
N006	C00F	1.467(7)				
C00E	C00F	1.475(8)				

Table C.7: Crystallographic details.

Formula	$\text{C}_{16}\text{H}_{24}\text{Cl}_2\text{N}_2\text{OP}_2\text{Ru}$
Formula weight	504.38
Temperature/K	120.0(2)
Crystal system	orthorhombic
Space group	Pbca
$a/\text{\AA}$	11.66720(10)
$b/\text{\AA}$	14.6107(2)
$c/\text{\AA}$	25.9491(3)
$\alpha/^\circ$	90
$\beta/^\circ$	90
$\gamma/^\circ$	90
Volume/ $\text{\AA}^3$	4423.44(9)
Z	10
$\rho_{\text{calc}}/\text{g/cm}^3$	1514
$\mu/\text{mm}^{-1}$	9377
F(000)	2077.0
Crystal size/ $\text{mm}^3$	? $\times$ ? $\times$ ?
Radiation	Cu $K\alpha$ ( $\lambda = 1.54184$ )
$2\Theta$ range for data collection/ $^\circ$	6.812 to 153.416
Index ranges	$-10 \leq h \leq 14,$ $-18 \leq k \leq 18,$ $-32 \leq l \leq 32$
Reflections collected	74114
Independent reflections	4652 ( $R_{\text{int}} = 0.0481,$ $R_{\text{sigma}} = 0.0179$ )
Data/restraints/parameters	4652/18/236
Goodness-of-fit on $F^2$	1.072
Final R indexes ( $I \geq 2\sigma(I)$ )	$R_1 = 0.0551,$ $wR_2 = 0.1365$
Final R indexes (all data)	$R_1 = 0.0601,$ $wR_2 = 0.1411$
Largest diff. peak/hole / $e \text{\AA}^{-3}$	1.06/-0.58



## C.4 Crystallographic details

For crystallographic details for complexes **1**/**1a** - **3** see Chapter 6.

Table C.8: Crystallographic details of the complexes described in main text.

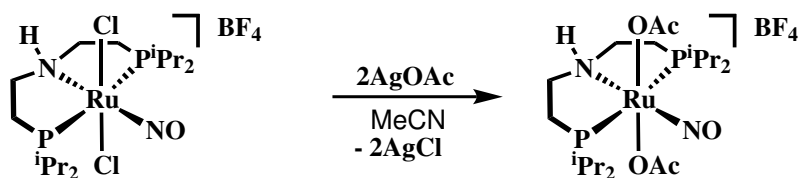
	8	5	7	6
Formula	C <sub>26</sub> H <sub>40</sub> Cl <sub>2</sub> N <sub>2</sub> OP <sub>2</sub> Ru	C <sub>16</sub> H <sub>34</sub> N <sub>2</sub> OP <sub>2</sub> Ru	C <sub>16</sub> H <sub>34</sub> N <sub>2</sub> O <sub>3</sub> P <sub>2</sub> Ru	C <sub>17</sub> H <sub>37</sub> IN <sub>2</sub> OP <sub>2</sub> Ru
Formula weight	630.54	433.48	465.46	575.42
Temperature/K	119.99(17)	120.02(2)	120.01(3)	120.01(11)
Crystal system	orthorhombic	monoclinic	orthorhombic	orthorhombic
Space group	<i>Fdd2</i>	<i>P2<sub>1</sub></i>	<i>P2<sub>1</sub>2<sub>1</sub>2<sub>1</sub></i>	<i>Pbca</i>
a/Å	34.4983(6)	10.67230(10)	7.62880(10)	11.3279(3)
b/Å	15.2664(3)	14.2908(2)	10.73180(10)	15.1555(3)
c/Å	10.7677(2)	13.82610(10)	25.2645(2)	26.9527(6)
α/°	90	90	90	90
β/°	90	99.3910(10)	90	90
γ/°	90	90	90	90
Volume/Å <sup>3</sup>	5670.97(18)	2080.44(4)	2068.42(4)	4627.24(18)
Z	25	5	4	10
ρ <sub>calc</sub> /cm <sup>3</sup>	1.477	1.384	1.495	1.653
μ/mm <sup>-1</sup>	7.443	7.570	7.731	17.317
F(000)	2625.3	904.0	968.0	2305.0
Crystal size/mm <sup>3</sup>	?×?×?	?×?×?	?×?×?	?×?×?
Radiation	CuKα (λ = 1.54184)	CuKα (λ = 1.54184)	CuKα (λ = 1.54184)	CuKα (λ = 1.54184)
2θ range for data collection/°	10.26 to 153.2	8.398 to 153.352	6.998 to 153.454	10.202 to 153.16
Index ranges	−40 ≤ h ≤ 43, −19 ≤ k ≤ 18, −13 ≤ l ≤ 10	−13 ≤ h ≤ 12, −17 ≤ k ≤ 18, −16 ≤ l ≤ 17	−8 ≤ h ≤ 9, −13 ≤ k ≤ 13, −31 ≤ l ≤ 31	−8 ≤ h ≤ 14, −15 ≤ k ≤ 18, −33 ≤ l ≤ 31
Reflections collected	6529	29797	53214	14676
Independent reflections	2408 (R <sub>int</sub> = 0.0213, R <sub>sigma</sub> = 0.0205)	8346 (R <sub>int</sub> = 0.0323, R <sub>sigma</sub> = 0.0299)	4362 (R <sub>int</sub> = 0.0523, R <sub>sigma</sub> = 0.0200)	4807 (R <sub>int</sub> = 0.0299, R <sub>sigma</sub> = 0.0292)
Data/restraints/parameters	2408/1/161	8346/19/460	4362/0/226	4807/25/287
Goodness-of-fit on F <sup>2</sup>	1.035	1.053	1.028	1.016
Final R indexes (I >= 2σ (I))	R <sub>1</sub> = 0.0194, wR <sub>2</sub> = 0.0550	R <sub>1</sub> = 0.0251, wR <sub>2</sub> = 0.0636	R <sub>1</sub> = 0.0324, wR <sub>2</sub> = 0.0784	R <sub>1</sub> = 0.0347, wR <sub>2</sub> = 0.0829
Final R indexes (all data)	R <sub>1</sub> = 0.0195, wR <sub>2</sub> = 0.0551	R <sub>1</sub> = 0.0264, wR <sub>2</sub> = 0.0648	R <sub>1</sub> = 0.0332, wR <sub>2</sub> = 0.0791	R <sub>1</sub> = 0.0418, wR <sub>2</sub> = 0.0871
Largest diff. peak/hole / e Å <sup>-3</sup>	0.35/-0.43	0.42/-0.69	1.83/-1.00	1.46/-1.02
Flack parameter	-0.014(5)	0.247(9)	0.385(16)	

	4	(PNP)RuClH(NO)Cl · HCl	Tetrazenido-complex
Formula	C <sub>17</sub> H <sub>40</sub> BF <sub>4</sub> IN <sub>2</sub> OP <sub>2</sub> Ru	C <sub>16</sub> H <sub>39</sub> Cl <sub>3</sub> N <sub>2</sub> OP <sub>2</sub> Ru	C <sub>28</sub> H <sub>44</sub> N <sub>6</sub> OP <sub>2</sub> Ru
Formula weight	665.25	544.87	429.13
Temperature/K	119.99(13)	120.00(14)	119.98(14)
Crystal system	monoclinic	monoclinic	triclinic
Space group	<i>P2<sub>1</sub>/n</i>	<i>P2<sub>1</sub>/m</i>	<i>P1̄</i>
a/Å	12.0593(2)	7.8026(2)	7.8500(4)
b/Å	15.4483(3)	11.8728(6)	11.7399(4)
c/Å	13.7279(2)	13.7802(4)	16.9921(7)
α/°	90	90	82.670(3)
β/°	91.942(2)	106.215(3)	83.290(4)
γ/°	90	90	74.829(4)
Volume/Å <sup>3</sup>	2555.98(8)	1225.80(8)	1493.33(11)
Z	5	5	3
ρ <sub>calc</sub> /cm <sup>3</sup>	1.827	1.476	1.432
μ/mm <sup>-1</sup>	1.990	9.479	5.511
F(000)	1392.9	568.7	672.0
Crystal size/mm <sup>3</sup>	?×?×?	?×?×?	?×?×?
Radiation	Mo Kα (λ = 0.71073)	CuKα (λ = 1.54184)	CuKα (λ = 1.54184)
2θ range for data collection/°	6.88 to 52.74	10 to 153.6	7.842 to 153.534
Index ranges	−16 ≤ h ≤ 16, −21 ≤ k ≤ 21, −19 ≤ l ≤ 19	−9 ≤ h ≤ 8, −13 ≤ k ≤ 14, −17 ≤ l ≤ 16	−9 ≤ h ≤ 8, −14 ≤ k ≤ 14, −20 ≤ l ≤ 21
Reflections collected	55813	12085	18759
Independent reflections	5164 (R <sub>int</sub> = 0.0451, R <sub>sigma</sub> = 0.0281)	2679 (R <sub>int</sub> = 0.0396, R <sub>sigma</sub> = 0.0301)	6203 (R <sub>int</sub> = 0.0399, R <sub>sigma</sub> = 0.0351)
Data/restraints/parameters	5164/0/322	2679/0/291	6203/6/396
Goodness-of-fit on F <sup>2</sup>	1.037	1.069	1.046
Final R indexes (I >= 2σ (I))	R <sub>1</sub> = 0.0315, wR <sub>2</sub> = 0.0809	R <sub>1</sub> = 0.0259, wR <sub>2</sub> = 0.0604	R <sub>1</sub> = 0.0256, wR <sub>2</sub> = 0.0615
Final R indexes (all data)	R <sub>1</sub> = 0.0352, wR <sub>2</sub> = 0.0839	R <sub>1</sub> = 0.0322, wR <sub>2</sub> = 0.0644	R <sub>1</sub> = 0.0310, wR <sub>2</sub> = 0.0647
Largest diff. peak/hole / e Å <sup>-3</sup>	0.89/-0.85	0.69/-0.54	0.42/-0.50

## Appendix D

### Synthesis of $[(^i\text{Pr}_2\text{PNP})\text{Ru}(\text{OAc})_2(\text{NO})]\text{BF}_4$



All manipulations were conducted under an  $\text{N}_2$  atmosphere using standard Schlenk techniques unless otherwise stated. Starting complex was synthesised as outlined in Chapter 6. Silver(I) acetate was purchased from Sigma-Aldrich and used without purification. Acetonitrile was purchased from VWR Denmark and was purged with  $\text{N}_2$  and dried over aluminium oxide prior to use.

A Schlenk flask was loaded with 75 mg (126  $\mu\text{moles}$ ) of  $[(^i\text{Pr}_2\text{PNP})\text{RuCl}_2(\text{NO})]\text{BF}_4$  which was subsequently stirred in acetonitrile together with 42 mg (126  $\mu\text{moles}$ ) silver(I) acetate at rt overnight under the exclusion of light. The precipitated silver(I) chloride was removed from the orange-red solution by filtering through a fine glass filter under ambient conditions. The solvent was removed under reduced pressure to yield the clean product as an orange powder. Yield: 80%.

High quality single-crystals suitable for X-ray diffraction were obtained by isothermal distillation at rt of diethyl ether into a concentrated ethanolic solution of the product. Elemental analysis on basis of  $\text{C}_{20}\text{H}_{43}\text{BF}_4\text{N}_2\text{O}_5\text{P}_2\text{Ru}$ :

<u>Calculated:</u>	C: 37.45	H: 6.76	N: 4.37
<u>Found:</u>	C: 37.49	H: 6.85	N: 4.36

## Crystallographic details

Table D.1: Experimental crystallographic details on  $[(^i\text{Pr}_2\text{PNP})\text{Ru}(\text{OAc})_2(\text{NO})]\text{BF}_4$ .

Formula	$\text{C}_{20}\text{H}_{43}\text{BF}_4\text{N}_2\text{O}_5\text{P}_2\text{Ru}$
Formula weight	641.39
Temperature/K	119.99(17)
Crystal system	monoclinic
Space group	$P2_1/c$
$a/\text{\AA}$	15.3995(4)
$b/\text{\AA}$	12.3734(3)
$c/\text{\AA}$	15.0830(4)
$\alpha/^\circ$	90
$\beta/^\circ$	99.124(3)
$\gamma/^\circ$	90
Volume/ $\text{\AA}^3$	2837.61(13)
Z	5
$\rho_{\text{calc}}/\text{g cm}^{-3}$	1.501
$\mu/\text{mm}^{-1}$	0.723
$F(000)$	1328.0
Crystal size/ $\text{mm}^3$	$? \times ? \times ?$
Radiation	$\text{MoK}\alpha$ ( $\lambda = 0.71073$ )
$2\Theta$ range for data collection/ $^\circ$	6.586 to 59.318
Index ranges	$-19 \leq h \leq 20,$ $-12 \leq k \leq 16,$ $-15 \leq l \leq 20$
Reflections collected	17011
Independent reflections	6830 [ $R_{\text{int}} = 0.0309,$ $R_{\text{sigma}} = 0.0425$ ]
Data/restraints/parameters	2408/1/161
Goodness-of-fit on $F^2$	1.042
Final R indexes [ $I \geq 2\sigma(I)$ ]	$R_1 = 0.0306,$ $wR_2 = 0.0633$
Final R indexes [all data]	$R_1 = 0.0390,$ $wR_2 = 0.0699$
Largest diff. peak/hole / $\text{e \AA}^{-3}$	0.44/-0.78

Table D.2: NMR chemical shift assignment of the diacetato complex presented in Section 4.0.1. NMR experiments (600 MHz, C<sub>2</sub>D<sub>2</sub>) and assignments have been conducted by the NMR Center at the Technical University of Denmark; experimentalist: PhD Kasper Enemark-Rasmussen.

$\delta(^{13}\text{C})$ / ppm	$\delta(^1\text{H})$ / ppm	Assignment	$J(^{13}\text{C} - ^{31}\text{P})$
17.9	1.40	CH <sub>3</sub>	s
18.0	1.38	CH <sub>3</sub>	t, 1.1
18.2	1.33	CH <sub>3</sub>	s
18.9	1.35	CH <sub>3</sub>	s
22.5	2.44	P-CH	t, 10.7
26.2	2.34	P-CH	t, 11.8
24.8	2.57/2.09	P-CH <sub>2</sub>	t, 11.6
51.0	3.41/3.06	N-CH <sub>2</sub>	t, 2.7
68.5		Ru-P	
68.1	5.85	NH	
		NO	
22.5	1.99	Me-Ace-1	s
22.6	2.01	Me.Ace-2	s
176.5		C=O Ace-1	s
175.8		C=O Ace-2	s

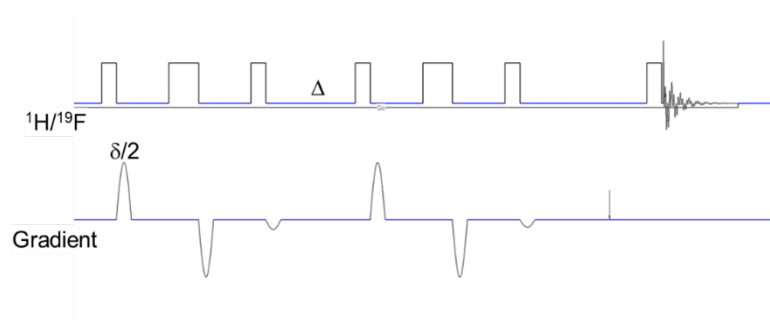
### Determination of diffusion coefficients using DOSY-NMR

Self-diffusion coefficients were determined by PhD Kasper Enemark-Rasmussen (DTU NMR Center) by the pulsed field gradient spin-echo method. For the Ru complex, a series of <sup>1</sup>H spectra with varying gradient strengths were measured and fitted according to the Stejskal-Tanner equation:<sup>381</sup>

$$I_G = I_0 e^{D(\delta\gamma G)^2(\Delta - \delta/\epsilon)}$$

$I_G$  is the observed intensity for a given gradient strength  $G$ ,  $I_0$  is the reference intensity with  $G = 0$ ,  $D$  is the diffusion coefficient,  $\delta$  is the gradient duration,  $\Delta$  is the diffusion time and  $\gamma$  is the gyromagnetic ratio. The gradient duration (“little delta”,  $\delta$ ) was set to 2 ms and the diffusion time (“big delta”,  $\Delta$ ) was set to 60 ms. 10 spectra were acquired with gradient strengths between 0.963 G/cm and 47.178 G/cm. For BF<sub>4</sub><sup>−</sup> a total of eight <sup>19</sup>F spectra using the same  $\delta$  and  $\Delta$  values were measured with gradient strengths between 0.963 G/cm and 38.520 G/cm.

Pulse sequence used: ledbpgp2s. Small rectangles indicate  $\pi/2$  pulses, large rectangles indicate  $\pi$  pulses. Four gradient pulses of strength  $G$  were applied, each with a duration of  $\delta/2$ . In addition, two weaker spoil gradient pulses were applied. Before the final read pulse, a 5 ms delay is inserted to allow for any eddy currents generated by the gradients to dissipate. The spectra were acquired at 25 °C with  $B_0 = 14.1$  T.



## Appendix E

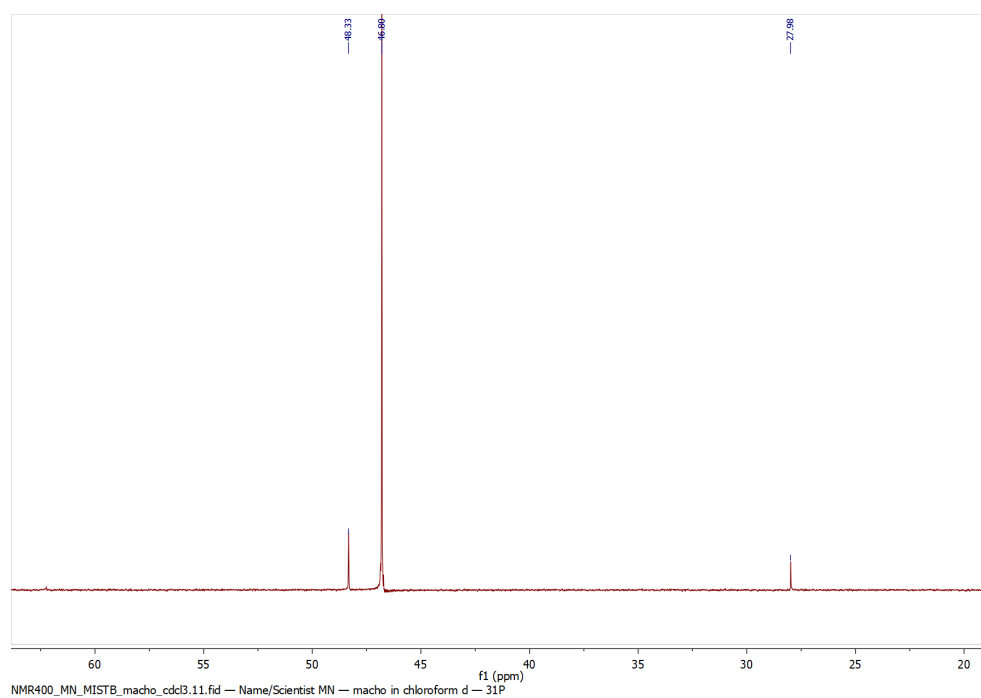


Figure E.1:  $^{31}\text{P}$ -NMR spectrum of ruthenium-MACHO in  $\text{CDCl}_3$ . Singlet peaks are observed at 48.33, 46.80 and 27.98 ppm.

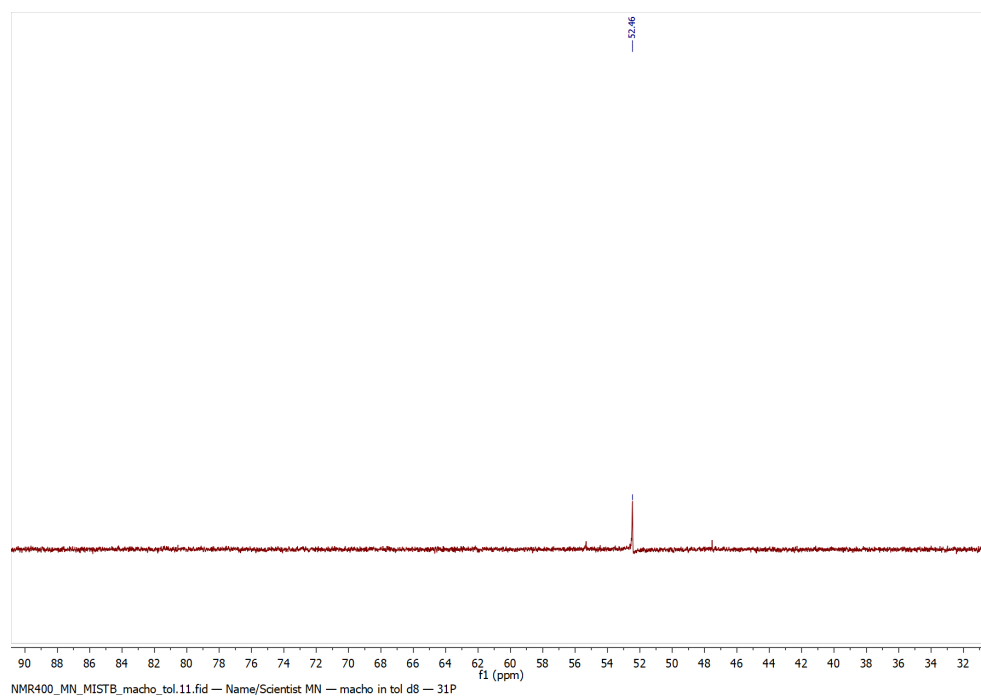


Figure E.2:  $^{31}\text{P}$ -NMR spectrum of ruthenium-MACHO in toluene- $d_8$ . Singlet at 52.46 ppm.



**Crystallographic details:** All crystal batches for X-ray diffraction analysis were immersed in polybutene oil (Aldrich, > 90%) as protection against air. A suitable crystal was harvested with a MiTeGen cryo loop and mounted on a goniometer attached to a SuperNova Dual Source CCD-diffractometer. Data were collected at 120 K using Mo K $\alpha$  radiation.

Table E.1: Crystallographic details for the RuCl<sub>2</sub>-MACHO and the Ru-MACHO complex for both models with and without solvent of crystallisation.

	RuCl <sub>2</sub> -MACHO	Ru-MACHO · 1.7DMSO	Ru-MACHO
Formula	C <sub>29</sub> H <sub>29</sub> NCl <sub>2</sub> OP <sub>2</sub> Ru	C <sub>32</sub> H <sub>39</sub> ClNO <sub>3</sub> P <sub>2</sub> Ru	C <sub>29</sub> H <sub>30</sub> ClNOP <sub>2</sub> Ru
Formula weight	641.47	748.26	461.53
Temperature/K	120.01(11)	119.99(10)	119.99(10)
Crystal system	monoclinic	orthorhombic	orthorhombic
Space group	<i>P</i> 2 <sub>1</sub> / <i>n</i>	<i>Pnma</i>	<i>Pnma</i>
a/Å	10.3685(3)	10.7725(7)	10.7725(7)
b/Å	19.5198(7)	22.0240(10)	22.0240(10)
c/Å	14.4048(5)	16.4907(8)	16.4907(8)
$\alpha$ /°	90	90	90
$\beta$ /°	104.110(3)	90	90
$\gamma$ /°	90	90	90
Volume/Å <sup>3</sup>	2827.44(17)	3912.5(4)	3912.5(4)
Z	7	6	6
$\rho_{\text{calc}}$ /cm <sup>3</sup>	1.936	1.404	1.428
$\mu$ /mm <sup>-1</sup>	1.339	0.746	0.748
F(000)	1722.0	1713.0	1744.0
Crystal size/mm <sup>3</sup>	? × ? × ?	? × ? × ?	? × ? × ?
Radiation	Mo K $\alpha$ ( $\lambda$ = 0.71073)	Mo K $\alpha$ ( $\lambda$ = 0.71073)	Mo K $\alpha$ ( $\lambda$ = 0.71073)
2 $\theta$ range for data collection/°	6.908 to 59.416	6.492 to 59.244	6.492 to 59.244
Index ranges	-13 ≤ h ≤ 14, -20 ≤ k ≤ 26, -19 ≤ l ≤ 15	-10 ≤ h ≤ 14, -30 ≤ h ≤ 30, -22 ≤ h ≤ 18	-10 ≤ h ≤ 14, -30 ≤ h ≤ 30, -22 ≤ h ≤ 18
Reflections collected	16073	15527	15527
Independent reflections	6728 (R <sub>int</sub> = 0.0306, R <sub>sigma</sub> = 0.0451)	4958 (R <sub>int</sub> = 0.0317, R <sub>sigma</sub> = 0.0382)	5489 (R <sub>int</sub> = 0.0317, R <sub>sigma</sub> = 0.0382)
Data/restraints/parameters	6728/0/325	4958/57/268	4958/0/169
Goodness-of-fit on F <sup>2</sup>	1.061	1.034	1.045
Final R indexes (I >= 2 $\sigma$ (I))	R <sub>1</sub> = 0.0345, wR <sub>2</sub> = 0.0691	R <sub>1</sub> = 0.0434, wR <sub>2</sub> = 0.1124	R <sub>1</sub> = 0.0323, wR <sub>2</sub> = 0.0756
Final R indexes (all data)	R <sub>1</sub> = 0.0465, wR <sub>2</sub> = 0.0740	R <sub>1</sub> = 0.0557, wR <sub>2</sub> = 0.1222	R <sub>1</sub> = 0.0421, wR <sub>2</sub> = 0.0756
Largest diff. peak/hole / e Å <sup>-3</sup>	0.54/-0.53	1.05/-0.85	0.48/-0.44

Table E.2: Selected bond lengths and angles for RuCl<sub>2</sub>-MACHO

Atom	Atom	Length/Å	Atom	Atom	Atom	Angle/°
Ru	Cl02	2.4053(6)	Cl03	Ru	Cl02	174.07(2)
Ru	Cl03	2.3909(6)	P004	Ru	Cl02	86.60(2)
Ru	P004	2.3494(7)	P004	Ru	Cl03	90.24(2)
Ru	P05	2.3365(7)	P05	Ru	Cl02	92.57(2)
Ru	N9	2.181(2)	P05	Ru	Cl03	89.02(2)
Ru	C	1.862(3)	P05	Ru	P004	163.44(2)
O	C	1.118(3)	N9	Ru	Cl02	86.41(5)
P004	C11	1.821(2)	N9	Ru	Cl03	88.19(5)
P004	C00A	1.837(3)	N9	Ru	P004	82.13(6)
P004	C00H	1.821(3)	N9	Ru	P05	81.32(6)
P05	C00B	1.819(3)	O	C	Ru	176.1(2)
P05	C00I	1.849(2)	C	Ru	Cl02	95.18(8)
P05	C00J	1.826(2)	C	Ru	Cl03	90.31(8)
N9	C00C	1.480(3)	C	Ru	P004	99.88(8)
N9	C00D	1.480(3)	C	Ru	P05	96.66(8)
			C	Ru	N9	177.50(10)
			C00C	N9	Ru	114.67(15)
			C00C	N9	C00D	112.01(18)
			C00D	N9	Ru	113.37(15)

Supplementary Information:  
Intrinsic Geometric Distortion of 5-Coordinate Halido Complexes of Ruthenium

## Supplementary Information

### Intrinsic Geometric Distortion of 5-Coordinate Halido Complexes of Ruthenium(0)

Mike S. B. Jørgensen<sup>a</sup>, K. Enemark-Rasmussen<sup>b</sup>, R. Wugt Larsen<sup>c</sup>, Martin Nielsen\*.

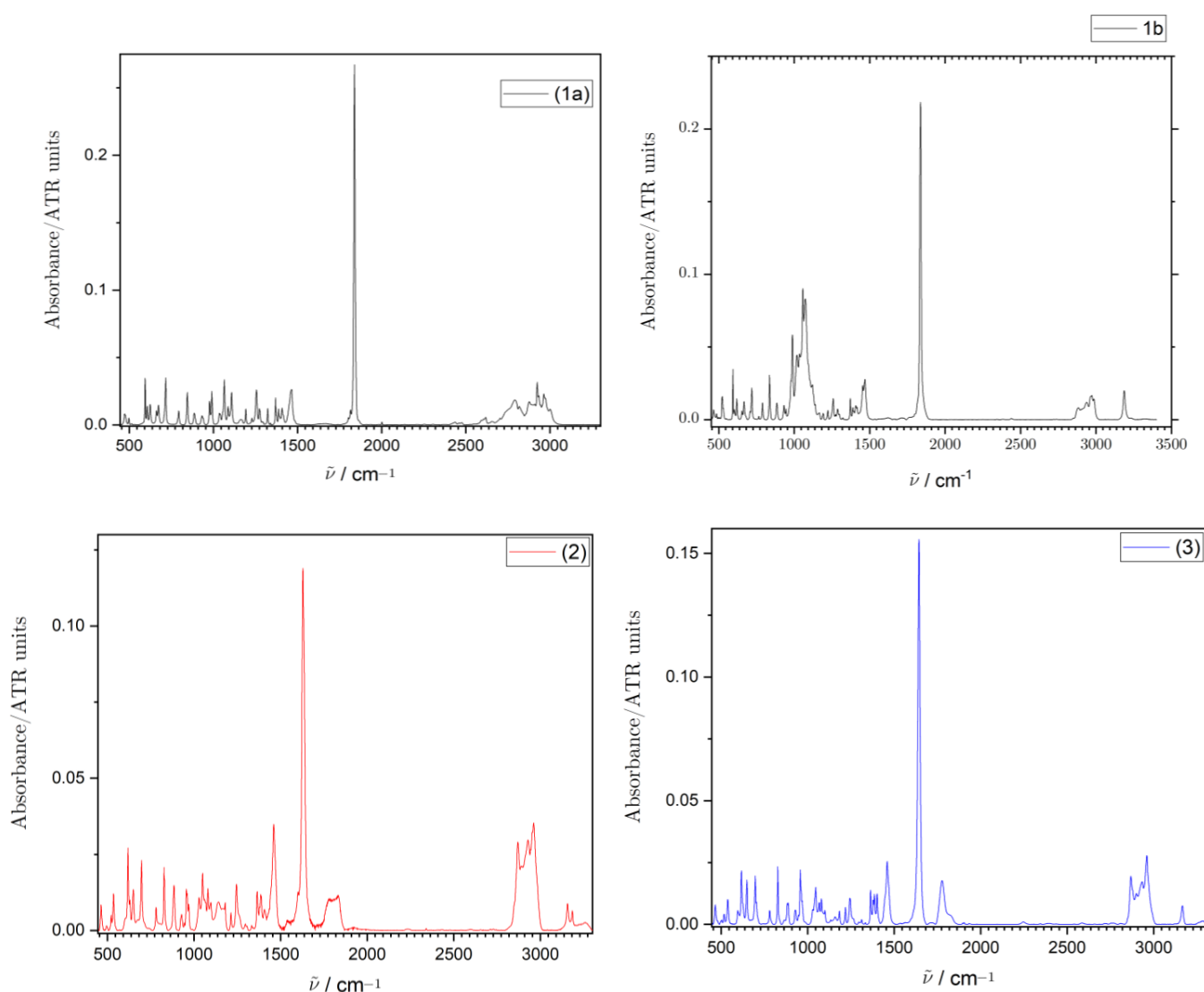
Technical University of Denmark, 2800 Kgs. Lyngby, Denmark.

Supplementary Information:

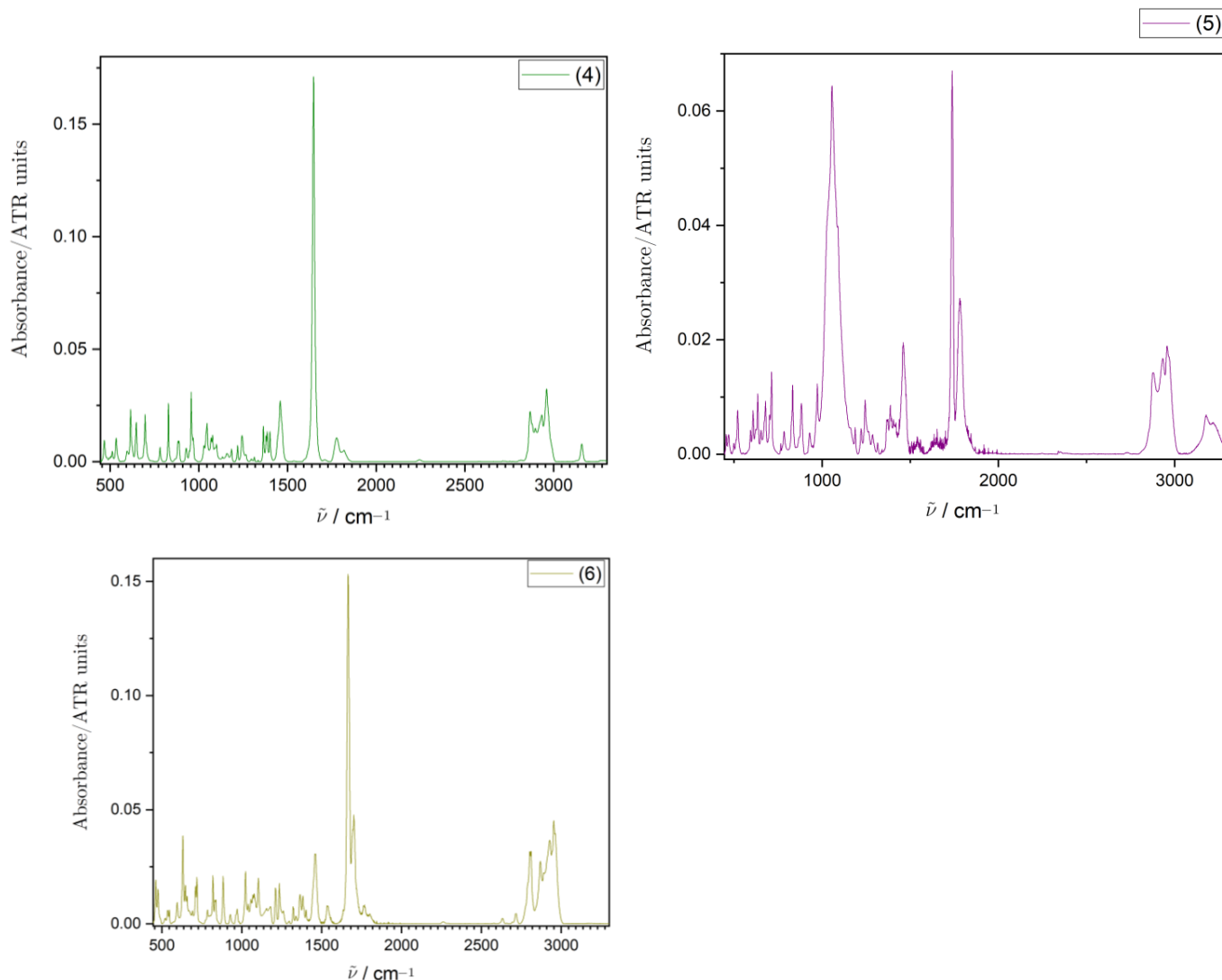
Intrinsic Geometric Distortion of 5-Coordinate Halido Complexes of Ruthenium

**Attenuated-Total-Reflection Fourier Transform Infrared Spectroscopy:** The attenuated-total-Reflectance (ATR) Fourier Transform infrared (FTIR) spectra were recorded on a VERTEX 80 vacuum FTIR spectrometer from Bruker Optics GmbH. The FTIR spectrometer was equipped with a Ge on KBr beam splitter, a liquid nitrogen cooled HgCdTe detector, a thermal global radiation source and a single-reflection germanium ATR accessory (IRIS) from PIKE Technologies Inc. Small traces of residual water vapor absorption from the interferometer were subtracted and the resulting absorption spectra were corrected for minor baseline drifts. Subsequently, extended ATR corrections were applied to account for the wavelength-dependent penetration depth of the infrared probe beam into the solid samples.

**Below, IR spectra of all complexes are represented by number as they appear in the main text.**



Supplementary Information:  
Intrinsic Geometric Distortion of 5-Coordinate Halido Complexes of Ruthenium



### NMR Spectroscopy:

The NMR spectra were measured using either a 18.8T Bruker Avance III or 14.1T Bruker Avance IIIHD spectrometer. The 18.8T system was mounted with a 5 mm TCI CryoProbe (Bruker) while the 14.1T system was mounted with a 5 mm RT BBFO probe (Bruker). All measurements were performed at 25°C. Resonance assignment was performed using 2D  $^1\text{H}$ - $^{13}\text{C}$  HSQC,  $^1\text{H}$ - $^{13}\text{C}$  HMBC and  $^1\text{H}$ - $^{31}\text{P}$  HMBC spectra measured at 14.1 T, while  $^1\text{H}$ - $^{15}\text{N}$  HMBC spectra and 1D  $^{13}\text{C}$  spectra were measured at 18.8 T.  $^1\text{H}$  and  $^{13}\text{C}$  Chemical shifts are reported relative to TMS,  $^{31}\text{P}$  chemical shifts are reported relative to  $\text{H}_3\text{PO}_4$  and  $^{15}\text{N}$  chemical shifts are reported relative to liquid ammonia (for comparison with  $\text{CH}_3\text{NO}_2$  subtract 380.2 ppm from the listed values). ‘

Supplementary Information:  
Intrinsic Geometric Distortion of 5-Coordinate Halido Complexes of Ruthenium

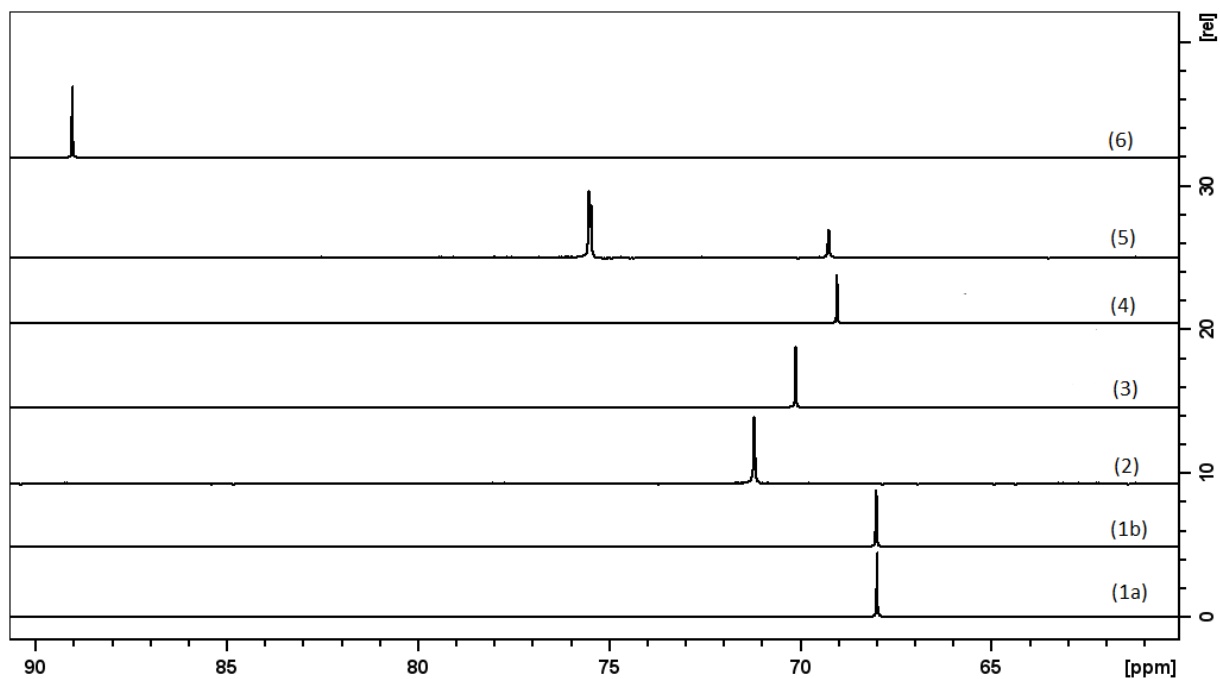


Figure S 1:  $^{31}\text{P}$  NMR spectra of all complexes indicated by number as they appear in the main text.

□

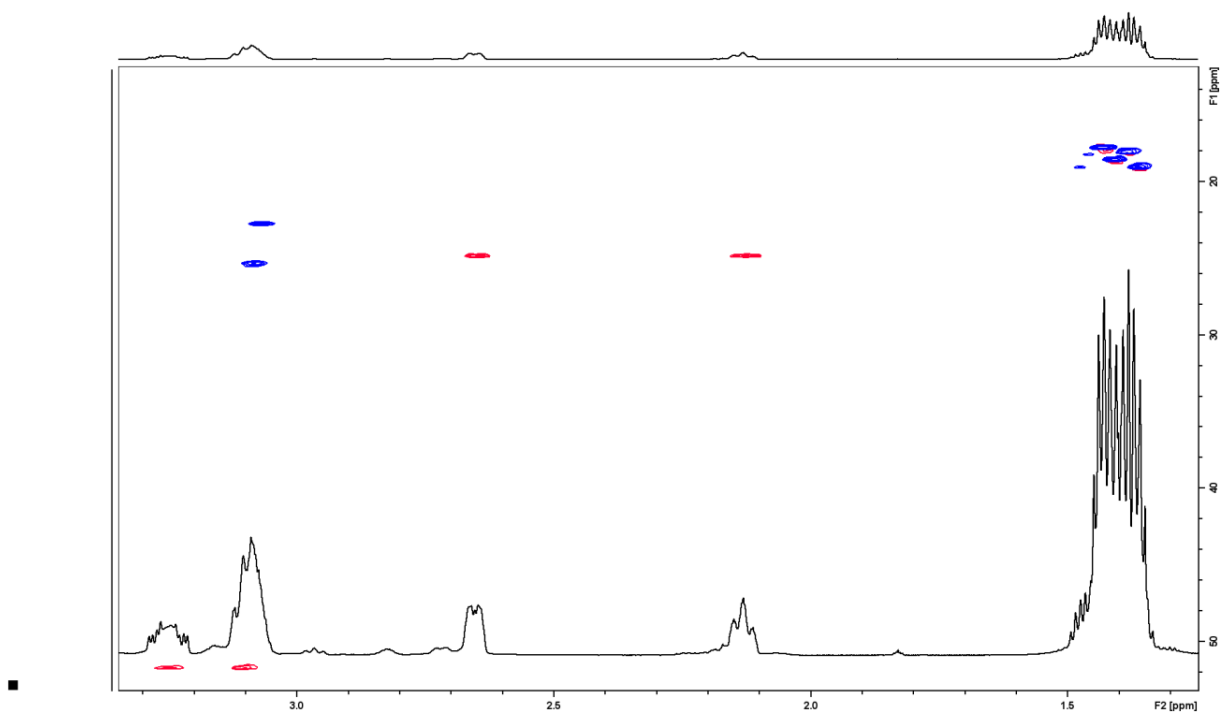


Figure S 2: HSQC NMR spectrum of **1a** with  $^1\text{H}$  spectrum attached for clarity.

Supplementary Information:  
Intrinsic Geometric Distortion of 5-Coordinate Halido Complexes of Ruthenium

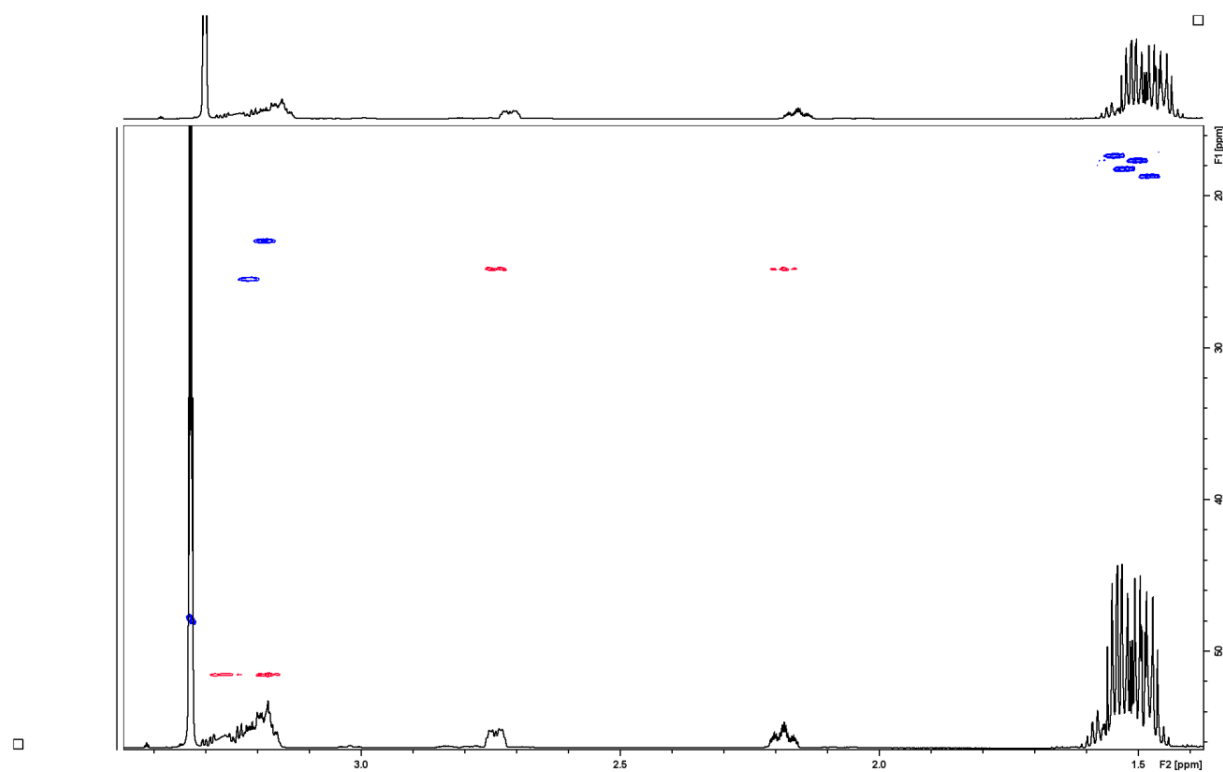


Figure S 3: HSQC NMR spectrum of **1b** with  $^1\text{H}$  NMR spectrum attached for clarity.

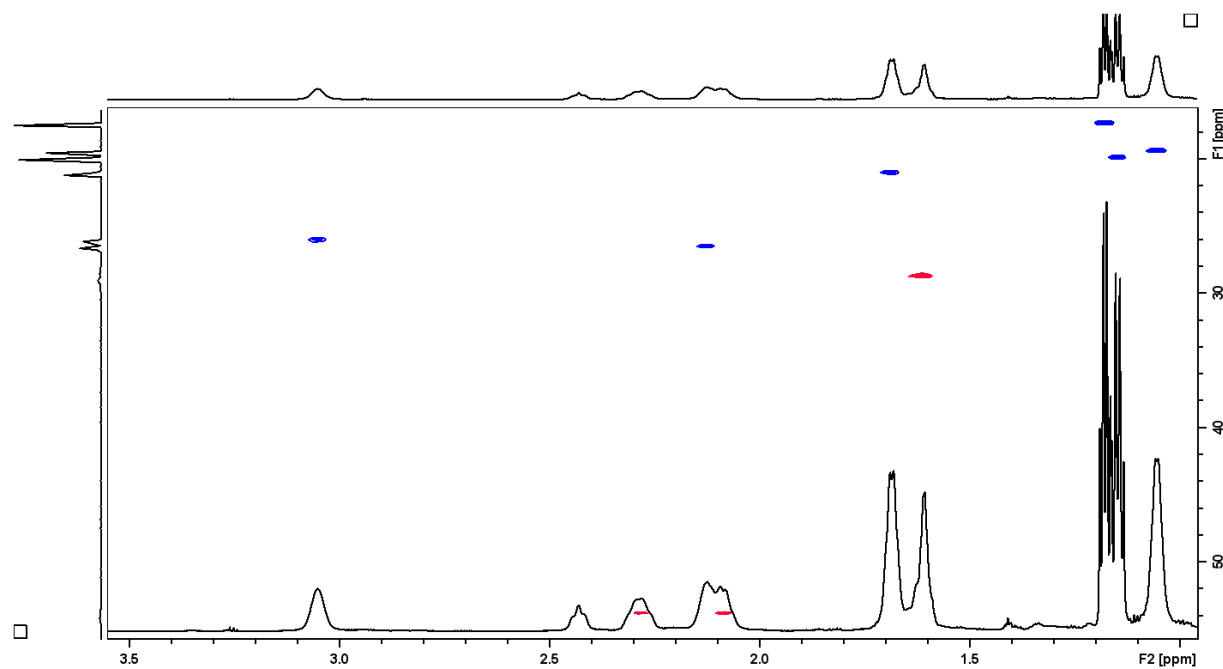


Figure S: 4 HSQC NMR spectrum of **2** with  $^1\text{H}$  NMR spectrum attached for clarity.

Supplementary Information:  
Intrinsic Geometric Distortion of 5-Coordinate Halido Complexes of Ruthenium

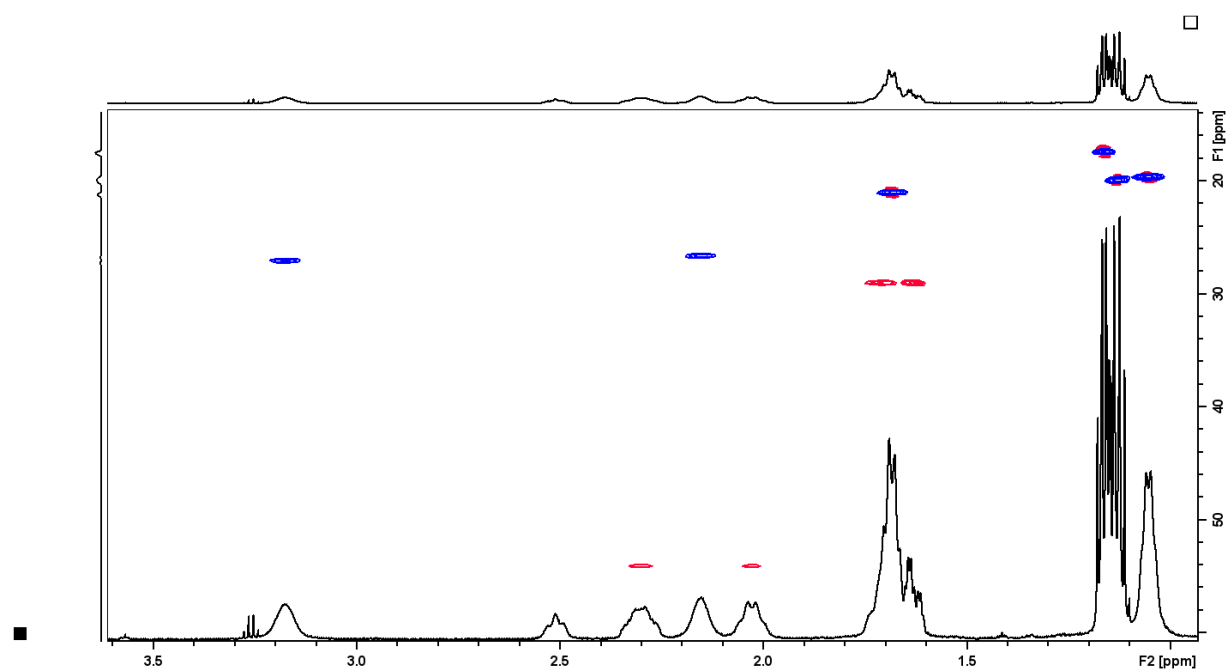


Figure S: 5 HSQC NMR spectrum of **3** with  $^1\text{H}$  NMR spectrum attached for clarity.

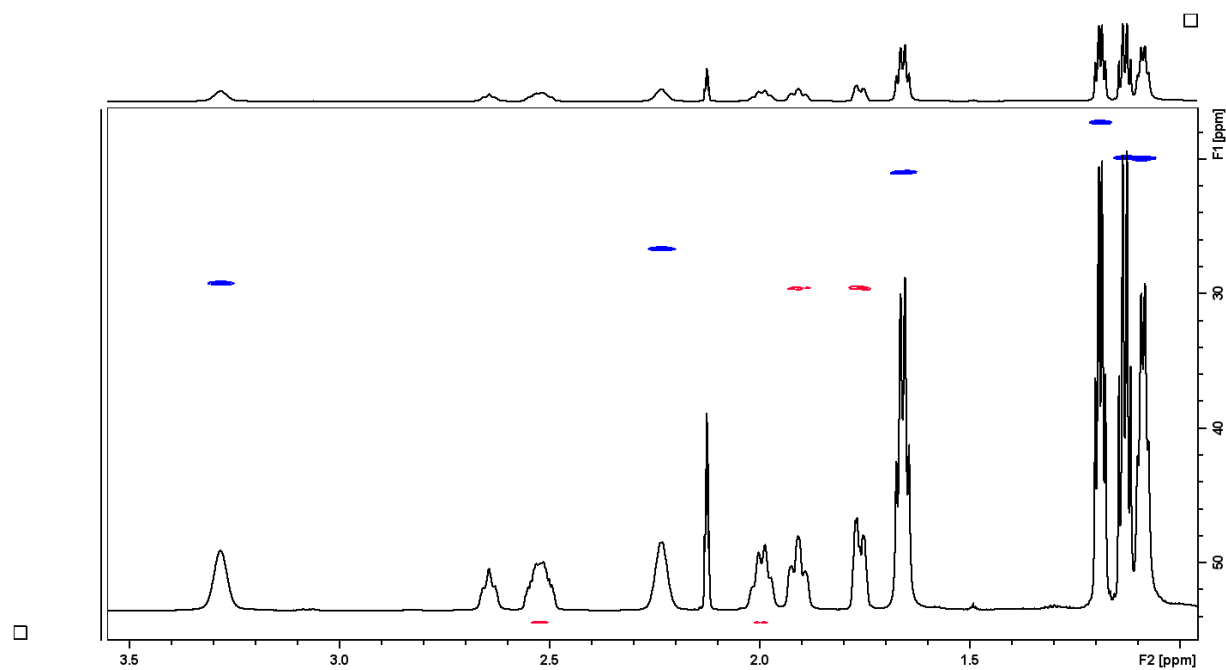


Figure S: 6 HSQC NMR spectrum of **4** with  $^1\text{H}$  NMR spectrum attached for clarity.



Supplementary Information:  
Intrinsic Geometric Distortion of 5-Coordinate Halido Complexes of Ruthenium

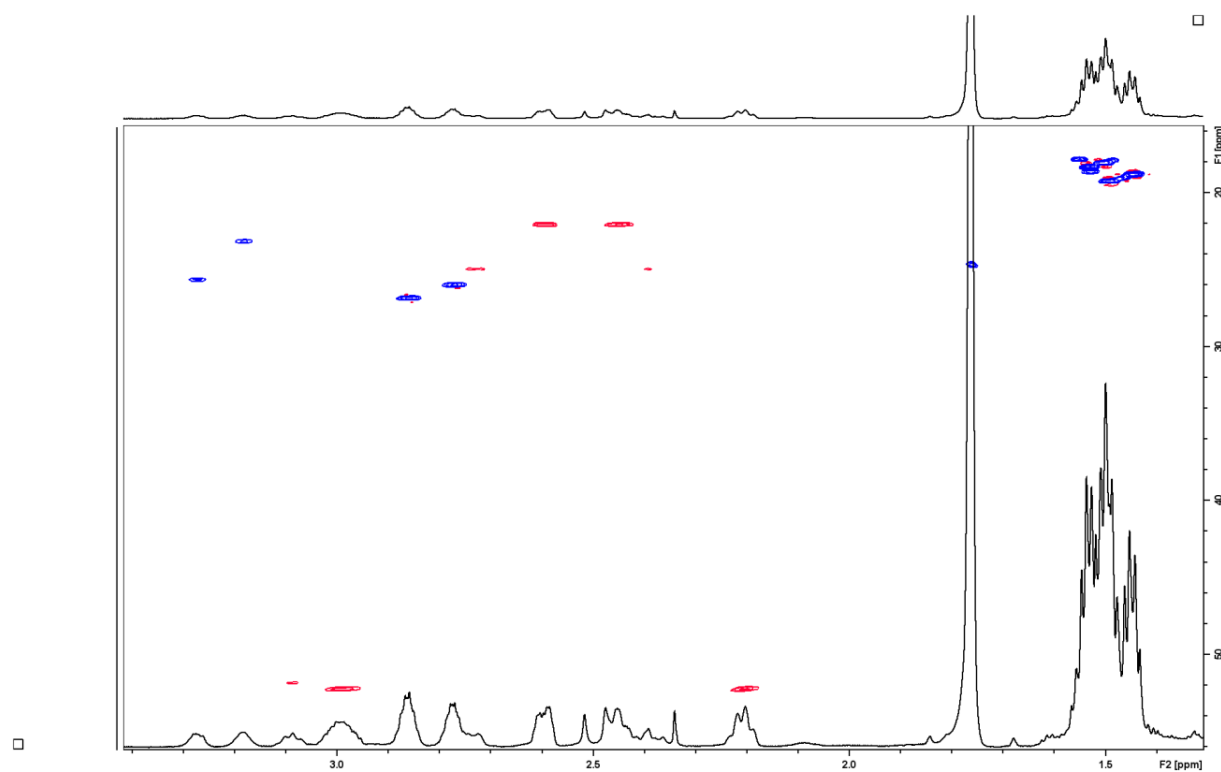


Figure S: 7 HSQC NMR spectrum of **5** with  $^1\text{H}$  NMR spectrum attached for clarity.

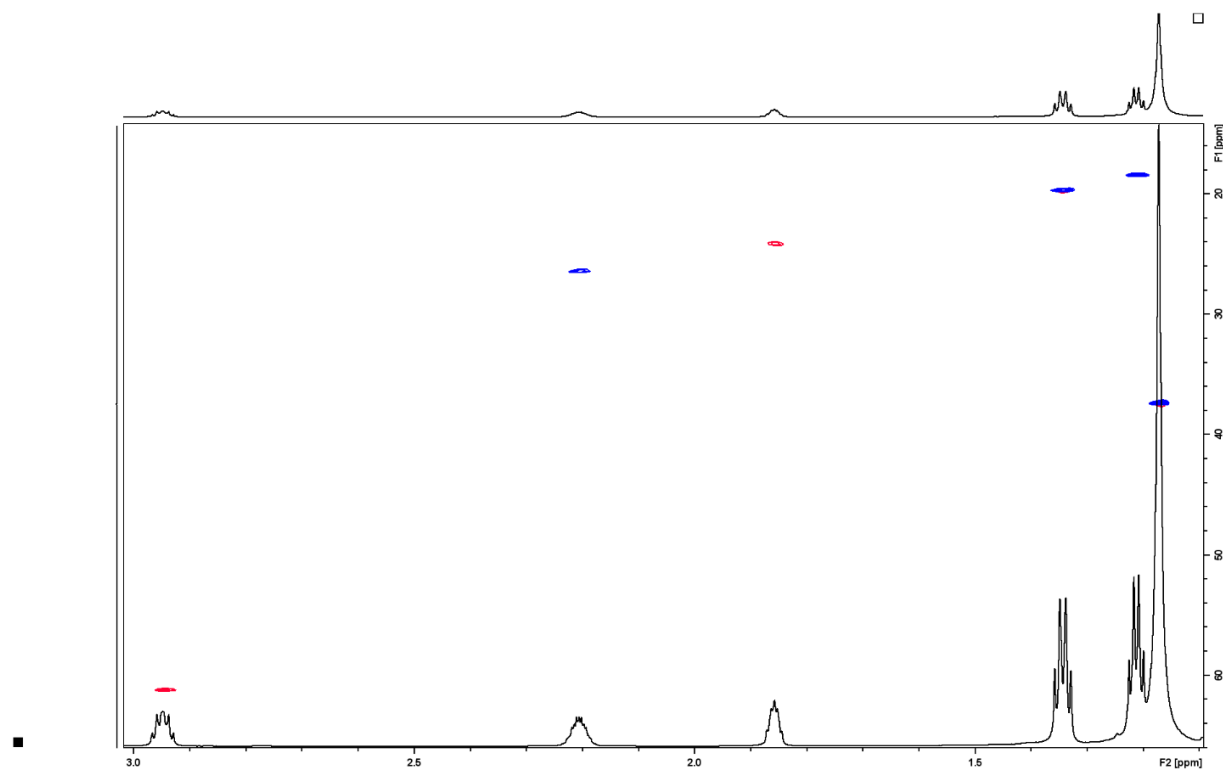


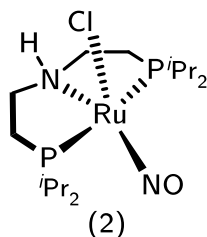
Figure S: 8 HSQC NMR spectrum of **6** with  $^1\text{H}$  NMR spectrum attached for clarity.

Supplementary Information:

Intrinsic Geometric Distortion of 5-Coordinate Halido Complexes of Ruthenium

DFT-optimised structures, xyz-coordinates

Ru	-3.8779663	5.8611499	6.6055191
P	-2.3574999	4.0685090	6.6511605
P	-4.9502949	7.9104565	7.0226401
N	-2.2831761	6.8087007	7.9405203
O	-4.9672571	5.4006630	3.9262215
N	-4.5153542	5.5899510	5.0161997
Cl	-4.4980669	5.2026828	9.0182356
C	-0.9962789	4.7081471	7.7820665
C	-1.4249161	3.5330672	5.0966591
C	-6.5316723	7.8671600	8.0541465
C	-4.2696493	1.9953747	7.0350329
C	-0.6895479	4.7230402	4.4607151
C	-3.7433260	8.7866729	8.1701219
C	-0.9370032	6.2385235	7.7485539
C	-5.2383644	9.1692598	5.6424061
C	-2.3534222	2.8512023	4.0786073
C	-3.9252115	9.4895961	4.9110437
C	-2.3150034	8.2831529	7.9424736
C	-2.8997215	2.4866169	7.5295551
C	-1.8374154	1.3804588	7.5795659
C	-7.5395017	6.8401415	7.5138953
C	-6.3191172	8.7004453	4.6543348
C	-7.1552435	9.2399539	8.3394297
H	-2.6815131	6.4535871	8.8389045
H	-1.2578714	4.3662192	8.8061238
H	-0.0095743	4.2686800	7.5276879
H	-0.6705663	2.7938216	5.4487044
H	-6.1268197	7.4360206	8.9963802
H	-4.2282965	1.5699132	6.0118026
H	-4.6484769	1.1987092	7.7096514
H	-5.0002686	2.8279389	7.0405309
H	-1.4013654	5.5342487	4.2025587
H	0.0884951	5.1484113	5.1264490
H	-0.1801402	4.3990268	3.5284836
H	-3.7959134	9.8896579	8.0589025
H	-4.0655815	8.5427977	9.2046247
H	-0.5547234	6.5984871	6.7714092
H	-0.2348745	6.6096923	8.5351188
H	-5.5954296	10.0897979	6.1574009
H	-1.7706335	2.5484603	3.1828009
H	-2.8312944	1.9387964	4.4845354
H	-3.1569841	3.5351565	3.7394999
H	-3.4778787	8.5696655	4.4808557
H	-4.1177221	10.2020934	4.0813056
H	-3.1713191	9.9595289	5.5747980

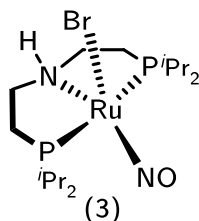


Supplementary Information:

Intrinsic Geometric Distortion of 5-Coordinate Halido Complexes of Ruthenium

H	-1.6362979	8.6916722	8.7310680
H	-1.9255050	8.6302007	6.9634596
H	-3.0674498	2.8918252	8.5521294
H	-0.8634531	1.7396474	7.9717870
H	-2.1747048	0.5591998	8.2474725
H	-1.6561494	0.9296862	6.5813669
H	-8.3560852	6.6921456	8.2516148
H	-8.0076499	7.1605102	6.5611411
H	-7.0420696	5.8639448	7.3507361
H	-7.3009773	8.5446458	5.1414571
H	-6.4605096	9.4662773	3.8625896
H	-6.0308372	7.7534259	4.1560393
H	-7.9765115	9.1377478	9.0805678
H	-6.4257681	9.9630976	8.7598751
H	-7.5975913	9.6948339	7.4287705

Ru	4.4863132	6.4360317	8.2097148
P	4.0477287	8.1773439	9.7302295
O	2.6866970	7.3487052	6.0880622
N	3.4055335	6.9661815	6.9614124
P	5.0165477	4.3419471	7.2742510
Br	7.1446785	6.8189228	8.6681337
C	5.1914483	9.6819495	9.7360461
H	6.1527452	9.1857455	9.9974359
N	4.8946567	5.2955401	10.1514820
H	5.9139527	5.5136443	10.2133282
C	4.2109313	5.8669289	11.3286589
H	3.1325528	5.6233165	11.2401676
H	4.5815126	5.3893198	12.2684051
C	4.7252152	3.8341517	10.0274496
H	5.1071095	3.3158410	10.9408160
H	3.6373286	3.6280736	9.9640799
C	6.5797842	4.1893310	6.2235652
H	7.3441842	4.4692029	6.9824557
C	4.4231534	7.3817356	11.3930361
H	3.8183963	7.8299340	12.2083430
H	5.4899053	7.6026927	11.6102926
C	5.4511757	3.3098170	8.7857931
H	6.5492834	3.4073320	8.9226301
H	5.2307216	2.2338209	8.6269025
C	3.6915344	3.3079701	6.4043843
H	4.1673080	2.3164333	6.2309559
C	2.2919712	8.8466876	9.9523507
H	2.3475631	9.5127796	10.8430000
C	1.8337222	9.6742222	8.7408172
H	2.4854101	10.5490267	8.5536412
H	1.8083435	9.0635725	7.8167475



Supplementary Information:

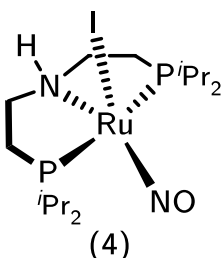
Intrinsic Geometric Distortion of 5-Coordinate Halido Complexes of Ruthenium

H	0.8064847	10.0586452	8.9164395
C	4.8592335	10.7414539	10.7961829
H	3.9208928	11.2868648	
	10.5633182		
H	4.7593538	10.3118899	
	11.8143135		
H	5.6696980	11.5001716	
	10.8411631		
C	1.3013275	7.7100829	10.2488391
H	1.3140336	6.9539414	9.4364863
H	1.5212223	7.1906346	11.2034615
H	0.2713104	8.1170463	10.3279547
C	5.3809207	10.2704849	8.3289235
H	5.6401306	9.4726263	7.6058283
H	4.4774106	10.7971900	7.9609606
H	6.2126079	11.0063244	8.3400263
C	6.6479542	5.2645643	5.1272825
H	5.9226088	5.0851696	4.3080801
H	6.4532634	6.2681185	5.5543992
H	7.6622143	5.2752933	4.6756187
C	3.2897122	3.9106056	5.0481775
H	2.5199667	3.2707320	4.5669837
H	2.8564735	4.9238930	5.1650712
H	4.1428208	3.9848586	4.3463873
C	2.4627150	3.1135280	7.3058174
H	2.0345511	4.0924760	7.6060631
H	1.6793297	2.5447592	6.7615409
H	2.6969927	2.5445230	8.2279350
C	6.8709057	2.7750215	5.7029335
H	6.8501471	2.0093222	6.5061979
H	6.1518798	2.4628682	4.9172153
H	7.8830004	2.7399394	5.2463910

Supplementary Information:

Intrinsic Geometric Distortion of 5-Coordinate Halido Complexes of Ruthenium

I	5.5450141	8.9357449	7.3846055
Ru	5.4338789	8.7153361	10.2952032
P	7.4980209	7.5796889	10.3000412
P	3.1247507	9.1857401	10.2555713
N	4.6843526	6.6576943	9.6231338
O	6.1690987	10.7645589	12.2515903
N	5.8603713	9.9072856	11.4822688
C	2.4423233	10.4563674	9.0316675
C	5.5852036	5.5441227	9.9902634
C	9.1370432	9.6229831	9.1655256
C	2.3862386	7.5826799	9.6132197
C	8.8652833	8.1114653	9.1054796
C	7.0373939	5.8804343	9.6453804
C	2.5547652	10.8342366	12.5116173
C	3.2047852	11.7900704	9.0874481
C	3.2743340	6.3928562	9.9812653
C	8.9485935	8.4668385	12.5905813
C	2.1910116	9.4821625	11.8772860
C	8.3680226	7.2004260	11.9396603
C	0.9177091	10.6339026	9.0695018
C	10.1463879	7.2671267	9.1746234
C	7.4332905	6.4649100	12.9119706
C	2.4160954	8.3323337	12.8709697
H	4.7424989	6.8038823	8.5920584
H	2.7310376	9.9704267	8.0721036
H	5.4702295	5.3704351	11.0793052
H	5.2745230	4.6046137	9.4720161
H	8.1917077	10.1949518	9.0869798
H	9.6539278	9.9267918	10.0983623
H	9.7867726	9.9198958	8.3157013
H	1.3521369	7.4296971	9.9853045
H	2.3312889	7.6862818	8.5086429
H	8.3538749	7.9233177	8.1340632
H	7.1635431	5.9296700	8.5429370
H	7.7226327	5.0941720	10.0245610
H	3.6304728	10.8862873	12.7726497
H	2.3243237	11.6906861	11.8496132
H	1.9767478	10.9750799	13.4494947
H	2.9821600	12.3708992	10.0053943
H	4.2982619	11.6192488	9.0373208
H	2.9190551	12.4204543	8.2194693
H	2.9092327	5.4688406	9.4707199



Supplementary Information:

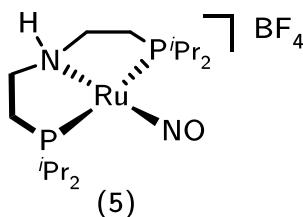
Intrinsic Geometric Distortion of 5-Coordinate Halido Complexes of Ruthenium

H	3.2406800	6.1991894	11.0726128
H	9.6901301	8.9760931	11.9454897
H	8.1546085	9.1987101	12.8377936
H	9.4634750	8.1978003	13.5372416
H	1.1158472	9.4988919	11.5895738
H	9.2060855	6.5203587	11.6673195
H	0.3714334	9.6712458	8.9951481
H	0.5789783	11.1472237	9.9935557
H	0.5898441	11.2619960	8.2139144
H	10.7154672	7.4459258	10.1106440
H	9.9473519	6.1781556	9.0996635
H	10.8196175	7.5340686	8.3325564
H	6.5136825	7.0578657	13.0980512
H	7.1288855	5.4664749	12.5386988
H	7.9467332	6.3064647	13.8838854
H	2.0144370	7.3667423	12.5036928
H	3.4978245	8.1983292	13.0797665
H	1.9026341	8.5552814	13.8302747

## Supplementary Information:

## Intrinsic Geometric Distortion of 5-Coordinate Halido Complexes of Ruthenium

Ru	1.9964844	7.9905434	9.5783857
P	2.6206012	10.2748714	9.4000123
P	1.4147650	5.7310810	9.1181704
N	2.4622621	8.0016838	7.4309429
H	3.4702814	7.7628327	7.4890294
O	1.5497703	7.9817403	12.4447093
N	1.7122305	7.9805330	11.2820248
C	2.2983933	4.3311472	10.0129301
H	2.0249039	3.4067134	9.4567864
C	1.3027136	11.5846971	9.6959005
H	1.7692069	12.5457050	9.3836136
C	1.7944980	6.9230237	6.6329101
H	0.7274399	7.2073739	6.5296759
H	2.2242147	6.8944909	5.6069634
C	3.0767492	10.4169891	7.5851647
H	2.8464687	11.4257381	7.1860680
H	4.1775117	10.2881398	7.5078595
C	4.1441088	10.8519297	10.3444792
H	3.7990965	10.8216106	11.4019359
C	1.9388311	5.5691594	7.3247756
H	2.9952569	5.2300458	7.3011831
H	1.3425161	4.7966774	6.7973338
C	2.3549334	9.3427670	6.7713386
H	2.7664222	9.2845770	5.7390144
H	1.2750229	9.5726398	6.6810490
C	5.2860958	9.8332271	10.1954453
H	4.9499753	8.8050548	10.4407948
H	5.7041152	9.8252195	9.1664772
H	6.1198134	10.0974253	10.8773522
C	0.0645047	11.3261623	8.8227613
H	0.2850937	11.3853067	7.7376993
H	-0.3758112	10.3299533	9.0386712
H	-0.7093514	12.0921634	9.0341004
C	-0.7270497	3.8399199	8.7805457
H	-0.1801892	3.4346892	7.9048166
H	-0.4827545	3.2084532	9.6579782
H	-1.8094292	3.7068377	8.5762260
C	-0.4302377	5.3252130	9.0431969
H	-0.7399185	5.9095343	8.1464145
C	0.9392032	11.6628797	11.1876228
H	0.5024413	10.7099411	11.5493297
H	1.8063544	11.9114515	11.8312051
H	0.1804169	12.4565968	11.3451019
C	3.8228295	4.5240742	9.9529573
H	4.2210305	4.5353475	8.9183952
H	4.1247376	5.4696737	10.4491844
H	4.3245956	3.6872314	10.4806911

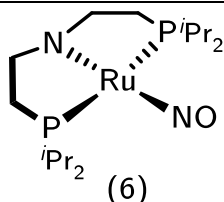


Supplementary Information:

Intrinsic Geometric Distortion of 5-Coordinate Halido Complexes of Ruthenium

C	-1.2091369	5.8874449	10.2437556
H	-0.9537788	5.3698696	11.1897083
H	-1.0136275	6.9692373	10.3819090
H	-2.2979858	5.7531070	10.0797947
C	1.8121950	4.2044219	11.4668927
H	2.0187163	5.1250567	12.0491754
H	0.7298469	3.9855459	11.5411362
H	2.3496106	3.3718688	11.9650452
C	4.5836206	12.2846491	10.0038523
H	4.8988521	12.3804530	8.9440186
H	3.7937504	13.0367808	10.1977736
H	5.4578694	12.5653600	10.6269687

Ru	-0.0555699	-0.3181043	-0.0577433
P	-0.8848422	0.4986832	-2.0849983
P	1.0270284	-0.5794270	1.9990217
N	0.9173097	1.4513660	-0.0471451
O	-1.6257771	-2.8021743	0.0074510
N	-0.9566334	-1.8178571	-0.0372197
C	0.6614297	2.5275684	-1.0034594
C	2.2023049	0.8658536	2.0051867
C	-0.6942838	-0.5429016	-3.6514749
C	0.1776777	2.0027929	-2.3615185
C	-1.0660825	0.1853835	-4.9519601
C	2.1112851	-2.1002997	2.2920899
C	-2.6720393	1.1049382	-2.1583305
C	0.7143216	-1.1555984	-3.7094298
C	1.6347360	1.9775849	1.1132637
C	0.0139926	-0.4333026	3.5857633
C	-0.9188162	-1.6451995	3.7451942
C	2.9565041	-2.3961100	1.0427066
C	2.9632912	-2.0385544	3.5688441
C	-3.6470554	-0.0774176	-2.0372566
C	-2.9242012	2.1500650	-1.0604663
C	-0.7784050	0.8831615	3.5880036
H	1.5950366	3.1264120	-1.1595556
H	-0.0836834	3.2607716	-0.5966537
H	2.4248399	1.2265477	3.0314291
H	3.1497999	0.4848383	1.5711264
H	-1.4150509	-1.3741798	-3.4846446
H	1.0454095	1.6543223	-2.9597175
H	-0.3437568	2.7864248	-2.9494343
H	-0.4013160	1.0553181	-5.1360944
H	-2.1127863	0.5498267	-4.9565643
H	-0.9537602	-0.4980010	-5.8205973





Supplementary Information:

Intrinsic Geometric Distortion of 5-Coordinate Halido Complexes of Ruthenium

H	1.3652648	-2.9193251	2.3955749
H	-2.8016701	1.5879074	-3.1529073
H	0.9715660	-1.6534593	-2.7526614
H	1.4892993	-0.3846265	-3.9036710
H	0.7775220	-1.9003345	-4.5310525
H	0.9776170	2.6513112	1.7232708
H	2.4770948	2.6325427	0.7730069
H	0.7429431	-0.4171151	4.4276744
H	-0.3666437	-2.6026872	3.8325874
H	-1.6105033	-1.7309869	2.8816565
H	-1.5343744	-1.5355665	4.6629235
H	3.7432262	-1.6276830	0.8887475
H	2.3260342	-2.4133448	0.1308241
H	3.4679502	-3.3765099	1.1462203
H	2.3543992	-1.9134726	4.4865745
H	3.6961075	-1.2048908	3.5305997
H	3.5464084	-2.9765255	3.6879319
H	-3.4931004	-0.6232693	-1.0835375
H	-3.5395734	-0.8068516	-2.8652580
H	-4.6956994	0.2877191	-2.0539969
H	-2.3010606	3.0575237	-1.1892631
H	-2.6994165	1.7235796	-0.0604040
H	-3.9874825	2.4706948	-1.0736445
H	-1.4440976	0.9368162	2.7010827
H	-0.1178291	1.7731890	3.5694196
H	-1.4048891	0.9526335	4.5024857

## Supplementary Information:

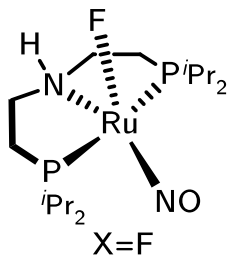
## Intrinsic Geometric Distortion of 5-Coordinate Halido Complexes of Ruthenium

C	-0.7507141	-2.1368412	0.4921739
Ru	-0.0425232	-0.1172696	0.0170440
P	2.1469326	-0.8464839	0.3654439
P	-2.2026478	0.6869650	0.3795868
N	-0.0202866	-0.0755148	2.3802210
O	0.2725322	0.8060228	-2.7489145
N	0.2122099	0.6225157	-1.5590609
C	-3.7158513	-0.3604210	-0.0921588
C	1.3428006	0.0705653	2.9183496
C	2.2637487	-2.9509668	-1.5590230
C	-2.3564577	0.7297305	2.2584354
C	2.6652179	-2.6103721	-0.1140599
C	2.3034193	-0.9139666	2.2432706
C	-2.7326214	2.6141083	-1.6517781
C	-3.6242328	-0.8770540	-1.5376307
C	-0.9872053	0.8924383	2.9261891
C	3.7595319	0.3272905	-1.6701985
C	-2.6544904	2.4590031	-0.1243250
C	3.6081972	0.2510946	-0.1424490
C	-5.0789629	0.2671504	0.2310139
C	4.1221069	-2.9793152	0.2017310
C	3.4718495	1.6575875	0.4612903
C	-1.6618297	3.4672939	0.4744275
H	-0.3561150	-1.0302503	2.5870712
H	-3.5690590	-1.2406716	0.5726346
H	1.6599421	1.1151614	2.7253407
H	1.3611815	-0.0790075	4.0273663
H	1.2249521	-2.6282232	-1.7677345
H	2.9254246	-2.4624891	-2.3022746
H	2.3320913	-4.0466259	-1.7276870
H	-3.0493310	1.5289533	2.5951978
H	-2.8126392	-0.2374500	2.5636956
H	2.0009349	-3.2049705	0.5521336
H	2.0529699	-1.9538362	2.5472357
H	3.3462904	-0.7270931	2.5741551
H	-1.7662174	2.3661533	-2.1350778
H	-3.5135584	1.9738936	-2.1059363
H	-2.9778192	3.6660482	-1.9107073
H	-3.8329528	-0.0813904	-2.2807977
H	-2.6145242	-1.2803753	-1.7498442
H	-4.3679220	-1.6851215	-1.7036368
H	-1.0890638	0.7851808	4.0354099
H	-0.5794057	1.9055664	2.7339304
H	3.9613686	-0.6604958	-2.1281852
H	2.8500844	0.7436991	-2.1473098
H	4.6108527	0.9915942	-1.9303231
H	-3.6619448	2.6460589	0.3115407

Chemical structure diagram showing a Ruthenium (Ru) complex. The Ru atom is coordinated by a bidentate ligand (likely a chiral phosphine), a monodentate phosphine (P<sup>i</sup>Pr<sub>2</sub>), a nitrosyl (NO) group, and a halide (X=OMe). The structure shows the Ru atom in the center, with the bidentate ligand forming a five-membered ring. The NO group is shown as a linear N-O bond. The X=OMe group is shown as a single bond to the Ru atom.

Supplementary Information:

Intrinsic Geometric Distortion of 5-Coordinate Halido Complexes of Ruthenium

H	4.5111504	-0.2370686	0.2884169	
H	-5.1545806	0.6089080	1.2840050	
H	-5.2996713	1.1351730	-0.4240606	
H	-5.8917145	-0.4730325	0.0683999	
H	4.8360949	-2.4408730	-0.4551718	
H	4.3997929	-2.7624699	1.2536946	
H	4.2886717	-4.0655475	0.0359675	
H	2.5132239	2.1232808	0.1510422	
H	3.5093663	1.6517656	1.5693620	
H	4.3042508	2.3038009	0.1099181	
H	-1.6868707	3.4841983	1.5826833	
H	-0.6254565	3.2285406	0.1564911	
H	-1.9070616	4.4931083	0.1262145	
H	-0.9377038	-2.6989419	-0.4485241	
H	-0.0418344	-2.7671922	1.0845532	
H	-1.7067194	-2.1841467	1.0692352	
Ru	4.1933916	6.3566744	8.2143306	
P	3.9491759	8.1403407	9.7104382	
O	1.9384452	6.9333472	6.4429154	
N	2.8909995	6.7216451	7.1386297	
P	4.9146559	4.3410827	7.2664050	
F	6.3011414	6.5655147	8.7283449	
C	5.2955413	9.4523784	9.5679630	
N	4.7275926	5.2569877	10.1343766	
C	4.1257767	5.8361710	11.3428303	
C	4.6435372	3.7943414	10.0301141	
C	6.5641611	4.4599169	6.3617418	
C	4.3520973	7.3529690	11.3788037	
C	5.3766884	3.3036048	8.7751286	
C	3.7765746	3.2132264	6.2739857	
C	2.3044490	9.0114380	10.0080425	
C	1.8721933	9.8428095	8.7891005	
C	5.2575837	10.5381426	10.6508925	
C	1.2217887	7.9878170	10.3891534	
C	5.4047870	10.0214599	8.1440926	
C	6.5501514	5.5394759	5.2677555	
C	3.4054166	3.8329261	4.9165853	
C	2.5172430	2.8783500	7.0896343	
C	7.1369306	3.1198537	5.8803652	
H	6.1819809	8.7955722	9.7122609	
H	5.7134264	5.5992535	9.9910578	
H	3.0402592	5.6011705	11.3344333	
H	4.5535282	5.3715423	12.2660615	
H	5.0791539	3.3024893	10.9354180	
H	3.5698199	3.5126307	9.9925364	
H	7.1813359	4.8650104	7.1942759	
H	3.7729653	7.8194482	12.2020976	

Supplementary Information:

Intrinsic Geometric Distortion of 5-Coordinate Halido Complexes of Ruthenium

H	5.4245351	7.5650172	11.5745639
H	6.4723886	3.4225998	8.9126057
H	5.1859703	2.2240249	8.6042612
H	4.3550033	2.2767307	6.1019138
H	2.4776983	9.6927343	10.8716847
H	2.5874129	10.6545172	8.5553219
H	1.7655879	9.2088582	7.8861302
H	0.8865247	10.3155052	8.9863365
H	4.3846038	11.2130295	10.5283392
H	5.2206933	10.1195370	11.6778000
H	6.1671278	11.1733002	10.5899311
H	1.0745490	7.2485508	9.5755543
H	1.4675489	7.4313052	11.3164534
H	0.2551597	8.5061541	10.5633104
H	5.3882207	9.2024093	7.3975792
H	4.5839019	10.7275614	7.9046377
H	6.3602529	10.5761404	8.0326715
H	5.9854542	5.2237165	4.3668322
H	6.0978684	6.4747250	5.6528340
H	7.5889632	5.7616674	4.9439547
H	2.7088032	3.1598512	4.3732264
H	2.8961932	4.8093515	5.0449949
H	4.2878220	3.9901827	4.2670219
H	1.9506508	3.7995345	7.3371885
H	1.8513305	2.2116360	6.5020234
H	2.7504900	2.3559312	8.0394629
H	7.1816689	2.3574028	6.6857079
H	6.5449305	2.6939089	5.0431422
H	8.1735074	3.2578381	5.5049922

Supplementary Information:  
Intrinsic Geometric Distortion of 5-Coordinate Halido Complexes of Ruthenium

Representative orbital plots

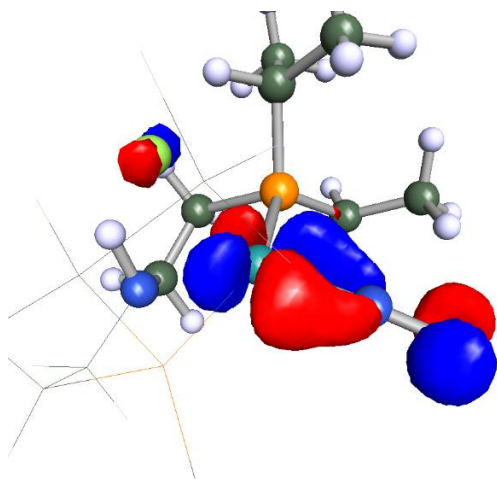


*Figure S 10* Plot of HOMO-3 orbital of the X=F compound.

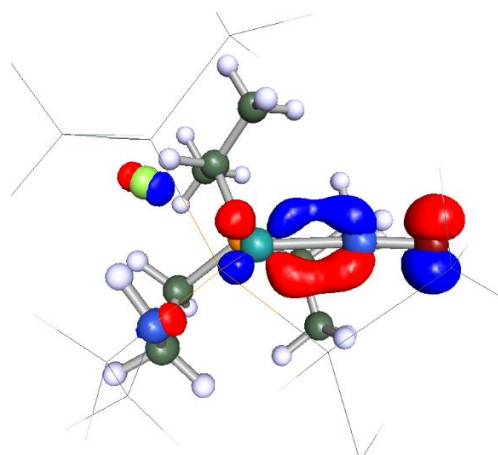


*Figure S 9*: Plot of the HOMO-2 orbital of the X=F compound.

Supplementary Information:  
Intrinsic Geometric Distortion of 5-Coordinate Halido Complexes of Ruthenium

*Table 1* Selected NPA charges for the compounds outlined in the main text.

Compound Atom	X=F	X=OMe	<b>2</b>	<b>3</b>	<b>4</b>	<b>5</b>	<b>6</b>
X	-0.73869	-0.86514	-0.66083	-0.64246	-0.61215		
N <sub>nitrosyl</sub>	0.11607	0.11590	0.12880	0.13329	0.14066	0.26757	0.16533
O <sub>nitrosyl</sub>	-0.32949	-0.33568	-0.31027	-0.30452	-0.29632	-0.20827	-0.30562
Ru	-0.00403	-0.02534	-0.09755	-0.11100	-0.12879	-0.17874	-0.18794

Supplementary Information:  
Intrinsic Geometric Distortion of 5-Coordinate Halido Complexes of Ruthenium

### Crystallographic details

Compound <b>1a</b>	
Empirical formula	C <sub>6.4</sub> H <sub>15.6</sub> Cl <sub>1.2</sub> N <sub>0.8</sub> O <sub>0.4</sub> P <sub>0.8</sub> Ru <sub>0.4</sub>
Formula weight	217.948
Temperature/K	120.00(14)
Crystal system	monoclinic
Space group	P2 <sub>1</sub> /m
a/Å	7.8026(2)
b/Å	11.8728(6)
c/Å	13.7802(4)
α/°	90
β/°	106.215(3)
γ/°	90
Volume/Å <sup>3</sup>	1225.80(8)
Z	5
ρ <sub>calc</sub> /g/cm <sup>3</sup>	1.476
μ/mm <sup>-1</sup>	9.479
F(000)	568.7
Crystal size/mm <sup>3</sup>	0.05 × 0.02 × 0.5
Radiation	Cu Kα (λ = 1.54184)
2θ range for data collection/°	10 to 153.6
Index ranges	-9 ≤ h ≤ 8, -13 ≤ k ≤ 14, -17 ≤ l ≤ 16
Reflections collected	12085
Independent reflections	2679 [R <sub>int</sub> = 0.0396, R <sub>sigma</sub> = 0.0301]
Data/restraints/parameters	2679/0/291
Goodness-of-fit on F <sup>2</sup>	1.069
Final R indexes [I > 2σ (I)]	R <sub>1</sub> = 0.0259, wR <sub>2</sub> = 0.0604
Final R indexes [all data]	R <sub>1</sub> = 0.0322, wR <sub>2</sub> = 0.0644
Largest diff. peak/hole / e Å <sup>-3</sup>	0.69/-0.54

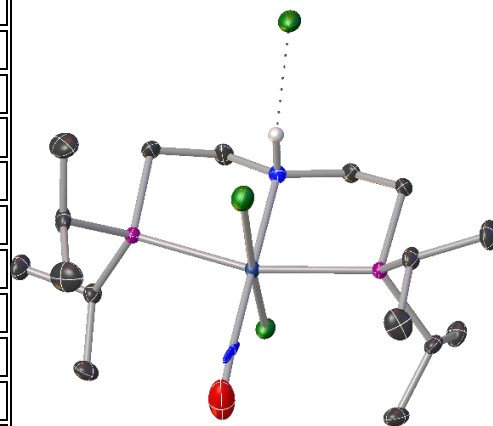


Figure S 11: Crystal structure of **1a**

## Supplementary Information:

## Intrinsic Geometric Distortion of 5-Coordinate Halido Complexes of Ruthenium

Compound <b>1b</b>	
Empirical formula	C <sub>12.8</sub> H <sub>29.6</sub> B <sub>0.8</sub> Cl <sub>1.6</sub> F <sub>3.2</sub> N <sub>1.6</sub> O <sub>0.8</sub> P <sub>1.6</sub> Ru <sub>0.8</sub>
Formula weight	475.376
Temperature/K	120
Crystal system	orthorhombic
Space group	Pbca
a/Å	12.85248(8)
b/Å	12.37239(10)
c/Å	31.3953(2)
$\alpha/^\circ$	90
$\beta/^\circ$	90
$\gamma/^\circ$	90
Volume/Å <sup>3</sup>	4992.36(6)
Z	10
$\rho_{\text{calc}}/\text{g/cm}^3$	1.581
$\mu/\text{mm}^{-1}$	8.636
F(000)	2450.3
Crystal size/mm <sup>3</sup>	0.2 × 0.05 × 0.05
Radiation	Cu K $\alpha$ ( $\lambda$ = 1.54184)
2 $\theta$ range for data collection/ $^\circ$	8.9 to 153.52
Index ranges	-10 ≤ h ≤ 16, -15 ≤ k ≤ 15, -39 ≤ l ≤ 39
Reflections collected	75751
Independent reflections	5250 [R <sub>int</sub> = 0.0404, R <sub>sigma</sub> = 0.0161]
Data/restraints/parameters	5250/0/396
Goodness-of-fit on F <sup>2</sup>	1.075
Final R indexes [I > 2 $\sigma$ (I)]	R <sub>1</sub> = 0.0221, wR <sub>2</sub> = 0.0547
Final R indexes [all data]	R <sub>1</sub> = 0.0263, wR <sub>2</sub> = 0.0587
Largest diff. peak/hole / e Å <sup>-3</sup>	0.83/-0.32



Supplementary Information:  
Intrinsic Geometric Distortion of 5-Coordinate Halido Complexes of Ruthenium

Compound 2	
Empirical formula	C <sub>14.22</sub> H <sub>32.89</sub> Cl <sub>0.89</sub> N <sub>1.78</sub> O <sub>0.89</sub> P <sub>1.78</sub> Ru <sub>0.89</sub>
Formula weight	419.50
Temperature/K	293(2)
Crystal system	monoclinic
Space group	P2 <sub>1</sub> /n
a/Å	20.6317(3)
b/Å	10.63432(12)
c/Å	20.7902(3)
α/°	90
β/°	107.5495(14)
γ/°	90
Volume/Å <sup>3</sup>	4349.15(10)
Z	9
ρ <sub>calc</sub> /g/cm <sup>3</sup>	1.442
μ/mm <sup>-1</sup>	8.390
F(000)	1968.0
Crystal size/mm <sup>3</sup>	0.05 × 0.2 × 0.23
Radiation	CuKα (λ = 1.54184)
2θ range for data collection/°	7.222 to 153.684
Index ranges	-21 ≤ h ≤ 25, -13 ≤ k ≤ 13, -26 ≤ l ≤ 25
Reflections collected	73385
Independent reflections	9148 [R <sub>int</sub> = 0.0478, R <sub>sigma</sub> = 0.0226]
Data/restraints/parameters	9148/0/638
Goodness-of-fit on F <sup>2</sup>	1.060
Final R indexes [I > 2σ (I)]	R <sub>1</sub> = 0.0243, wR <sub>2</sub> = 0.0586
Final R indexes [all data]	R <sub>1</sub> = 0.0304, wR <sub>2</sub> = 0.0621
Largest diff. peak/hole / e Å <sup>-3</sup>	0.52/-0.89

Supplementary Information:  
Intrinsic Geometric Distortion of 5-Coordinate Halido Complexes of Ruthenium

Compound <b>3</b>	
Empirical formula	C <sub>12.8</sub> H <sub>29.6</sub> Br <sub>0.8</sub> N <sub>1.6</sub> O <sub>0.8</sub> P <sub>1.6</sub> Ru <sub>0.8</sub>
Formula weight	413.11
Temperature/K	119.98(10)
Crystal system	monoclinic
Space group	P2 <sub>1</sub> /n
a/Å	11.6241(2)
b/Å	13.6495(3)
c/Å	14.3557(2)
α/°	90
β/°	98.609(2)
γ/°	90
Volume/Å <sup>3</sup>	2252.06(7)
Z	5
ρ <sub>calc</sub> /cm <sup>3</sup>	1.523
μ/mm <sup>-1</sup>	2.618
F(000)	1056.0
Crystal size/mm <sup>3</sup>	0.02 × 0.2 × 0.1
Radiation	Mo Kα (λ = 0.71073)
2θ range for data collection/°	6.47 to 59.374
Index ranges	-15 ≤ h ≤ 15, -18 ≤ k ≤ 18, -18 ≤ l ≤ 20
Reflections collected	42958
Independent reflections	5926 [R <sub>int</sub> = 0.0425, R <sub>sigma</sub> = 0.0271]
Data/restraints/parameters	5926/0/216
Goodness-of-fit on F <sup>2</sup>	1.073
Final R indexes [I > 2σ (I)]	R <sub>1</sub> = 0.0278, wR <sub>2</sub> = 0.0659
Final R indexes [all data]	R <sub>1</sub> = 0.0357, wR <sub>2</sub> = 0.0698
Largest diff. peak/hole / e Å <sup>-3</sup>	0.87/-0.76

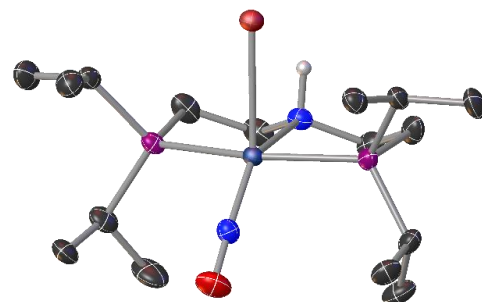


Figure S: 12 Crystal structure of **3**

Supplementary Information:  
Intrinsic Geometric Distortion of 5-Coordinate Halido Complexes of Ruthenium

Compound <b>4</b>	
Empirical formula	C <sub>10.67</sub> H <sub>24.67</sub> I <sub>0.67</sub> N <sub>1.33</sub> O <sub>0.67</sub> P <sub>1.33</sub> Ru <sub>0.67</sub>
Formula weight	375.601
Temperature/K	120.15
Crystal system	monoclinic
Space group	P2 <sub>1</sub> /n
a/Å	11.7201(3)
b/Å	13.6883(3)
c/Å	14.4385(3)
α/°	90
β/°	97.710(2)
γ/°	90
Volume/Å <sup>3</sup>	2295.40(9)
Z	6
ρ <sub>calc</sub> /cm <sup>3</sup>	1.630
μ/mm <sup>-1</sup>	2.173
F(000)	1122.6
Crystal size/mm <sup>3</sup>	0.2 × 0.3 × 0.5
Radiation	Mo Kα (λ = 0.71073)
2θ range for data collection/°	6.6 to 59.34
Index ranges	-15 ≤ h ≤ 16, -17 ≤ k ≤ 18, -20 ≤ l ≤ 20
Reflections collected	44583
Independent reflections	6050 [R <sub>int</sub> = 0.0540, R <sub>sigma</sub> = 0.0358]
Data/restraints/parameters	6050/0/316
Goodness-of-fit on F <sup>2</sup>	1.189
Final R indexes [I > 2σ (I)]	R <sub>1</sub> = 0.0283, wR <sub>2</sub> = 0.0513
Final R indexes [all data]	R <sub>1</sub> = 0.0468, wR <sub>2</sub> = 0.0637
Largest diff. peak/hole / e Å <sup>-3</sup>	1.56/-0.98

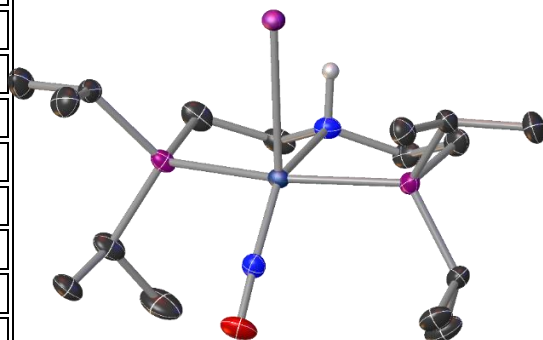


Figure S: 13 crystal structure of **4**

## Supplementary Information:

## Intrinsic Geometric Distortion of 5-Coordinate Halido Complexes of Ruthenium

Compound 5	
Empirical formula	C <sub>12.8</sub> H <sub>29.6</sub> B <sub>0.8</sub> F <sub>3.2</sub> N <sub>1.6</sub> O <sub>0.8</sub> P <sub>1.6</sub> Ru <sub>0.8</sub>
Formula weight	418.652
Temperature/K	119.99(14)
Crystal system	monoclinic
Space group	P2 <sub>1</sub> /c
a/Å	8.4411(4)
b/Å	11.3123(5)
c/Å	24.7636(10)
α/°	90
β/°	92.257(4)
γ/°	90
Volume/Å <sup>3</sup>	2362.80(18)
Z	5
ρ <sub>calc</sub> /g/cm <sup>3</sup>	1.471
μ/mm <sup>-1</sup>	7.010
F(000)	1086.1
Crystal size/mm <sup>3</sup>	0.1 × 0.05 × 0.01
Radiation	Cu Kα (λ = 1.54184)
2θ range for data collection/°	7.14 to 153.08
Index ranges	-10 ≤ h ≤ 10, -14 ≤ k ≤ 13, -30 ≤ l ≤ 31
Reflections collected	12504
Independent reflections	4799 [R <sub>int</sub> = 0.0373, R <sub>sigma</sub> = 0.0413]
Data/restraints/parameters	4799/40/327
Goodness-of-fit on F <sup>2</sup>	1.069
Final R indexes [I > 2σ (I)]	R <sub>1</sub> = 0.0445, wR <sub>2</sub> = 0.0933
Final R indexes [all data]	R <sub>1</sub> = 0.0549, wR <sub>2</sub> = 0.0981
Largest diff. peak/hole / e Å <sup>-3</sup>	0.72/-0.48

Supplementary Information:  
Intrinsic Geometric Distortion of 5-Coordinate Halido Complexes of Ruthenium

Compound <b>6</b>	
Empirical formula	C <sub>5.82</sub> H <sub>13.09</sub> N <sub>0.73</sub> O <sub>0.36</sub> P <sub>0.73</sub> Ru <sub>0.36</sub>
Formula weight	158.35
Temperature/K	120.02(13)
Crystal system	triclinic
Space group	P-1
a/Å	7.5909(3)
b/Å	13.3883(4)
c/Å	21.9117(7)
$\alpha/^\circ$	97.039(2)
$\beta/^\circ$	98.845(3)
$\gamma/^\circ$	106.408(3)
Volume/Å <sup>3</sup>	2078.16(13)
Z	11
$\rho_{\text{calc}}/\text{g/cm}^3$	1.392
$\mu/\text{mm}^{-1}$	7.578
F(000)	912.0
Crystal size/mm <sup>3</sup>	0.005 × 0.01 × 0.015
Radiation	Cu K $\alpha$ ( $\lambda$ = 1.54184)
2 $\theta$ range for data collection/ $^\circ$	6.99 to 153.816
Index ranges	-9 ≤ h ≤ 9, -16 ≤ k ≤ 14, -27 ≤ l ≤ 25
Reflections collected	21788
Independent reflections	8637 [R <sub>int</sub> = 0.0293, R <sub>sigma</sub> = 0.0371]
Data/restraints/parameters	8637/0/414
Goodness-of-fit on F <sup>2</sup>	1.048
Final R indexes [I > 2 $\sigma$ (I)]	R <sub>1</sub> = 0.0292, wR <sub>2</sub> = 0.0731
Final R indexes [all data]	R <sub>1</sub> = 0.0340, wR <sub>2</sub> = 0.0767
Largest diff. peak/hole / e Å <sup>-3</sup>	0.97/-1.03